Research Topics

Advances in reservoir modeling and simulation

Edited by
Jinze Xu, Zhangxing Chen, Jinghong Hu, Keliu Wu and Desheng Zhou

Published in
Frontiers in Earth Science

ISSN 1664-8714
ISBN 978-2-83251-127-5
DOI 10.3389/978-2-83251-127-5

About Frontiers

Frontiers is more than just an open access publisher of scholarly articles: it is a pioneering approach to the world of academia, radically improving the way scholarly research is managed. The grand vision of Frontiers is a world where all people have an equal opportunity to seek, share and generate knowledge. Frontiers provides immediate and permanent online open access to all its publications, but this alone is not enough to realize our grand goals.

Frontiers journal series

The Frontiers journal series is a multi-tier and interdisciplinary set of open-access, online journals, promising a paradigm shift from the current review, selection and dissemination processes in academic publishing. All Frontiers journals are driven by researchers for researchers; therefore, they constitute a service to the scholarly community. At the same time, the *Frontiers journal series* operates on a revolutionary invention, the tiered publishing system, initially addressing specific communities of scholars, and gradually climbing up to broader public understanding, thus serving the interests of the lay society, too.

Dedication to quality

Each Frontiers article is a landmark of the highest quality, thanks to genuinely collaborative interactions between authors and review editors, who include some of the world's best academicians. Research must be certified by peers before entering a stream of knowledge that may eventually reach the public - and shape society; therefore, Frontiers only applies the most rigorous and unbiased reviews. Frontiers revolutionizes research publishing by freely delivering the most outstanding research, evaluated with no bias from both the academic and social point of view. By applying the most advanced information technologies, Frontiers is catapulting scholarly publishing into a new generation.

What are Frontiers Research Topics?

Frontiers Research Topics are very popular trademarks of the *Frontiers journals series*: they are collections of at least ten articles, all centered on a particular subject. With their unique mix of varied contributions from Original Research to Review Articles, Frontiers Research Topics unify the most influential researchers, the latest key findings and historical advances in a hot research area.

Find out more on how to host your own Frontiers Research Topic or contribute to one as an author by contacting the Frontiers editorial office: frontiersin.org/about/contact

Advances in reservoir modeling and simulation

Topic editors
Jinze Xu — University of Calgary, Canada
Zhangxing Chen — University of Calgary, Canada
Jinghong Hu — China University of Geosciences, China
Keliu Wu — China University of Petroleum, China
Desheng Zhou — Xi'an Shiyou University, China

Citation
Xu, J., Chen, Z., Hu, J., Wu, K., Zhou, D., eds. (2023). *Advances in reservoir modeling and simulation*. Lausanne: Frontiers Media SA. doi: 10.3389/978-2-83251-127-5

Table of contents

frontiers | Frontiers in Earth Science

TYPE Editorial
PUBLISHED 09 December 2022
DOI 10.3389/feart.2022.1106622

OPEN ACCESS

EDITED AND REVIEWED BY
Alexander Kokhanovsky,
German Research Centre for
Geosciences, Germany

*CORRESPONDENCE
Jinze Xu,
✉ jinzxu@ucalgary.ca

SPECIALTY SECTION
This article was submitted to
Environmental Informatics and Remote
Sensing,
a section of the journal
Frontiers in Earth Science

RECEIVED 24 November 2022
ACCEPTED 02 December 2022
PUBLISHED 09 December 2022

CITATION
Xu J, Chen Z, Hu J, Wu K and Zhou D
(2022), Editorial: Advances in reservoir
modelling and simulation.
Front. Earth Sci. 10:1106622.
doi: 10.3389/feart.2022.1106622

Editorial: Advances in reservoir modelling and simulation

Jinze Xu[1,2]*, Zhangxing Chen[1], Jinghong Hu[3], Keliu Wu[4] and Desheng Zhou[2]

[1]Department of Chemical and Petroleum Engineering, University of Calgary, Calgary, AB, Canada, [2]College of Petroleum Engineering, Xi'an Shiyou University, Xi'an, Shaanxi, China, [3]Beijing Key Laboratory of Unconventional Natural Gas Geology Evaluation and Development Engineering, China University of Geosciences, Beijing, China, [4]State Key Laboratory of Petroleum Resources and Prospecting in China University of Petroleum (Beijing), Beijing, China

KEYWORDS

reservoir simulation, reservoir modelling, unconventional reservoir, shale gas, shale oil

Editorial on the Research Topic
Advances in reservoir modelling and simulation

In light of the current energy crisis, the development of oil and gas resources must adhere to a higher standard of both efficiency and precision. Reservoir simulation and modelling has been a significant tool in increasing oil and gas recovery. Engineers are able to better visualize the subsurface environment, study fluid dynamics, and come up with ideas for production improvement by applying reservoir simulation and modelling (Fanchi, 2005; Islam et al., 2016). The growing complexity of reservoirs promotes the further advancement of reservoir modelling and simulation. In recent years, there has been a significant development in the investigation of reservoir modelling and simulation, particularly in the fields of heavy oil, shale gas, and shale oil. For instance, in the numerical simulation of heavy oil reservoirs, large-scale reservoir models directly serve production, and certain heterogeneity, such as lean zone, can also be successfully examined (Xu et al., 2014; Xu et al., 2016). The flow law of gas at the micro and nano scales is transferred to the real field size in the numerical modelling of the shale gas reservoir (Xu et al., 2017; Xu et al., 2018; Xu et al., 2019). The simulation technology of *in-situ* conversion is emerging at a quick pace with considering the effects of thermochemical reaction and thermophysical reaction on the production process (Xu et al., 2021).

This special issue gives a summary of the most current advancements in numerical reservoir modelling. We shall outline briefly to present this special issue:

To improve gas reservoir development, Xiao et al. built a CBM (coalbed methane) prediction model for wells. In this study, the influence of coal characteristics and reservoir geology conditions on CBM production was examined. They discovered that a larger absorption capacity increases CBM production.

Wang et al. used numerical and physical simulation to investigate the water control process in a gas field. In addition, their research revealed that the water-blocking and water-sensing capacities affect the water control process. The use of a continuous packer is suggested based on simulation findings.

Using panel data modelling and simulation methods, Shi et al. evaluated China's oil resources. In this study, the Malmquist-Luenberger Index was used to more accurately measure the static efficiency of time nodes. Their research demonstrated that the development of oil fields in China's eastern area is superior to the west.

Cai et al. used deep learning into the indicator modelling and simulation. In this study, the AlexNet model was enhanced by adding more convolution layers. The comparison to actual working situations revealed that the model presented in this study is greatly enhanced in terms of estimation precision.

The influence of natural gas hydrates on the pressure of a deep-water pipeline was anticipated by Mo et al. In this study, a mathematical model connecting pipeline flow and hydrate volume is constructed. The modelling findings indicate that hydrate development will result in a more severe pipeline obstruction.

Deng et al. analyzed the production of a multilayer heterogeneous reservoir using a production model that took experimental data into account. Their research shown that an increase in the permeability gradient increases oil output, with the high-permeability layer contributing more to oil recovery.

To analyze the flow efficiency, Li et al. devised a gas/water relative permeability model based on fractal theory. In this study, the authors linked the geomechanical equation, the flow equation, and the fractal equation to demonstrate that stress and slip flow jointly govern the gas/water flow efficiency. Also noted is the link between wettability and relative permeability.

Liu et al. conducted research on the mechanism of hydraulic fracture propagation in infill horizontal wells. Based on geomechanical models, they examined the interactions between original fractures and artificial fractures. Their research revealed that fracture spacing and well spacing influence the propagation trajectory.

Author contributions

JX-Draft manuscript; ZC, JH, KW, and DZ-Review and revision.

Conflict of interest

The authors declare that the research was conducted in the absence of any commercial or financial relationships that could be construed as a potential conflict of interest.

Publisher's note

References

Fanchi, J. R. (2005). *Principles of applied reservoir simulation*. Amsterdam, Netherlands: Elsevier.

Islam, M. R., Abou-Kassem, J. H., Hossain, M. E., Mousavizadegan, S. H., and Mustafiz, S. (2016). *Advanced petroleum reservoir simulation: Towards developing reservoir emulators*. Hoboken, NJ: John Wiley & Sons.

Xu, J., Chen, Z., and Li, R. (2014). *3D Geological modeling and uncertainty analysis of pilot pad in the Long Lake field with lean zone and shale layer.GeoConvention*

Xu, J., Chen, Z., Wu, K., Li, R., Liu, X., and Zhan, J. (2019). *On the flow regime model for fast estimation of tight sandstone gas apparent permeability in high-pressure reservoirs*. London, UK: Energy Sources, Part A: Recovery, Utilization, and Environmental Effects, 1–12.

Xu, J., Chen, Z., Zhou, D., Nie, W., and Li, R. (2021). Review on the characteristics of pyrolysis during *in-situ* conversion of oil shale. *J. Southwest Petroleum Univ. Sci. Technol. Ed.* 43 (5), 220.

Xu, J., Pan, Y., and Chen, Z. (2016). "Understanding impacts of lean zones on thermal recovery in view of mobile water," in SPE Canada Heavy Oil Technical Conference (Calgary, Canada: OnePetro).

Xu, J., Wu, K., Li, Z., Pan, Y., Li, R., Li, J., et al. (2018). A model for gas transport in dual-porosity shale rocks with fractal structures. *Ind. Eng. Chem. Res.* 57 (18), 6530–6537. doi:10.1021/acs.iecr.8b00021

Xu, J., Wu, K., Yang, S., Cao, J., and Chen, Z. (2017). "Nanoscale free gas transport in shale rocks: A hard-sphere based model," in SPE Unconventional Resources Conference (Calgary, Canada: OnePetro).

frontiers | Frontiers in Earth Science

ORIGINAL RESEARCH
published: 27 May 2022
doi: 10.3389/feart.2022.906949

Evaluation of the Effectiveness and Adaptability of a Composite Water Control Process for Horizontal Wells in Deepwater Gas Reservoirs

Dianju Wang[1,2,3]*, **Yihe Li**[4], **Lan Ma**[5], **Fahao Yu**[6], **Shufen Liu**[4], **Tong Qi**[1] **and Siyuan Jiang**[1]

[1]Heilongjiang Key Laboratory of Gas Hydrate Efficient Development, Daqing, China, [2]College of Offshore Oil and Gas Engineering, Northeast Petroleum University, Daqing, China, [3]Sanya Offshore Oil and Gas Research Institute, Northeast Petroleum University, Sanya, China, [4]College of Earth Science, Northeast Petroleum University, Daqing, China, [5]Northeast Petroleum University Qinhuangdao, Northeast Petroleum University, Qinhuangdao, China, [6]Bohai Oilfield Research Institute of CNOOC Ltd., Tianjin, China

Edited by:
Jinze Xu,
University of Calgary, Canada

Reviewed by:
Jun Zhou,
Southwest Petroleum University, China
Zhiyuan Wang,
China University of Petroleum, Huadong, China
Li Zhonghui,
Yangtze University, China

***Correspondence:**
Dianju Wang
djwang@nepu.edu.cn

Specialty section:
This article was submitted to Environmental Informatics and Remote Sensing,
a section of the journal Frontiers in Earth Science

Received: *29 March 2022*
Accepted: *08 April 2022*
Published: *27 May 2022*

Citation:
Wang D, Li Y, Ma L, Yu F, Liu S, Qi T and Jiang S (2022) Evaluation of the Effectiveness and Adaptability of a Composite Water Control Process for Horizontal Wells in Deepwater Gas Reservoirs.
Front. Earth Sci. 10:906949.
doi: 10.3389/feart.2022.906949

Deepwater gas fields have high bottom water energy and a high risk of seeing water. Higher requirements are put forward for the water control process to control the water effect. This article is based on the actual background and well design of the X gas field in the South China Sea and on three sets of physical simulation experiments and three sets of numerical simulation experiments. An analysis and comparison of the water control effect of a combination of continuous packer, continuous packer and variable density screen tube, and their adaptability evaluation in deepwater gas reservoirs were performed. The results obtained from the numerical and physical simulations are consistent. The experimental results show that the water control process of a continuous packer is mainly based on the water-seeing and water-blocking ability. It is less capable of extending the time to produce water in the horizontal section. However, its water-blocking ability is strong and is able to seal the water spot quickly. It extends the total production time by 12.29% and increases the total gas production by 5.96%; the combined water control process of the continuous packer and variable density screen tube can effectively play their respective advantages of water control. The combination of the continuous packer and variable density screen tube can effectively be advantageous of their respective water control processes, enabling the gas–water interface to advance in a balanced manner, extending the water-free gas recovery period by 11.61%, extending the total gas production time by 15.76%, and increasing the total gas production volume by 13.75%. Both water control processes have good applicability in deepwater gas fields and have certain sand control capability. It is conducive to the one-time completion operation for the commissioning of deepwater gas fields.

Keywords: deepwater gas field, water control process, continuous packer, variable density screen tube, physical simulation

INTRODUCTION

As China's gas reservoir exploration and development in the Southeast Qiongdongnan Basin moves toward deeper water, some of the reservoirs are experiencing difficulty in moving water reserves (Chen et al., 2020). This is especially true in terms of gas reservoir production seeing water. The Lingshui 25–1 gas field, for example, faces a water depth of nearly 1,000 m. The design well depth is nearly 4,000 m, the pressure coefficient of the target layer is 1.7–1.9, and the temperature reaches 150°C. In the gas reservoir production environment (Shi, 2015), there are challenges of high bottom water multiples and high energy (Chen et al., 2020). These place higher demands on the water control process and its effectiveness during extraction. By increasing the contact area between the wellbore and the reservoir, the production capacity can be effectively increased. Especially in deepwater gas reservoirs, horizontal wells have become the main production well type. However, the problem of excessive water production has also become more prominent (Sun and Bai, 2017). At present, domestic and foreign horizontal well water control processes are widely used mainly in oil reservoirs. The compressibility of natural gas allows it to be extracted at a higher seepage rate than oil wells, and water intrusion poses a greater risk to gas reservoir development than to oil reservoir development (Xu et al., 2018; Xu et al., 2021).The ability of horizontal wells to produce gas rapidly decreases or even stops when water is present. As a result, the implementation of simple "drainage" and "plugging" water control techniques at a later stage is limited (Wang et al., 2001). A combination of pre- and post-water control techniques needs to be applied. Therefore, there is still much room for exploration of water control techniques for gas reservoirs and their effective implementation. A great deal of research and experimentation has been carried out on water control techniques for horizontal wells. However, they have mainly been applied to oil reservoirs. Considering the high temperature and high pressure production background and characteristics of deepwater gas reservoirs, in this study, it is concluded that both the variable density screen tube and continuous packer water control processes have good water control effects in gas reservoirs.

The principle of the variable density screen tube water control process is to compare the non-homogeneity of the producing formation in horizontal wells. Changing the horizontal well borehole density effectively delays the bottom water or gas top cone entry time in horizontal wells (Zhou, 2007; Pang et al., 2012). Horizontal wells use a low borehole density in the high-permeability section of the producing formation to reduce the rate of inflow at this location. High-density boreholes are used in the low-permeability section of the formation to increase the rate of inflow at this location, equalising the rate of bottom water rise throughout the horizontal section and preventing early cone in of bottom water and see water (Zhou, 2007; Wei et al., 2009; Li et al., 2010). Due to the limitations of the process technology, it is not possible to achieve a completely uniform inflow profile by varying the density of the orifice (Xu et al., 2019; Xu et al., 2020). Hence, it is necessary to improve this by staging different density orifices (Sun et al., 2011). However, the effectiveness of segmented variable density water control is guaranteed by the requirement that the different sections of the borehole have the desired inflow velocity (Wei et al., 2009). Therefore, this requires that in practice, a packer is placed between each section to achieve out-of-tube containment. The packers have high sealing capacity and stability (Rao et al., 2010). However, the high temperature and pressure conditions in deepwater gas reservoirs place higher demands on the packers used in horizontal well section completions (Zhao et al., 2012). In addition, considering that non-uniform flow of crude oil is due to reservoir non-homogeneity and frictional pressure drop along the wellbore, one practical way to reduce this problem is to use inflow control devices between packers by adjusting the inflow and distribution of production within each isolated section (Sun et al., 2011; Wang et al., 2011; Irani et al., 2021). However, the device itself and the packers used in conjunction with it need to meet both high-temperature and high-pressure conditions.

The principle of the AICD flow regulating screen tube water control process in oil reservoirs is based on the difference in viscosity coefficients of oil and water. The different effects of fluid inertia forces and viscous resistance are used to control the discs to achieve water flow inhibition (Yan et al., 2021). This mitigates the "heel–toe effect", leading to an uneven inflow of crude oil at the "heel" and "toe" ends of the horizontal well, resulting in an uneven cone of bottom water (Zeng et al., 2014). Oil is more viscous than water, but gas is less viscous than water. This opposite viscosity class causes AICD to be non-applicable for gas field applications. The nozzle-type ICD controls the fluid velocity in the horizontal section to maintain uniformity by adjusting the nozzle size and density. It has achieved good water control and oil enhancement results in offshore oil fields. However, its anti-clogging performance and anti-flushing performance make it difficult for its application in high production gas wells. The continuous packer is the annulus between the well wall and the screen tube filled with fine coated polymer granular gravel. The film on the surface increases the resistance to the axial flow of the fluid in the annulus and acts as a barrier to water movement in the annulus. This is similar to the presence of a bare eye external packer between each screen tube, which has the effect of continuously preventing water from entering the horizontal section. The water-blocking, breathable cladding is now fully compatible with high-temperature, high-pressure gas reservoir production environments (Liu et al., 2020). This combination significantly reduces the fugitive flow of produced fluids in the outer annulus by filling the naked eye annulus with lightweight particles. In combination with the downstream ICD/AICD, it reduces the production pressure differential in the high-permeability water-seeing layer and increases the production pressure differential in the low-permeability oil-producing layer, which enables subdivision of the entire well section to regulate the flow and control water (Wan et al., 2020; Yan et al., 2021; Zhang et al., 2021). However, in deepwater reservoirs, the density and viscosity of natural gas are less than those of water. Therefore, ICD/AICD screen tubing cannot be used to produce gas and control water in

TABLE 1 | Main relevant parameters for numerical simulation experiments.

Gas reservoirs		Horizontal wells	
Initial pressure (Mpa)	43.3	Length of the horizontal production section (m)	580
Gas reservoir thickness (m)	20	Inner diameter of the screen tube (m)	0.1491
Gas density (kg/m^3)	0.65	Single-hole diameter of the screen tube (m)	0.01
Gas viscosity (mPa-s)	0.045	Maximum hole density (holes/m)	300
Volume factor (10^{-3} m^3/m^3)	3.5	Reasonable gas extraction rate (%)	3.5–4.0
Average porosity	0.2	Daily gas production (10^4 m^3/d)	50
Bottom water multiplier	100	Height of water avoidance (m)	59.1
Average permeability (mD)	13.7	Well control area (cm^2)	4.9×10^9

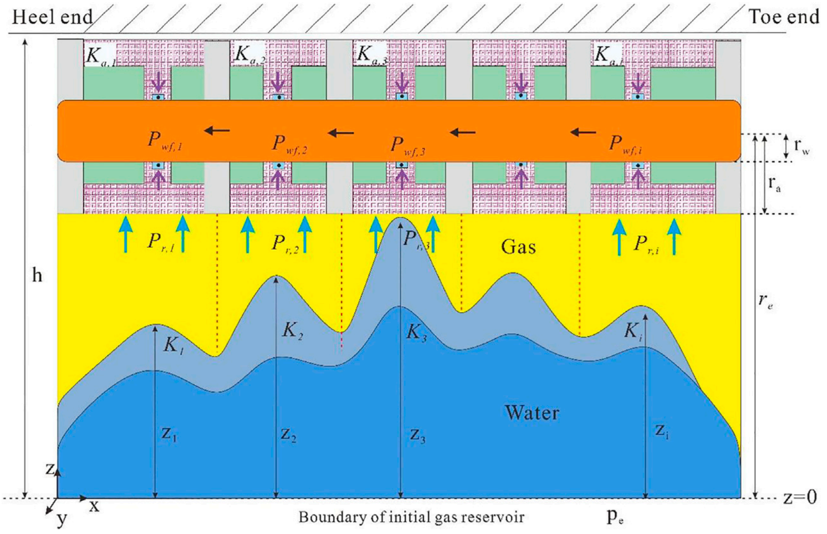

FIGURE 1 | Compound water control process production pressure drop model.

gas reservoirs. The ICD/AICD is a passive device, and once it is placed in the completion tubing column, it cannot be adjusted during production to ensure flow equalization (Sun et al., 2011).

In response to the abovementioned problems with the water control process, this study considers the advantage of continuous packers to mitigate fluid cascading in the annulus outside the pipe. It can effectively enhance the coincidence of the gas production rate and reservoir inhomogeneity at different locations of the variable density screen tube. By combining the advantages of the two water control processes, a water control process combining a variable density screen tube and a continuous packer is designed. The water control effect of this combination in deepwater gas reservoirs is also evaluated by combining physical and numerical simulation methods.

MATHEMATICAL MODEL

Model-Related Parameters

The H1 well is a designed well location for the Nanhai X gas reservoir, with bare-hole completion and gravel-filled sand control. The gas reservoir temperature is approximately 128°C, the reservoir pressure is nearly 40 MPa, the bottom water multiple is 100 times, the height of water avoidance in the horizontal section is 59.1m, the horizontal section length of the design is 580 m, and the screen tube diameter is approximately 15 cm (**Table 1**).

Mathematical Models

Considering the H1 well is a bare-borehole completion, continuous packer technology allows for an “infinite section” completion. Flow control was applied to each section by separately modeling the pressure and pressure drop distribution in the horizontal section. The analysis of the effect of different water control processes on the evolution of the gas–water interface under constant production conditions was carried out. The gas reservoir seepage model was readjusted to consider the higher percolation rates of natural gas during the extraction of the gas reservoir. The model was adjusted to better match the parameters of the water control process (**Figure 1**).

It is assumed that each section of the horizontal well flows in a continuous packer plane radially; the gas reservoir is bottom water–bounded and the fluid conforms to the Darcy flow law.

$$q_r = \frac{2\pi rhk}{\mu}\frac{dp}{dr}. \tag{1}$$

According to the continuity equation, it follows that

$$\rho q = \rho_1 q_1 = \rho_2 q_2 = \text{constant}. \tag{2}$$

Joint compression factor gas equation of state

$$\rho = \frac{pM}{ZRT}. \tag{3}$$

The flow at the radius r can be converted to the standard state flow at q_r q'_r

$$q_r = q'_r B_g = q'_r \frac{p_{sc}}{Z_{sc}T_{sc}}\frac{ZT}{p}. \tag{4}$$

Separating the variables yields

$$\frac{2\pi KhT_{sc}Z_{sc}}{q'_r p_{sc}T\mu Z} p dp = \frac{dr}{r}. \tag{5}$$

For steady-state flow, the outer boundary pressure is constant and the mass flow rate in each horizontal section of the packer is constant. Then, there is

$$\frac{774.6Kh}{q_{sc}T} 2\int_{pwf}^{p} \frac{p}{\mu Z} dp = \ln\frac{r}{r_w}. \tag{6}$$

The aforementioned equation can be converted to

$$\frac{p}{\mu Z} = f(p). \tag{7}$$

Using the concept of anthropomorphic pressure, there is

$$\psi = 2\int_{p0}^{p} \frac{p}{\mu Z} dp. \tag{8}$$

Applying the mean pressure equation is equivalent to

$$q_{sc} = \frac{774.6Kh\left(p_e^2 - p_{wf}^2\right)}{T\bar{\mu}\bar{Z}In\frac{r_e}{r_w}}. \tag{9}$$

$$p_e^2 - p_{wf}^2 = \frac{1.291\times 10^{-3} q_{sc}T\bar{\mu}\bar{Z}}{Kh} In\frac{r_e}{r_w}. \tag{10}$$

According to the Hawkins equation, the epidermal coefficient is expressed as

$$S = \left(\frac{K}{K_a} - 1\right)\ln\frac{r_a}{r_w}. \tag{11}$$

When Ka < K, the additional pressure drop is greater than 0; then, we have

$$\Delta p_{skin}^2 = \frac{1.291\times 10^{-3} q_{sc}T\bar{\mu}\bar{Z}}{Kh} S. \tag{12}$$

$$p_e^2 - p_{wf}^2 = \frac{1.291\times 10^{-3} q_{sc}T\bar{\mu}\bar{Z}}{Kh}\left(In\frac{r_e}{r_w} + S'\right). \tag{13}$$

Combining the pressure drop from the epidermal effect into the total pressure drop, the stable flow Darcy capacity equation is

$$q_{sc} = \frac{774.6Kh\left(p_e^2 - p_{wf}^2\right)}{T\bar{\mu}\bar{Z}\left(In\frac{r_e}{r_w} + S\right)}. \tag{14}$$

$$p_e^2 - p_{wf}^2 = \frac{1.291\times 10^{-3} q_{sc}T\bar{\mu}\bar{Z}}{Kh}\left(In\frac{r_e}{r_w} + S\right). \tag{15}$$

According to the distribution characteristics of the permeability size of the horizontal section of the horizontal well, it was mainly divided into five sections. The distance of each section from the location of the heel end is 0–33 m, 33–178, 178–307, 307–358, and 358–580, and the numerical model determines that the average permeability of the formation in the near horizontal section of the well is 23.5 mD, that is, 0.0232 μm2. Combined with the analysis of the coefficient of variation of the permeability of the near well, that is,

$$C = \sqrt{\frac{1}{n}\sum\nolimits_{i=1}^{n}\left(k_i - \bar{k}\right)^2}\Big/\bar{k}, \tag{16}$$

where k_i is the near-well permeability of the micro-element of the wellbore in section i, m^2 and $\bar{k}$ is the average permeability of the near-well, m^2. Based on the characteristics of the permeability distribution of the six sections of the horizontal section reservoir, the permeability distribution of each section was more homogenous. Therefore, this analysis will be approximated as six horizontal section microelements to obtain the coefficient of variation between each section of the near analysis. The coefficient of variation for the horizontal section of well H1 was calculated to be 0.4 (**Table 2**, **Figure 1**). We believe that the production profile can be improved by optimizing the pore density, but there are fluctuations (Wang et al., 2012). The optimization of the sieve tube borehole density in this study was carried out based on the horizontal well shot hole optimization model (Wang et al., 2012). By setting the flow rate distribution in the horizontal section to the equilibrium state, a system of equations with borehole density as the decision variable is solved. Initially, the screen tube hole densities of the six horizontal section microelements were determined to be 51holes/m, 263holes/m, 62holes/m, 300holes/m, 44holes/m (**Table 2**).

PHYSICAL SIMULATION EXPERIMENTS

Experimental Setup and Procedure

The interior of this experimental setup is a 50 cm × 50 cm × 50 cm square kettle (**Figure 2**). The 100 water saturation measurement sensors inside the kettle and 20 pressure sensors are evenly distributed throughout the chamber. According to the target gas reservoir conditions, air was used instead of natural gas and distilled water instead of experimental bottom water during the experiments. There was one gas injection valve at the top of the kettle. The gas reservoir bottom water multiplier was large and vigorous. In order to simulate the ability of the bottom water to cone in at the horizontal section position during gas reservoir production, three inlet valves were installed at the bottom of the unit. The valves were connected to uniformly open water injection pipes. The kettle was recharged by an ISCO pump

TABLE 2 | Horizontal sieve pipe section segments and shot hole density.

Penetration segment	Length interval (m)	Penetration rate		Average permeability of near wells		Coefficient of variation	Sieve tube hole density
		mD	μm^2	mD	μm^2		pcs/m
First paragraph	0–33	30	0.03	23.5	0.0232	0.4	51
Second paragraph	33–178	12	0.012				263
Third paragraph	178–307	28	0.028				62
Paragraph 4	307–358	10	0.01				300
Paragraph 5	358–580	31	0.03				44

FIGURE 2 | Physical simulation equipment for water control processes. **(A)** kettle body; **(B)** measuring points and laying inside the equipment; **(C)** kettle body sealing; **(D)** sieve tube; **(E)** measuring points; **(F)** sand compaction in sections; **(G)** sand sampling.

at constant pressure, and a panel with uniform openings was installed above the three water injection pipes to create a bottom water layer by "surface injection" instead of "spot injection." The balanced injection design prevents the effect of injection operation on the bottom water cone. A small condensing unit was added to the middle of the gas extraction pipe, and the lower part of the unit was connected to a water collection device. A gas flow meter was connected at the end of the gas extraction pipe to determine the rate of gas extraction and count the volume of gas extracted.

Based on the different phases of the physical simulation experiment, the overall procedure was divided into three processes: initial model building, simulation of the water-free gas extraction period, and simulation of the water-seeing period and production shutdown.

1) Initial model building includes sand filling, sand segment compaction, horizontal segment laying, kettle sealing, gas and water injection equipment connection, and gas–water interface building. In particular, the gas–water interface was established considering that the actual reservoir had 23% bound water saturation formation. Therefore, a full model sand body with 100% water content was used to replace the upper aquifer by top pressure gas injection through the kettle body. This was carried out until the formation was 23% saturated with bound water. The final gas–water interface was determined after the criteria were adjusted by cyclic water and gas injection. A stable gas–water interface was obtained for the entire experimental setup for 12 h. That is, the gas–water saturation field of the entire model no longer changes significantly. At this point, the water avoidance height conforms to the geometric model settings.
2) Gas reservoir extraction simulation—The gas production valve of the horizontal well was opened and the gas recovery rate was set to a reasonable recovery rate. The gas recovery situation and total gas recovery volume every 1 h were recorded and the gas recovery rate was calculated. The characteristics of gas and water distribution at different section locations at each time are recorded through 3D visualization software. When the extraction channel began

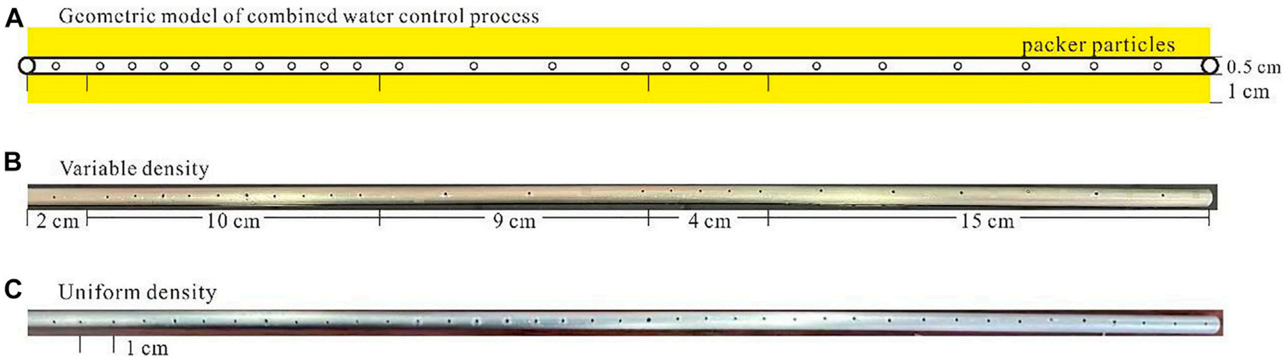

FIGURE 3 | Composite water control process geometry model and screen tube design. **(A)** Geometric model of combined water control process. **(B)** Variable density, and **(C)** uniform density.

TABLE 3 | Table of H1 well segmentation and physical model parameter design.

Horizontal segment/cm	0–2	2–12	12–21	21–25	25–40
Reservoir segmental permeability/mD	30	12	28	10	31
Model segmental permeability/mD	300	120	280	100	310
Uniform density eyelets (pcs/cm)	1	1	1	1	1
Variable density eyelets (pcs/cm)	0.5	0.9	0.44	1	0.4

to produce water, the production time and gas-water saturation field were recorded, and the gas–water interface and the location of water production at this time were determined. Total water production was collected and recorded until the gas well stopped producing.

3) The gas well was shut down, and the experiment was completed. The standard for gas well shutdown was when the water content reached 98%. The gas production valve was closed and the experimental data were collated. The total production time, total gas production, and gas–water saturation field were recorded, focusing on completing the characterization of the distribution of water bodies in the horizontal section location.

Experimental Model Design

The geometric model of the physical simulation experiment was designed with a gas–water interface height of 20 cm and a water avoidance height of 20 cm. The horizontal well section was located in the middle position of the kettle. The length was 40 cm, internal diameter 0.5 cm, and borehole diameter 0.1 cm (**Figure 3**). The model stratigraphic setting was completed by filling with sand and compacting. Reservoir construction was based on the permeability distribution characteristics of the horizontal section trajectory of the H1 horizontal well. That is, a non-homogenous reservoir with five permeability stages. In order to effectively enhance the vertical segmentation characteristics of the reservoir, the kettle was divided into five separate spaces by combining four thin steel plates with sieve holes embedded in the joints of each section of the formation. Each separate space was filled and compacted with quartz sand of different mesh sizes. This was used to simulate water intrusion in a non-homogenous gas reservoir. The sand model was completed by mechanical compaction. The reservoir permeability of each section of the sand-filled model was equated with the corresponding core at a ratio of 10:1. The non-homogenous character of the original formation was ensured (**Table 3**). This process was achieved by repeated sampling and testing with a core hole and percolation tester until the permeability ratio between the two on the core scale was met.

The physical experiments were divided into three groups: the no water control process experiments, the continuous packer water control process, and the combined variable density sieve tube and continuous packer process experiments. The pore density of the production screen without the water control process model and continuous packer water control process model is of uniform density, that is, 1/cm (**Figure 3C**, **Table 3**). The variable screen tube pore density was calculated based on the permeability of different reservoir sections (**Table 3**). Both the continuous packer water control process model and the combined water control process model were lined with laminated packer particles at the screen tube and bare eye annulus. Based on the experiments, it was found that the filling thickness of the laminated particles had a significant effect on the effective additional resistance generated by the particles themselves. The greater the filling thickness, the greater the additional pressure drop. Thus, a large lateral filling thickness can effectively reduce the lateral gas fugacity. Based on the results of the analysis of the additional pressure drop generated by the thickness of the clad gravel, a thickness of 1 cm was set for this physical simulation experiment (**Figure 3**, **Figure 4**). Finally, the results of the simulations on the effect of different water control processes on the water intrusion profile characteristics, time to water production, and the final total production were used to complete the evaluation of the suitability of water control processes in gas reservoirs.

With the assurance that the model and the formation use the same pore medium and that the fluid density and viscosity are constant, if the two similar criteria of the ratio of the gravity and driving forces of the gas and water phases are to be satisfied, the gas recovery rate ratio will be the square of the length ratio (Shen et al., 2013). The experimental model was scaled down to 103:1 based on the actual parameters of well H1. From the similarity criterion, the gas recovery rate was the square of the length ratio, that is, 106:1. The

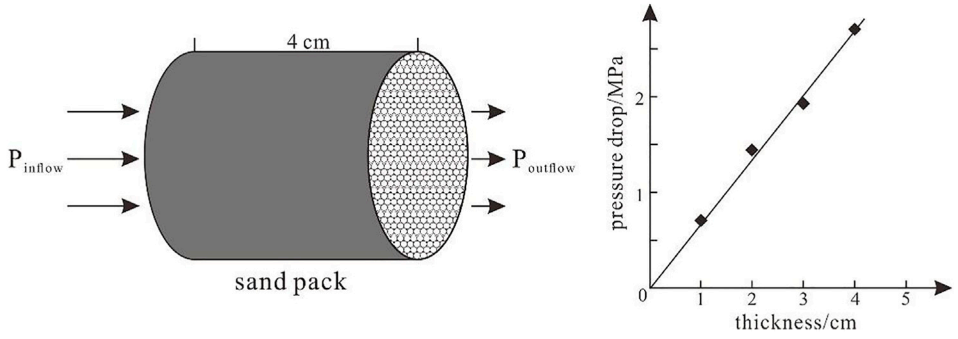

FIGURE 4 | Pressure drop test results from filling thickness on gas flow.

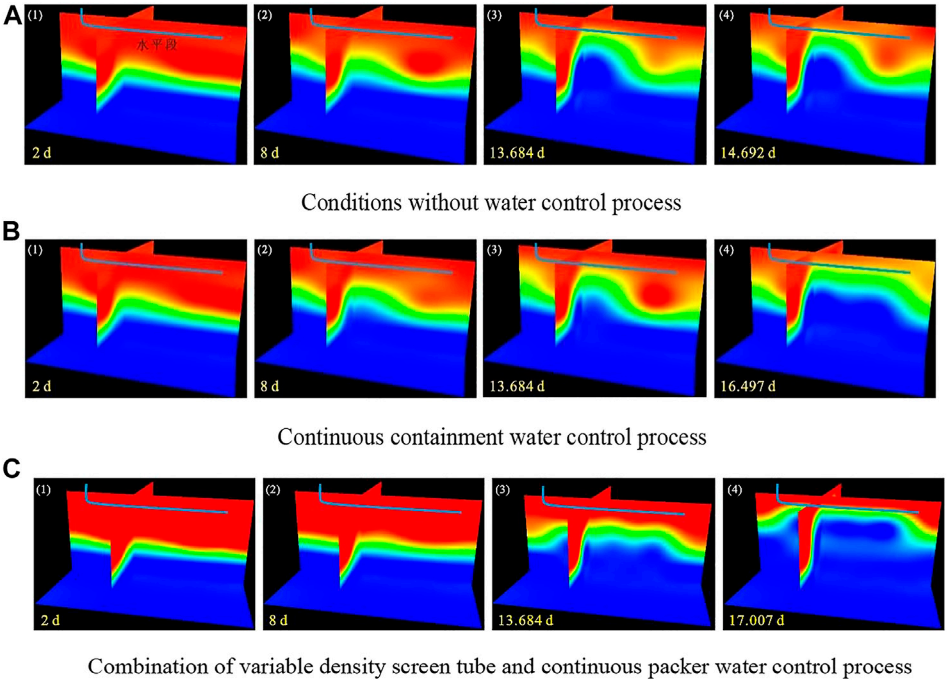

FIGURE 5 | Evolution of the gas–water saturation field under different water control measures. **(A)** Conditions without water control process. **(B)** Continuous containment water control process. **(C)** Combination of variable density screen tube and continuous packer water control process.

equivalent gas recovery rate for the physical model was thus calculated to be approximately 200 L/d. The reactor volume was 100 L, the average porosity after sand compaction was 22.4%, and the height of the water body in the reactor was 20 cm, so the space occupied by gas was approximately 16.8 L. The ideal gas state equation calculated the gas reservoir environment to be 43.3 MPa. The volume of gas filling in the kettle at ambient temperature and pressure was approximately 5379 L. This met the reasonable gas recovery rate setting for well H1 (**Table 1**).

Physical Simulation Results

Model 1 was an experiment model without water control measures. Based on the gas–water saturation evolution, the results show that as production progresses, the bottom water starts to cone in from the middle of the horizontal section and finally water is produced in the middle of the horizontal section (**Figure 5A**). Model 1 gas production began to show water at 13.684 days. When gas production reached 14.692 days, the water content reached above 98% and production stopped, with a total gas production of approximately 2,864.34 L (**Table 4**).

The experimental results of the Model 2 continuous packer water control process showed essentially no change in the bottom water cone inlet characteristics before water was seen. It was still a central cone inlet. After water emergence, the overlying gravel rapidly sealed the water emergence location, and the other horizontal sections continued to produce. The gas–water

TABLE 4 | Quantitative comparison statistics of simulation results from different models.

	Waterless gas extraction period		Total gas production time		Total gas production	
	See water time/d	Extension rate/%	Total production time/d	Extension rate/%	Total gas production/L	Growth rate/%
Model 1	13.684	—	14.692	—	2,864.34	—
Model 2	13.693	—	16.497	12.29	3,035.05	5.96
Model 3	15.273	11.61	17.007	15.76	3,258.19	13.75

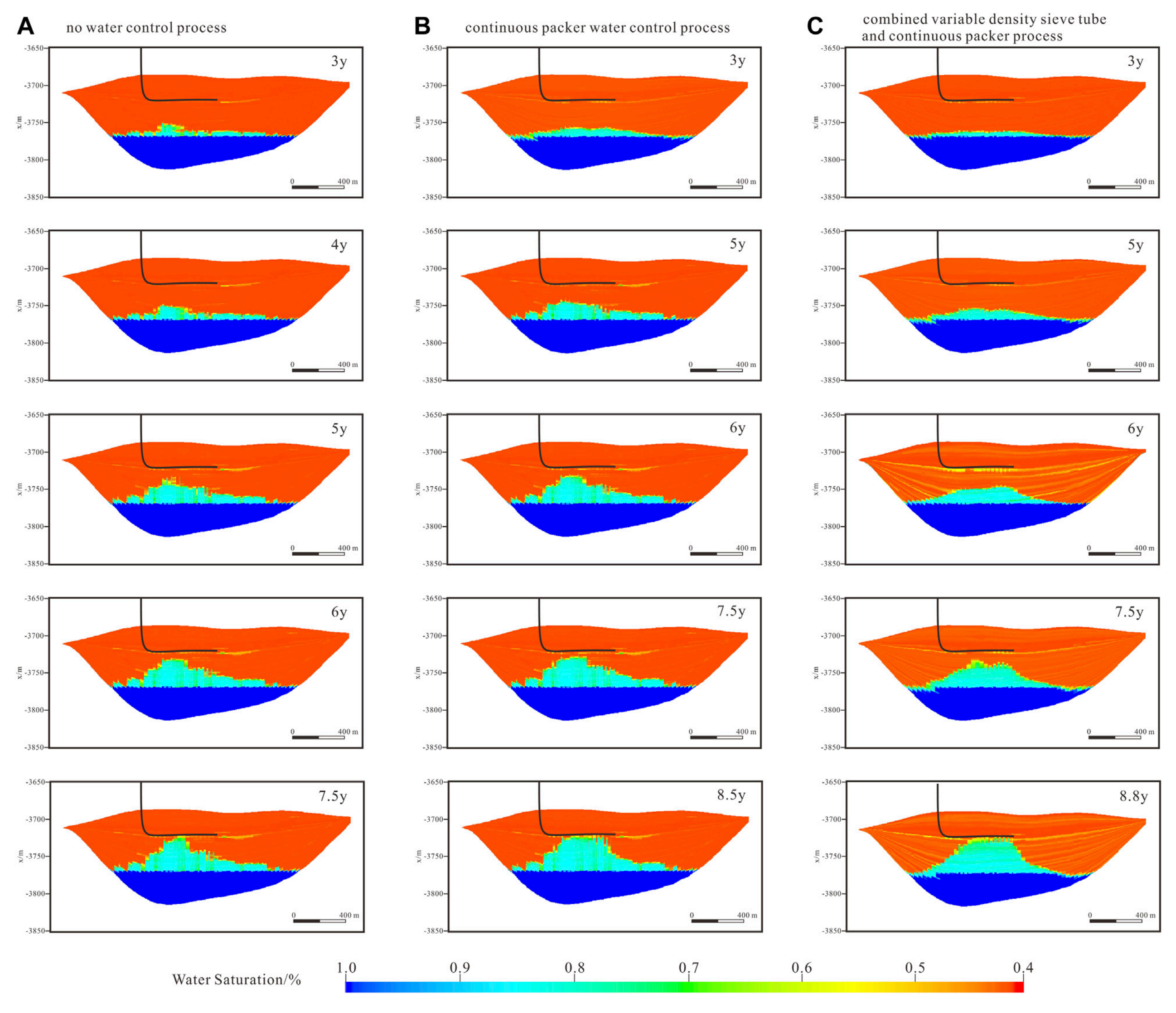

FIGURE 6 | Diagram of the water intrusion process in well H1 for different water control models. **(A)** No water control process. **(B)** Continuous packer water control process. **(C)** Combined variable density sieve tube and continuous packer process.

interface began to migrate laterally along the horizontal section from the water spot (**Figure 5B**). When the horizontal section was fully producing water, the gas–water interface profile features were parallel to the horizontal section. Model 2 showed water at 13.693 days of production, approximately 13 min longer than Model 1. Consideration was given to the laying of the overlying gravel, error between models, and total production time. The time difference between the two models was ignored in the later analysis. The time to water was considered to be in approximate agreement. The total gas production time for

TABLE 5 | Quantitative comparison statistics of simulation results from different models.

	Waterless gas extraction period		Total gas production time		Total gas production	
	Time to see water/year	Extension rate/%	Total production time/year	Extension rate/%	Total gas production/10^8 m^3	Growth rate/%
Model 1	7.1	—	7.5	—	13.42	—
Model 2	8.0	12.67	8.8	17.33	15.47	15.27

Model 2 was approximately 16.497 days, and the total gas production was approximately 3,035.05 L. The gas production time was approximately 12.29% longer, and the total gas production was approximately 5.96% higher than that of Model 1 (**Table 4**).

The combined water control process of Model 3 demonstrated a balanced bottom water cone inlet interface during gas production. It made it more homogenous, and after seeing water, the location of the water is effectively blocked without affecting the continued production of other horizontal sections (**Figure 5C**). Therefore, it had better water control effect. Model 3 saw water at an extension rate of approximately 11.61% compared with Models 1 and 2. The total production time was extended by 15.76% compared with the no water control condition, extending to 17.007 days. The total gas production was 3,258.19 L, with a gas production growth rate of approximately 13.75% compared with the no water control condition (**Table 4**).

NUMERICAL SIMULATION EXPERIMENTAL ANALYSIS

Numerical Model Design

Numerical simulations of the combined water control process model were carried out to validate the physical simulations against each other (**Figure 6**). The radial resistance of the laminated particles before they see water is very small and it hardly affects the flow of the fluid. In contrast, the resistance to axial flow is large, about 10^4 times the resistance to radial seepage (Wan et al., 2020). Therefore, in the model setup with lamella-sealed particles, the axial permeability of the particle-filled annulus is equivalently reduced by a factor of 10^4. The radial permeability parameter is not changed so that no lateral fugitive flow occurs during gas production.

Numerical Simulation Results

The results of Model 1 show that the H1 well, without the implementation of a water control process, began to lift the initial bottom water as a whole upward as production progressed. The bottom water starts to cone in at the middle of the horizontal section. After 7.1 years of production, the bottom water tapered into the horizontal section and started to produce water (**Figure 6A**). Due to the high reservoir pressure, the bottom water multiplier was high. The horizontal section floods rapidly after water production. Water production rises in a near-linear fashion in the short term (approximately 0.4 years). When the gas production time is 7.5 years, the horizontal well section is completely filled with water. Total gas production was 13.42×10^8 m^3 (**Table 5**).

Model 2 is a water control process with a combination of a variable density screen tube and a continuous packer. Due to the lateral flow stopping capacity of the continuous packer for the gas, the mutual interference of gas production in each section is reduced and radial seepage is dominant. The percolation rate is related to reservoir inhomogeneity and sieve tube density (**Figure 6B**). Therefore, based on the basic design of the model, the bottom water below the horizontal section is characterized by a more gentle morphology of the gas–water interface profile during the cone advance. Initially, the main feature is an overall uplift, with a “double-peaked” structure around 7.5 years of production but still with a gentle overall profile. Water starts to appear after 8.0 years of production and ceases after 0.8 years of production. This is 0.9 years later than the time taken by Model 1 and represents an extension of time of approximately 12.67%. Total gas production was 15.47×10^8 m^3, with a gas production growth rate of approximately 15.27% of that under uncontrolled water conditions (Tab 5).

DISCUSSION

The physical and numerical simulations carried out in this study for the continuous packer and its combined water control process with the variable density screen tube yielded consistent results. The results of the two simulation methods, Model 2 and Model 3, for both water control processes were within 10% error in the water-free recovery period, total gas production time, and total gas production volume (**Table 6**). Both the continuous containment and composite water control processes achieved considerable production enhancement.

A comparison of the simulation results for both physical and numerical simulations, Model 1 and Model 2, shows that the continuous packer is predominantly water-seeking and water-blocking. The total production time of the process pair with the horizontal well is effectively extended, and the rate of water production is significantly reduced, indicating that the continuous packer has a high water-stopping capacity. Although able to directly stop the bottom water from entering the horizontal section at the-water-seeing location, it does not affect the normal production of gas at other locations in the horizontal section. The gas permeable water blocking effect is more consistent with the physical simulation results recognized (Liu et al., 2020). The process belongs to the late extraction water blocking measures and the main advantages are as follows: 1) no need to find water operation; 2) the whole well section is set up to prevent adaptive water blocking and solve the problem of out-of-tube fugitive flow; 3) once blocking water, there is no need to worry about the problem of extra increase of water outlet point later, and long-term effective; 4) gravel filling has good anti-

TABLE 6 | Comparison of error statistics between physical and numerical simulation results.

Extension of the water-free gas extraction period/%			Total gas production time extension rate/%			Total gas production extension/%		
Physical simulation	Numerical simulation	Error	Physical simulation	Numerical simulation	Error	Physical simulation	Numerical simulation	Error
11.61	12.67	8.37	15.76	17.33	9.06	13.75	15.27	9.95

sand effect. However, there are still certain shortcomings for water control operations, that is, the failure to change the bottom water cone in speed or form. The simulation results of the water control model with the combination of the continuous packer and variable density screen tube solved the abovementioned problems well. The resistance to percolation in the axial direction of the laminated packer particles reduces the out-of-tube fugitive flow. The gas percolation rate at each location in the horizontal section is controlled mainly by the reservoir properties. This, combined with the variable density distribution of the orifice of the screen tube, matches the inhomogeneity of the reservoir. The gas percolation rate is balanced across the horizontal section. The gas–water interface during bottom water ascent in Model 3 has a greater extensional width (along the horizontal production section). The bottom water beneath the entire horizontal section has a smoother gas–water interface during ascent. This ensures efficient and long-term production of the horizontal well.

In terms of physical model design, this is influenced by factors such as size of the kettle itself, ratio of the kettle to the horizontal section, reservoir pore and seepage conditions, and inhomogeneous characteristics. It is not possible to avoid an exact match between the physical model and the relevant parameters or ratios of the actual gas reservoir and its production process. Based on the similarity principle (Shen et al., 2013), it can show the ability of bottom water coning upward under different permeability conditions according to the gas production capacity and pressure drop characteristics of different positions in the horizontal section and complete the characterization of the bottom water coning process. Of course, it is affected by the degree of reservoir inhomogeneity. The absolute flatness of the gas–water interface cannot be satisfied (Wang et al., 2012). In this experiment, due to the large coefficient of variation between sections, the gas–water interface appears to have a "waveform" structure during ascent. Therefore, the best water control effect of the combination of continuous packer and variable density screen tube requires a low degree of reservoir inhomogeneity. When the gas–water interface reaches the horizontal section, the clad packer particles continue to produce the same water control effect as in Model 2. This further enhances the production time after water is seen. However, due to the larger width and gentler morphology of the air–water interface below the horizontal section in Model 3, the initial contact with the horizontal section at the onset of water is extensive, resulting in insufficient ability to extend the total gas production time after the onset of water.

CONCLUSION

1) Numerical and physical simulation studies and comparative analyses were carried out based on production well data from the LS 25–1 gas field. We found that a single water control technique has limited effectiveness in controlling water in deepwater gas reservoirs. A combination of multiple water control techniques is required to achieve the desired results.
2) The results of the study also demonstrate the advantages of the continuous containment water control process for deepwater gas reservoirs. The water control principle is applicable to deepwater gas reservoirs. When a horizontal well starts producing water, no other measures are required to locate the location of the water produced. It is then possible to effectively reduce the amount of water produced at that location. Rapid water flooding of the horizontal well is prevented, thereby ensuring that the horizontal section continues to produce gas at locations where no water was produced.
3) The combination of the continuous packer and variable density screen tube can maximize the water control effect of both processes. It can greatly enhance the recovery rate of the producing wells. At the early stage of gas reservoir production, the overlaid packer particles can greatly reduce the water tampering effect in the annulus of the horizontal section. The radial percolation rate of gas at each location in the horizontal section is consistent with the inhomogeneity of the reservoir, ensuring that the gas production rate in each section of the horizontal well matches the density of the screen tube borehole and slows the bottom water cone in and balancing the gas–water interface during production. After water is seen, the overburden sealing particles continue to prevent bottom water from entering the horizontal section and causing flooding.

DATA AVAILABILITY STATEMENT

The data used to support the findings of this study are available from the corresponding author upon request.

AUTHOR CONTRIBUTIONS

DW: conceptualization; YL: methodology; LM: validation; FY: formal analysis; SL: investigation; YQ: writing the original draft; SJ: writing— review and editing.

ACKNOWLEDGMENTS

The authors are grateful for the Hainan province major Science and Technology Project (ZDKJ2021025), Heilongjiang Province

Key Research and Development project (GZ20210015), Heilongjiang Province Joint Guide Fund project (LH2021E017), Northeast Petroleum University start up funding project for talent introduction and scientific (1305021856), and College of Petroleum Engineering excellent scientific research talent cultivation project (15041260507). We thank Sun Zaixing for his comments and suggestions in the writing of this paper.

REFERENCES

Chen, K., Yang, X. B., Li, M., Li, A. Q., Wang, Z. Z., Li, F. X., et al. (2020). Research and Application Effectiveness of Target Search Technology System in the deepwater Exploration Mature Area of Qiongdongnan Basin. *China Offshore Oil and Gas.* 32 (3), 33–42. *(In Chinese)*. doi:10.11935/j.issn.1673-1506.2020.03.004

Irani, M., Bashtani, F., and Kantzas, A. (2021). Control of Gas Cresting/coning in Horizontal wells with Tubing-Deployed Inflow Control Devices. *Fuel.* 293, 120328. doi:10.1016/j.fuel.2021.120328

Li, H., Chen, D. C., and Meng, H. X. (2010). Optimized Design Model for Horizontal wells with Variable Density Injection. *Pet. Exploration Development.* 37 (3), 363–368. *(In Chinese)*. doi:10.1016/S1872-5813(11)60005-4

Liu, Y. K., Wang, H. D., Meng, W. B., Zhang, C., Zhi, J. Q., and Shen, A. Q. (2020). Experiments on Production Enhancement of Horizontal Wells Filled With Gas Reservoirs With Gas-Permeable Water-Barrier Gravels in Deep Subsea Water Reservoirs. *Nat. Gas Industry.* 40 (1), 61–68. *(In Chinese)*. doi:10.3787/j.issn.1000-0976.2020.01.008

Pang, W., Chen, D. C., Zhang, Z. P., Jiang, L. F., Li, C. H., Zhao, X., et al. (2012). Optimization Model for Segmented Variable Density Injection of Horizontal Wells in Non-Homogeneous Reservoirs. *Pet. Exploration Development.* 39 (2), 214–221. *(In Chinese)*. doi:10.1016/s1876-3804(12)60036-6

Rao, F. P., Dong, Y. L., Wu, J. S., Qi, Y. K., Tang, Q., and Wang, X. B. (2010). Water Control Completion Process for Horizontal Wells in Bottom Water Reservoirs in Dagang Oilfield. *Pet. Drilling Technology.* 32 (3), 107–109. *(In Chinese)*. doi:10.13639/j.odpt.2010.03.025

Shen, W. J., Li, X. Z., Lu, J. L., and Liu, X. H. (2013). Similar Theoretical Study on Physical Simulation of Anomalous High-Pressure Gas Reservoir Development. *Sci. Technology Eng.* 13 (35), 10460–10465. *(In Chinese)*. doi:10.1006/j.issn.2013.09.13

Shi, Y. (2015). China's First deepwater High-Temperature and High-Pressure Exploratory Well Completed in South China Sea. *Oil Drilling Prod. Technology* 37 (5), 45. *(In Chinese)*.

Sun, K., Guo, B. Y., and Saputelli, S. (2011). Multinode Intelligent-Well Technology for Active Inflow Control in Horizontal Wells. *SPE Drilling and Completion.* 26 (3), 386–395. doi:10.2118/130490-pa

Sun, X. D., and Bai, B. J. (2017). Status of Research on Water Control Technology in Horizontal wells at home and Abroad. *Pet. Exploration Development* 44 (6), 967–973. *(In Chinese)*. doi:10.1016/s1876-3804(17)30115-5

Wan, X. J., Wu, S. W., Zhou, H. Y., Yuan, H., and Song, L. Z. (2020). Research and Experiments on Water Control Technology of Flow-Controlled Screen Tube With Particle Filling. *Drilling Prod. Technology.* 43 (5), 61–63. *(In Chinese)*. doi:10.3969/J.ISSN.1006-768X.2020.05.17

Wang, H. J., Xue, S. F., and Gao, C. F. (2012). Methodology of Variable-Density Hole-Shot Profiling in Horizontal wells. *Oil Gas Geology. Recovery.* 19 (6), 87–90. *(In Chinese)*. doi:10.13673/j.cnki.cn37-1359/te.2012.06.022

Wang, P. M., Luo, J. H., Bai, F. L., Yang, J. B., and Bu, R. Y. (2001). Research Progress on Water Plugging Technology for Gas Wells at Home and Abroad. *Drilling Prod. Technology.* 24 (4), 28–30. *(In Chinese)*. doi:10.3969/j.issn.1006-768X.2001.04.008

Wang, Q., Liu, E., Zhang, H. L., and Zheng, J. P. (2011). Preferred Model for Flow and Water Control Sieve Pipe in Coupled Horizontal wells in Oil Reservoirs. *Acta Petrolei Sinica.* 32 (2), 346–349. *(In Chinese)*. doi:10.7623/syxb201102026

Wei, J. G., Wang, Z. M., and Wang, S. Q. (2009). Segmental Optimization Model for Injection Parameters of Horizontal Wells in Non-Homogeneous Reservoirs. *J. China Univ. Pet. (Natural Sci. Edition).* 33 (2), 75–79. *(In Chinese)*. doi:10.3321/j.issn:1673-5005.2009.02.014

Xu, J., Wu, K., Li, R., Li, Z., Li, J., Xu, Q., et al. (2018). Real Gas Transport in Shale Matrix With Fractal Structures. *Fuel* 219, 353–363.

Xu, J., Wu, K., Li, R., Li, Z., Li, J., Xu, Q., et al. (2019). Nanoscale Pore Size Distribution Effects on Gas Production from Fractal Shale Rocks. *Fractals* 27 (8), 1950142.

Xu, J., Chen, Z., and Li, R. (2020). Impacts of Pore Size Distribution on Gas Injection in Intraformational Water Zones in Oil Sands Reservoirs. *Oil Gas Sci. Technol.* 75 (6), 75.

Xu, X., Li, X., Hu, Y., Mei, Q., Shi, Y., and Jiao, C. (2021). Physical Simulation for Water Invasion and Water Control Optimization in Water Drive Gas Reservoirs. *Sci. Rep.* 11, 6301. doi:10.1038/s41598-021-85548-0

Yan, H. T., Xu, W. J., Jiang, W. D., and Zou, X. B. (2021). Adaptive Water Control Technology for Horizontal Wells in Offshore Bottom Water Reservoirs. *Pet. Geology. Oilfield Development Daqing.* 40 (3), 71–76. *(In Chinese)*. doi:10.19597/j.issn.1000-3754.202009019

Zeng, C., Duan, Y. G., and Liu, Y. F. (2014). The Role of Downhole Inflow Controller in Water Control and Dissection in Horizontal Wells in Bottom Water Reservoirs. *Drilling Prod. Technology.* 37 (3), 67–70. *(In Chinese)*. doi:10.3969/J.ISSN.1006-768X.2014.03.20

Zhang, J. B., An, Y. S., Wang, H. L., Xiong, M. S., and Li, Q. Q. (2021). Numerical Simulation Method for the Production Dynamics of ICD Completions in Horizontal Wells with Continuous Packers. *China Offshore Oil and Gas.* 33 (3), 121–125. *(In Chinese)*. doi:10.11935/j.issn.1673—1506.2021.03.014

Zhao, Y., Yang, H. B., and He, S. R. (2012). Flow Control Completion Technology for Horizontal Wells With Screen Tubing in the Shengli Low-Permeability Oilfield. *Pet. Drilling Tech.* 40 (3), 18–22. *(In Chinese)*. doi:10.3969/j.issn.1001-0890.2012.03.004

Zhou, S. T. (2007). Optimization Analysis of Borehole Density in Shot-Hole Horizontal wells. *Pet. Drilling Tech.* 35 (5), 55–57. *(In Chinese)*. doi:10.3969/j.issn.1001-0890.2007.05.016

Conflict of Interest: FY was employed by Bohai Oilfield Research Institute of CNOOC Ltd.

The remaining authors declare that the research was conducted in the absence of any commercial or financial relationships that could be construed as a potential conflict of interest.

frontiers | Frontiers in Earth Science

ORIGINAL RESEARCH
published: 17 June 2022
doi: 10.3389/feart.2022.906276

Triple-Porosity and Dual-Permeability Productivity Prediction Model of CBM Wells Considering Complex Flow Regimes

Qianhua Xiao[1]*, Huailin Wang[1]*, Yanhui Yang[2,3], Zhiqiang Li[1]*, Bocai Jiang[4]*, Jiahao Li[1] and Zuping Xiang[1]

[1]College of Petroleum Engineering, Chongqing University of Science and Technology, Chongqing, China, [2]Pilot Test Base for CBM Production of China National Petroleum Corporation, Renqiu, China, [3]PetroChina Huabei Oilfield Company, Renqiu, China, [4]College of Science, Guilin Institute of Aerospace Technology, Guilin, China

The productivity evaluation of CBM wells can yield significant insights into exploring the patterns of CBM production, predicting the effectiveness of the CBM well and reservoir stimulation, optimizing the gas reservoir development program, and developing a reasonable production system, for the purpose of facilitating efficient development of CBM. In particular, to accurately evaluate CBM productivity, we should establish the corresponding mathematical model of fluid flow through porous media and productivity evaluation model based on a clear understanding of CBM occurrence states and mechanisms of its flow through porous media. After considering the effects of slip flow, Knudsen diffusion, surface diffusion, stress sensitivity, and matrix shrinkage on fluid mass transfer, we have put forward a triple-porosity and dual-permeability mathematical model to predict CBM productivity that incorporates matrix gas desorption, complex flow in matrix pores, and gas–water two-phase flow in a cleat system. In combination with reservoir characteristic parameters, a case study of Ma-26 well in the Mabidong block in the south of the Qinshui Basin, we carried out a numerical simulation of the productivity of a fractured CBM well and analyzed the effects (on production performance) of occurrence states, cleat system permeability, complex flow regimes in the matrix, Langmuir pressure, and Langmuir volume on production are provided. The results show that 1) in the initial drainage and production stage of CBM wells, both free gas and adsorbed gas are produced simultaneously, while adsorbed gas dominates the production in later stages; 2) the peak output and cumulative output of CBM wells increase significantly with the rise in cleat system permeability; 3) the increase of Langmuir pressure, volume, and matrix porosity are conducive to the increase of CBM production. The research has considerable reference value for work on mechanisms of CBM flow in porous media and post fracturing productivity evaluation of CBM and also provides a theoretical basis for fieldwork in CBM development.

Keywords: CBM, triple porosity and dual permeability, production performance simulation, gas slip effect, surface diffusion

Edited by:
Jinze Xu,
University of Calgary, Canada

Reviewed by:
Yadong Qi,
Research Institute of Petroleum Exploration and Development (RIPED), China
Xuewu Wang,
Shandong Institute of Petroleum and Chemical Technology, China
Wei Lin,
Yangtze University, China
Feng Tian,
Guizhou University, China

***Correspondence:**
Qianhua Xiao
xqh159@gmail.com
Huailin Wang
848617030@qq.com
Zhiqiang Li
447320487@qq.com
Bocai Jiang
jbcai@guat.edu.cn.com

Specialty section:
This article was submitted to Environmental Informatics and Remote Sensing, a section of the journal Frontiers in Earth Science

Received: 28 March 2022
Accepted: 14 April 2022
Published: 17 June 2022

Citation:
Xiao Q, Wang H, Yang Y, Li Z, Jiang B, Li J and Xiang Z (2022) Triple-Porosity and Dual-Permeability Productivity Prediction Model of CBM Wells Considering Complex Flow Regimes. Front. Earth Sci. 10:906276. doi: 10.3389/feart.2022.906276

INTRODUCTION

As an unconventional natural gas, CBM has entered the stage of commercial exploitation in China. At present, the prevalent view among both Chinese and foreign researchers is that CBM is mainly adsorbed on the surface of coal matrix blocks. In the process of depressurized production, the gas desorbs from the matrix surface and then diffuses to the cleat-fracture system, before flowing into the wellbore through the cleat-fracture system, in a process that satisfies Darcy's law regarding fluid flow through porous media. There are three processes of desorption, diffusion, and porous flow in the process of CBM recovery (Dong et al., 2017), and the reservoir porosity and permeability vary continuously with changes in reservoir stress. During the production of CBM wells, an increase in effective stress reduces the permeability of the fracture system, while the gas is desorbed from the matrix surface, and the shrinkage of the matrix increases the permeability of coalbed fractures (Palmer and Mansoori, 1996; Clarkson et al., 2010).The net effect of the two will have an important impact on the production of CBM wells. Researchers around the world have put forward many mathematical models considering the abovementioned mechanisms (Seidle and Huitt, 1995; Moore and Higgs, 2015; Ye et al., 2021). Based on the S&D permeability change model, Meng et al. (2018) established a dynamic prediction model of coal seam permeability considering effective stress, coal matrix shrinkage, and gas slip effect, revealing the dynamic change law of permeability during coalbed methane development. Luo et al. (2021) proposed a fractal permeability model for dual-porosity media with curved natural fractures based on the analysis of pore-fracture structure characteristics of real coal samples. Compared with the traditional dual porous media model with embedded parallel planar fractures, Both the characteristics of pore and fracture curvatures are considered in the model. The results show that the permeability prediction value of this model is 1–2 orders of magnitude lower than that of the traditional model, which indicates that the permeability of coal seam is overestimated in the conventional model. Wei et al. (2022) adopted a strain rate-based permeability model to characterize the effect of matrix expansion on permeability during gas adsorption and evaluate the competing effects of pressure depletion and desorption contraction on permeability changes. Shaw et al. (2019), used an indoor test method to study the effects of stress sensitivity and coal seam matrix shrinkage on the relative permeabilities of gas and water in coalbed fractures. Currently, CBM productivity evaluation mostly involves mathematical models for numerical simulation considering coalbed gas desorption, diffusion, and gas–water two-phase flow in fractures (Wei and Zhang, 2013). In this process, fluid–solid coupling flow mathematical models were developed in consideration of the changes of reservoir parameters, including porosity and permeability (Jiang et al., 2011; Moore et al., 2015; Kong et al., 2017). By introducing the S&D permeability change model, (Yan et al. (2012). established a three-dimensional gas–water two-phase dual-porosity single-permeability mathematical model of coal reservoir considering permeability variation, and a software is developed to study the effects of coal reservoir, adsorption and characteristic parameters on production performance. The research shows that the production of CBM is directly proportional to initial gas content, effective thickness, fracture permeability, and Langmuir pressure. On the basis of comprehensive consideration of the gas desorption, diffusion and flow mechanisms through porous media, a dynamic two-dimensional gas-water two-phase dual-porosity and single-permeability mathematical model was proposed by Zhang et al. (2015), to simulate production performance of fractured CBM wells, and the impacts of relative parameters incorporating Langmuir volume, Langmuir pressure, desorption time, coalbed pressure, cleat permeability and porosity on production of fractured CBM wells are analyzed. With consideration of effective stress, matrix shrinkage, and Klinkenberg effect, Yang (2016) established a permeability model and a three-dimensional dual-medium gas-water two-phase CBM porous flow production model to carry out production simulation research of fractured CBM wells. In addition, He also designed a dynamic simulation program to study self-stimulation effect on CBM production and predict the development performance of fractured CBM wells. Ma et al. (2017) put forward a dual-porosity, single-permeability, fluid-solid fully-coupled production simulation model of CBM wells. The effects of coal seam porosity, permeability, water phase retention and relative permeability change on productivity are investigated in the model. The results indicate that the desorption and matrix shrinkage effect will lead to an increase in permeability near the wellbore and a decrease in permeability at places far away from the wellbore. A large desorption strain and elastic modulus but a small Poisson's ratio is conducive to increasing the permeability and production of gas wells. Chen et al. (2013) proposed a dual-porosity, dual-permeability, and fluid-solid coupled model to investigate the effects of different reservoir parameters on productivity. The gas transport process of desorbed gas moving into the macroscopic pores of matrix, and then to fractures are took into consideration, and an analysis of the effects of desorption time, fracture permeability, fracture spacing, matrix shrinkage effect, bottom-hole pressure, Langmuir volume, matrix and fracture porosity on production performance are performed in the paper. Wei and Zhang (2010) developed a set of triple-porosity, and dual-permeability flow model of CBM coupled with solid deformation. It is believed that after gas desorption, CBM does not directly enter the fractures, but first moves into the macropores and then transport from these pores into the natural fractures and that there are gas-water two-phase flow in both the matrix pores and fractures. On the basis of the characteristics of gas–water two-phase flow in the early stage of CBM reservoir production Qiao et al. (2018) treated the critical desorption pressure of the reservoir as the supply pressure, and developed the productivity formula suitable for

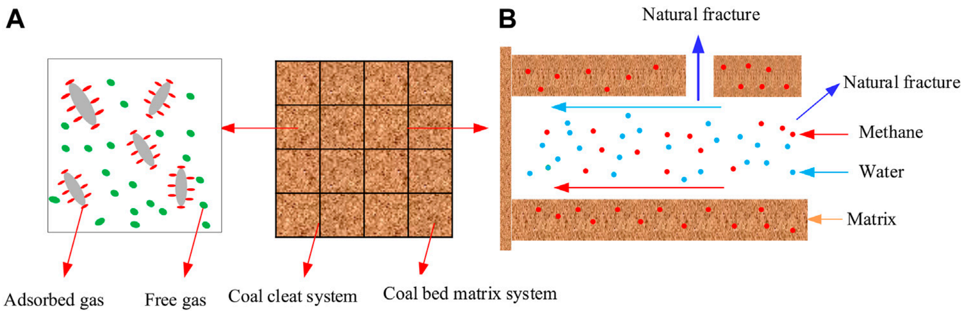

FIGURE 1 | (A) Schematic diagram of occurrence state of CBM **(B)** Schematic diagram of the physical model of gas-water two-phase flow in a natural cleat system.

CBM reservoir by combining numerical simulation and mathematical derivation.

For CBM flow through porous media and its production models, previous models created by the research community take only of the adsorbed gas into account, considering that the adsorbed gas in the matrix desorbs directly into the cleat system during CBM production, without considering the free gas in the micropores of the matrix. Xiao et al. (2021) studied the micro-occurrence and mass transfer patterns of CBM by using NMR online detection. The research shows that about 90% of CBM exists in adsorbed manner. Adsorbed gas is the main source of CBM production, followed by free gas. About 70% of the gas produced from dry coal samples comes from adsorbed gas. The contribution of gas in different occurrence states to production varies greatly. In the early stage, it is chiefly the free gas and pore-confined gas that are produced, and in the later stage, it is mainly the adsorbed gas (Xiao et al., 2021). In addition, the model mainly focuses on the effects of fracture system stress sensitivity and matrix shrinkage on fracture permeability and does not account for the flow of gas desorbed from the matrix surface into micropores and the complex flow states of gas in them (Duan et al., 2017; Huang et al., 2018; Liu et al., 2018). In the present study, we take into consideration the gas slip flow, Knudsen diffusion, and surface diffusion in the micropores of the coal seam matrix, the stress sensitivity of the coal seam, and the matrix shrinkage effect, and then develop a triple-porosity, double permeability productivity evaluation mathematical model that incorporates the desorption of the gas from coal seam matrix, the transport of gas in micropores and the gas-water two-phase flow in the fracture system. Then, we proceed to derive the numerical solution equations of the model by the finite difference method and design the corresponding calculation program. In combination with reservoir characteristic parameters, the effects of different reservoir parameters on the production of CBM wells are simulated and analyzed.

MATHEMATICAL MODEL FOR PRODUCTIVITY PREDICTION OF FRACTURED CBM WELLS

As shown in **Figure 1A**, coal bed matrix includes matrix bulk and matrix micropores. CBM exists on the surface of matrix grains as adsorbed gas and then enters matrix micropores through desorption and diffusion. The free gas in the matrix micropores flows into the natural cleat system together with the desorbed gas. Under the original reservoir conditions, the coal seam natural cleat system is saturated with water. With the progress of production, due to the pressure difference between the cleat system and matrix, the methane in the matrix will flow into the natural cleat system, resulting in gas-water two-phase flow in the natural cleat system, as shown in **Figure 1B**.

Mathematical Model of Porous Flow in the Coal Seam Matrix System

The gas flow equation in the matrix should incorporate gas adsorption, desorption, and diffusion on the surface of matrix grains, and gas flow in the macro-pores of the matrix.

1) Gas adsorption and diffusion:

The mechanism of desorption from the micropores of the coal seam matrix is shown that with the decrease of pore pressure in production, the gas desorbs from the surface of the coal seam matrix. This process is described by Langmuir isothermal adsorption equation:

$$C\left(P_{\mathrm{gm}}\right) = V_L \frac{P_{\mathrm{gm}}}{P_{\mathrm{gm}} + P_L}, \tag{1}$$

where $C(P_{gm})$ is the amount of gas adsorbed in unit mass coal seam(m^3/kg), V_L is the Langmuir volume, (m^3/kg), P_{gm} is the pressure of matrix system (MPa), and P_L is the Langmuir pressure (MPa).

Based on the pseudo steady non-equilibrium adsorption model, the diffusion of gas in micropores is described by Fick's first law as follows:

$$-\frac{\partial C}{\partial t} = \frac{1}{\tau}\left(C - C\left(P_{\mathrm{gm}}\right)\right), \tag{2}$$

where t is desorption time (day). The amount of gas desorbed in micropores is finally expressed as:

$$q_{\mathrm{gms}} = \rho s\left(1 - \phi_t\right)\frac{1}{\tau}\left(C - C\left(P_{\mathrm{gm}}\right)\right), \tag{3}$$

where ρ_s is coal density (kg/s), and φ_t is total porosity (dimensionless quantity).

2) Gas flow in matrix pores

The pores of the coal matrix include micropores with adsorbed gas and macropores with the free gas phase. The gas desorbed from the micropores is transported into the macropores that in turn provide the gas source to natural fractures, which is similar to the triple porosity model.

Considering the viscous flow and slippage flow in the macropores of the matrix, the adsorption and desorption of gas in the micropores of the matrix, and the interporosity flow between the matrix and natural fractures, the flow equation in the coal seam matrix is obtained on the basis of the continuous medium theory as follows:

$$\frac{\partial}{\partial x}\left(\frac{\rho_{\mathrm{g}} K_{\mathrm{mapp}}}{\mu_{\mathrm{g}}}\frac{\partial P_{\mathrm{m}}}{\partial x}\right)+\frac{\partial}{\partial y}\left(\frac{\rho_{\mathrm{g}} K_{\mathrm{mapp}}}{\mu_{\mathrm{g}}}\frac{\partial P_{\mathrm{m}}}{\partial y}\right)+q_{\mathrm{gms}}-q_{\mathrm{gmf}} = \frac{\partial\left(\phi_{\mathrm{m}}\rho_{\mathrm{g}}\right)}{\partial t}, \tag{4}$$

where q_{gmf} is the amount of interporosity flow between natural fractures and matrix $kg/(m^3 \cdot d^{-1})$, K_{mapp} is the apparent permeability (mD) of the matrix; ρ_g is gas density (kg/m^3), φ_m is matrix porosity (dimensionless), μ_g is gas viscosity (mPa·s), and t is the time (d).

The coal seam with developed natural fractures can be treated as a dual-porosity medium containing matrix and fractures. When there is a pressure difference between matrix and fractures, the fluid will exchange mass between the two media.

The mass interporosity flow between fractures and matrix per unit grid volume is:

$$q_{\mathrm{gmf}} = \frac{\sigma\rho_{\mathrm{g}} K_{\mathrm{mapp}}\left(P_{\mathrm{m}}-P_{\mathrm{f}}\right)}{\mu_{\mathrm{g}}}, \tag{5}$$

where P_f is the pore pressure in natural fractures (MPa) and σ is the shape factor ($1/m^2$), defined as:

$$\sigma = 4\left(\frac{1}{L_{\mathrm{x}}^2}+\frac{1}{L_{\mathrm{y}}^2}\right), \tag{6}$$

where L_X is the length of the matrix block in the *x* direction (m); L_y is the length of the matrix block in the *y* direction (m).

3) Matrix apparent permeability

The diffusion flux of mass transfer in the micropores of coal seam matrix is the sum of surface diffusion flux and free gas diffusion flux, and the gas transport in the micropores includes viscous slip flow and Knudsen diffusion (Wu et al., 2016a; Wu et al., 2016b). Combined with the Darcy equation, the apparent permeability model of the coal seam matrix is proposed as follows:

$$K_{map} = -\frac{\phi_m}{\tau}\left[\begin{array}{l} f_s\dfrac{r_{ef}^2}{8}\left(1+\alpha_r Kn_r\right)\left(1+\dfrac{4Kn_r}{1-bKn_r}\right)+f_k\left(\dfrac{2r_{ef}\delta^{D_{\mathrm{f}}-2}}{3}\right)\left(\dfrac{8ZRT}{\pi M_{\mathrm{g}}}\right)^{1/2}\mu_g C_g \\ +\dfrac{D_{\mathrm{s}}\mu_g ZRT\rho_s V_L}{V_{std}\,p}\dfrac{p_L}{\left(p_L+p\right)^2} \end{array}\right], \tag{7}$$

$$f_s = \frac{1}{\left(1+Kn_r\right)}, \tag{8}$$

$$f_{\mathrm{k}} = \frac{1}{\left(1+1/Kn_r\right)}, \tag{9}$$

where Kn_r represents the Knudsen number of real gas, a dimensionless quantity, r_{ef} is the effective pore radius(nm), D_s is the surface diffusion coefficient(m^2/s), b is the gas slip constant(dimensionless), M_g is the molecular weight of gas(kg/mol), R is the general gas constant, Pa/mol/K. δ Represents the dimensionless ratio of molecular diameter to local pore diameter, D_f represents the fractal dimension of pore wall (dimensionless); C_g is the gas compression factor(MPa^{-1}), V_{std} represents the molar volume of gas in standard state, m^3/mol, α_r is the rare effect coefficient of the ideal gas, dimensionless, ρ_s is the density of coal (kg/m^3), and τ indicates pore tortuosity, a dimensionless quantity.

When both the shrinkage and stress sensitivity of organic matrix is considered (Sheng et al., 2019), the nanopore radius can be expressed as:

$$r_{ef} = \left(r_o\left(p_e/p_o\right)^{0.5\,(q-s)}\right)\left(\sqrt{1+\frac{\left(1-\phi_{\mathrm{m}}\right)}{\phi_{\mathrm{m}}}\frac{\varepsilon_L p_L\left(p_{in}-p\right)}{\left(p_L+p\right)\left(p_{in}+p_L\right)}}\right), \tag{10}$$

where P_{in} is the initial pore pressure(MPa), r_o is the initial pore radius (m), s is the permeability coefficient of coal obtained by fitting experimental data (dimensionless), q is the porosity coefficient of coal obtained by fitting experimental data (dimensionless), P_e is the effective overlying stress (MPa), P_o is atmospheric pressure(MPa), ε_L is Langmuir strain (dimensionless).

Mathematical Model of Flow Through the Natural Cleat System of Coal Seam

Darcy flow is assumed in the natural cleat system, and the mathematical model of gas-water dual-phase two-dimensional plane flow in coal reservoir can be obtained from Darcy's law and continuity equation. The expression is as follows.

Water-phase flow differential equation:

$$\frac{\partial}{\partial x}\left(\frac{K_{fx}K_{rw}\rho_w}{\mu_w}\frac{\partial P_{fw}}{\partial x}\right)+\frac{\partial}{\partial y}\left(\frac{K_{fy}K_{rw}\rho_w}{\mu_w}\frac{\partial P_{fw}}{\partial y}\right)-q_{w\,(f-F)} = \frac{\partial\left(\rho_w S_{fw}\phi_f\right)}{\partial t}. \tag{11}$$

Gas flow differential equation:

$$\frac{\partial}{\partial x}\left(\frac{K_{fx}K_{rg}\rho_g}{\mu_g}\frac{\partial P_{fg}}{\partial x}\right)+\frac{\partial}{\partial y}\left(\frac{K_{fy}K_{rg}\rho_g}{\mu_g}\frac{\partial P_{fg}}{\partial y}\right)+q_{gmf} - q_{g\,(f-F)}=\frac{\partial\left(\rho_g S_{fg}\phi_f\right)}{\partial t}. \tag{12}$$

Auxiliary equations:

$$S_{fg}+S_{fw}=1, \tag{13}$$

$$p_{fcgw}\left(S_w\right)=p_{fg}-p_{fw}, \tag{14}$$

where K_f is the absolute permeability of cleat (mD), K_{frg} is the relative permeability of gas phase in cleats (dimensionless quantity), K_{frw} is the relative permeability of water phase in cleats (dimensionless quantity), μ_w is the viscosity of water phase (mPa·s), ρ_w is water phase density(kg/m^3), φ_f is the porosity of cleat system (dimensionless quantity), P_{fg} is the pressure of gas in cleat system (MPa), P_{fw} is water phase pressure of cleat system (MPa), S_{fw} is water saturation in natural fractures(dimensionless quantity), S_{fg} is gas saturation in natural fractures (dimensionless quantity), $q_{w\ (f\text{-}F)}$ is interporosity gas flow between natural fractures and artificial fractures p$_{er}$ unit volume of reservoir in unit time (kg/m$^3\cdot$ d^{-1}); $q_{g\ (f\text{-}F)}$ is interporosity water flow between natural fractures and artificial fractures per unit volume of reservoir in unit time (kg/m$^3\cdot$ d^{-1}) and P_{fcgw} is capillary pressure (MPa).

Mathematical Model of Porous Flow Through the Artificial Fracture System in Coal Seam

After hydraulic fracturing of vertical wells in a coal reservoir, the productivity is actually controlled by discrete large-scale artificial fractures, which are relatively independent systems of flow through porous media. In line with the law of mass conservation, the differential equations of gas–water two-phase flow due to artificial fractures are obtained as follows:

$$\frac{\partial}{\partial x}\left(\frac{K_F K_{Frg}\rho_g}{\mu_g}\frac{\partial P_F}{\partial x}\right)+q_{g\,(f-F)}-q_{gwell}=\frac{\partial\left(\rho_g S_{Fg}\phi_F\right)}{\partial t}, \tag{15}$$

$$\frac{\partial}{\partial x}\left(\frac{K_F K_{Frw}\rho_w}{\mu_w}\frac{\partial P_F}{\partial x}\right)+q_{w\,(f-F)}-q_{wwell}=\frac{\partial\left(\rho_w S_{Fw}\phi_F\right)}{\partial t}, \tag{16}$$

where K_F is the absolute permeability of artificial fractures (mD), K_{Frg} is the relative permeability of the gas phase in artificial fractures (dimensionless quantity), K_{Frw} is the relative permeability of the water phase in artificial fractures (dimensionless quantity), φ_F is the porosity of artificial fracture system (dimensionless), P_F is pore pressure in artificial fracture system (MPa), S_{Fw} is water saturation in artificial fractures (dimensionless quantity), S_{Fg} is gas saturation in artificial fractures (dimensionless quantity), q_{wwell} is water production per unit volume of reservoir in unit time (kg/m^3 .d^{-1}), q_{gwell} is gas production per unit volume of reservoir in unit time (kg/m^3 .d^{-1}).

During coalbed methane well production, the conductivity of hydraulic fracture decreases with the increase of effective stress, showing strong stress sensitivity. Based on relevant experimental results, the relationship between permeability and effective stress of artificial fracture system is (Li et al., 2019; Li et al., 2020)

$$\boldsymbol{K}_F=\boldsymbol{K}_{\mathrm{Fi}}\exp\left(-d_f\delta_{me}\right), \tag{17}$$

where K_F is the absolute permeability of artificial fractures (mD), K_{Fi} is the initial fracture permeability (mD), d_f is the stress sensitivity coefficient of the fracture system (MPa^{-1}), and δ_{me} represents the mean effective stress (MPa).

It is assumed that, after the hydraulic fracturing of the coal reservoir and during the production of the gas well, the gas will vertically flow from the natural fractures into the main artificial fractures in the form of linear flow.

By approximating the artificial fractures by the well sources in the natural fracture grid unit, we can obtain the interporosity flow of gas and water between the natural fractures and the artificial fractures:

$$q_{l\,(f-F)}=\frac{4\cdot h_f\cdot\Delta x}{\Delta y}\frac{\rho_l K_F K_{Frl}\left(P_f-P_F\right)}{\mu_l}. \tag{18}$$

For a hydraulically fractured vertical well, the well production mainly comes from the vertical fractures on both flanks, and the fluid near the wellbore changes from radial flow to linear flow in artificial fractures.

According to Darcy's law, the well production can be expressed as

$$q_{lwell}=\frac{4\rho_l K_F K_{Frl} h_F W_F}{\mu_l}\frac{P_F-P_{wf}}{\Delta x}, \tag{19}$$

where subscript l is either w or g, representing water or gas, P_{wf} is bottom-hole flow pressure (MPa), Δx and Δy represent the size of the grid (where the artificial fracture is located) along with the *X* and *Y* directions (m), h_F is hydraulic fracture height (m) and W_F is the width of artificial fracture (m).

Productivity Prediction of the Fractured CBM Well

Historical fitting and Projection of well Ma 26 in the Mabidong block.

For the historical fitting, we selected the actual production data of well Ma 26, a vertical well. Through relevant tests, the reservoir parameters of well Ma 26 in No. 15 coal seam of the Mabidong block are obtained and shown in **Table 1**. The bottom-hole flow pressure is calculated based on the initial drainage and production data (for both water and gas) of well Ma 26, and the actual bottom-hole flow pressure is fitted by adjusting the artificial fracture parameters (uncertain parameters) in the model. The fitting fracture length and fracture conductivity are 100 m and 2 D·cm, respectively. Based on the historical fitting method, the projection of gas production of well Ma 26 is obtained and the results are shown in **Figure 2**. In the stage of production allocation, if the production is assumed at 500 m^3/day, the gas well can produce stably for about 600 days, then the cumulative figure of well Ma 26 in five years is predicted to be about 75 × 10^4 m^3.

TABLE 1 | Reservoir parameters of well Ma 26 in No. 15 coal seam of the Mabidong block.

Coal seam thickness (m)	4.30	Reservoir pressure (MPa)	9.85
Critical desorption pressure (MPa)	4.28	Bottom-hole flow pressure (MPa)	0.10
Langmuir pressure (MPa)	1.66	Reservoir porosity (%)	6.07
Langmuir volume(m^3/t)	8.64	Matrix permeability(mD)	0.01

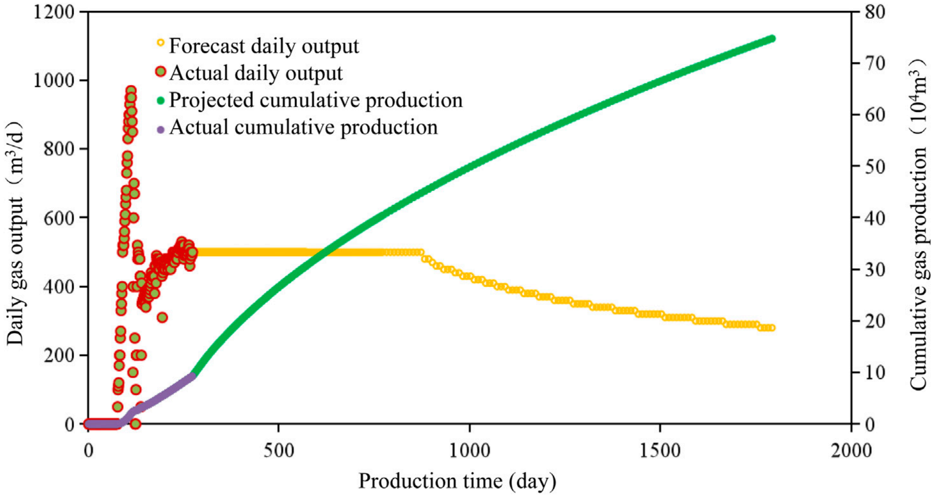

FIGURE 2 | Historical fitting and production prediction of well Ma 26 in No. 15 coal seam of the Mabidong block.

TABLE 2 | Main parameters of the coal seam.

Coal seam thickness (m)	9.80	Reservoir pressure (MPa)	9.85
Fracture length (m)	100.0	Bottom-hole flow pressure(MPa)	0.10
Langmuir pressure(MPa)	1.96	Reservoir porosity (%)	4.07
Langmuir volume(m^3/t)	20.00	Average throat diameter(nm)	30.00
Cleat density (number of cleats/cm)	3.00	Cleat porosity (%)	3.00
Permeability of cleat system (mD)	20.00	Coal density(kg/m^3)	1360
Formation water viscosity(mPa·s)	1.00	Gas reservoir width (m)	400
Langmuir strain constant (-)	0.01	Length of the gas reservoir (m)	400
Formation water density (kg/m^3)	1000	Stress sensitivity coefficient(MPa^{-1})	0.02

Next, a systematic research on the productivity prediction and influencing factors of CBM wells after fracturing are carried out, focusing on the variation of coalbed free gas and adsorbed gas with production time, and the effects of permeability of coal cleat system, adsorption and desorption characterization parameters, matrix porosity and complex flow regimes on production performance. For this purpose, the reservoir parameters of Ma Bidong block in the south of Qinshui Basin are shown in **Table 2**, the reservoir parameters of the Mabidong block in the south of the Qinshui Basin, which is a typical CBM development block of PetroChina.

Production Change of Free Gas and Adsorbed Gas

Figure 3 shows the production performance curves of adsorbed gas and free gas during the production of CBM wells. **Figure 4** shows the variation of free gas and adsorbed gas in the production process. It can be seen from the figures that the output of a CBM well mainly comes from adsorbed gas. At the initial stage of production, it mainly produces free gas and adsorbed gas in pores. With the progress of production, the proportion of free gas output decreases rapidly, while that of adsorbed gas increases rapidly, accounting for more than 80%. This research result is consistent with the occurrence and production law of CBM in the Mabidong block tested by Xiao et al. (2021) using low field NMR online detection.

Effect of Cleat System Permeability on Production

Figure 5 and **Table 3** show the influence of cleat system permeability on CBM production. It can be seen from the figures that when the

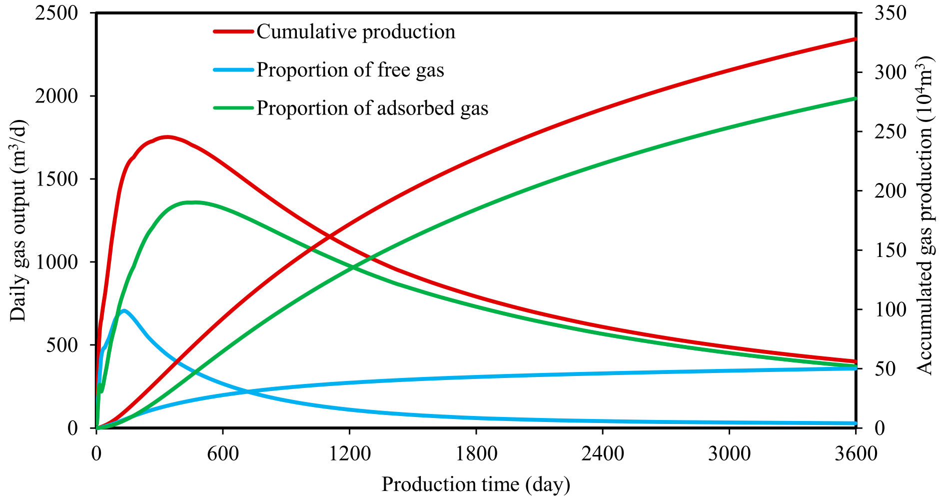

FIGURE 3 | Variation of free gas and adsorbed gas with production time.

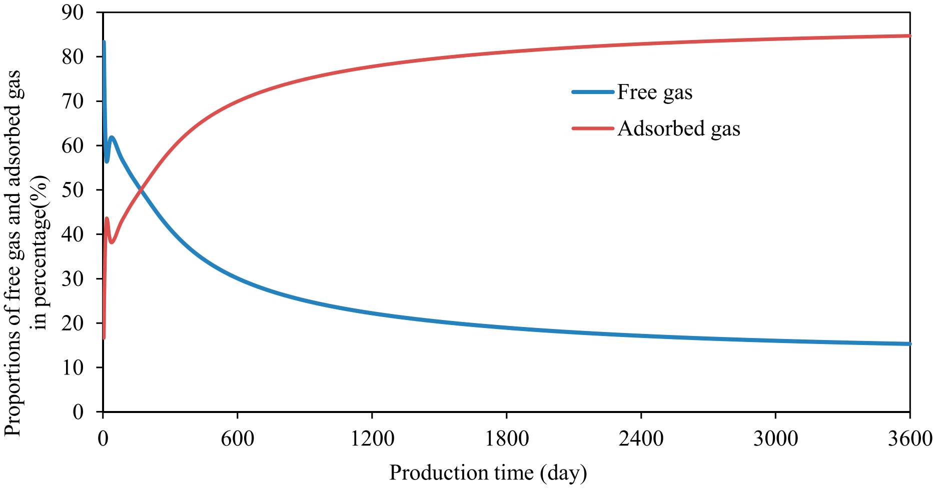

FIGURE 4 | Proportion of free gas and adsorbed gas with production time.

permeability of the cleat system increases from 10 mD to 20 mD, and then from 20 mD to 30 mD, the cumulative output of CBM wells increases from 2.08 million m^3 to 3.07 million m^3, and then from 3.07 million m^3 to 3.64 million m^3, representing a rise of 47.3% and 74% respectively. Meanwhile, peak output increases from 768m^3/d to 1493 m^3/d and then to 2225 m^3/d and the peaking time of daily CBM output is also advanced. Therefore, the permeability of the cleat system has a great influence on the gas production, peak daily output, and peaking time of CBM wells.

Effect of Complex Flow Regimes in the Matrix on Production

In the process of CBM production, a decrease in pore pressure results in an increase in effective stress and a decrease in coal seam permeability. However, the gas desorption causes matrix shrinkage with the progress of production. In addition, the decrease of pore pressure leads to a rise in slip flow, Knudsen diffusion, and surface diffusion in the micropores of the matrix, resulting in an increase in the permeability of the coal seam matrix. The combined effects cause the dynamic change in the permeability of the coal seam matrix in the production process of CBM wells. **Figure 6** shows the production curve of CBM wells with and without consideration of complex flow regimes. It can be seen that when complex flow regimes in the matrix are taken into account, both peak output and cumulative output of CBM are higher than those without complex flow regimes. As shown in **Table 4**, the cumulative output considering only the slippage effect is 6.2% higher than that of without

TABLE 3 | Effect of the permeability of the coal seam cleat system on CBM production.

Permeability of the cleat system (mD)	Peak output (m^3/d)	10-year cumulative gas production (10^4 m^3)	Percentage increase in cumulative gas production (%)
10	768.373	208.651	/
20	1492.986	307.343	47.3
30	2225.42	364.566	74.7

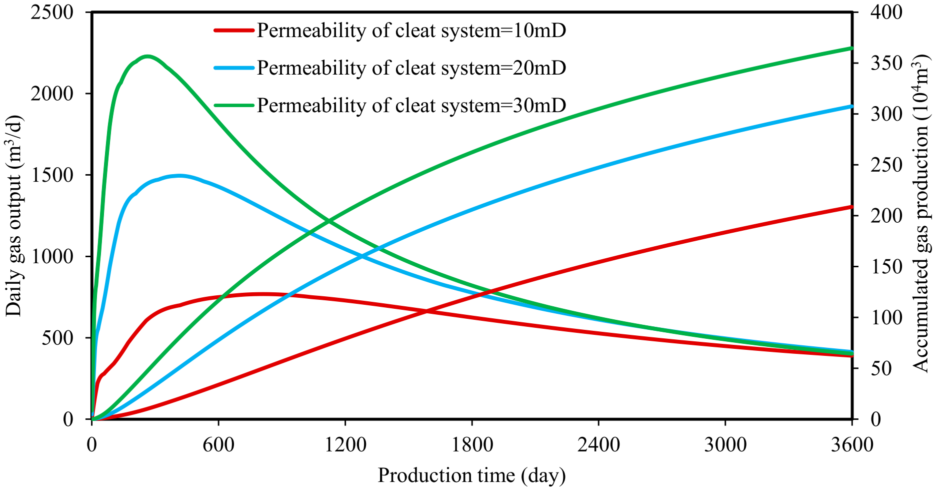

FIGURE 5 | Effect of permeability of coal seam cleat system on production.

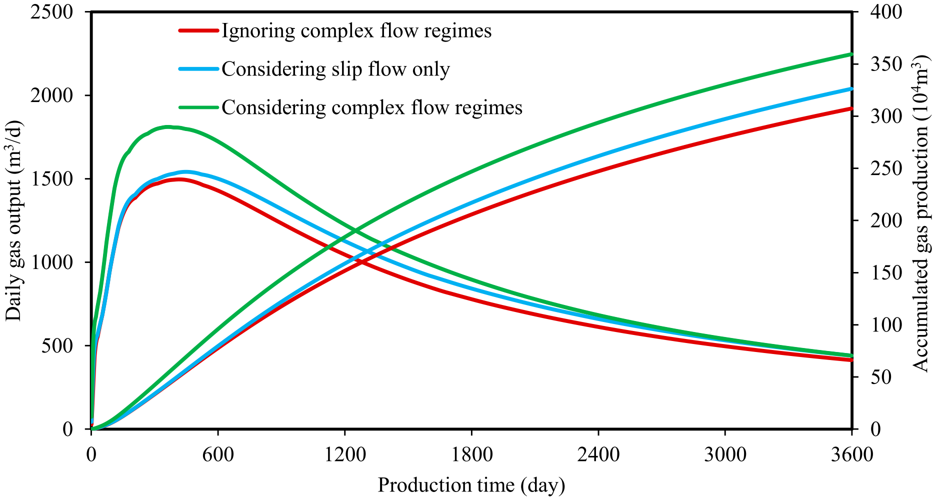

FIGURE 6 | Effects on gas production when whether complex flow regimes are considered or not.

considering any flow regime, and the output difference is 17% according to whether complex flow regimes are considered or not.

The above results show that during the production of CBM wells, the matrix shrinkage, diffusion, and slippage effects cause an increase in matrix permeability, offsetting the negative impact

TABLE 4 | Effects on gas production when complex flow regimes are and are not considered.

Matrix gas flow pattern	Peak output (m^3/d)	10-year cumulative gas output (10^4 m^3)	Percentage rise in cumulative gas production (%)
Complex flow regimes are ignored	1496.145	307.343	/
Only slip flow is considered	1541.475	326.246	6.2
Considering complex flow regimes	1810.359	359.397	16.9

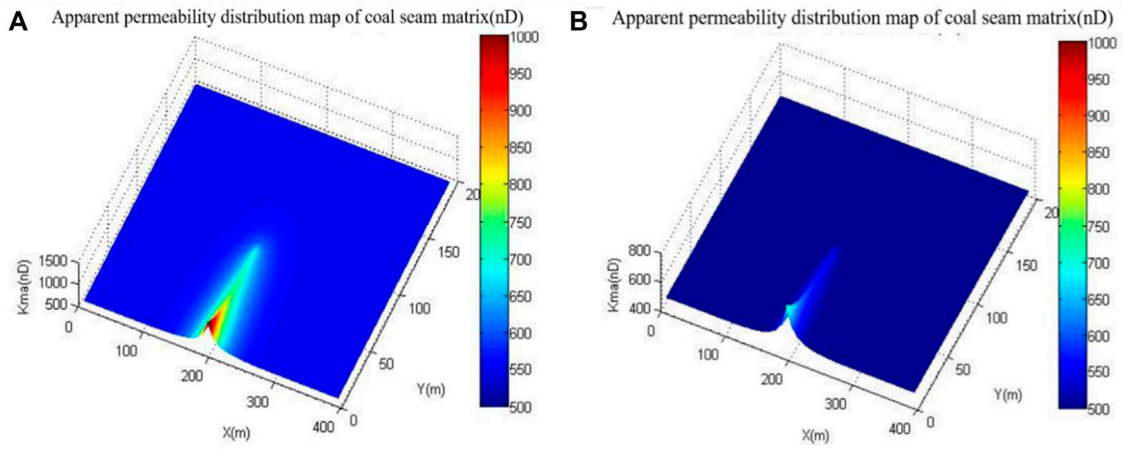

Considering complex flow regimes considering slippage flow only

FIGURE 7 | Apparent permeability distribution of CBM reservoir matrix. **(A)** Considering complex flow regimes **(B)** considering slippage flow only.

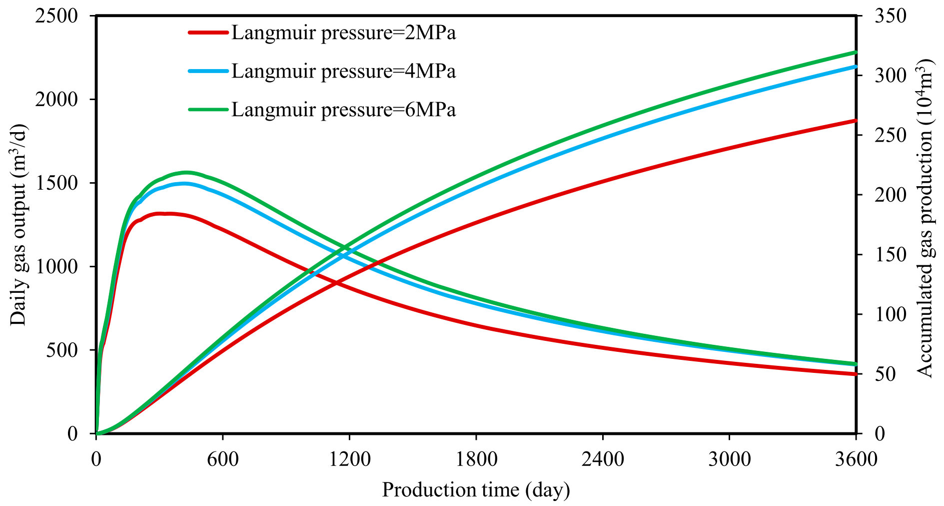

FIGURE 8 | Effect of Langmuir pressure on CBM production.

of stress sensitivity on permeability, which causes a higher CBM production under dynamic permeability than constant permeability. Pore pressure is the key factor affecting the complex transport mechanisms in the matrix. With the progress of production, the apparent permeability of the matrix increases as the pore pressure declines. The apparent

TABLE 5 | Effect of Langmuir pressure on CBM production.

Langmuir pressure (MPa)	Peak output (m^3/d)	10-year cumulative gas production (10^4m^3)	Percentage rise in cumulative gas production (%)
2	1316.379	262.232	/
4	1496.145	307.343	17.2
6	1561.773	319.422	21.8

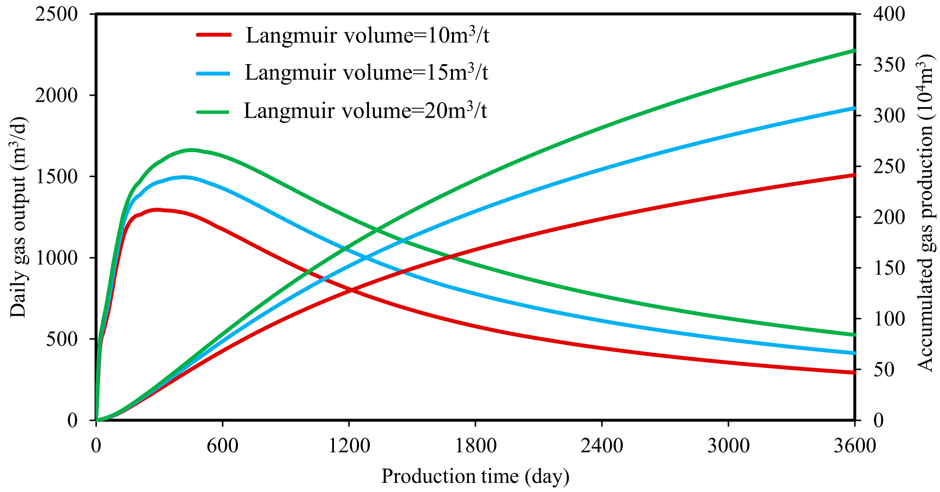

FIGURE 9 | Influence of Langmuir volume on CBM production.

TABLE 6 | Effect of Langmuir volume on output.

Langmuir volume (m^3/t)	Peak output (m^3/d)	10-year cumulative gas production/(10^4m^3)	Percentage rise in cumulative gas production/(%)
10	1295.607	241.478	/
15	1496.145	307.343	27.3
20	1661.92	363.866	50.7

permeability distribution of the coal seam matrix is shown in **Figure 7**.

Impact of Langmuir Pressure on Production

Figure 8 illustrates the effect of Langmuir pressure on CBM production performance. It can be seen that when the Langmuir pressure rises from 2 MPa to 4 MPa and then to 6MPa, the peak CBM output increases from 1316 m^3/d to 1496 m^3/d and then to 1561 m^3/d. Meanwhile, the cumulative output rises from 2.62 million m^3 to 3.07 million m^3 and then to 3.19 million m^3, representing a gain of 17.2% and 21.8% respectively, as shown in **Table 5**. The peak output and cumulative output of CBM increase with rises in Langmuir pressure, but the margin of growth slows. This is because a rise in Langmuir pressure causes an increase in the desorption pressure of CBM, which means it is then easier for CBM to desorb, and more adsorbed gas will desorb into free gas.

Effect of Langmuir Volume on Production

The influence of Langmuir volume (gas adsorption capacity of coal) on the daily production and cumulative production of gas wells are illustrated in **Figure 9**. It can be seen that Langmuir volume has an important effect on the daily output and cumulative output of CBM. A rise in (**Figure 9**). Langmuir volume will bring a significant increase in CBM peak output, daily output, and cumulative output. When the Langmuir volume increases from 10 m^3/t to 15 m^3/t and then to 20 m^3/t, the peak output increases from 1295 m^3/d to 1496 m^3/d and then to 1661 m^3/d, and the cumulative output increases from 241 × 10^4 m^3 to 307 × 10^4 m^3 and then to 363 × 10^4 m^3. As provided in **Table 6**, the cumulative output increases by 27.3% and 50.7% respectively. The time required for CBM to reach the peak daily output also increases slightly with the rise in Langmuir volume. This is because when the reservoir pressure is constant, the total gas content of the coal reservoir rises with the increase of the Langmuir volume, which is equivalent to increasing the geological reserves of CBM. It can also be seen from the daily gas output in **Figure 9** that the Langmuir volume has no effect on the initial daily output. This is because the free gas phase in the matrix micropores is mainly produced in the initial stage of production, while the contribution of adsorbed gas to the output becomes gradually apparent with the passage of production time.

CONCLUSION

Taking into consideration the comprehensive effects of coalbed matrix shrinkage effect, gas slippage, Knudsen diffusion, surface diffusion, and fracture stress sensitivity on CBM flow, a mathematical model of production performance that incorporates coalbed matrix gas desorption, complex flow regimes in micropore gas, fracture stress sensitivity and gas-water two-phase flow is developed. We selected the reservoir parameters of the Mabidong block in the south of the Qinshui Basin to carry out the numerical simulation and projection of CBM well output and focused on the impact of some key parameters on CBM well production performance. The following conclusions are drawn:

1) The productivity simulation shows that free gas and adsorbed gas are produced simultaneously in the stage of coalbed methane drainage and production, but the free gas is the main gas, and the percentage of free gas production decreases rapidly with production time, while the percentage of adsorbed gas production increases rapidly. By the late production stage,70–80% of daily gas comes from adsorbed gas.
2) The complex flow regimes in the coal seam matrix has some effect on the output of CBM. Considering the complex flow regimes, the output is increased by about 17% compared with output where these regimes are not considered, and the output is increased by 6.2% if only the slip effect is considered. In the later stage of production, the gas transport in the micropores of the coal seam matrix is mainly surface diffusion and Knudsen diffusion.
3) The permeability of the coalbed cleat system has a great impact on CBM production. The peak output and cumulative output of CBM increase significantly with a rise in cleat system permeability. The greater the permeability of the cleat system, the earlier the CBM production reaches the peak output.
4) The cumulative output and peak output of CBM wells are directly proportional to Langmuir volume and pressure. When Langmuir volume increases from 10 m^3/t to 20 m^3/t, the cumulative production of CBM wells will increase by about 50%. When the Langmuir pressure increases from 2 MPa to 6 MPa, the cumulative output of CBM will increase by about 21.8%.

DATA AVAILABILITY STATEMENT

The raw data supporting the conclusion of this article will be made available by the authors, without undue reservation.

AUTHOR CONTRIBUTIONS

Drafting of the article: QX and BJ; analysis and interpretation of data: HW, YY, and ZL; numerical modeling: ZL and ZX; and revision of the manuscript: QX, HW, and JL.

FUNDING

This research was financially supported by the National Science and Technology Major Special Support Program (Grant No. 2017ZX05064); Major Science and Technology Special Support Program of CNPC (Grant No. 2017E-1404); Chongqing Natural Science Foundation (cstc20jcyj-msxmx0216); and Bayu Scholars Program, College-Level Fund of Guilin Institute of Aerospace Technology (Grant No. XJ20KT04). These sources of funding are all gratefully acknowledged.

REFERENCES

Chen, Z., Liu, J., Kabir, A., Wang, J., and Pan, Z. (2013). Impact of Various Parameters on the Production of Coalbed Methane. *SPE J.* 18 (05), 910–923. doi:10.2118/162722-pa

Clarkson, C. R. R., Pan, Z., Palmer, I., and Harpalani, S. (2010). Predicting Sorption-Induced Strain and Permeability Increase with Depletion for Coalbed-Methane Reservoirs. *Spe J.* 15 (01), 152–159. doi:10.2118/114778-pa

Dong, J., Cheng, Y., Jin, K., Zhang, H., Liu, Q., and Jiang, J., (2017). Effects of Diffusion and Suction Negative Pressure on Coalbed Methane Extraction and a New Measure to Increase the Methane Utilization Rate. *Fuel* 197, 70–81. doi:10.1016/j.fuel.2017.02.006

Duan, X., Gao, S., Hu, Z., and Jin, C. (2017). *Research Progress in Multi-Scale Percolation Theory in Shale Micro-nano Pores. Special Oil & Gas Reservoirs.*

Huang, S., Wu, Y., Cheng, L., Liu, H., Xue, Y., and Ding, G. (2018 2018). Apparent Permeability Model for Shale Gas Reservoirs Considering Multiple Transport Mechanisms. *Geofluids*,2186194 1–18. doi:10.1155/2018/2186194

Jiang, Y., Yang, X., Xiong, L., and Zheng, Q. (2011). *Multi-field Coupling Effect on Coalbed Methane Seepage Characteristics and Numerical Simulation*. Journal of Chongqing University 34 (4), 30–35.

Kong, X., Wang, E., Liu, Q., Li, Z., Li, D., Cao, Z., et al. (2017). Dynamic Permeability and Porosity Evolution of Coal Seam Rich in CBM Based on the Flow-Solid Coupling Theory. *J. Nat. Gas Sci. Eng.* 40, 61–71. doi:10.1016/j.jngse.2017.02.011

Li, Z., Qi, Z., Yan, W., Xiang, Z., Ao, X., Huang, X., et al. (2020). Prediction of Production Performance of Refractured Shale Gas Well Considering Coupled Multiscale Gas Flow and Geomechanics.*Geofluids* 2020 (4) 1–21 doi:10.1155/2020/9160346

Li, Z., Yan, W., Qi, Z., Dong, D., Huang, X., and Yu, R. (2019). Production Performance Model Based on Quadruple-Porosity Medium in Shale Gas Reservoirs Considering Multi-Transport Mechanisms. *Energy Sources, Part A Recovery, Util. Environ. Eff.*, 1–19. doi:10.1080/15567036.2019.1662520

Liu, J., Zhang, Y., Hu, Z., Li, Y., and Yang, X. (2018). An Experimental Study on the Mass Transfer Mechanism and the Flow Regime of Gas in Nano-Scale Pores of Shale Gas Reservoirs. *Nat. Gas. Ind.* 38 (12), 87–95.

Luo, Y., Xia, B., Li, H., Hu, H., Wu, M., and Ji, K. (2021). Fractal Permeability Model for Dual-Porosity Media Embedded with Natural Tortuous Fractures. *Fuel* 295, 120610. doi:10.1016/j.fuel.2021.120610

Ma, T., Rutqvist, J., Oldenburg, C. M., Liu, W., and Chen, J. (2017). Fully Coupled Two-phase Flow and Poromechanics Modeling of Coalbed Methane Recovery: Impact of Geomechanics on Production Rate. *J. Nat. Gas Sci. Eng.* 45, 474–486. doi:10.1016/j.jngse.2017.05.024

Meng, Y., Wang, J. Y., Li, Z., and Zhang, J. (2018). An Improved Productivity Model in Coal Reservoir and its Application during Coalbed Methane Production. *J. Nat. Gas Sci. Eng.* 49, 342–351. doi:10.1016/j.jngse.2017.11.030

Moore, R., and Higgs, N. (2015). Anisotropic Model for Permeability Change in Coalbed-Methane Wells. *SPE Reserv. Eval. Eng.* 18 (04), 456–462. doi:10.2118/169592-pa

Palmer, I., and Mansoori, J. (1996). "How Permeability Depends on Stress and Pore Pressure in Coalbeds: a New Model," in *SPE Annual Technical Conference and Exhibition: SPE-30010-MS)*. doi:10.2118/36737-ms

Qiao, Y., Peng, X., Zhu, S., and Sun, H. (2018). *Coalbed Methane Productivity Model Considering Desorption and Phase Permeability*. China Coalbed methane 15 (1), 19–22.

Seidle, J. R., and Huitt, L. (1995). "Experimental Measurement of Coal Matrix Shrinkage Due to Gas Desorption and Implications for Cleat Permeability Increases," in *International Meeting on Petroleum Engineering: SPE-30010-MS)*. doi:10.2118/30010-ms

Shaw, D., Mostaghimi, P., and Armstrong, R. T. (2019). The Dynamic Behaviour of Coal Relative Permeability Curves. *Fuel* 253, 293–304. doi:10.1016/j.fuel.2019.04.107

Sheng, G., Javadpour, F., and Su, Y. (2019). Dynamic Porosity and Apparent Permeability in Porous Organic Matter of Shale Gas Reservoirs. *Fuel* 251, 341–351. doi:10.1016/j.fuel.2019.04.044

Wei, M., Liu, C., Liu, Y., Liu, J., Elsworth, D., Tivane, O. A., et al. (2022). Long-term Effect of Desorption-Induced Matrix Shrinkage on the Evolution of Coal Permeability during Coalbed Methane Production. *J. Petroleum Sci. Eng.* 208, 109378. doi:10.1016/j.petrol.2021.109378

Wei, Z., and Zhang, D. (2013). A Fully Coupled Multiphase Multicomponent Flow and Geomechanics Model for Enhanced Coalbed-Methane Recovery and CO2 Storage. *SPE J.* 18 (03), 448–467. doi:10.2118/163078-pa

Wei, Z., and Zhang, D. (2010). Coupled Fluid-Flow and Geomechanics for Triple-Porosity/dual-Permeability Modeling of Coalbed Methane Recovery. *Int. J. Rock Mech. Min. Sci.* 47 (8), 1242–1253. doi:10.1016/j.ijrmms.2010.08.020

Wu, K., Chen, Z., Li, X., Guo, C., and Wei, M. (2016a). A Model for Multiple Transport Mechanisms through Nanopores of Shale Gas Reservoirs with Real Gas Effect–Adsorption-Mechanic Coupling. *Int. J. Heat Mass Transf.* 93, 408–426. doi:10.1016/j.ijheatmasstransfer.2015.10.003

Wu, K., Li, X., Guo, C., Wang, C., and Chen, Z. (2016b). A Unified Model for Gas Transfer in Nanopores of Shale-Gas Reservoirs: Coupling Pore Diffusion and Surface Diffusion *SPE Journal* 21 (1), 1583–1611. doi:10.2118/2014-1921039-pa

Xiao, Q., Yang, Y., Jiang, B., Zhao, X., Yu, R., Liu, Z., et al. (2021). Evaluation Method of the Micro-occurrence and Utilization Patterns of Gas via a Novel Method Based on Nuclear Magnetic Resonance. *J. Nat. Gas Sci. Eng.* 86, 103721. doi:10.1016/j.jngse.2020.103721

Yang, Z. (2016). *Dynamic Simulation of Self-Modification of Fractured Wells in Coalbed Methane Reservoirmaster's Degree*. Southwest Petroleum University.

Zhang, Y., Shang, F., Sun, X., Li, S., and Sun, R. (2012). Research on Coalbed Methane Numerical Simulation Considering Permeability Changes and Parameter Sensitivity Analysis. *Coal Geol. Chi- na* 24 (4), 18–23.

Ye, D., Liu, G., Gao, F., Xu, R., and Yue, F. (2021). A Multi-Field Coupling Model of Gas Flow in Fractured Coal Seam. *Adv. Geo-Energy Res.* 5 (1), 104–118. doi:10.46690/ager.2021.01.10

Zhang, L., Hu, Y., Zhang, P., Zhao, J., Wu, J., and Sun, H. (2015). Influencing Factors Of The Production Performances For The Fractured CBM Wells In QinShui Basin. *Petroleum Geology anf Oilfield Development in Daqing* 34 (5), 170–174.

Conflict of Interest: YY was employed by the company Pilot Test Base for CBM Production of the China National Petroleum Corporation and PetroChina Huabei Oilfield Company.

The remaining authors declare that the research was conducted in the absence of any commercial or financial relationships that could be construed as a potential conflict of interest.

frontiers | Frontiers in Earth Science

TYPE Original Research
PUBLISHED 16 August 2022
DOI 10.3389/feart.2022.983735

Indicator diagram analysis based on deep learning

Wenbin Cai[1]*, Zirui Sun[1], Zhaohuan Wang[1], Xuecheng Wang[1], Yi Wang[1], Guoqiang Yang[1] and Shaowei Pan[2]

[1]College of Petroleum Engineering, Xi'an Shiyou University, Xi'an, Shaanxi, China, [2]College of Computer Science, Xi'an Shiyou University, Xi'an, Shaanxi, China

OPEN ACCESS

EDITED BY
Keliu Wu,
China University of Petroleum, China

REVIEWED BY
Songyan Li,
China University of Petroleum, Huadong, China
Shengnan Chen,
University of Calgary, Canada

*CORRESPONDENCE
Wenbin Cai,
caiwenbin@xsyu.edu.cn

SPECIALTY SECTION
This article was submitted to Environmental Informatics and Remote Sensing,
a section of the journal
Frontiers in Earth Science

RECEIVED 01 July 2022
ACCEPTED 18 July 2022
PUBLISHED 16 August 2022

CITATION
Cai W, Sun Z, Wang Z, Wang X, Wang Y, Yang G and Pan S (2022), Indicator diagram analysis based on deep learning.
Front. Earth Sci. 10:983735.
doi: 10.3389/feart.2022.983735

At present, more than 90% of China's oil production equipment comprises rod pump production systems. Indicator diagram analysis of the pumping unit is not only an effective method for monitoring the current working condition of a rod pump production system but also the main way to prevent, detect, and rectify various faults in the oil production process. However, the identification of the pumping unit indicator diagram mainly involves manual effort, and the identification accuracy depends on the experience of the monitoring personnel. Automatic and accurate identification and classification of the pumping unit indicator diagram using new computer technology has long been the research focus of studies for monitoring the pumping unit working condition. In this paper, the indicator diagram is briefly introduced, and the AlexNet model is presented to distinguish the indicator diagram of abnormal wells. The influence of the step size, convolution kernel size, and batch normalization (BN) layer on the accuracy of the model is analyzed. Finally, the AlexNet model is improved. The improved model reduces the calculation cost and parameters, accelerates the convergence, and improves the accuracy and speed of the calculation. In the experimental analysis of abnormal well diagnosis, the data are preprocessed *via* data deduplication, binary filling, random line distortion, random scaling and stretching, and random vertical horizontal displacement. In addition, the image is expanded by transforming several well indicator diagrams. Finally, data sets of 10 types of indicator diagrams are created for better adaptability and application in the analysis and classification of indicator diagrams, and the ideal application effect is achieved in actual working conditions. In summary, this technology not only improves the recognition accuracy but also saves manpower. Thus, it has good application prospects in the field of oil production.

KEYWORDS

indicator diagram, deep learning, convolutional neural network, AlexNet, batch normalization

Introduction

Rod pump production systems constitute the predominant equipment in crude oil exploitation. Owing to the specific nature of their structural characteristics and working environment, their failure rate is high. Therefore, it is crucial to understand the working state of the pumping unit as well as to analyze and rectify faults in a timely and accurate manner (Li et al., 2013a; Reges et al., 2015). The indicator diagram is a closed curve composed of the load-versus-displacement curves. In the working process of the rod pumping unit, the obtained indicator diagram can be used to qualitatively analyze the working condition of the pumping unit, adjust the working parameters in a timely manner, and detect and eliminate faults. However, in actual production, the recognition and classification of the indicator diagram mainly involves manual effort, and the recognition efficiency is low. Deep learning, a new area of machine learning with successful applications in computer vision, speech recognition, and other fields, provides a new idea for solving problems such as image classification (Zhang, 2000; Xu et al., 2007; Bezerra et al., 2010; Sun et al., 2012; Li et al., 2013b)·. As the analysis of the indicator diagram can be regarded as a type of image classification, it is technically feasible and of great practical significance to study the application of convolutional neural networks (CNNs) to the automatic identification and classification of the indicator diagram (Luan et al., 2011; Li, 2015).

Diagnosis of abnormal wells based on AlexNet model

In recent years, the use of computer technology for the diagnosis of abnormal wells has attracted considerable research attention. For example, expert systems, support vector machines, and fuzzy theory are used in the diagnosis of abnormal wells (Krizhevsky et al., 2012; Krizhevsky, 2014). These methods involve artificial feature extraction, i.e., feature extraction using classification methods such as pattern classification. However, the extraction process is manual and hence suffers from information loss and extraction errors, which affect the performance of the subsequent classification algorithms. In deep learning, a large amount of historical data can be used to automatically extract and learn features, which compensates for the shortcomings of manual feature extraction. According to the characteristics of the indicator diagram, the CNN algorithm is an innovative and widely applicable tool for the diagnosis of abnormal wells.

Figure 1 shows the AlexNet network model. The network model for image recognition consists of four basic elements: convolution layer, pooling layer, fully connected layer, and activation function (Xu et al., 2020). The pooling layer generally follows the convolution layer, and the fully connected layer is located at the end of the network to output the final feature vector. The activation function determines whether the neurons are activated for transmitting information. The main function of the convolution layer is to extract the features of the input indicator diagram. The core idea of convolution involves the local receptive field and weight sharing convolution process. After the convolution layer extracts the features, the generated feature map is passed to the next layer. The main function of the pooling layer is to compress the feature map and eliminate the influence of the space conversion of the indicator map. The last layer of the CNN is generally the fully connected layer, whose function is to convert the feature map of the input indicator diagram extracted by the previous convolution layer and pooling layer into the feature vector output. Thus, the diagnosis of abnormal wells is completed.

The AlexNet experiment involves 80 iterations. The model is saved once every 10 iterations, and the accuracy, number of iterations, and loss error of the model are recorded. The accuracy of the network model is gradually stable after more than 20 iterations, and the recognition accuracy of the model test set is 97.3%, as shown in Figure 2A. Similarly, after around

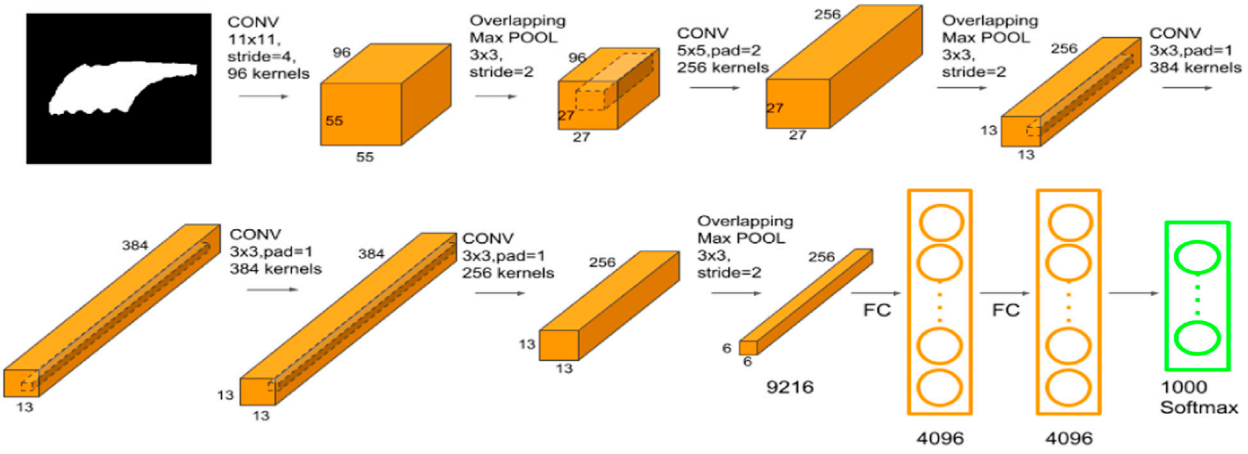

FIGURE 1
AlexNet network model.

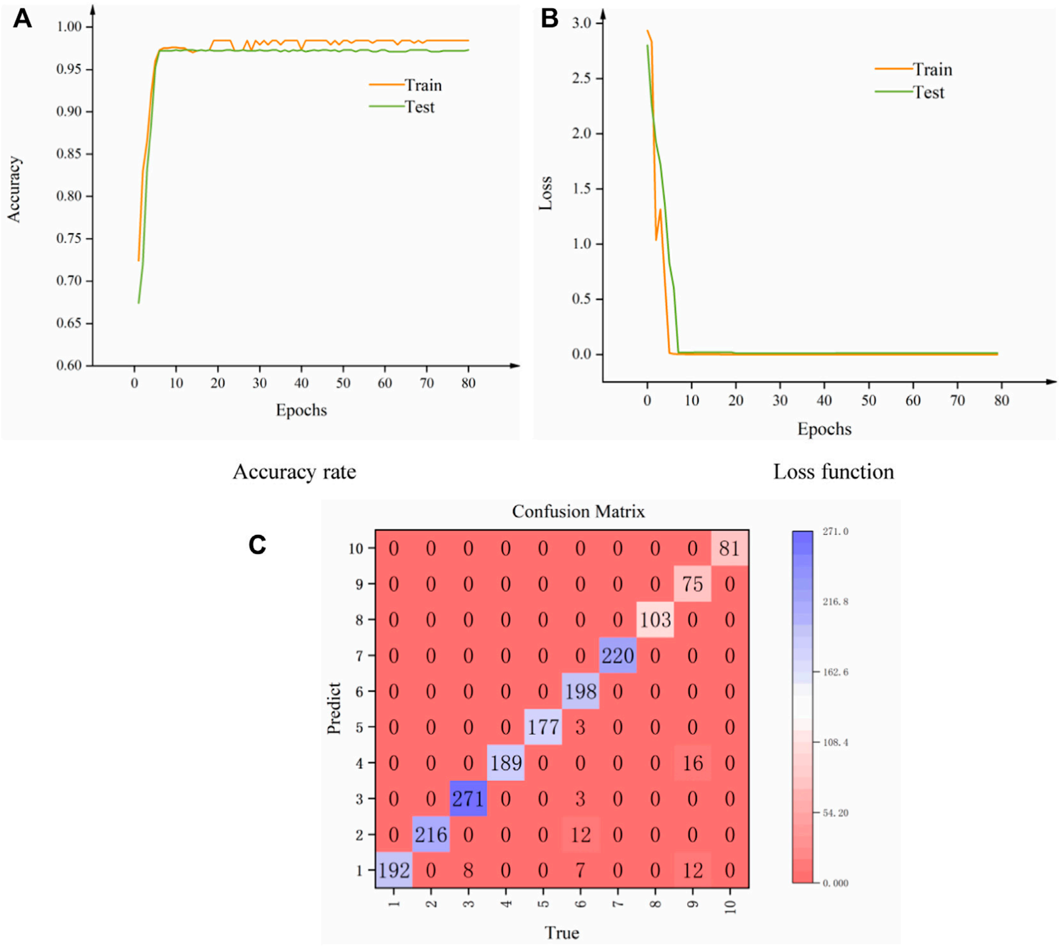

Accuracy rate

Loss function

Predict \ True	1	2	3	4	5	6	7	8	9	10
10	0	0	0	0	0	0	0	0	0	81
9	0	0	0	0	0	0	0	0	75	0
8	0	0	0	0	0	0	0	103	0	0
7	0	0	0	0	0	0	220	0	0	0
6	0	0	0	0	0	198	0	0	0	0
5	0	0	0	0	177	3	0	0	0	0
4	0	0	0	189	0	0	0	0	16	0
3	0	0	271	0	0	3	0	0	0	0
2	0	216	0	0	0	12	0	0	0	0
1	192	0	8	0	0	7	0	0	12	0

Confusion matrix

FIGURE 2
AlexNet training process. **(A)** Accuracy rate **(B)** Loss function **(C)** Confusion matrix.

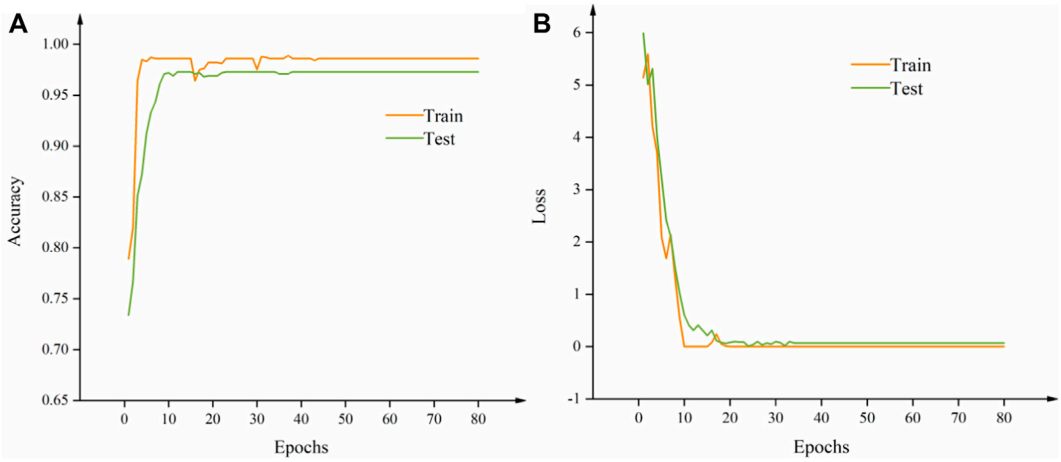

Accuracy rate

Loss function

FIGURE 3
5*5 Convolutional training process. **(A)** Accuracy rate **(B)** Loss function.

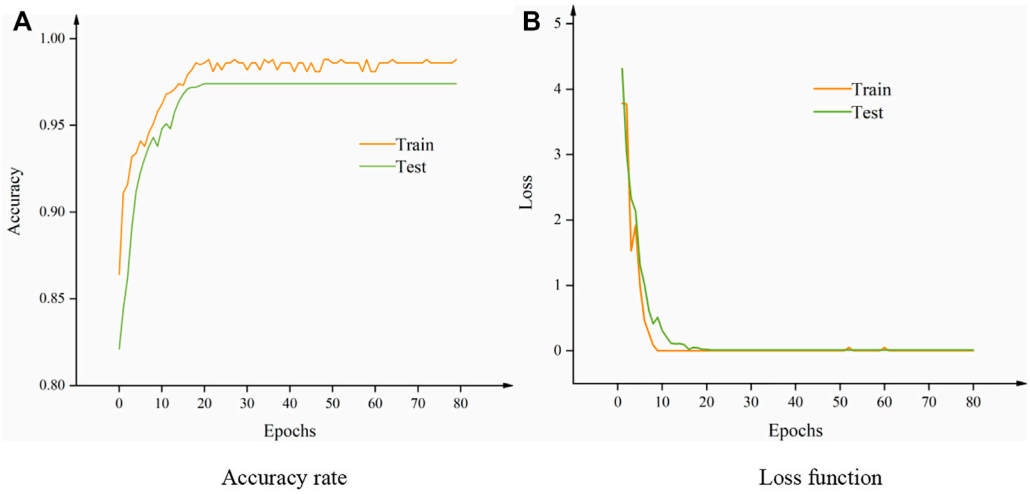

FIGURE 4
3*3 Convolutional training process. **(A)** Accuracy rate **(B)** Loss function.

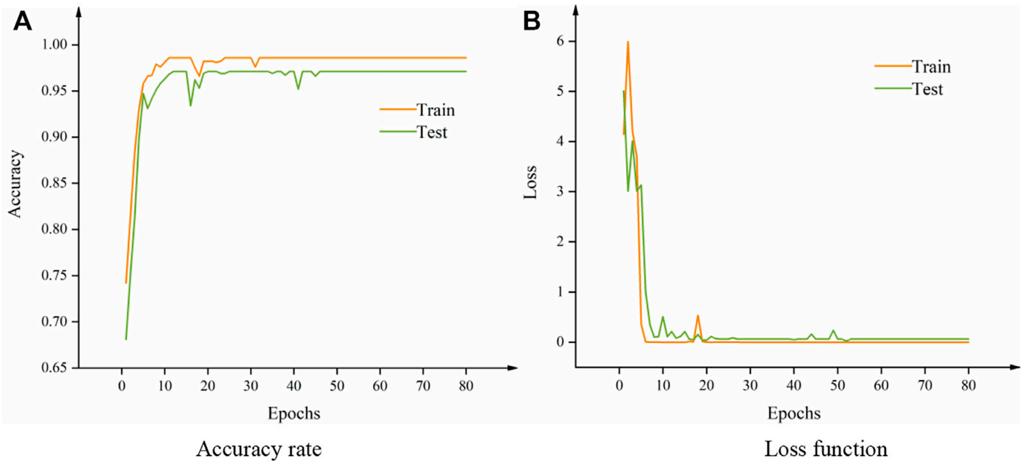

FIGURE 5
2*2 convolution training process. **(A)** Accuracy rate **(B)** Loss function.

TABLE 1 Performance comparison of three convolution kernel sizes.

Size of convolution kernel	Number of iterations to convergence	Test accuracy (%)	Parameters	Memory (MB)
5*5	20	96.9	32,741,674	127
3*3	20	97.4	49,352,746	191
2*2	20	97.1	63,571,290	248

20 iterations, the loss value gradually becomes stable and reaches convergence; the loss of the test set is around 0.02, as shown in Figure 2B. As can be seen from the confusion matrix shown in Figure 2C, the diagnostic accuracy of the AlexNet model for abnormal wells is relatively high. According to the diagnosis, error-prone situations that occur include fixed valve leakage, insufficient

TABLE 2 Influence of step size on network performance.

Model/step size	Number of iterations to convergence	Test accuracy (%)	Parameters	Memory (MB)
5cs1	20	96.5	196,153,386	766
1cs2_4cs1	20	97.2	49,352,650	192
2cs2_3cs1	20	97.9	14,487,594	56
3cs2_2cs1	20	94.9	7,409,706	28
4cs2_1cs1	20	93.6	5,312,458	20
1cs3_4cs1	18	95.8	21,827,530	85
2cs3_3cs1	18	87.5	6,098,986	23

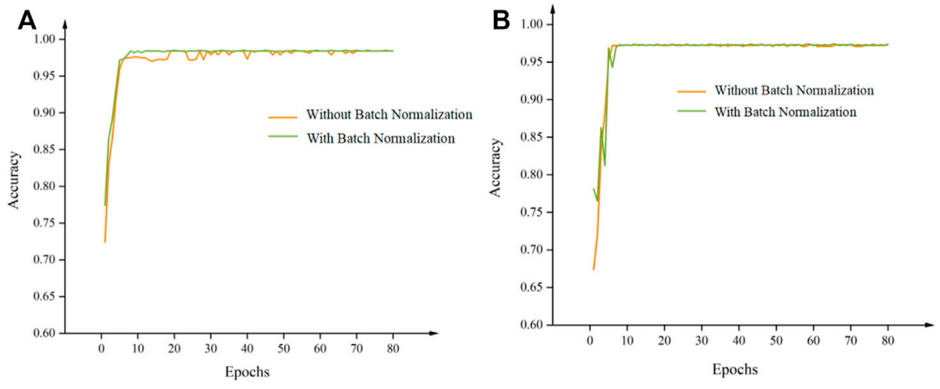

Accuracy map of training set

Accuracy map of test set

FIGURE 6
Comparison of step accuracy. **(A)** Accuracy map of training set **(B)** Accuracy map of test set.

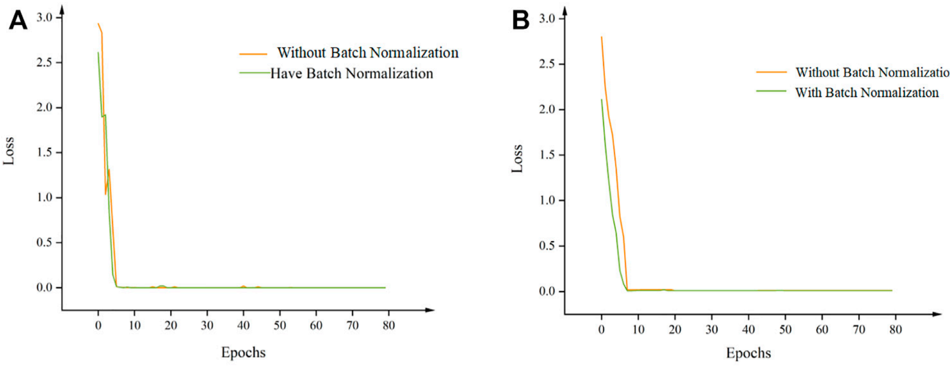

Loss value of training set

Loss value of test set

FIGURE 7
Comparison of step loss rate. **(A)** Loss value of training set **(B)** Loss value of test set.

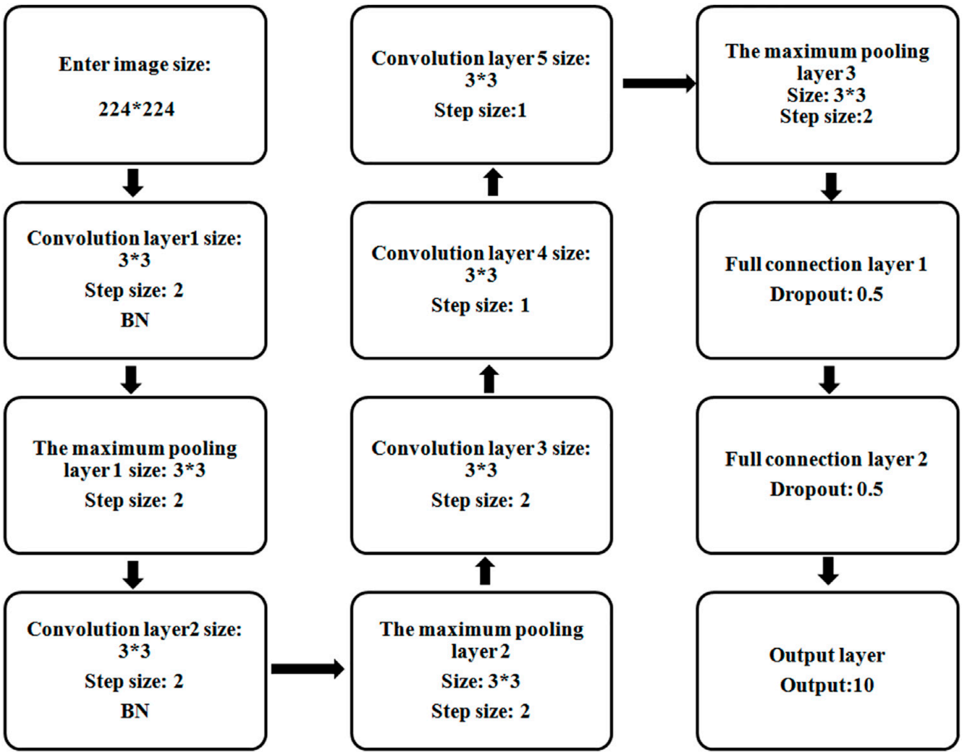

FIGURE 8
Improved AlexNet network model. In this study, VGG, LeNet, and other models are used for comparison.

TABLE 3 Comparison of two models.

Model	Test accuracy (%)	Number of parameters	Memory (MB)
AlexNet	97.3	5,700 myriad	230
Improved AlexNet	97.9	1,400 myriad	56

liquid supply and gas influence, and slow closing of the moving valve. However, the test set comprising nearly 1700 data includes less than 40 error data. Thus, the AlexNet network achieves high accuracy in indicator diagram classification for abnormal well diagnosis. Finally, the evaluation indexes of the model are as follows: accuracy rate, 96.58%; precision rate, 97.18%; recall rate, 95.97%; and F1 score, 96.22%.

Improvement of AlexNet model

Owing to the high memory consumption and low accuracy of the AlexNet model, the model is improved accordingly. The influence of various parameters on the diagnosis accuracy of abnormal wells is studied in detail. The model is optimized in terms of the convolution kernel size, batch normalization (BN) layer, and step length, and the parameters suitable for the diagnosis model of abnormal wells are selected. The early stopping method and dropout layer are used to prevent overfitting of the model. The number of iterations/epochs is set to 80, and the accuracy and error of the training and test sets are recorded once per epoch.

Influence of convolution kernel size on network model

1) 5*5 convolution kernel

The network model converges after around 20 iterations, and the loss converges to 0.08 for the test set. Figure 3 shows the good fitting performance of the network model.

2) 3*3 convolution kernel

TABLE 4 Transformation of indicator diagram.

Conversion type of indicator diagram	**Indicator diagram**	**Indicator diagram with 180° rotation**
Conversion of normal indicator diagram	 normal hexane indicator diagram	 normal hexane indicator diagram
Conversion of indicator diagram of upper bump pump and lower bump pump	 indicator diagram of down-impact pump	 indicator diagram of bump pump
Conversion of indicator diagram of moving valve leakage and fixed valve leakage	 indicator diagram of valve leakage	 indicator diagram of fixed valve leakage
Conversion of indicator diagram of insufficient fluid supply and slow closing of valve	 indicator diagram of insufficient liquid supply  indicator diagram of insufficient liquid supply	 indicator diagram of valve closing delay  indicator diagram of valve closing delay

TABLE 5 Classification of indicator diagram.

Category	Number	Label	Storage path	Category	Number	Label	Storage path
Normal work	837	1	img/1	Slow closing of swimming valve	743	6	img/6
Insufficient fluid supply	719	2	img/2	Piston outlet pump barrel	730	7	img/7
Gas influence	919	3	img/3	Valve Leakage	342	8	img/8
Up-impact pump	628	4	img/4	Fixed valve leakage	342	9	img/9
Lower bump pump	589	5	img/5	Sand effect and insufficient liquid supply	270	10	img/10

The network model converges after around 20 iterations, and the deviation is small. The 3*3 convolution kernel achieves better performance than the 5*5 convolution kernel, as shown in Figure 4. Hence, the 3*3 convolution kernel is a better choice。

3) 2*2 convolution kernel

There is a certain gap between the 2*2 and 3*3 convolution kernels in terms of the fitting and accuracy, as shown in Figure 5. Hence, the usage rate of the 2*2 convolution kernel is low in common network models.

4) Comparative analysis of experiments

The size of the convolution kernel influences the performance of the network model. From the aforementioned experiments, the 3*3 convolution kernel is selected because it has the highest accuracy, relatively small number of parameters, and moderate memory consumption. Table 1 compares the performances of the three convolution kernel sizes.

Influence of step size on network model

As can be seen from Table 2, the 2cs2 _ 3cs1 model outperforms the AlexNet model in terms of the accuracy, number of parameters, and memory consumption.

Influence of BN layer on network model

In the training and testing processes of the network model, any change in the network input will affect the accuracy of the model. In particular, in the case of the deep network model, the number of iterations until convergence will increase (Huang, 2007; Yang, 2011). In the training process, if the distribution of the input in the previous layer changes significantly, the model will suffer from poor adaptability, which leads to difficulty in adjusting the parameters. Using the BN layer can reduce the dependence on data initialization and prevent problems caused by it (Chen et al., 2014; Yuan and Hu, 2015; Xu et al., 2019).

The experiment uses the AlexNet network model to add the BN layer in order to test the influence of the BN layer on the abnormal well diagnosis model. The number of iterations is 80, the initial learning rate is 0.01, and the batch size is 16.

Figures 6A,B show the accuracy curves of the abnormal well diagnosis model before and after adding the BN layer for the training and test sets, respectively. Figures 7A,B show the loss value curves of the abnormal well diagnosis model before and after adding the BN layer for the training and test sets, respectively. As can be seen from the curve of the training set, the loss value of the model with the BN layer decreases faster as the number of iterations increases, and the loss value is minimized when the number of iterations is around 10. Thus, adding the BN layer accelerates the convergence of the network model and makes it easier to extract the characteristics of image information. For the test set, the loss value of the model changes relatively smoothly. In general, the loss value of the model with the BN layer decreases faster than that of the model without BN layer. As can be seen from the accuracy change diagram, the model with the BN layer can achieve the highest accuracy faster, which can effectively reduce the training time to a certain extent.

Abnormal well diagnosis model based on improved AlexNet

The improved AlexNet model uses the 3*3 convolution kernel instead of the 11*11 or 5*5 convolution kernel, which reduces the calculation cost and number of parameters and accelerates the convergence. Figure 8 shows a schematic of the improved AlexNet network model.

The experimental results of the two models on the test set data are summarized in Table 3. The number of parameters and memory size of the AlexNet model are 57 million and 230 MB, respectively. The minimum memory consumption of the improved AlexNet is 56 MB. Compared with AlexNet, the number of parameters is reduced by more than 43 million and the memory consumption is reduced by 174 MB. Finally, the diagnostic classification accuracy of abnormal wells using the two models on the test set is listed in the table. As can be seen, the accuracy of the improved AlexNet is 97.9%.

TABLE 6 Diagnostic results of indicator diagram.

Enter indicator diagram	Diagnostic conditions	Actual operation
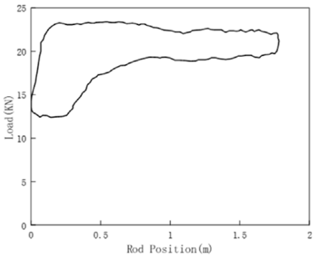	Gas influence	Gas influence
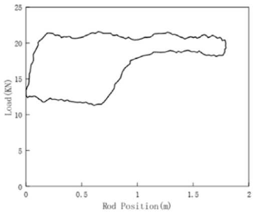	Insufficient for liquid	Insufficient for liquid
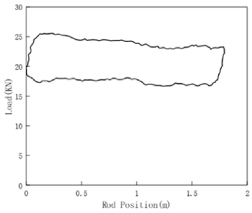	Pump normal	Pump normal
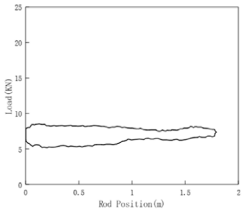	Sucker rod break	Sucker rod break
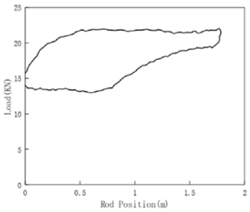	Gas influence	Gas influence
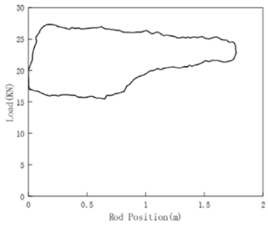	Gas influence	Insufficient for liquid

Experimental analysis of deep learning model

Experimental data preparation

In deep learning, owing to the small number of samples of training data, under-fitting will occur while training the network model (Wen et al., 2016; Zhang et al., 2016; Lu and Goodson, 2017; Xu et al., 2018). Therefore, an image expansion method based on the characteristics of the indicator diagram is proposed. Table 4 summarizes the transformation of the indicator diagram.

For an actual oil well, the abnormal indicator diagram data are less whereas the normal indicator diagram data are more. To ensure the generalization ability of the model and the balance of data, the normal indicator diagram is randomly deleted.

Creation of data sets

In this study, 10 types of indicator diagrams are collected, and 10 folders are created accordingly, as shown in Table 5. The indicator diagram data in Table 5 from Shengli Oilfield in China, there have been tens of thousands of rod pumping wells. Due to serious sand production, high water cut, strong corrosion, high viscosity of crude oil, insufficient liquid supply and other reasons, downhole accidents such as rod breaking, pump leakage and sand sticking often occur.

Each indicator diagram is saved in a .txt file and named with a picture path tag, such as img/1/a001.jpg 1, for the model to read. After storage, the sequence is randomly disrupted; 70% is randomly selected as the training set and the remaining 30% is employed as the test set by using the method of leaving the set.

Application of improved AlexNet model to indicator diagram analysis

The trained CNN is used to analyze and diagnose the indicator diagram of the pumping unit, which is input to the improved AlexNet network model to judge the working condition type. The judgment results are shown in Table 6:

As can be seen from the table, the accuracy of the improved model in the judgment of the working condition is 83.3%, which is basically consistent with the actual working condition, indicating that the improved model has good application prospects in actual working condition analysis.

Conclusion

In this study, an improved AlexNet model with a total of five convolution layers and a 3*3 convolution kernel was employed. In the first two convolution layers, the step size was 2, and in the last three convolution layers, the step size was 1. The pooling layer used was the maximum pooling layer, and the step size was 2. The BN layer was added behind convolution layers 1 and 2. Moreover, the memory consumption of the improved AlexNet model was reduced considerably, which accelerated the convergence and resulted in high accuracy in the analysis of actual working conditions. Finally, a comparison of the model parameters and calculation cost showed that the performance of the improved AlexNet model is superior. (Duan et al., 2018).

Data availability statement

The raw data supporting the conclusion of this article will be made available by the authors, without undue reservation.

Author contributions

Conceptualization, WC; methodology, ZS; validation, ZW; formal analysis, XW; investigation, YW; resources, GY; data curation, SP.

Funding

This work is supported by the National Natural Science Foundation of China (Grant No. 52074225). Xi'an petroleum university undergraduate innovation and entrepreneurship training program (Grant No. 202110705021).

Acknowledgments

The authors would like to thank all the reviewers who participated in the review, as well as MJEditor (www.mjeditor.com) for providing English editing services during the preparation of this manuscript.

Conflict of interest

The authors declare that the research was conducted in the absence of any commercial or financial relationships that could be construed as a potential conflict of interest.

Publisher's note

References

Yang, Y. (2011). *And fault diagnosis system for rod pump wells based on pump power diagram analysis*. Dailan: Dalian University of Technology.

Bezerra, M. A. D., Schnitman, L., Filho, M. D. A. B., and de Souza, J. A. M. F. (2010). "Pattern recognition for downhole dynamometer card in oil rod pump system using artificial neural networks," in ICEIS2009—Proceedings of the 11th International Conference on Enterprise Information Systems,Volume AIDSS, Milan,Italy, May 6-10,2009 (DBLP), 351–355.

Chen, Y., Li, H., and Ji, Y. (2014). Expert system for downhole fault diagnosis of pumping unit based on neural network. *Electron. Des. Eng.* 22 (01), 130–132. doi:10.14022/j.cnki.dzsjgc.2014.01.006

Duan, Y., Yu, L., Sun, Q., and Xu, D. (2018). Improved Alexnet model and its application in well indicator diagram classification. *Comput. Appl. Softw.* 35 (07), 226–230+272. doi:10.3969/j.issn.1000-386x.2018.07.041

Huang, X. (2007). Research on intelligent integrated system for fault diagnosis of pumping wells. *J. Petroleum Nat. Gas* 29 (3), 156–158.

Krizhevsky, A. One weird trick for parallelizing convolutional neural networks [DB] ar Xiv preprint ar Xiv: 1404 5997, 2014

Krizhevsky, A., Sutskever, I., and Hinton, G. E. (2012). Imagenet classification with deep convolutional neural networks. *Adv. neural Inf. Process. Syst.*, 25, 1097–1105. doi:10.1145/3065386

Li, K., Gao, X., Tian, Z., and Qiu, Z. (2013). Using the curve moment and the PSO-SVM method to diagnose downhole conditions of asucker rod pumping unit. *Petroleum Sci.* 10 (1), 73–80. doi:10.1007/s12182-013-0252-y

Li, K., Gao, X., Yang, W., Dai, Y-L., and Tian, Z. (2013). Multiple fault diagnosis of down-hole conditions of sucker-rod pumping wells based on Freeman chain code and DCA. *Petroleum Sci.* 10 (3), 347–360. doi:10.1007/s12182-013-0283-4

Li, P. (2015). *Intelligent recognition of oil well work diagram based on deep learning*. China: Henan University of Science and Technology.

Lu, M., and Gu, D. Application of fuzzy theory in diagnosis of rod pumping well indicator diagram, Western prospecting project, 2017 1004-5716 (2002) 04-01-03.

Luan, G. H., He, S. L., Yang, Z., Zhao, H-Y., Xie, Q., Hu, J. H., et al. (2011). A prediction model for a new deep-rod pumping system. *J. Petroleum Sci. Eng.* 80 (1), 75–80. doi:10.1016/j.petrol.2011.10.011

Reges, G. D., Schnitman, L., Reis, R., and Mota, F. (2015). "A new approach to diagnosis of sucker rod pump systems by analyzing segments of downhole dynamometer cards," in SPE artificial lift conference—Latin America and Caribbean, Salvador, Bahia, Brazil, May 27–28, 2015 (Society of Petroleum Engineers).

Sun, Z., lei, X., and Xu, Y. (2012). Overview of deep learning. *Appl. Res. Comput.* 29 (8), 2807–2809. doi:10.3969/j.issn.1001-3695.2012.08.002

Wen, B., Wang, Z., and Jin, Z. (2016). etc. Fault diagnosis of pumping unit combined with indicator diagram and fuzzy neural network. *Comput. Syst. Appl.* 25 (1), 121–125.

Xu, J., Chen, Z., and Li, R. (2020). Impacts of pore size distribution on gas injection in intraformational water zones in oil sands reservoirs. *Oil Gas. Sci. Technol. –. Rev. IFP. Energies Nouv.* 75, 75. doi:10.2516/ogst/2020047

Xu, J., Wu, K., Li, R., Li, Z., Li, J., Xu, Q., et al. (2018). Real gas transport in shale matrix with fractal structures. *Fuel* 219, 353–363. doi:10.1016/j.fuel.2018.01.114

Xu, J., Wu, K., Li, R., Li, Z., Li, J., Xu, Q., et al. (2019). Nanoscale pore size distribution effects on gas production from fractal shale rocks. *Fractals* 27 (08), 1950142. doi:10.1142/s0218348x19501421

Xu, P., Xu, S., and Yin, H. (2007). Application of self-organizing competitive neural network in fault diagnosis of suck rod pumping system. *J. Petroleum Sci. Eng.* 58 (1), 43–48. doi:10.1016/j.petrol.2006.11.008

Yuan, W., and Hu, M. (2015). Research on oil well fault diagnosis expert system based on indicator diagram. *Electron. Des. Eng.* 23 (18), 119–122. doi:10.3969/j.issn.1674-6236.2015.18.038

Zhang, J., Yang, J., and Xu, X. Research on discrimination algorithm of oil well indicator diagram based on fuzzy pattern recognition, computer and modernization, 2016-07-0058-03.2016

Zhang, X. (2000). Introduction to statistical learning theory and support vector machines. *Acta atuomatica sin.* 26 (1), 32–42. doi:10.16383/j.aas.2000.01.005

frontiers | Frontiers in Earth Science

TYPE Original Research
PUBLISHED 16 August 2022
DOI 10.3389/feart.2022.987594

OPEN ACCESS

EDITED BY
Jinze Xu,
University of Calgary, Canada

REVIEWED BY
Chaowen Wang,
Southwest Petroleum University, China
Lan Wang,
China University of Geosciences, China

*CORRESPONDENCE
Fei Mo,
mofei_cqust@163.com
Zhilin Qi,
qizhilin76@sina.com
Xiaoliang Huang,
2009022@cqust.edu.cn

SPECIALTY SECTION
This article was submitted to Environmental Informatics and Remote Sensing,
a section of the journal
Frontiers in Earth Science

RECEIVED 06 July 2022
ACCEPTED 18 July 2022
PUBLISHED 16 August 2022

CITATION
Mo F, Qi Z, Huang X, Li Q, Yan W and Wang S (2022), Pressure prediction in deep-water pipeline considering formation of natural gas hydrate.
Front. Earth Sci. 10:987594.
doi: 10.3389/feart.2022.987594

Pressure prediction in deep-water pipeline considering formation of natural gas hydrate

Fei Mo[1]*, Zhilin Qi[1]*, Xiaoliang Huang[1]*, Qingping Li[2], Wende Yan[1] and Shuai Wang[1]

[1]School of Petroleum Engineering, Chongqing University of Science and Technology, Chongqing, China, [2]China National Offshore Oil Corporation Research Institute Co., Ltd., Beijing, China

Pressure in the deep-water pipeline is an important parameter that should be carefully predicted to control the natural gas transport in petroleum industry. However the present methods to predict pressure along the deep-water pipeline are complex and time-consuming. Some methods even ignore the formation of natural gas hydrate leading to the inaccurate pressure prediction. In this work, we proposed a model to predict the pressure along the deep-water pipeline considering the reduction of pipeline radius induced by the formation of natural gas hydrate. The model was validated by experimental data and was applied to the real deep-water pipeline in China. Results indicate that the decline of pressure in the pipeline is mainly caused by the reduction of pipeline radius due to the formation of natural gas hydrate compared with the flow resistance caused by viscous flow. The decline of pressure becomes faster against time with the 40% pressure loss at the fifth year of natural gas transport. This model enables to obtain the pressure values in the deep-water pipeline with high accuracy and good convenience.

KEYWORDS

natural gas hydrate, pressure, blockage, pipeline, deep water

Introduction

Development and transport of oil and gas are significant in petroleum industry (Xu et al., 2018, Xu et al., 2019; Mo et al., 2020; Xu et al., 2020; Wang C. et al., 2021; Wang C. et al., 2022; Mo et al., 2022). The formation of natural gas hydrate is a great threat to the transport of natural gas in the deep-water pipeline (depth of water >1000 m) (Li et al., 2016; Ren, 2018). Natural gas transport in the deep-water pipeline is under complex conditions: 1) the complicated pipeline system affected by the pipeline design, pipeline laying, pipeline management, pipeline maintenance, etc.; 2) the extreme environment, especially the low temperature and high pressure; 3) the components of gas mixture, i.e., liquid or gaseous hydrocarbons, water, etc. Natural gas hydrate is likely to form at the low temperature (lower than around 11°C) and high pressure (higher than about 2.5 MPa) (Zhang et al., 2010), which is in accordance with the temperature and pressure conditions in the deep-water environment. As a result, the natural gas hydrate can easily form and grow inside the submarine pipeline during the transport of natural gas.

The formation of natural gas hydrate causes severe problems. Natural gas hydrate adheres to the inner pipeline surface, which reduces the pipeline radius and causes the loss of pipeline pressure. And the layer of natural gas hydrate at the pipeline surface can become thicker against time. If effective treatments are not carried out promptly, the pipeline can be blocked. The blockage caused by the natural gas hydrate, on the one hand, significantly reduces gas flow rate and severely affects gas transport. On the other hand, it damages the pipelines, valves and other transportation equipment (Gao, 2018). As the formation of natural gas hydrate causes various problems during natural gas transport in deep-water pipeline, the pressure inside pipeline is worth great attention. Because the pressure affects both the formation of natural gas hydrate and the gas transport efficiency (Li et al., 2013). An accurate prediction of pressure inside deep-water pipeline is of great significance.

The pressure along the deep-water pipeline can usually be obtained by two methods: experiment and numerical simulation. Li and Dong (2019) investigated 12 experimental pipelines worldwide and found that the pressure design inside the experimental pipelines was lower than the pressure in the real deep-water pipeline systems. Among the 12 pipeline systems, the high-pressure Petreco A/S pipeline system in Norway could reach the highest pressure of about 25 MPa (Li and Dong, 2019). However, the pipeline system in laboratory is still very different from the true deep-water environment. As a result, the pressure obtained from experiments is not able to reflect the accurate pressure in the real pipeline. Numerical simulation is an effective way to predict the pressure in the submarine pipeline. In 2003, the CSMHyK model was firstly built by the Center for Hydrate Research of Colorado University of Mines (Boxall, 2009; Davies, 2009; Zerpa et al., 2012). The model is utilized to describe the formation of natural gas hydrate and is widely used in commercial software like OLGA to calculate the pressure in the real pipeline systems (Boxall et al., 2009; Davies et al., 2010; Zerpa et al., 2012). The CSMHyK model and the software OLGA are one of the most widely used methods to calculate pipeline pressure in natural gas industry (Ding et al., 2019; Wang et al., 2022). Moreover, Sonne and Pedersen (2009) used a compositional hydrate kinetics model to simulate the hydrate growth rate. Sonne and Pedersen's model was utilized to develop the software Flowasta and predict pressure in pipeline (Creek et al., 2011). There are other methods to acquire the pressure in pipeline system, i.e., neural network (Ke et al., 2021), inward and outward natural gas hydrates growth shell model (Shi et al., 2011), etc. However, Ke et al. (2021)'s method is not able to describe the formation of hydrate. Shi et al. (2011)'s model needs complex calculation, because it requires the computation of hydrate growth before obtaining the pressure values. Overall, although there are many ways to calculate the pressure inside the deep-water pipeline, the experiments differ from the real deep water environment, while the establishment and calibration of numerical model are time-consuming. A convenient method with relatively high accuracy is needed to predict the pressure along the deep-water pipeline considering the formation of natural gas hydrate.

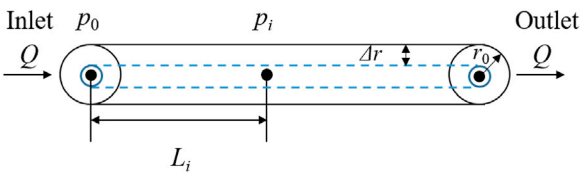

FIGURE 1
Illustration of the geometry of the pipeline and the hydrate layer.

In this work, a mathematical model to predict the pressure in the deep-water pipeline was derived considering the reduction of pipeline radius caused by the formation of natural gas hydrate. This model is able to obtain the pressure values in the deep-sea pipeline transporting the gaseous natural gas with high accuracy and good convenience.

Mathematical model

The mathematical model was established based on the following assumptions.

(1) The deep-water pipeline is horizontally laid (Figure 1). Fluid flowing through the pipeline is the gaseous mixture consisting of methane and water vapor.
(2) The flow of methane and water vapor mixture conforms the laminar flow.
(3) The natural gas hydrate deposits uniformly on the pipeline inner surface and causes the reduction of pipeline radius. The hydrate grows against time. Therefore, the pipeline radius is a function of time.

The Poiseuille's law was used to describe the laminar flow of gas mixture in the horizontal pipeline:

$$Q = \frac{\pi r(t)^4 (p_0 - p_i)}{8\mu L_i} \tag{1}$$

where Q is the gas mixture flow rate in the pipeline, m^3/s; $r(t)$ is the pipeline inner radius, m, which is a function of time t; p_0 is the pressure at the inlet of pipeline, Pa; p_i is the pressure at the location i, Pa; μ is the viscosity of gas mixture, Pa·s; L_i is the distance between the inlet and the location i, m. Therefore, p_i can be expressed as:

$$p_i = p_0 - \frac{8\mu L_i Q}{\pi r(t)^4} \tag{2}$$

TABLE 1 Data of the parameters for model verification.

Parameter	Value	Parameter	Value
Initial Pipeline radius r_0, m	0.01	Average temperature in pipeline T, K	286.6
Pressure at the inlet of the pipeline p_0, Pa	8.6×10^6	Viscosity of the gas mixture μ, Pa·s	6.8×10^{-4}
Volume factor of gas mixture B_g	0.9	Flow rate of gas mixture on surface Q_s, m³/s	2.76×10^{-3}
Heat transfer coefficient F_k	0.5	Kinetic constant $C1$	3.63
Activation temperature coefficient of natural gas hydrate C_2	4,400	Molar mass of natural gas hydrate M_g, kg/mol	0.16
Molar density of natural gas hydrate $\rho_g{}^h$, mol/m³	44.6	Equilibrium temperature of natural gas hydrate T_{eq}, K	292.54
Length of the pipeline L, m	39.6		

Because the formation of natural gas hydrate reduces the pipeline inner radius, the pipeline inner radius $r(t)$ is given by:

$$r(t) = r_0 - \Delta r(t) \tag{3}$$

Where r_0 is the initial pipeline inner radius, m; $\Delta r(t)$ is the thickness of hydrate layer, m, which is also a function of time.

The thickness of hydrate layer (also the reduction of pipeline inner radius) $\Delta r(t)$ needs to be determined to accurately predict the pressure in the pipeline. Based on Cai (2018)'s work, the model of natural gas hydrate formation is given by:

$$\frac{\Delta V_h}{\Delta t} = F_k \exp(C_1) \exp\left(-\frac{C_2}{T}\right) \frac{1}{M_g \rho_g^h} (T_{eq} - T) A \tag{4}$$

Where V_h is the volume of natural gas hydrate, m³; F_k is the heat transfer coefficient; C_1 is the kinetic constant, $\exp(C_1) = 37.8$; C_2 is the activation temperature coefficient of natural gas hydrate, K; T is the temperature, K; M_g is the molar mass of natural gas hydrate, kg/mol; $\rho_g{}^h$ is the molar density of natural gas hydrate, mol/m³. T_{eq} is the equilibrium temperature of natural gas hydrate, K; A is the area of hydrate-gaseous mixture interface, m³. Using Cai (2018)'s model, the thickness of natural gas hydrate layer Δr during Δt can be written as:

$$\frac{\Delta r}{\Delta t} = F_k \exp(C_1) \exp\left(-\frac{C_2}{T}\right) \frac{1}{M_g \rho_g^h} (T_{eq} - T) \tag{5}$$

Hence, the pipeline inner radius considering the formation of natural gas hydrate is given by:

$$r(t) = r_0 - F_k \exp(C_1) \exp\left(-\frac{C_2}{T}\right) \frac{1}{M_g \rho_g^h} (T_{eq} - T) t \tag{6}$$

The pressure along the deep-water horizontal pipeline at the presence of natural gas hydrate is derived as:

$$p_i = p_0 - \frac{8\mu L_i Q}{\pi \left[r_0 - F_k \exp(C_1) \exp\left(-\frac{C_2}{T}\right) \frac{1}{M_g \rho_g^h} (T_{eq} - T) t \right]^4} \tag{7}$$

Eq. 7 is the model to predict the pressure in the deep-water pipeline considering formation of natural gas hydrate. This model can be used to compute the pressure along the horizontal pipeline when natural gas hydrate forms at the inner surface of pipeline during deep-water natural gas transport.

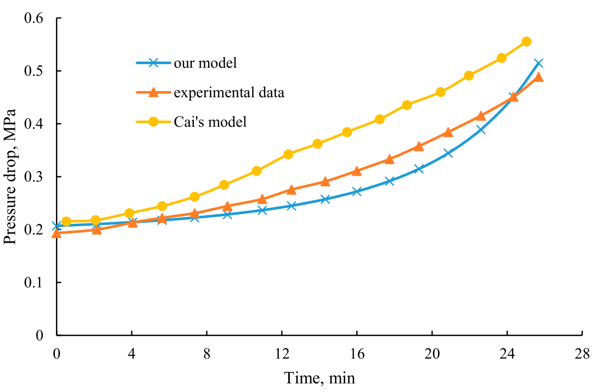

FIGURE 2
Results of our model, Cai's model and the experimental data.

Model verification

The model was validated using the experimental data obtained by Lorenzo et al. (2014) and the computation from Cai (2018)'s model.

Lorenzo et al. (2014)'s carried out experiments on natural gas hydrate formation in pipeline transporting gas-dominant fluids, and they measured the pressure drop inside the pipeline. The information of their experiments is exhibited in Table 1. The experimental results are plotted in Figure 2. Cai (2018) used Lorenzo et al. (2014)'s experimental data to validate her model for the formation of natural gas hydrate. The calculation of Cai (2018)'s model is also shown in Figure 2. In our work, we compared our model with the experimental data in Lorenzo et al. (2014)'s work and Cai (2018)'s computations to verify our model (Figure 2). The

TABLE 2 Data of the parameters for model application.

Parameter	Value	Parameter	Value
Initial Pipeline radius r_0, m	0.1651	Average temperature in pipeline T, K	278.15
Pressure at the inlet of the pipeline p_0, Pa	5×10^6	Viscosity of the gas mixture μ, Pa·s	7.6×10^{-4}
Volume factor of gas mixture B_g	0.9	Flow rate of gas mixture on surface Q_s, m³/s	10.4
Heat transfer coefficient F_k	0.5	Kinetic constant C_1	3.63
Activation temperature coefficient of natural gas hydrate C_2	6,877	Molar mass of natural gas hydrate M_g, kg/mol	0.16
Molar density of natural gas hydrate $\rho_g{}^h$, mol/m³	44.6	Equilibrium temperature of natural gas hydrate T_{eq}, K	292.54
Length of the pipeline L, m	1,000		

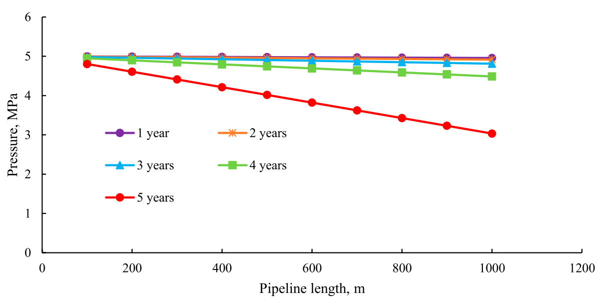

FIGURE 3
Pressure along the pipeline during 5 years of natural gas transport.

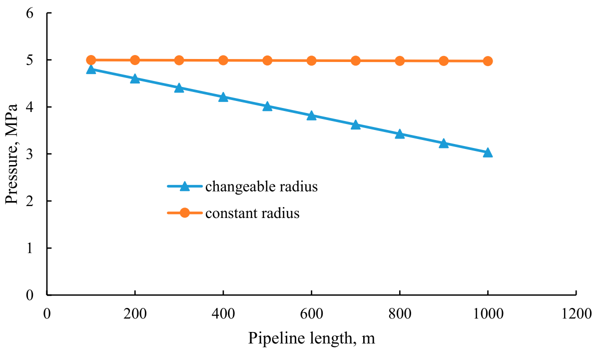

FIGURE 4
Pressure along the pipelines with changeable radius and constant radius at the fifth year of natural gas transport.

comparison demonstrates that the results of our model approximate the experimental data much better than Cai (2018)'s model with an average error less than 8%. Cai (2018)'s model focuses on the formation and collapse of natural gas hydrate in pipeline. In her model, the radius reduction is only considered after the collapse of natural gas hydrate. However, the loss of pipeline radius occurs at the point that the hydrate starts to form not collapse. As a result, Cai (2018)'s model overestimates the pressure along the pipeline. Because the calculation in our model is relatively simple, our model provides a more convenient and reliable way to predict the pressure in deep-water pipeline considering the pipeline radius reduction induced by natural gas hydrate.

Model application

The model was used to predict the pressure along the real deep-water pipeline of China at the presence of natural gas hydrate. The data of the parameters in the model come from the real pipeline systems (Liang et al., 2009; Cai, 2018; Ding et al., 2019), which are exhibited in Table 2.

Influence of natural gas hydrate on pipeline pressure

Pressure along the pipeline during 5 years of natural gas transport was calculated using our model. Results are shown in Figure 3.

Figure 3 illustrates that the pressure decreases almost linearly along the pipeline. The decline of pressure is mainly caused by two aspects: laminar flow resistance in viscous flow and the reduction of pipeline radius due to the formation of natural gas hydrate. In order to compare the effects of these two aspects, we calculated the pressure along the pipelines with changeable radius and constant radius at the fifth year of natural gas transport in Figure 4. In the pipeline with changeable radius, fluid flow encounters the resistances caused by both laminar flow resistance and the reduction of pipeline radius. While in the pipeline with constant radius, fluid flow only encounters the laminar flow resistance. Results show that the reduction of pipeline radius plays a dominant role in the pressure drop inside the pipeline, because the pressure drop in the pipeline with changeable radius (1.97 MPa) is much more significant than the pipeline with constant radius (0.02 MPa). It also implies that

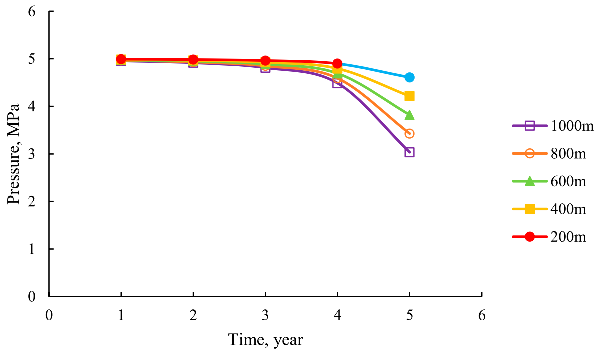

FIGURE 5
Pressure at 200, 400, 600, 800, and 1000 m of pipeline against time.

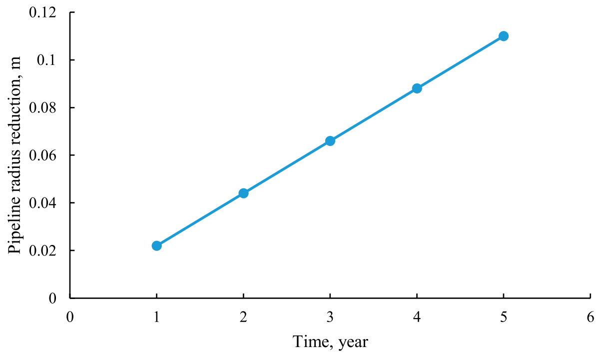

FIGURE 6
Average pipeline radius reduction during 5 years of natural gas transport.

taking into account the formation of natural gas hydrate is important to predict the pressure in the pipeline which transports natural gas in deep sea.

Characteristics of pipeline pressure decline

The decline of pressure during the first 3 years is much slower than the fifth year based on Figure 3. In order to investigate the pressure drop against time, we plot the pressure at 200, 400, 600, 800, and 1000 m of the pipeline during 5 years of natural gas transportation in Figure 5. In the first 3 years, the maximum pressure drop is only 0.19 MPa, accounting for a 3.8% of pressure loss, which occurs at the 1000 m of the pipeline. However at the fifth year, the pressure declines drastically to around 3 MPa at 1000 m with the 1.97 MPa of pressure drop. Nearly 40% of the pressure is reduced.

The drastic pressure drop is caused by the reduction of pipeline radius due to the formation of natural gas hydrate. The average reduction of pipeline radius during 5 years is shown in Figure 6. After 5 years of natural gas transport, 66.63% of pipeline radius is occupied by natural gas hydrate. This means that the formation and deposition of natural gas hydrate significantly affect the natural gas transport by blocking the pipeline. The growth of natural gas hydrate becomes faster as time goes by. And the blockage of pipeline tends to be more serious if the transportation continues without any treatments. As a result, the natural gas hydrate inside the pipeline should be cleared in time to maintain the good transport efficiency.

Conclusion

1. The model considers changeable pipeline radius induced by the formation of natural gas hydrate. Therefore it provides a convenient and reliable way to predict the pipeline pressure, which is validated by the experimental data.
2. The decline of pressure inside the pipeline is mainly due to the reduction of pipeline radius caused by natural gas hydrate compared with the flow resistance induced by viscous flow.
3. The growth of natural gas hydrate becomes faster against time, and the blockage of pipeline tends to be more serious. This leads to the decline of pressure along the pipeline with a nearly 40% of pressure loss at the fifth year.

Data availability statement

The original contributions presented in the study are included in the article/supplementary material, further inquiries can be directed to the corresponding authors.

Author contributions

FM: Model establishment; Model verification; Methodology; Data analysis; Original draft preparation; Funding receiver. ZQ: Model application; Review and editing; Funding receiver. XH: Review and editing; Funding receiver. WY: Model verification; Review and editing. SW: Review and editing. QL: Data analysis; Preparation of the revised manuscript.

Funding

This work was financially supported by the Science and Technology Research Project of Chongqing Municipal Education Commission (Grant No. KJQN202001512), the Chongqing

Research Program of Basic Research and Frontier Technology (Grant Nos cstc2019jcyj-zdxmX0032 and cstc2018jcyjAX0700), and the Research Foundation of Chongqing University of Science and Technology (Grant No. ckrc2019023).

Conflict of interest

Author QL was employed by the company China National Offshore Oil Corporation Research Institute Co., Ltd.

The remaining authors declare that the research was conducted in the absence of any commercial or financial relationships that could be construed as a potential conflict of interest.

Publisher's note

References

Boxall, J., Davies, S., Koh, C., and Sloan, E. D. (2009). Predicting when and where hydrate plugs form in oil-dominated flowlines. *SPE Proj. Facil. Constr.* 4 (3), 80–86. doi:10.2118/129538-pa

Boxall, J. (2009). *Hydrate plug formation from <50% water content water-in-oil emulsions* (Golden, Colorado, U.S.: Colorado School of Mine). Dissertation for Doctoral Degree.

Cai, T. (2018). Model for predicting deposition and collapse of natural gas hydrate in pipeline. *Drill. Prod. Technol.* 41 (6), 46–50. doi:10.3969/JISSN1006-768X.2018.06.14

Creek, J., Subramanian, S., and Estanga, D. (2011). "Project design hydrate management by application of multiphase flow simulations tools with hydrate formation and transport," in Proceedings of the 7th International Conference on Gas Hydrates, Edinburgh, UK, 17-21 July 2011.

Davies, S. R., Boxall, J. A., Dieker, L. E., Sum, A. K., Koh, C. A., Sloan, E. D., et al. (2010). Predicting hydrate plug formation in oil-dominated flowlines. *J. Pet. Sci. Eng.* 72, 302–309. doi:10.1016/j.petrol.2010.03.031

Davies, S. R. (2009). *The role of transport resistances in the formation and remediation of hydrate plugs* (Golden: Colorado School of Mine). Dissertation for Doctoral Degree.

Ding, J., Liu, J., and Liang, D. (2019). OLGA based simulation on the formation laws of hydrates in pipelines. *Oil Gas Storage Transp.* 38 (2), 235–240. doi:10.6047/j.issn.1000-8241.2019.02.018

Gao, J. (2018). *Prediction and prevention of hydrate in LW submarine pipeline* (Chengdu, China: Southwest Petroleum University). Dissertation for Master's Degree.

Ke, W., Zhang, J., Deng, L., Xu, Z., Zhao, D., and Jiang, X. (2021). Application of feedforward neural network in predicting subsea pipeline pressure under slug flow. *Pet. Eng. Constr.* 47 (6), 7–10. doi:10.3969/j.issn.1001-2206.2021.06.002

Li, C., Huang, T., and Jia, W. (2016). A review of natural gas hydrates and its pipeline transportation technologies in deep water. *Chin. Sci. Bull.* 61 (22), 2449–2462. doi:10.1360/n972015-01344

Li, W., and Dong, J. (2019). Experimental device and testing technology for hydrate in multiphase flow in large-scale submarine pipeline. *Chem. Eng. Equip.* 10, 123–125. doi:10.19566/j.cnki.cn35-1285/tq.2019.10.046

Li, W., Gong, J., Lu, X., Zhao, J., Feng, Y., and Yu, D. (2013). A study of hydrate plug formation in a subsea natural gas pipeline using a novel high-pressure flow loop. *Pet. Sci.* 10, 97–105. doi:10.1007/s12182-013-0255-8

Liang, F., Cao, X., Wei, J., and Chen, J. (2009). Application of accumulated liquid volume prediction method in submarine gas pipeline. *Nat. Gas. Ind.* 29 (1), 103–105. doi:10.3787/j.issn.1000.0976.2009.01.029

Lorenzo, M. D., Aman, Z. M., Soto, G. S., Johns, M., and May, E. F. (2014). Hydrate formation in gas-dominant systems using a single-pass flowloop. *Energy fuels.* 28 (5), 3043–3052. doi:10.1021/ef500361r

Mo, F., Qi, Z., Huang, X., Yan, W., Wang, S., Yuan, Y., et al. (2022). Knudsen diffusion in pore-scale water-bearing shales: Modelling and case study. *J. Pet. Sci. Eng.* 214, 110457. doi:10.1016/j.petrol.2022.110457

Mo, F., Qi, Z., Yan, W., Huang, X., and Li, J. (2020). Influence of water on gas transport in shale nanopores: Pore-scale simulation study. *Energy fuels.* 34 (7), 8239–8249. doi:10.1021/acs.energyfuels.0c01278

Ren, J. (2018). *Numerical Simulation of Natural Gas Leakage in Deep-sea Pipeline Based on Pressure Gradient Change and Hydrate Formation, Dissolution and Decomposition Mechanisms* (Tianjin, China: Tianjin University). Dissertation for Master's Degree.

Shi, B. H., Jing, G., Sun, C. Y., Zhao, J. K., Ding, Y., and Chen, G. J. (2011). An inward and outward natural gas hydrates growth shell model considering intrinsic kinetics, mass and heat transfer. *Chem. Eng. J.* 171 (3), 1308–1316. doi:10.1016/j.cej.2011.05.029

Sonne, J., and Pedersen, K. (2009). "Simulation of hydrate growth in steady state flow lines," in Proceedings of the BHR 14th International Conference on Multiphase Production Technology, Cannes, France, June 17–19, 2009, 2009, 17–19.

Wang, C., Peng, X., Liu, J., Jiang, R., Li, X. P., Liu, Y. S., et al. (2022). A novel formulation representation of the equilibrium constant for water gas shift reaction. *Int. J. Hydrogen Energy*, 2022. doi:10.1016/j.ijhydene.2022.06.105

Wang, C., Wang, J., Liu, Y., Li, J., Peng, X. L., Jia, C. S., et al. (2021). Prediction of the ideal-gas thermodynamic properties for water. *J. Mol. Liq.* 321 (2021), 114912. doi:10.1016/j.molliq.2020.114912

Wang, H., Lian, Z., and Wang, S. (2021). The hydrate formation and its influencing factors in submarine pipeline by using OLGA. *Ocean Dev. Manag.* 2, 87–92. 1005-9857(2021)02-0087-06

Xu, J., Chen, Z., and Li, R. (2020). Impacts of pore size distribution on gas injection in intraformational water zones in oil sands reservoirs. *Oil Gas. Sci. Technol. –. Rev. IFP. Energies Nouv.* 75, 75. doi:10.2516/ogst/2020047

Xu, J., Wu, K., Li, R., Li, Z., Li, J., Xu, Q., et al. (2018). Real gas transport in shale matrix with fractal structures. *Fuel* 219, 353–363. doi:10.1016/j.fuel.2018.01.114

Xu, J., Wu, K., Li, R., Li, Z., Li, J., Xu, Q., et al. (2019). Nanoscale pore size distribution effects on gas production from fractal shale rocks. *Fractals* 27 (08), 1950142. doi:10.1142/s0218348x19501421

Zerpa, L. E., Sloan, E. D., Sum, A. K., and Koh, C. A. (2012). Overview of CSMHyK: A transient hydrate formation model. *J. Pet. Sci. Eng.* 98-99, 122–129. doi:10.1016/j.petrol.2012.08.017

Zhang, L., Ma, R., Su, J., Zhang, X., and Miao, D. (2010). Formation mechanism and effective clearup of gas hydrate. *Oil Drill. Prod. Technol.* 32 (3), 33–36. 1000-7393(2010)03-0033-04

frontiers | Frontiers in Earth Science

TYPE Original Research
PUBLISHED 19 August 2022
DOI 10.3389/feart.2022.990554

OPEN ACCESS

EDITED BY
Jinze Xu,
University of Calgary, Canada

REVIEWED BY
Wenlian Xiao,
Southwest Petroleum University, China
Bo Yang,
Chengdu University of Technology,
China

*CORRESPONDENCE
Xiaoliang Huang,
121347074@qq.com

SPECIALTY SECTION
This article was submitted to
Environmental Informatics and Remote
Sensing,
a section of the journal
Frontiers in Earth Science

RECEIVED 10 July 2022
ACCEPTED 21 July 2022
PUBLISHED 19 August 2022

CITATION
Deng X, Huang X, Ye Q, Li S, Yu C,
Zhang X and Wang Z (2022),
Experimental research on production
law of multilayer
heterogeneous reservoirs.
Front. Earth Sci. 10:990554.
doi: 10.3389/feart.2022.990554

Experimental research on production law of multilayer heterogeneous reservoirs

Xuan Deng[1], Xiaoliang Huang[2]*, Qing Ye[3], Sainan Li[3], Chengchao Yu[3], Xu Zhang[2] and Zuohao Wang[2]

[1]CNOOC China Limited Zhanjiang Branch, Guangdong, China, [2]Chongqing University of Science and Technology, Chongqing, China, [3]CNOOC China Limited Hainan Branch, Hainan, China

In the development of multi-layer co-production heterogeneous reservoirs, problems such as serious inter-layer heterogeneity and interference always exist, resulting in an unclear understanding of inter-layer production. A clear understanding of the interference mechanism and influence of main controlling factors of multi-layer heterogeneous reservoirs on the production of small layers is the key to the effective development of the reservoirs. On the basis of clarifying the main controlling factors affecting the production of multi-layer heterogeneous reservoirs, this paper developed a multi-pipe parallel displacement experiment system to carry out indoor heterogeneous reservoir multi-layer water injection flooding experiments. Combined with dynamic and static parameters, the experiments simulated and evaluated the effects of factors such as permeability ratio, water cut, shutting down high permeability layers, production pressure difference, and change in crude oil viscosity in high permeability layers. The primary objective of this work is to reveal the mechanism of small-layer interference under different conditions, and clarify the influence of main control factors on the production of small-layer. The results show that the smaller the permeability ratio is, the weaker the difference in physical properties among layers along the vertical direction is. The reduction in the difference in seepage resistance decreases the dynamic interference among layers. The reduction in the water ratio among layers and shutting down high permeability layers can reduce the interlayer interference effectively. Increasing production pressure difference effectively improves the oil displacement efficiency of reservoirs with poor physical properties. A lower fluidity in the high permeability layers can effectively improve the oil displacement efficiency of other layers.

KEYWORDS

multi-layer co-production heterogeneous reservoirs, interference mechanism, multi-pipe parallel displacement experiment system, water injection flooding experiments, oil displacement efficiency

1 Introduction

In a heterogeneous reservoir with multiple layers producing oil, due to the vertical heterogeneity among layers, the interlayer and intralayer contradictions in the production process cannot be ignored. The interference phenomenon is serious, which leads to high production in the high-permeability layer(s), early water breakthrough time and high oil recovery (Huang et al., 2015; Liu et al., 2017; Xu et al., 2018; Renan et al., 2019). The low-permeability layers are inhibited by the high-permeability layers, leading to low oil production, late water breakthrough, which ultimately affects the total oil recovery (Cui and Zhao, 2010; Liu et al., 2019).

The research on the influence law of production of small-layers in multi-layer producing reservoirs mainly focuses on the interlayer interference mechanism and the establishment of small-layer production splitting models (Liu et al., 2012; Jiang et al., 2016; Zhao et al., 2016). The known interlayer interference mechanism is that, the greater the permeability ratio is, the greater the mutual influence among various flow units is, and the greater the oil displacement efficiency difference (Xu et al., 2019; Xu et al., 2020) is. When the permeability ratio exceeds a certain limit, production of the low-permeability layers is extensively reduced (Rahman and Mattar, 2007; Shen et al., 2018). Increasing the production pressure difference can enhance the production capacity of the low-permeability layer, and also make the small layer with higher starting pressure be used, thereby reducing the impact of interlayer interference (Larsen, 1981; Fetkovich et al., 1990). However, the existing research on the interlayer interference mechanism considers limited factors, the change of the minimum permeability and the water content of different layers are not considered. In terms of small-layer production splitting models: at present, the small-layer production splitting models mainly include the KH splitting model, KHK splitting model, KNK splitting model, and dynamic splitting model, etc. (Kuppe et al., 2000; Hu et al., 2018; Mi et al., 2019). However, the existing splitting models mainly focus on the study of the basic physical properties of the reservoir, do not consider the impact of dynamic factors on the production law of the small layer. It is difficult to accurately describe the impact of dynamic factors such as the different water content of each small layer on their productions.

Generally speaking, the research on the production influence law of small layers in a multi-layer production reservoir is not comprehensive. This article focuses on the development of a multi-layer production reservoir. For the problem of unclear understanding of the production law, through the development of a multi-tube displacement system, an indoor multi-layer water injection displacement experiment was carried out. The experiment simulated and evaluated the impacts of different factors on interlayer production, such as permeability ratios, different water cuts, shutting down high permeability layers, and changing production pressure and viscosity, etc. The experiment is designed to reveal the interference mechanism of the small layer under different conditions and clarify the law of influence of main control factors on the production of the small layer. The research results show that the degree of dynamic interference among layers decreases as the decreasing permeability ratio decreases, and increases as the increasing water cut. Shutting down the high-permeability layer, increasing the production pressure difference, and increasing the oil viscosity of the high-permeability layer can reduce vertical production differences and inter-layer interference. The research results can provide a more comprehensive understanding of mechanisms for the effective development of multi-layer heterogeneous reservoirs.

2 Multi-tube parallel displacement experiment

Aiming at solving the problems of strong inter-layer heterogeneity, serious interference, and unclear understanding in the development of heterogeneous reservoirs, we carried out multi-layer water flooding experiments to simulate and evaluate the impact factors on the inter-layer production, such as permeability ratio, water content, shutting down high-permeability layers, changing production pressure differences and fluid viscosity. The experiment was carried out to reveal the mechanism of small-layer interference under different conditions, and clarify the law of influence of main control factors on the production of small-layer.

2.1 Experimental equipment and procedures

The multi-pipe parallel displacement experiment equipment included a high temperature and high-pressure displacement device, which was mainly composed of a set of parallel sand filling pipes, a displacement pump, a constant temperature device, and an intermediate container. The main technical indicators included a temperature range of 20–200°C, and a pressure range of 0.1–50 MPa. The experimental process is shown in Figure 1. The specific experimental process steps are described as follows:

① Sand filling. According to the experimental requirements, select quartz sand of different meshes and fill the sand-filled tube for use.
② Cleaning. Clean the filled sand pipe to remove impurities.
③ Drying. Use nitrogen to dry the cleaned sand-filled pipe for later use.
④ Vacuuming. Use a vacuum pump to vacuum the blow-dried sand-packed pipe to saturate the fluid in the next step.

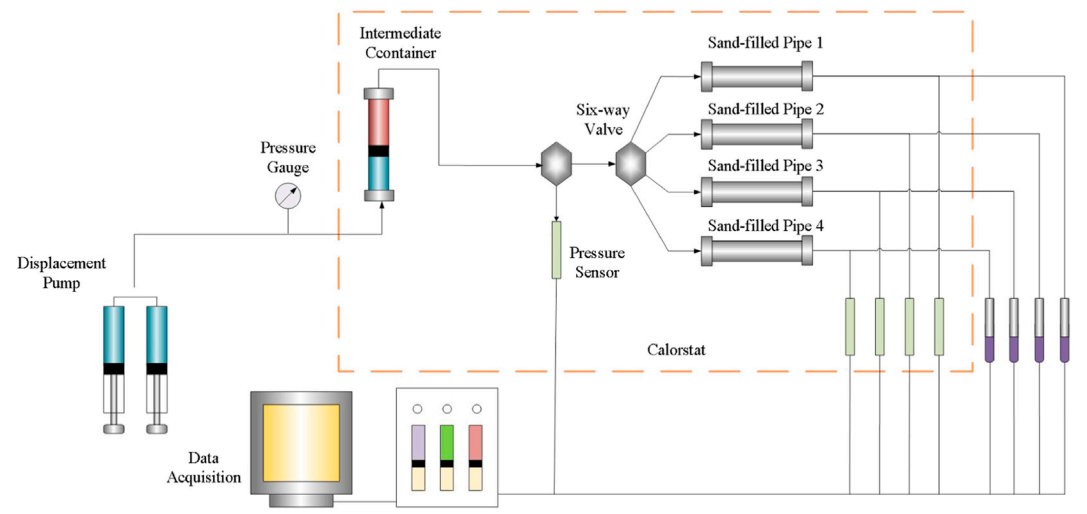

FIGURE 1
Experimental flow chart.

TABLE 1 Basic parameter table of the sand filling pipe.

Sand filling pipe number	**1**	**2**	**3**	**4**	**5**	**6**	**7**	**8**
The inside diameter of (mm)	30.9	30.9	30.9	30.9	30.8	30.9	30.9	30.8
Length (cm)	34.9	34.8	34.8	34.8	35.0	34.9	34.9	34.9
Sand filling mesh (mesh)	600	500	450	325	450	325	206	206
Porosity (%)	29.5	30.1	32.4	33.2	34.3	38.3	40.2	42.8
Permeability (mD)	48	98	146	265	726	845	1,196	2,412

⑤ Saturating water and measuring porosity. Saturate the evacuated sand pipe with water, record the volume, pressure, rate of flow and other data, and calculate the porosity and permeability of the sand pipe.
⑥ Saturating oil. Use oil to displace water and inject oil into the sand-packed pipe to establish oil saturation.
⑦ Waterflooding. Displacing the sand-packing pipe with water.
⑧ Layer measurement. Simulate the production situation of different layers and split the production.

2.2 Experimental materials

To ensure the comparability in the experimental research, the experiment used 200–600 mesh quartz sand to fill eight sand-filling pipes, and then tested them in sequence. The basic parameters of each sand-filling pipe are shown in Table 1. In the experiment, the crude oil used 2# white oil (viscosity 2 mPa·s, density 800 kg/m^3), 5# white oil (viscosity 5 mPa·s, density 820 kg/m^3), 10# white oil (viscosity 10 mPa·s, density kg/m^3); the injected water is pure water with a density of 1,000 kg/m^3. After each experiment, the sand-filled tube was cleaned, and the procedures were repeated for the next experiment.

2.3 Experimental plan

In general, a parallel displacement experiment was designed to analyze the inter-layer interference phenomenon and reveal the interference mechanism. In the multi-pipe parallel flooding experiment, four sand-packed pipes were selected each time in different combinations. The permeability gradually decreased from the first layer to the fourth layer. The experiment separately considered the influence of factors such as permeability ratio, different water-bearing stages, production

TABLE 2 Summary of the design of the multi-layer water experiments.

Experiment number	Permeability ratio	Minimum permeability (mD)	Initial water content	Shutting down layers	Production pressure difference (MPa)	Viscosity (mPa·s)	Remarks
1	5.5	48	0	—	1	2	Different permeability ratio
2	15	48	0	—	1	2	Different permeability ratio
3	25	48	0	—	1	2	Different permeability ratio
4	50	48	0	—	1	2	Different permeability ratio
5	8	146	0	—	1	2	Different permeability ratio
6	5.5	48	40%, 30%, 20%, 10%	—	1	2	Low water cut stage
7	5.5	48	60%, 50%, 40%, 30%	—	1	2	Medium and low water cut stage
8	5.5	48	80%, 70%, 60%, 50%	—	1	2	Medium and high water cut stage
9	5.5	48	95%, 90%, 85%, 80%	—	1	2	High water cut stage
10	5.5	48	90%, 60%, 40%, 20%	—	1	2	Different water-bearing stages
11	5.5	48	0	1	1	2	Shutting down 1 layer
12	5.5	48	0	1, 2	1	2	Shutting down 2 layers
13	5.5	48	0	1, 2, 3	1	2	Shutting down 3 layers
14	5.5	48	0	—	2	2	Different pressure difference
15	5.5	48	0	—	3	2	Different pressure difference
16	5.5	48	0	—	4	2	Different pressure difference
17	5.5	48	0	—	5	2	Different pressure difference
18	5.5	48	0	—	1	5	The viscosity of the high permeability layer is 5 mPa·s
19	5.5	48	0	—	1	10	The viscosity of the high permeability layer is 10 mPa·s

pressure difference, shutting down layers and crude oil viscosity on the interlayer production. The design of experiments was divided into five categories and 19 groups of experiments (Table 2).

2.4 Evaluation parameters

2.4.1 Production splitting coefficient

The ratio of the production of each layer to the sum of the total production of each layer, which can be shown as:

$$\alpha = \frac{Q_i}{\sum Q_i} \tag{1}$$

2.4.2 Cumulative oil production ratio

The ratio between the displacement amount of each sublayer to the total displacement amount of all production layers, which can be shown as:

$$f_i = 100 \times \frac{V_{oi}}{\sum_{i=1}^{n} V_{oi}} \tag{2}$$

TABLE 3 Test combination schemes for different permeability ratios of sand filling pipe.

Scheme	Permeability ratio	Layer 1 (mD)	Layer 2 (mD)	Layer 3 (mD)	Layer 4 (mD)
1	5.5	265	146	98	48
2	8	1,196	845	265	146
3	15	726	265	98	48
4	25	1,196	845	265	48
5	50	2,412	1,196	265	48

Where α—Production splitting coefficient, dimensionless; Q_i—The production of the i-th layer, m^3; ΣQ_i—The total production of all layers, m^3. V_{oi}—The amount of oil displaced by the i-th layer, cm^3; fi—Portion of cumulative oil production in i-th layer, %; n—Total floors.

3 Results and discussion

3.1 The influence of permeability ratio

3.1.1 Experimental plan

According to the actual loading situation of a single sand-filling pipe, and the designing requirements of the overall experimental plans, pipes with permeability from 48 mD to 2,412 mD were selected, and five groups of test plans with permeability ratios of 5.5, 8, 15, 25, and 50 were designed (Table 3). In these tests, the formation pressure was 14 MPa. The formation temperature was 90°C, and the experimental pressure difference was 1 MPa. When the water production rate at the outlet end of the low permeability layer reached 98%, the experiment stopped.

3.1.2 Experimental results and analysis

3.1.2.1 The impact of permeability ratio on the production of small layers when the minimum value of permeability is the same

The minimum permeability is 48 mD, and the permeability ratio is 5.5, 8, 15, 25, 50 respectively. The experiment results show that:

① From the perspective of fluid production, the fluid production of the high-permeability layer is absolutely dominant, reflecting the high-permeability layer's contribution to fluid production (Table 4; Figure 2). When the permeability ratio is 5.5, the high-permeability layer accounts for more than 48% of the liquid production, and the low-permeability layer accounts for less than 7%. As the permeability ratio increases, the proportion of liquid production in the high-permeability layer increases, and the proportion of liquid production in the low-permeability layer gradually decreases. When the permeability ratio is 50, the proportion of liquid production in the high-permeability layer exceeds 74.32%, and the proportion of liquid production in the low-permeability layer is 1.15%.

② From the perspective of cumulative oil production, the cumulative oil production of the high-permeability layer has an absolute advantage (Table 4; Figure 3). When the permeability ratio is 5.5, the cumulative oil production of the high-permeability layer accounts for more than 42%, and the cumulative oil production of the low permeable layer accounts for less than 11%. With the increase of the permeability ratio, the cumulative oil production of the high-permeability layer also gradually increases, and the percentage of fluid production in the low-permeability layer also gradually decreases. When the permeability ratio is 50, the cumulative oil production of the high-permeability layer accounts for over 80.93%, and the cumulative oil production of the low-permeability layer accounts for 2.47%.

The main reason is that the greater the permeability ratio in multi-layer production is, the greater the mutual influence among the flow in each layer is, and the higher the seepage resistance of the low-permeability layer is, and the lower the oil production. When the permeability ratio is small, the difference of physical properties among vertical layers in the flow resistance is reduced, and the difference in seepage resistance is reduced. The degree of utilization is more uniform, and the degree of dynamic interference among layers is reduced.

3.1.2.2 The influence of different minimum permeability on the production of small layers

The minimum permeability is 48 mD and 146 mD (Table 3), and the permeability of the other three layers keeps the same (Schemes 2, 4). The experiment results show that increasing the minimum permeability means the permeability ratio difference between the high-permeability layer and the low-permeability layer is reduced, which leads to the reduction of interlayer interference. When the minimum permeability changes from

TABLE 4 Summary of the liquid production splitting coefficient and the cumulative oil production proportion of different permeability ratio.

Scheme	Permeability ratio	Liquid production splitting coefficient, %				Proportion of cumulative oil production, %			
		Layer 1	Layer 2	Layer 3	Layer 4	Layer 1	Layer 2	Layer 3	Layer 4
1	5.5	48.48	33.26	12.13	6.12	42.80	29.56	17.10	10.54
2	8	54.34	29.01	11.63	5.02	49.38	28.51	14.04	8.07
3	15	61.41	25.00	9.94	3.65	55.72	25.83	11.89	6.56
4	25	67.33	22.50	7.92	2.25	67.3	20.18	8.78	3.74
5	50	74.32	18.66	5.87	1.15	80.93	12.06	4.54	2.47

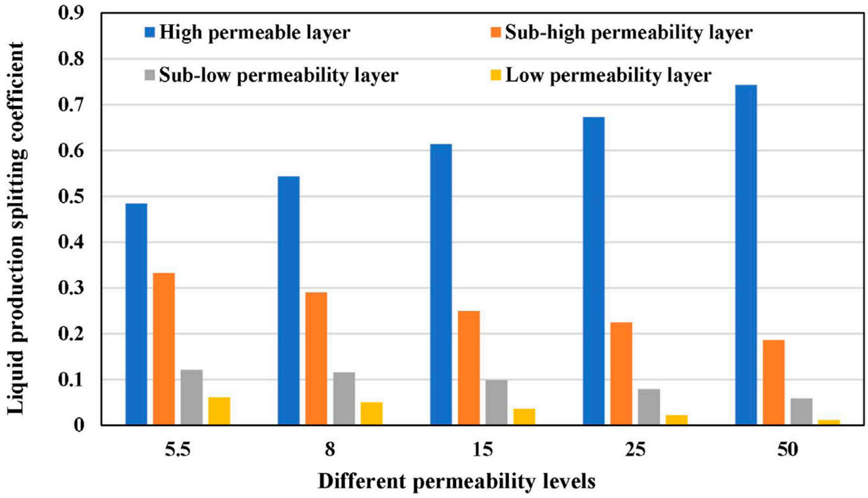

FIGURE 2
Comparison chart of splitting coefficients of produced liquid with different permeability ratios.

48 mD to 146 mD, and the difference in liquid production ratio between the high-permeability layer and the low-permeability layer changes from 65.08% to 49.32%, with a decrease of 15.76%; the cumulative oil production ratio difference dropped from 63.56% to 41.31%, with a decrease of 22.25%.

3.2 The influence of different water content

3.2.1 Experimental test plan

The permeability ratio of 5.5 with relatively small interference is selected as the basis of the experimental scheme. The experiments consider the low water cut stage, the medium and low water cut stage, the medium-high water cut stage, the high water cut stage and the mixed water cut stage. The five groups of different water content combination schemes are shown in Table 5. In these tests, the formation pressure is designed to be 14 MPa, the formation temperature is designed to be 90°C, the experimental pressure difference is 1 MPa. When the water production rate at the outlet end of the low permeability layer reaches 98%, the experiment stops.

3.2.2 Experimental results and analysis

The experimental results show that the fluid production of the high permeability layer always has an absolute advantage (Table 5; Figure 4), which is mainly indicated in the following aspects:

① The difference between high and low permeability layers increases with the increase of water content. As the water content increases, the liquid production ratio of the high permeability layer increases from 56.92% in the low water cut stage to 75.54% in the high water cut stage. The low permeability layer is the opposite. It shows that the change in water content has aggravated the level difference among layers. The greater the difference in water content among layers is, the greater the difference in liquid production

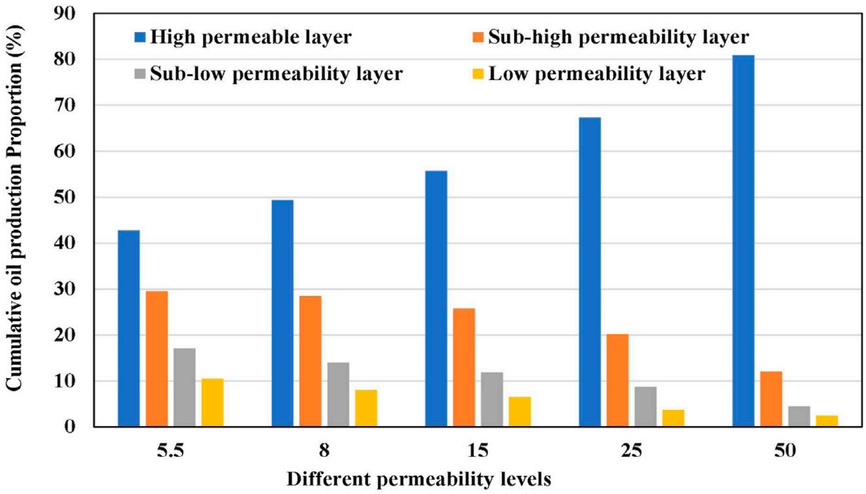

FIGURE 3
Comparison of the proportion of cumulative oil production in each layer with different permeability ratios.

TABLE 5 Different water content test combination scheme and result table.

Scheme	Permeability ratio	Initial water content %				Water-cut stage	Liquid production splitting coefficient			
		Layer 1	Layer 2	Layer 3	Layer 4		Layer 1	Layer 2	Layer 3	Layer 4
1	5.5	40	30	20	10	Low	56.92	24.33	12.5	6.25
2	5.5	60	50	40	30	Sub-low	60.21	22.89	11.11	5.79
3	5.5	80	70	60	50	Sub-high	68.18	18.22	9.12	4.48
4	5.5	95	90	85	80	High	75.54	14.06	7.25	3.15
5	5.5	90	60	40	20	Mix	86.52	8.61	3.42	1.45

splitting coefficient is. The main reason is that the seepage resistance of the high-permeability layer is small. The water injection breaks through and the seepage resistance decreases early, which leads to an increase in liquid production and an increase in water content, and causes an increase in the water content difference of each layer in the longitudinal direction.

② In the mixed water-bearing stage, the fluid production of the high-permeability layer reaches the maximum value of 86.52%, mainly because the mixed water-bearing and high-water-bearing layer is a high-permeability layer, which leads to higher liquid production in the high-permeability layer. Therefore, reducing the difference in water content of each vertical layer is an important factor to effectively reduce the interference for the layers with more serious interference.

3.3 The effect of shutting down high permeability layer

3.3.1 Experimental test plan

The permeability ratio of 5.5 with relatively small interference was selected as the basis of the experimental plan to simulate the impact of closing the high permeability layer on the overall development of the reservoir. The experiments compared the effects of shutting down 1 layer, shutting down 1 and 2 layers, shutting down 1, 2, and 3 layers (Table 6). The layers were shutting down when the water content reaches 90. In these tests, the formation pressure was 14 MPa, the formation temperature was 90°C, the experimental pressure difference was 1 MPa. When the water production rate at the outlet end of the low permeability layer reached 98%, the experiment stopped.

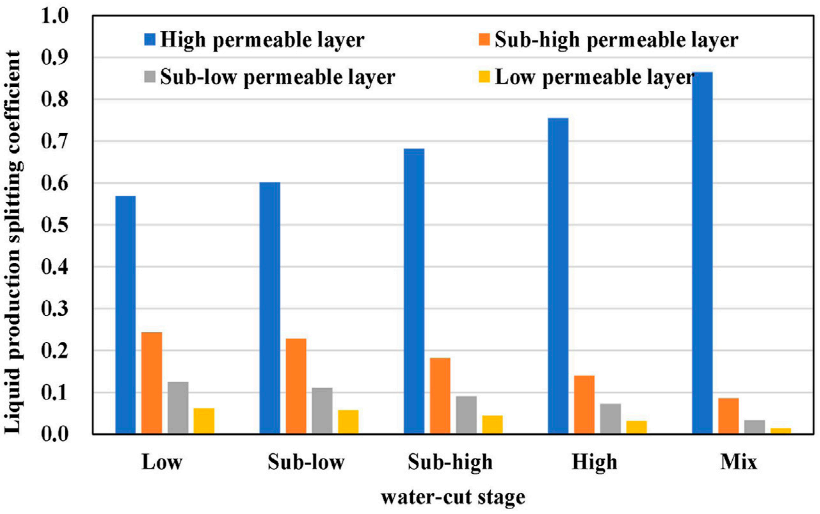

FIGURE 4
Comparison of liquid production splitting in different water cut layers.

TABLE 6 Combination scheme of layer change test for sand-filled pipe clamps.

Scheme	Shutting down layers	Layer 1 (mD)	Layer 2 (mD)	Layer 3 (mD)	Layer 4 (mD)
1	None	265	146	98	48
2	Shutting down 1 layer	Shutting	146	98	48
3	Shutting down 2 layers	Shutting	Shutting	98	48
4	Shutting down 3 layers	Shutting	Shutting	Shutting	48

3.3.2 Experimental results and analysis

The experiments were carried out by closing one, two and three high permeability layers respectively. The experimental results show that:

① From the perspective of liquid production, after closing the high permeability layer, the production splitting coefficient in the low permeability layer has increased significantly (Figures 5–7), and the permeability ratio has also decreased from 5.5 to 3, 2, and 1. After shutting down the high permeability layer, the difference in permeability among the layers is substantially reduced, thereby reducing the interference among the layers. As the permeability ratio decreases, the difference in physical properties among vertical layers decreases, the difference in seepage resistance decreases, the degree of production becomes more uniform, and the dynamic interference among layers decreases. Therefore, for the production layer with more serious interference, closing the high permeability layer to

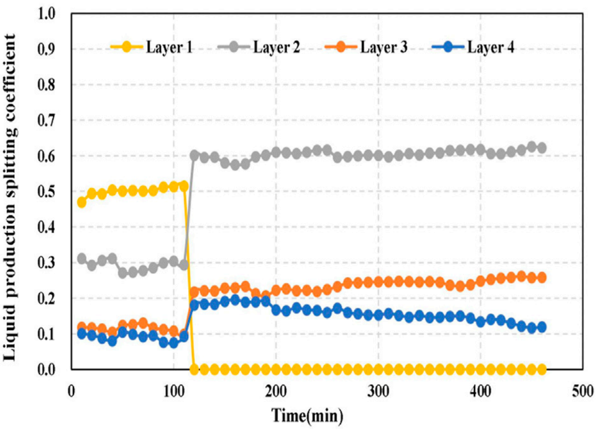

FIGURE 5
Liquid production splitting coefficient of each layer when one layer is shutting down.

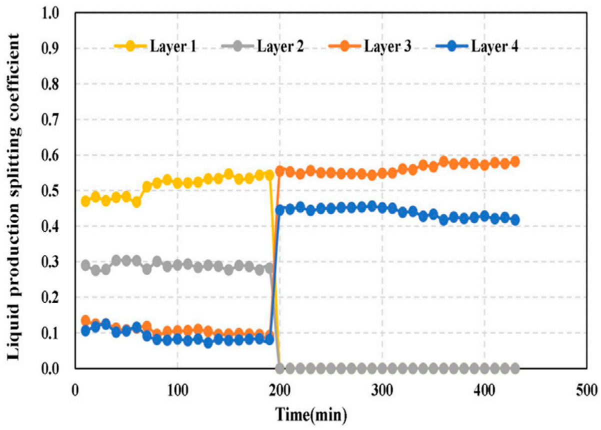

FIGURE 6
Liquid production splitting coefficient of each layer when two layers are shutting down.

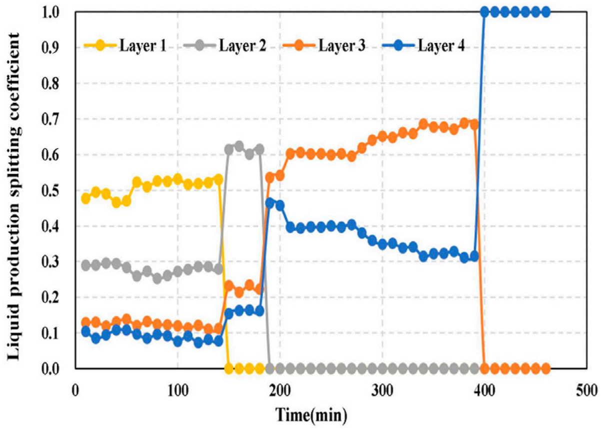

FIGURE 7
Liquid production splitting coefficient of each layer when three layers is shutting down.

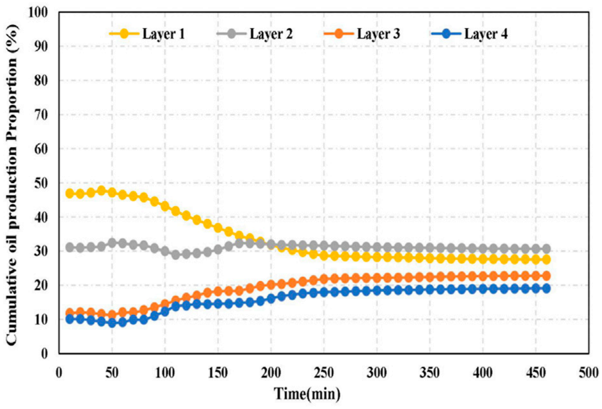

FIGURE 8
The cumulative oil production of each layer when layer 1 is shutting down.

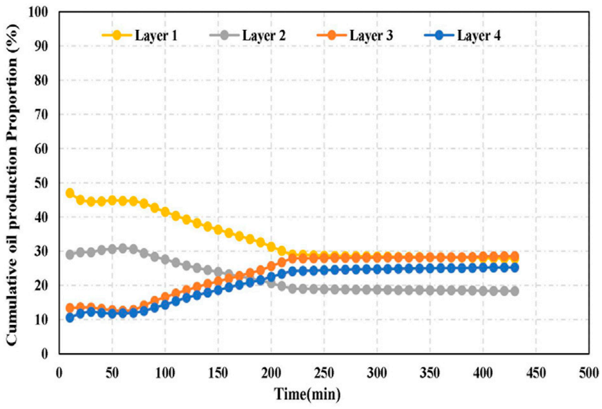

FIGURE 9
The cumulative oil production of each layer when layer 2 is shutting down.

reduce the permeability ratio can effectively reduce the interference. It can be seen that closing the high permeability layer is an effective method to reduce interlayer interference.

② From the perspective of cumulative oil production, after shutting down the high-permeability layer, the cumulative oil production ratio of the minimum permeability layer increases from 10.54% to 25.25% (Figures 8–10). The crude oil in the low-permeability layer has been effectively produced, and the degree of production has been significantly improved. Therefore, by shutting down the high permeability layer, the oil displacement efficiency of the reservoir with poor physical properties can be effectively improved.

3.4 The influence of different pressure differences

3.4.1 Experimental test plan

The permeability ratio of 5.5 with relatively small interference was selected as the basis of the experimental program, and five sets of tests with different pressure differences of 1, 2, 3, 4, and 5 MPa were designed. In these tests, the formation pressure was designed to be 14 MPa, the formation temperature was designed to be 90°C, the experimental

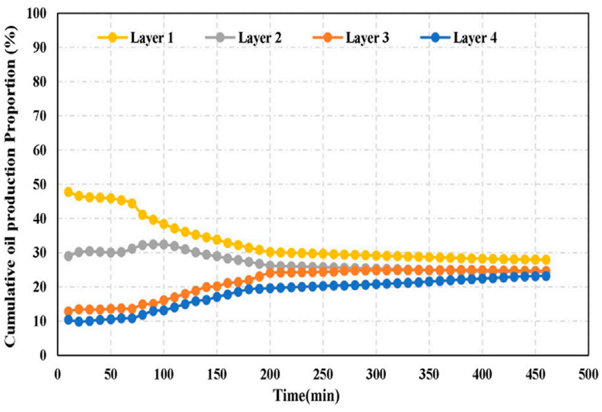

FIGURE 10
The cumulative oil production of each layer when layer 3 is shutting down.

pressure difference was 1 MPa. When the water production rate at the outlet end of the low permeability layer reached 98%, the experiment stopped.

3.4.2 Experimental results and analysis

The experimental results (Table 7) showed:

① From the perspective of liquid production, as the production pressure difference increased from 1 to 5 MPa, the production splitting coefficient in the high permeability layer gradually decreases from 48.48% to 38.61% (Figure 11). And production splitting coefficient in the low permeability layer gradually increases, from 6.13% to 12.18%. It can be concluded that when the physical properties of each layer do not change, as the production pressure difference increases, the low-permeability layer in the vertical direction is used, and the difference in the degree of production among layers is reduced, showing that the dynamic interference among layers decreases with the increase in the production pressure difference. Therefore, for the production layer with more serious inter-layer interference, increasing the production pressure difference can effectively reduce the interference degree.

② From the perspective of cumulative oil production, as the production pressure difference increased from 1 to 5 MPa, and the proportion of cumulative oil production from high-permeability layers gradually decreased (Figure 12) from 42.8% to 37.25%, and the proportion of cumulative oil production from low-permeability layers gradually increased from 10.54% to 15.78%. It shows that increasing the production pressure difference enables the effective development of crude oil in the low-permeability layer, and the degree of production is significantly improved. By increasing the pressure difference, the oil displacement efficiency of reservoirs with poor physical properties can be effectively improved.

3.5 The influence of crude oil viscosity

3.5.1 Experimental test plan

Different viscosities were used to carry out comparative displacement experiments to simulate the interference mechanism of different crude oil viscosities. The permeability ratio of 5.5 with relatively small interference was selected as the basis of the experimental plan. The crude oil viscosity of the high permeability layer was designed to be 2, 5, and 10 mPa·s respectively. In these tests, the formation pressure was designed to be 14 MPa, the formation temperature was designed to be 90°C, the experimental pressure difference was 1 MPa. When the water production rate at the outlet end of the low permeability layer reached 98%, the experiment stopped.

3.5.2 Experimental results and analysis

Experiments were carried out with different crude oil viscosities in the highly permeable layer, and the experimental results (Table 8) showed that:

① From the perspective of fluid production, when the viscosity of crude oil in the high permeability layer

TABLE 7 Different pressure difference test liquid production splitting coefficient and accumulative oil production ratio table.

Scheme	Production pressure difference (MPa)	Liquid production splitting coefficient, %				Proportion of cumulative oil production %			
		Layer 1	Layer 2	Layer 3	Layer 4	Layer 1	Layer 2	Layer 3	Layer 4
1	1	48.48	33.27	12.13	6.13	42.8	29.56	17.1	10.54
2	2	45.85	31.62	14.32	8.21	41.25	28.46	18.03	12.26
3	3	43.31	30.76	16.46	9.47	39.51	27.24	19.48	13.77
4	4	40.88	29.81	18.62	10.69	38.42	26.35	20.7	14.53
5	5	38.61	29.29	19.92	12.18	37.25	26.02	20.95	15.78

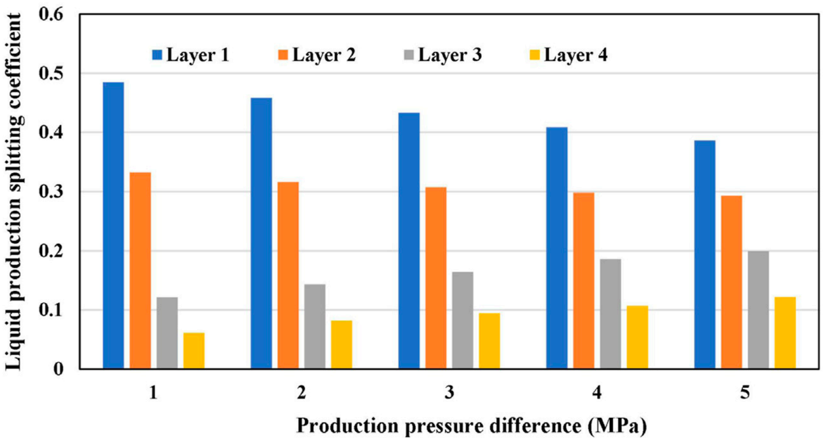

FIGURE 11
Comparison of splitting coefficients of liquid production in each layer with different pressure differences.

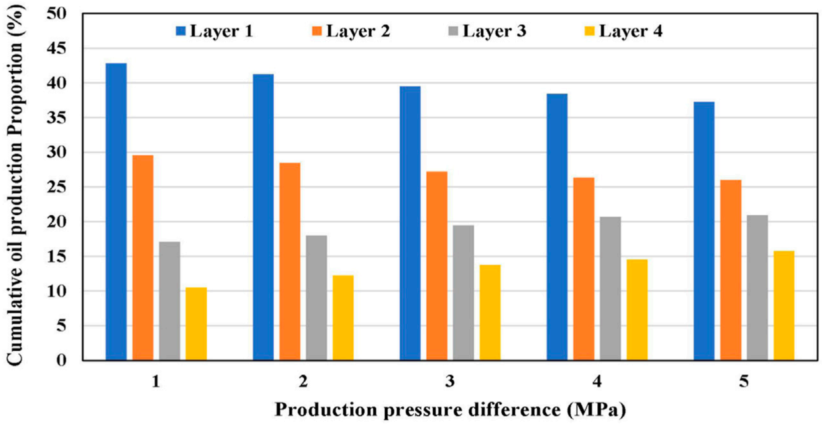

FIGURE 12
Comparison of the proportion of cumulative oil production in each layer with different pressure differences.

TABLE 8 Different pressure difference test liquid production splitting coefficient and accumulative oil production percentage table.

Crude oil viscosity of high permeability layer mPa·s	Liquid production splitting coefficient %				Proportion of cumulative oil production %			
	Layer 1	Layer 2	Layer 3	Layer 4	Layer 1	Layer 2	Layer 3	Layer 4
2	48.48	33.27	12.13	6.13	42.8	29.56	17.1	10.54
5	34.57	46.3	13.36	5.76	32.1	29.72	20.52	17.65
10	19.88	68.98	7.41	3.73	26.28	31.51	22.89	19.32

increases from 2 mPa·s to 10 mPa·s, the proportion of fluid produced from the sub- high permeability layer rises faster and has an absolute advantage, and the proportion of fluid production increases from 33.27% to 68.98%. The proportion of fluid production in the high permeability, low permeability, and sub-low permeability layers gradually decreased, the proportion of fluid production in the high permeability layer decreased from 48.48% to

19.88%, and the proportion of fluid production in the low permeability and sub-low permeability layers decreases from 18.3% to 11.14%. The main reason is that the viscosity of the high permeability layer increases, and the sub-high permeability layer will be the main channel for liquid flow.

② From the perspective of cumulative oil production, as the viscosity of crude oil in the high-permeability layer gradually increases, the proportion of cumulative oil produced from the high-permeability layer gradually decreases from 42.8% to 26.28%, while the proportion of cumulative oil produced from other layers all rise. The percentage of cumulative oil production in the second-highest permeable layer increased from 29.56% to 31.51%, the proportion of the second-lowest permeability layer increased from 17.1% to 22.89%, and the lowest permeability layer increased from 10.54% to 19.32%. The main reason is that after the oil viscosity of the high-permeability layer increases, the fluidity decreases, the seepage resistance increases, and the production degree of the relatively low-permeability layer increases, which promotes the effective development of the low-permeability layer. The mobility of the permeable layer can effectively improve the oil displacement efficiency of other reservoirs.

4 Conclusion and understanding

Due to the strong inter-layer heterogeneity and serious interference in the development of multi-layer production reservoirs, the interlayer production law is unclear. By carrying out an indoor multi-tube parallel displacement experiment, the influence of different permeability ratios, water content, shutting down layers, different production pressure, and viscosity on the interlayer production was simulated and evaluated. This research is to reveal the mechanism of small-layer interference under different conditions and provide a basis for the effective development of multi-layer production reservoirs. The following understandings have been obtained during the study:

① When the permeability difference is from 5 to 50, the cumulative oil production of high permeability layer increases from 42% to 80.93%.

② During multi-layer production, the crude oil displaced by water injection mainly comes from the high-permeability layer. The high-permeability layer has a higher water injection utilization rate, which makes a large contribution to the overall recovery. The low permeability layer makes a small contribution to the overall recovery.

③ The degree of dynamic interference among layers decreases as the permeability difference decreases. It increases as the water cut increases. Shutting down the production layer, increasing the production pressure difference, and increasing the oil viscosity of the high-permeability layer can reduce the longitudinal production difference and alleviate vertical conflicts and reduce inter-layer interference.

④ According to the results of the production interference mechanism and the law of the small layers of multi-layer production reservoirs, it is suggested that the small layers with similar reservoir physical properties should be firstly combined and developed. Controlling the difference among layers in water content, and shutting down the high water-bearing layers can better reduce the contradictions among the layers. At the same time, for multi-layer producing reservoirs with large differences in physical properties, the production pressure difference can be increased because the utilization degree of low-permeability layers is low.

Data availability statement

The original contributions presented in the study are included in the article/supplementary material, further inquiries can be directed to the corresponding author.

Author contributions

XD, XH, SL, XZ, and QY contributed to conception and design of the study. CY and ZW organized the database. SL performed the statistical analysis. SL wrote the first draft of the manuscript. All authors contributed to manuscript revision, read, and approved the submitted version.

Conflict of interest

XD was employed by CNOOC China Limited Zhanjiang Branch. QY, SL, and CY were employed by CNOOC China Limited Hainan Branch.

The remaining authors declare that the research was conducted in the absence of any commercial or financial relationships that could be construed as a potential conflict of interest.

Publisher's note

References

Cui, C., and Zhao, X. (2010). Method for calculating production indices of multilayer water drive reservoirs. *J. Pet. Sci. Eng.* 75 (1–2), 66–70. doi:10.1016/j.petrol.2010.10.003

Fetkovich, M. J., Bradley, M. D., Works, A. M., and Thrasher, T. S. (1990). Depletion performance of layered reservoirs without crossflow. *SPE Form. Eval.* 5 (03), 310–318.

Hu, Q., Wang, X., Tan, Y., Yang, H., Zhang, F., and Lu, M. (2018). The production split method in multilayer reservoir based on grey relational analysis. *IOP Conf. Ser. Earth Environ. Sci.* 113 (1), 012018. doi:10.1088/1755-1315/113/1/012018

Huang, S., Kang, B., Cheng, L., Zhou, W., and Chang, S. (2015). Quantitative characterization of interlayer interference and productivity prediction of directional wells in the multilayer commingled production of ordinary offshore heavy oil reservoirs. *Pet. Explor. Dev.* 42 (4), 533–540. doi:10.1016/s1876-3804(15)30046-x

Jiang, W., Wu, C., Wang, Q., Xiao, Z., and Liu, Y. (2016). Interlayer interference mechanism of multi-seam drainage in a CBM well: an example from Zhucang syncline. *Int. J. Min. Sci. Technol.* 26 (6), 1101–1108. doi:10.1016/j.ijmst.2016.09.020

Kuppe, F., Chugh, S., and Connell, P. (2000). “Material balance for multi-layered, commingled, tight gas reservoirs,” in SPE/CERI gas technology symposium. Society of petroleum engineers. doi:10.2118/59760-MS

Larsen, L. (1981). “Wells producing commingled zones with unequal initial pressures and reservoir properties,” in SPE annual technical conference and exhibition. Society of petroleum engineers. doi:10.2118/10325-MS

Liu, G., Meng, Z., Luo, D., Wang, J., Gu, D., and Yang, D. (2019). Experimental evaluation of interlayer interference during commingled production in a tight sandstone gas reservoir with multi-pressure systems. *Fuel* 262, 116557. doi:10.1016/j.fuel.2019.116557

Liu, H., Pang, J., Wang, X., Xinan, Y., and Qing, L. (2012). Analysis of interlayer interference and research of development strategy of multilayer commingled production gas reservoir. *Energy Procedia* 16, 1341–1347. doi:10.1016/j.egypro.2012.01.214

Liu, Y., Luo, X., Kang, K., Li, T., Jiang, S., Zhang, J., et al. (2017). Permeability characterization and directional wells initial productivity prediction in the continental multilayer sandstone reservoirs: a case from penglai 19-3 oil field, bohai bay basin. *Pet. Explor. Dev.* 44 (1), 97–104. doi:10.1016/s1876-3804(17)30012-5

Mi, L., Hu, X., Jia, Y., and Liu, Q. (2019). “A novel dynamic production splitting method based on the catastrophe theory,” in SPE middle east oil and gas show and conference. Society of petroleum engineers. doi:10.2118/194968-MS

Rahman, N. M. A., and Mattar, L. (2007). New analytical solution to pressure transient problems in commingled, layered zones with unequal initial pressures subject to step changes in production rates. *J. Pet. Sci. Eng.* 56 (4), 283–295. doi:10.1016/j.petrol.2006.10.002

Renan, V., Sinesio, P., and Barreto, A. (2019). Modeling falloff tests in multilayer reservoirs. *J. Pet. Sci. Eng.* 174, 161–168. doi:10.1016/j.petrol.2018.10.101

Shen, F., Cheng, L., Sun, Q., and Huang, S. (2018). Evaluation of the vertical producing degree of commingled production via waterflooding for multilayer offshore heavy oil reservoirs. *Energies* 11 (9), 2428. doi:10.3390/en11092428

Xu, J., Chen, Z., and Li, R. (2020). Impacts of pore size distribution on gas injection in intraformational water zones in oil sands reservoirs. *Oil Gas. Sci. Technol. –. Rev. IFP. Energies Nouv.* 75, 75. doi:10.2516/ogst/2020047

Xu, J., Wu, K., Li, R., Li, Z., Li, J., Xu, Q., et al. (2018). Real gas transport in shale matrix with fractal structures. *Fuel* 219, 353–363. doi:10.1016/j.fuel.2018.01.114

Xu, J., Wu, K., Li, R., Li, Z., Li, J., Xu, Q., et al. (2019). Nanoscale pore size distribution effects on gas production from fractal shale rocks. *Fractals* 27 (08), 1950142. doi:10.1142/s0218348x19501421

Zhao, H., Kang, Z., Sun, H., Zhang, X., and Li, Y. (2016). An interwell connectivity inversion model for waterflooded multilayer reservoirs. *Pet. Explor. Dev.* 43 (1), 106–114. doi:10.1016/s1876-3804(16)30012-x

frontiers | Frontiers in Earth Science

ORIGINAL RESEARCH
published: 07 September 2022
doi: 10.3389/feart.2022.911646

Green Growth Efficiency Evaluation of Major Domestic Oil-Gas Resource-Based Cities——Based on Panel Data of SBM Model and Malmquist-Luenberger Index

Hongjing Shi, Pengtai Li, Jingzhu Wei and Songbai Shi*

School of Economics and Management, Northeast Petroleum University, Daqing, China

Based on the panel data of Jinzhou, Panjin, Songyuan, Daqing, Yangzhou, Dongying and other 20 oil and gas resource-based cities from 2010 to 2018, combined with DEA-SBM model and Malmquist-Luenberger index, using DEA-SOLVERPro 5.0 and MaxDEA software. This paper evaluates the green growth efficiency of oil and gas resource-based cities from static and dynamic perspectives.The results show that the average static efficiency of green growth of the main oil and gas resource-based cities in China does not reach 1, there is efficiency loss, and it does not reach Pareto optimum.The static efficiency of green growth of the eastern oil and gas resource-based cities is higher than that of other regions, which is in line with the law of the Environmental Kuznets Curve. The environment has been improved. More than half of the oil and gas resource-based cities have a dynamic efficiency value of green growth greater than 1, and the development trend of green growth is better.

Keywords: oil and gas resource-based city, green growth, efficiency evaluation, SBM model, malmquist-luenberger index

Edited by:
Jinze Xu,
University of Calgary, Canada

Reviewed by:
Liangbin Dou,
Xi'an Shiyou University, China
Ting Sun,
China University of Petroleum, China
Cong Lu,
Southwest Petroleum University, China
Xiong Qingshan,
Yangtze University, China

***Correspondence:**
Pengtai Li
dqlipengtai@163.com

Specialty section:
This article was submitted to Economic Geology, a section of the journal Frontiers in Earth Science

Received: *02 April 2022*
Accepted: *05 May 2022*
Published: *07 September 2022*

Citation:
Shi H, Li P, Wei J and Shi S (2022) Green Growth Efficiency Evaluation of Major Domestic Oil-Gas Resource-Based Cities——Based on Panel Data of SBM Model and Malmquist-Luenberger Index. Front. Earth Sci. 10:911646. doi: 10.3389/feart.2022.911646

INTRODUCTION

Since the founding of the People's Republic of China in 1949, a number of oil and gas resource-based cities have been established relying on oil and gas resources, which has provided tremendous dynamic support for the economic development of the Republic. These oil and gas resource-based cities are inevitably trapped in development dilemma because of the imbalance of industrial structure and the reduction of resources, so it is very important to explore a new economic growth model for oil and gas resource-based cities. Therefore, economic green growth is an inevitable choice for oil and gas resource-based cities in the new era. What is the efficiency of green economic growth in oil and gas resource-based cities? Which indicators can be used to evaluate the green growth efficiency of oil and gas resource-based cities? Starting from these two problems, combing the literature on the efficiency evaluation of green growth at home and abroad, this paper constructs the evaluation index system of green growth of oil and gas resource-based cities, based on the panel data of 20 oil and gas resource-based cities such as Jinzhou, Panjin, Songyuan, Daqing, Yangzhou and Dongying from 2010 to 2018, using MaxDEA software. Based on DEA-SBM model and Malmquist-Luenberger index, this paper evaluates the green growth efficiency of oil and gas resource-based cities from static and dynamic perspectives.

At present, there are relatively few literatures on the green growth efficiency of oil and gas resource-based cities in academia, and most of them study the green growth efficiency of a specific region or province. In 1991, Hall constructed a green growth evaluation index system with two dimensions of green status and green policy, and used it to evaluate the environmental quality status of the United States (Hall and Kerr, 1991), which opened the prelude of quantitative analysis of regional green growth efficiency evaluation in academia. Beginning in 2010, China's Green Development Index, co-authored by Beijing Normal University, Southwest University of Finance and Economics and the National Bureau of Statistics, is the first edition of China's Green Development Index framework, which provides more than 60 indicators for the three dimensions of economic growth greening, resource and environment carrying potential and government policy support. It can be used to calculate the annual green index of provinces and municipalities in China.In 2013, Qian Zhengming and other scholars used the input-output theory to calculate the green growth efficiency of each province in China. The selected input indicators are labor, capital and energy, the expected output is GDP, and the unexpected output is the emission of three wastes. They divided China into three regions: the eastern region, the central region and the western region, and compared the green growth efficiency of the three regions (Qian and Liu, 2013). In 2014, Vlontzos et al. Based on the data from 2001 to 2008, used the non-radial DEA method to evaluate the energy and environmental efficiency of EU member States, and compared the impact of environmental protection on environmental efficiency (Vlontzos et al., 2014). In 2015, Wu Chunyou's team at Dalian University of Technology measured the green growth efficiency of G20 countries (Wang and Wu, 2015). In 2017, Moutinho et al. Evaluated the eco-efficiency of 26 countries by using DEA model based on output-oriented variable scale and immutable scale model (Xu et al., 2018). In 2016, Guo Lingling and others constructed China's green growth evaluation index system, which selected 19 indicators in five aspects of nature, resources, economy, policy and quality of life (Guo et al., 2016). In 2017, Wen Chaoxiang and other scholars based on the 1999-2012 provincial panel data, with the help of SBM model, evaluated the green development efficiency of each province in China, and found that the green development efficiency of each province in China is uneven, the gap is obvious, and the gap shows an upward trend over time (Yang and Wen, 2017). Many experts and scholars have made great contributions to measuring the green growth efficiency of individual provinces and cities. In 2016, Zhang Huan and others measured the green development level of cities in Hubei Province (Zhang et al., 2016). In 2017, Feng Zhijun and others measured the level of green growth in Guangdong Province (Xu et al., 2019). In 2009, Ouyang Zhiyun and others measured the green development level of 286 cities in China (Ouyang et al., 2009). In 2018, Wu Chuanqing measured the green development efficiency of major cities in the Yangtze River Economic Belt (Wu and Song, 2018).

Experts and scholars at home and abroad have done a lot of work on the efficiency evaluation of green growth, and DEA (Data Envelopment Analysis) is the most commonly used method to evaluate the efficiency of green growth for specific objectives, because there are differences in the research objects and their backgrounds, and there is no unified evaluation index system at present. The most accurate and scientific index system should be constructed according to the attributes of the research object and its background.In addition, when domestic and foreign scholars study the efficiency of green growth, they mostly choose various countries, provinces or an economic belt, lacking more in-depth subdivision research, such as the efficiency of green growth of oil and gas resource-based cities, so this paper aims at oil and gas resource-based cities, referring to the evaluation methods and indicators selected by previous scholars. It aims to establish a more scientific evaluation system to study the green growth efficiency of oil and gas resource-based cities.

THEORETICAL BASIS

Selection Basis of Evaluation Method

In the long river of exploring the efficiency evaluation of green growth, scholars have used a variety of efficiency evaluation methods, of which the most common six methods are: data envelopment analysis, comprehensive index method, fuzzy comprehensive evaluation method, TOPSIS analysis, grey relational analysis and analytic hierarchy process. A comparison of the six methods is shown in **Table 1**.

This paper evaluates the green growth efficiency of 20 oil and gas resource-based cities, and the sample size is relatively large, which is aimed at the efficiency evaluation of 20 decision-making units, multi-input and multi-output. Therefore, this paper chooses DEA to evaluate the green growth efficiency of oil and gas resource-based cities.

DEA-SBM Model

In 2001, in order to solve the problem of angle assumption, Tone put forward DEA-SBM model, which is based on Pareto-Koopmans economic theory, and introduced slack variable into DEA model, which makes it unnecessary to assume that input and output change in the same direction and different outputs change in the same direction when measuring efficiency. Therefore, DEA-SBM model is a non-radial non-angle efficiency evaluation model, which can be used to evaluate the efficiency of decision making units containing undesirable output. The model is as follows.

TABLE 1 | Comparison of evaluation and analysis method.

Method	Explanation	Merit	Shortcoming
Data Envelopment Analysis	Based on the concept of relative efficiency, this paper evaluates the efficiency of multiple input and multiple output of multiple decision making units	It is not necessary to determine the weight according to the subjective will of the researchers, follow the original data, and be objective and accurate. The method is simple and easy to use	Based on the concept of relative efficiency, the effectiveness of evaluation is relative
Comprehensive Index Method	The indexes of each evaluation object are transformed into the relative evaluation value of the same quantity, and these values are synthesized to obtain the comprehensive evaluation index	The method is simple and easy to understand	It is difficult to determine the evaluation system and the index processing is more complex
Fuzzy comprehensive evaluation method	Based on the comprehensive evaluation method of fuzzy mathematics, the object limited by multiple factors is solved by qualitative evaluation to quantitative evaluation	Solving the problem of uncertainty and non-quantification	The subjectivity of index weight is strong, and the calculation process is stable and complex
TOPSIS analysis method	Advantages and disadvantages of the solution example method, the existing evaluation object and the best program and the distance between the worst program relative sort	The requirements for the data of the research objects are low, and the operation is simple	Cannot resolve duplicate information between metric
Grey correlation degree analysis method	Quantitative analysis of the dynamic change of the system development is proposed to determine the correlation degree of various factors, and the close degree of the relationship is determined by the geometric shape similarity of the reference data and the comparative data column	The method is simple and intuitive	Cannot resolve duplicate information between metric
Analytic Hierarchy Proc	The multi-objective decision-making problem as a system, through qualitative analysis of the multi-objective decomposition, decomposed into different groups of factors, and through continuous comparison to determine the weight, and finally come to the total sort	It needs less quantitative data and more systematic and comprehensive thinking	There are more subjective elements, more quantitative and less qualitative, which are difficult to be convinced. When the number of indicators is large, it is easy to have the problem that the weight is difficult to determine

$$
\begin{aligned}
&\rho = \min \frac{1 - \frac{1}{N}\sum_{n=1}^{N} s_n^x \big/ x'^{t}_{k'n}}{1 + \frac{1}{\mathrm{M}+1}\left(\sum_{\mathrm{m}=1}^{M} s_m^y \big/ y'^{t}_{k'm} + \sum_{i=1}^{I} s_i^b \big/ b'^{i}_{k'i}\right)} \\
&\sum_{t=1}^{T}\sum_{k=1}^{K} z_k^t x_{kn}^t + s_n^x = x'^{t}_{kn'}, n = 1, 2, \ldots, N \\
&\sum_{\mathrm{t}=1}^{T}\sum_{k=1}^{K} z_k^t y_{km}^t - s_m^y = y'^{t}_{k'm}, \mathrm{m} = 1, 2, \ldots M \\
&\sum_{t=1}^{T}\sum_{k=1}^{K} z_k^t b_{ki}^t + s_i^b = b'^{t}_{k'i}, \mathrm{i} = 1, 2, \ldots I \\
&z_k^t \geq 0 \\
&\mathrm{s}_n^x \geq 0 \\
&\mathrm{s}_m^y \geq 0 \\
&\mathrm{s}_i^b \geq 0 \\
&\mathrm{k} = 1, 2, \ldots K
\end{aligned}
\tag{1}
$$

In the formula (1), ρ denotes the target efficiency value of the decision-making unit, $\rho \in [0,1]$, when $\rho = 1$, the decision-making unit is completely effective, as long as $\rho \neq 1$, the efficiency loss of the decision-making unit exists, the closer ρ is to 0, the more the efficiency loss of the decision making unit exists, and the larger the improvement space is.$\mathrm{z}_\mathrm{k}^\mathrm{t}$ represents the weight coefficient, the number of factor inputs is represented by N, M represents the number of expected outputs, and I represents the number of non-expected outputs.$\mathrm{s}_\mathrm{n}^\mathrm{x}$ is the slack variable of the input factor.$\mathrm{s}_\mathrm{m}^\mathrm{y}$ is the slack variable of the expected output. $\mathrm{s}_\mathrm{i}^\mathrm{p}$ represents the slack variable of the undesired output. The $\mathrm{x}_\mathrm{kn}^\mathrm{i'}$ and $\mathrm{y}_\mathrm{km}^\mathrm{t'}$respectively represent two different types of outputs of the k'decision-making unit at t'. The$\mathrm{b}_\mathrm{ki}^\mathrm{t'}$ represents the investment of the decision making unit k' at time t'.

Malmquist-Luenberger Index

When evaluating the static efficiency of a specific time node with undesirable output in a DMU, DEA-SBM model can effectively measure the utilization degree of input factors in the DMU. However, when evaluating the vertical change of DMU efficiency, that is, considering the time factor, we need to use the dynamic efficiency evaluation method to analyze the trend, causes and potential of efficiency growth.The Malmquist index proposed by Swedish economist Sten Malmquist in 1953 is recognized and used by most scholars. Compared with other dynamic efficiency analysis methods, the combination of Malmquist index and DEA model has significant advantages. In the process of dynamic efficiency evaluation, the traditional Malmquist index also has some drawbacks, it ignores the undesirable output. So in 1997, Chungetal and other scholars proposed Malmquist—Luenberger index (ML) model, which introduced the directional distance function into the Malmquist index to solve the problem of undesirable output. The directional distance function is as follows:

$$\overrightarrow{D_0^{\mathrm{t}}}\left(x^t, y^t, b^t; g\right) = \sup\{\beta\colon \left(y^t, b\right) + \beta g \in p^t\left(x^t\right)\} \tag{2}$$

In the formula (2), g represents a direction vector, g^t=(y,-b^t), in the formula, y and b are respectively used to represent the expected output and the unexpected output, and the minus sign represents a direction, which means that the directions of the expected output and the unexpected output are opposite. βrepresents the state of complete efficiency, that is, there is the maximum expected output and the minimum unexpected output.

The functional expression of Talmudist-Gutenberg index is as follows:

$$ML_{\mathrm{t}}^{t+1} = \left\{\frac{1 + \vec{D}_0^t\left(x^t, y^t, b^t; y^t, -b^t\right)}{1 + \vec{D}_0^{\mathrm{t}}\left(x^{t+1}, y^{t+1}, \overrightarrow{b^{t+1}}, y^{t+1}, -b^{t+1}\right)} * \frac{1 + \vec{D}_0^{t+1}\left(x^t, y^t, b^t; y^t, -b^t\right)}{1 + D_0^{t+1}\left(x^{t+1}, \overrightarrow{y^{t+1}, b^{t+1}}; y^{t+1}, -b^{t+1}\right)}\right\}^{\frac{1}{2}} \tag{3}$$

There are three cases, namely ML > 1,ML = 1 and ML < 1,ML > 1, it shows that the static efficiency of green growth shows an upward trend. If ML = 1, it shows that the efficiency of green growth has no obvious trend. If ML < 1, the efficiency of green growth shows a downward trend. The ML index can be decomposed into EFFch and TEch, EFFch represents the technical efficiency change index, TEch represents the technical progress index, and the judgment criteria of the two values are consistent with those of the ml index. The decomposition function is as follows:

$$ML_{\mathrm{t}}^{t+1} = EFFch*TEch$$

$$EFFch_t^{t+1} = \frac{1 + \vec{D}_0^{t+1}\left(x^t, y^t, b^t; y^t, -b^t\right)}{1 + D_0^{\mathrm{t+1}}\left(x^{t+1}, \overrightarrow{y^{t+1}}, b^{t+1}; y^{t+1}, -b^{t+1}\right)} \quad TEch_1^{t+1}$$

$$= \left\{\frac{1 + \vec{D}_0^{t+1}\left(x^t, y^t, b^t; y^t, -b^t\right)}{1 + D_0^{\mathrm{t}}\left(x^t, \overrightarrow{y^t}, b^t; y^t, -b^t\right)} * \frac{1 + D_0^{\mathrm{t+1}}\left(x^{t+1}, \overrightarrow{y^{t+1}}, b^{t+1}; y^{t+1}, -b^{t+1}\right)}{1 + \vec{D}_0^{\mathrm{t}}\left(x^{t+1}, y^{t+1}, b^{t+1}; y^{t+1}, -b^{t+1}\right)}\right\}^{\frac{1}{2}} \tag{4}$$

SELECTION OF INDICATORS AND DATA SOURCES

In order to evaluate the green growth efficiency of major oil and gas resource-based cities in China, 20 oil and gas resource-based cities in China were selected as the research objects, and the DEA-SBM model was used to evaluate the static efficiency of green growth of oil and gas-based cities. Combined with Malmquist-Luenberger index, this paper evaluates the dynamic efficiency of green growth of oil and gas resource-based cities.

Selection of Indicator

Drawing on the green growth evaluation indicators of OECD (OECD, 2011), World Bank (World Bank, 2012), UNEP (UNEP, 2012), Chinese Academy of Sciences (Research Group of Sustainable Development Strategy of Chinese Academy of Sciences, 2011) and Beijing Normal University (Beijing Normal University Scientific Development Concept and Economic Sustainable Development Research Base and etc, 2012) and other authoritative institutions, this paper collates a large number of relevant literatures on green growth evaluation indicators. For example, Qu Ying used pollution emissions, energy consumption and labor input and other input indicators to measure the green growth efficiency of pollution-intensive industries in Liaoning Province (Qu et al., 2017). When Jiao Linlin and others measure the green growth efficiency of coastal cities, the input indicators are labor input, total energy consumption, pollutant emissions and CO2 emissions, and the output indicators are regional GDP (Xu et al., 2020). Under the guidance of these institutions' green growth evaluation index and these literatures, considering the characteristics of oil and gas resource-based cities, this paper finally determines GDP, the number of employees, industrial electricity, industrial wastewater emissions, industrial sulfur dioxide emissions, total fixed assets investment and science and technology expenditure as the evaluation index system of this paper.Labor input, capital input, energy input and technology input are taken as input indicators, and the expected output is GDP. Considering the characteristics of large pollutant emissions in oil and gas resource-based cities, industrial pollutants are taken as non-expected output, and the evaluation index system is shown in **Table 2**.

Data Sources

Oil and gas resource-based cities are not only an important energy base in China, but also an important pillar of China's urban economy. Considering the distribution of oil and gas resource-based cities and the availability of data, this paper selects 20 typical oil and gas resource-based cities as the research object. They are: Cangzhou, Ordos, Jinzhou, Panjin, Songyuan, Daqing, Yangzhou, Dongying, Binzhou, Puyang, Nanyang, Jingzhou, Hengyang, Zhanjiang, Suining, Yan'an, Yulin, Jiuquan, Qingyang and Karamay.According to the geographical location and economic development of these cities, they can be divided into three regions. According to the experience of predecessors, this paper divides Jinzhou City and Panjin City of Liaoning Province into the eastern region, Daqing City of Heilongjiang Province and Songyuan City of Jilin Province into the central region, the specific division is: The oil and gas resource-based cities in the eastern region include Dongying, Yangzhou, Panjin, Cangzhou, Zhanjiang, Jinzhou and Binzhou, the oil and gas resource-based cities in the central region include Daqing, Songyuan, Puyang, Nanyang, Jingzhou, Hengyang and Ordos, and the oil and gas resource-oriented cities in the western region include Qingyang, Jiuquan, Yan'an, Yulin, Karamay and Suining.This paper studies the green growth efficiency of oil and gas resource-based cities based on the data from 2010 to 2018. The data mainly come from China Urban Statistical Yearbook, China Environmental Statistical Yearbook, China Energy Statistical Yearbook and China Science and Technology Statistics Yearbook.

TABLE 2 | Evaluation index system of green growth efficiency of oil and gas resource-based cities.

Indicator Type	Index Meaning	Index Calculation	Unit
Input index	Labor input	number of people employed	person
	Capital investment	Total investment in fixed assets	Ten thousand yuan
	Energy input	Industrial power consumption	10,000 kWh
	Technical input	Science and technology expenditure	Ten thousand yuan
Output indicators	Expected output	GDP	Ten thousand yuan
	Unexpected output	Industrial pollutant emission	Ton

TABLE 3 | Static efficiency evaluation results of green growth of Oil and gas resource-based cities.

City	2010	2011	2012	2013	2014	2015	2016	2017	2018	Mean Value	Ranking
Yangzhou	1.0000	1.0000	1.0000	0.6570	1.0000	0.6721	1.0000	0.5755	1.0000	0.8783	1
Binzhou	1.0000	1.0000	1.0000	0.7816	0.6403	1.0000	0.7989	0.6503	1.0000	0.8746	2
Erdos	1.0000	1.0000	1.0000	1.0000	0.9026	1.0000	0.2007	0.3364	1.0000	0.8266	3
Zhanjiang	1.0000	1.0000	1.0000	1.0000	0.9026	1.0000	0.2007	0.3364	1.0000	0.8266	4
Dongying	0.8041	0.7304	0.7240	0.6867	0.6571	0.7699	0.8093	0.5337	1.0000	0.7462	5
Jingzhou	1.0000	1.0000	0.5989	1.0000	0.6768	0.5064	0.7289	0.5067	0.6138	0.7368	6
Daqing	0.5714	0.6038	0.6566	0.5361	0.5985	0.6875	0.8033	0.8612	1.0000	0.7020	7
Cangzhou	0.7549	1.0000	1.0000	0.7161	0.6672	0.7624	0.4600	0.3354	0.4260	0.6802	8
Yulin	0.5794	0.7304	0.6856	0.4530	0.5883	0.7045	0.5727	1.0000	0.6256	0.6599	9
Hengyang	0.8445	0.7455	1.0000	0.6055	0.5340	0.5034	0.5486	0.3740	0.3854	0.6157	10
Jinzhou	0.6254	0.7181	0.6358	0.4797	0.3562	0.5985	0.5717	0.3737	1.0000	0.5954	11
Songyuan	1.0000	1.0000	0.1942	0.7052	0.6486	0.5038	0.4156	0.4025	0.4712	0.5935	12
Karamay	1.0000	1.0000	0.7597	0.6341	0.5569	0.5396	0.3073	0.2520	0.2767	0.5918	13
Suining	1.0000	1.0000	0.4891	0.2788	0.3670	0.3278	0.2270	0.7624	0.2883	0.5267	14
Puyang	1.0000	0.5607	0.6297	0.5287	0.4825	0.5193	0.3328	0.2621	0.3077	0.5137	15
Jiuquan	1.0000	0.6348	1.0000	0.3562	0.3842	0.2592	0.1573	0.1859	0.1777	0.4617	16
Yan'an	1.0000	1.0000	0.7404	0.3218	0.2367	0.2411	0.2554	0.1990	0.1574	0.4613	17
Panjin	0.2546	0.5443	0.4999	0.6127	0.3573	0.4280	0.3603	0.3368	0.5143	0.4342	18
Nanyang	0.5585	0.4327	0.4015	0.3353	0.3433	0.3569	0.2440	0.2572	0.3073	0.3597	19
Qingyang	0.9990	0.9992	0.1237	0.0750	0.0792	0.0533	0.0576	0.0888	0.1561	0.2924	20

EMPIRICAL RESEARCH

In the course of the study, because of the existence of undesirable environmental pollutants, this paper chooses DEA-SBM model to evaluate the green growth efficiency of oil and gas resource-based cities, but wants to explore the dynamic changes of green growth efficiency of oil and gas resource-based CIT ies vertically and conduct more in-depth research. A combination of the DEA-SBM model and the Malmquist-Luenberger index is required.

Static Efficiency Evaluation

According to the DEA-SBM model, the static efficiency of green growth of 20 oil and gas resource-based cities is evaluated by using DEA-SOLVERPro5.0 software, and the evaluation results are shown in **Table 3**.

As shown in **Table 3**, the average static efficiency of 20 oil and gas resource-based cities is Yangzhou, Binzhou, Ordos, Zhanjiang, Dongying, Jingzhou, Daqing, Cangzhou, Yulin, Hengyang, Jinzhou, Songyuan, Karamay, Suining, Puyang, Jiuquan, Yan'an, Panjin, Nanyang and Qingyang from large to small. The average static efficiency of green growth of all oil and gas resource-based cities does not reach 1,It shows that there are efficiency losses in the green growth of various oil and gas resource-based cities in 2010–2018, but the efficiency value of some cities in some years, such as Zhanjiang in 2010–2013, Yangzhou, Ordos, Binzhou, Zhanjiang and Dongying in 2018, has reached 1, indicating that these cities have reached Pareto optimal state and achieved green economic growth in these years, But there are also cities like Qingyang with extremely low efficiency of green economic growth.In order to better compare the green growth efficiency of oil and gas resource-based cities in various regions, the static efficiency evaluation results of green growth of oil and gas resource-based cities in different regions are sorted out according to the data in **Table 3**, as shown in **Table 4**.

In order to more intuitively reflect the comparison of the static efficiency of green growth in different regions and their respective development trends, the static efficiency comparison chart of green growth in different regions is drawn according to **Table 4**, as shown in **Figure 1**.

Since 2010, under the premise of the steady improvement of green growth efficiency in China, the static efficiency of green growth of oil and gas resource-based cities has generally shown a downward trend, which also shows that the green growth of oil and gas resource-based cities in China is not ideal. Among all the oil and gas resource-based cities, Yangzhou's green growth static

TABLE 4 | Static efficiency evaluation results of green growth of oil and gas resource-based cities in different regions.

Particular year	Youcheng Average	Eastern region	Central Region	Western region
2010	0.8496	0.7770	0.8534	0.9297
2011	0.8349	0.8561	0.7632	0.8940
2012	0.7069	0.8371	0.6401	0.6330
2013	0.5881	0.7048	0.6729	0.35315
2014	0.5489	0.6544	0.5980	0.3687
2015	0.5716	0.7472	0.5824	0.35425
2016	0.4526	0.6001	0.4677	0.2628
2017	0.4315	0.4488	0.4285	0.4146
2018	0.5854	0.8486	0.5836	0.2803

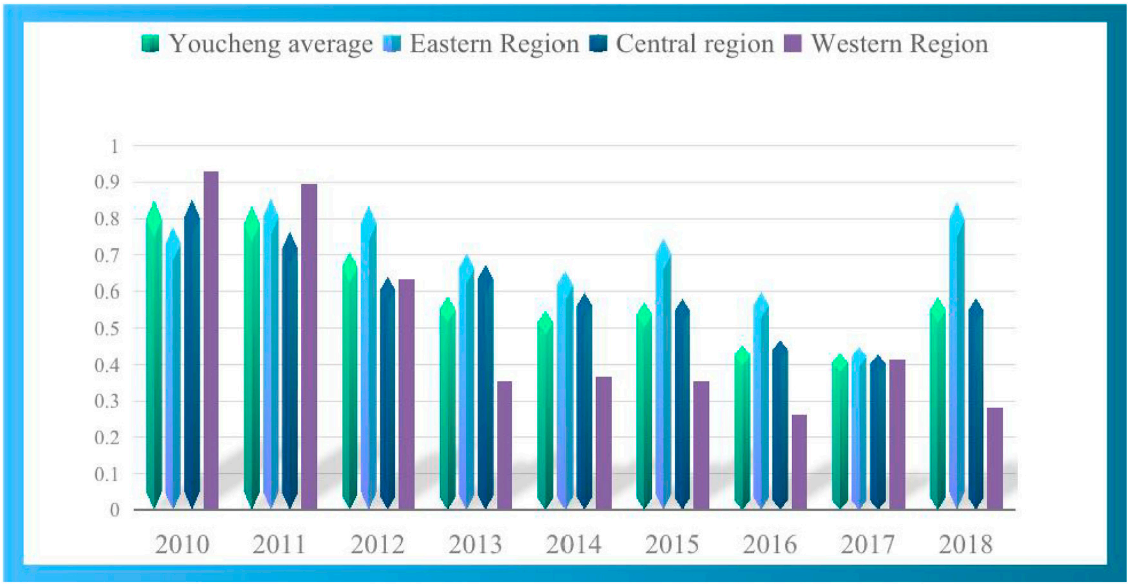

FIGURE 1 | Comparison of static efficiency of green growth in different regions.

efficiency ranks first, the green growth efficiency value is greater than 0.5, and the average green growth efficiency is 0.8,783, which indicates that compared with other oil and gas resource-based cities, Yangzhou's economic development model is relatively healthy and its resource allocation is relatively reasonable.However, from the perspective of efficiency, green growth still has efficiency loss. The average static efficiency of green growth in Jiuquan, Yan'an, Panjin, Nanyang, Qingyang and other cities is less than 0.5, the economic development model is extremely unhealthy, the input factors of production have not been ideal output, there are waste of resources, environmental pollution and other factors that damage green growth in the region.From the perspective of spatial dimension, the static efficiency of green growth of oil and gas resource-based cities in the eastern region is higher than that of other regions, which is in line with the law of environmental Kuznets curve. After economic development to a certain extent, the degree of environmental pollution has been gradually alleviated, and the environmental quality has been improved. The static efficiency value of green growth of oil and gas resource-based cities in central and western regions is the largest in 2010, and after 2010, the static efficiency of green growth has a significant downward trend. The overall water level of the western, central and eastern regions and oil and gas resource-based cities showed a straight downward trend, and the green growth efficiency did not reach 1. It shows that the green growth of all oil and gas resource-based cities has efficiency loss and does not reach the Pareto optimal state, which further illustrates that the green growth of 20 oil and gas resource-based cities in the past nine years is not optimistic, and there are problems such as slow economic development, waste of resources, environmental pollution and so on. How to improve the green growth efficiency of oil and gas resource-based cities has become a difficult problem that the government of oil and gas resource-based cities has to face and solve.

Dynamic Efficiency Evaluation

The static evaluation results show that the static efficiency of green growth of oil and gas resource-based cities is generally low.

TABLE 5 | Evaluation results of green dynamic growth efficiency.

City	2010-2011	2011-2012	2012-2013	2013-2014	2014-2015	2015-2016	2016-2017	2017-2018
Binzhou	1.4687	0.9807	0.7688	0.6953	0.8728	0.9823	1.0402	1.1023
Cangzhou	1.1716	0.5129	0.9496	0.8700	1.0411	1.1386	1.1364	1.2787
Daqing	1.3582	0.9500	0.9885	1.1537	0.9860	0.6768	1.1594	0.9730
Dongying	1.1331	0.8991	0.9736	1.0436	1.1270	1.0870	1.2832	1.0371
Erdos	1.0244	1.0312	0.9641	1.0283	0.9616	1.0613	0.7741	1.0692
Hengyang	1.2591	1.0077	0.4734	1.0255	0.9980	1.0759	0.8879	1.0551
Jinzhou	1.0696	0.9595	1.0202	1.0662	1.0934	1.2272	1.0529	1.0187
Jingzhou	1.0528	0.9667	0.9045	0.9568	0.9529	1.0587	0.9992	1.1100
Jiuquan	0.9232	0.8242	0.9984	0.7167	0.4417	1.5907	1.2638	0.8772
Karamay	1.0635	0.5396	0.7886	1.1815	0.7530	1.0931	1.0546	1.1192
Nanyang	1.0726	0.9782	0.9898	0.9677	1.0120	1.4101	1.1125	1.0276
Panjin	1.0630	1.0011	0.9510	1.0180	1.0165	0.9988	1.2815	1.1094
Puyang	1.0779	0.9511	0.9680	1.0527	0.9980	1.0198	1.0499	1.0099
Qingyang	0.6612	1.3452	0.9720	0.9853	1.0772	1.0484	1.3504	1.9957
Songyuan	0.8913	0.9948	0.9734	0.9993	1.0188	1.0813	1.0695	0.9271
Sui ning	0.9941	0.7155	1.0717	0.8026	1.0019	0.9957	1.0012	0.9952
Yan'an	1.0060	0.7981	0.5485	0.8547	0.7146	0.8752	1.1474	1.3485
Yangzhou	1.1235	1.0460	0.8096	1.0863	1.0440	1.0779	1.1500	1.0487

TABLE 6 | Decomposition results of green total factor growth efficiency of Oil and gas resource-based cities.

City	ML	Ranking	EC	Ranking	TC	Ranking
Binzhou	0.9889	15	0.9426	18	1.0677	3
Cangzhou	1.0123	10	1.0040	11	1.0135	7
Daqing	1.0306	8	1.0000	13	1.0306	6
Dongying	1.0729	3	1.1067	3	1.0093	8
Erdos	0.9893	14	1.0000	13	0.9893	16
Hengyang	0.9728	16	1.0016	12	0.9885	17
Ji zhou	1.0635	5	1.1302	1	0.9755	18
Jingzhou	1.0002	11	1.0125	9	0.9966	12
Jiuquan	0.9545	17	0.9752	16	1.0002	11
Karamay	0.9491	18	0.9556	17	1.0056	10
Nanyang	1.0713	4	1.0449	7	1.0385	4
Panjin	1.0549	6	1.0673	5	0.9898	15
Puyang	1.0159	9	1.0308	8	0.9929	14
Qingyang	1.1794	1	1.0926	4	1.2340	1
Songyuan	0.9945	13	1.0000	13	0.9945	13
Suining	0.9472	19	1.0061	10	0.9454	19
Yan'an	0.9116	20	0.9857	14	0.9448	20
Yangzhou	1.0483	7	1.0507	6	1.0067	9
Yulin	1.1609	2	1.1211	2	1.0861	2
Zhanjiang	0.9971	12	0.9763	15	1.0328	5

Combined with DEA-SBM model and Malmquist-Luenberger index, the dynamic efficiency of green growth of 20 oil and gas resource-based cities from 2010 to 2018 is evaluated and analyzed by using MaxDEA software. Because the dynamic efficiency of green growth is a dynamic evaluation of the efficiency of green growth, only eight periods can be evaluated in the nine-year period. The evaluation results are shown in **Tables 5**, **6**.

The evaluation results show that more than half (11) of the oil and gas resource-based cities have a green dynamic growth rate ML value greater than 1, including Cangzhou, Daqing, Dongying, Jinzhou, Jingzhou, Nanyang, Panjin, Puyang, Qingyang, Yangzhou and Yulin, and their green growth is on the rise. The green growth momentum of Qingyang, Yulin and Dongying is remarkable. The ML values of Binzhou, Ordos, Hengyang, Jiuquan, Karamay, Songyuan, Suining, Yan'an and Zhanjiang are less than 1, and the green growth is in a downward trend.In order to better understand the green growth efficiency of oil and gas resource-based cities, this paper decomposes the total elements of green growth into green growth technology index (EC) and green growth technology progress index (TC), as shown in **Table 6**.

The evaluation result of green dynamic growth efficiency reflects the development trend of green growth of oil and gas resource-based cities. When the dynamic evaluation result ML > 1, the green growth efficiency of oil and gas resource-based cities shows an upward trend during the evaluation period. If ML < 1, it indicates that the green growth efficiency of oil and gas resource-based cities shows a downward trend during the evaluation period. If ML = 1, It means that the green growth efficiency of oil and gas resource-based cities has not changed significantly during the evaluation period.In order to conduct a more in-depth study on the green growth of oil and gas resource-based cities, the green total factor growth efficiency can be decomposed into TC and EC indexes. TC is the index of green technological progress, which represents how technological progress affects the efficiency of green growth of oil and gas resource-based cities. EC is a green technology efficiency index, which represents how the comprehensive factors such as the proficiency of technology users and market environment affect the green growth efficiency of oil and gas resource-based cities when technology remains stable. In the research literature at home and abroad, many scholars mentioned that TC and EC change in the same direction. The static efficiency of green growth indicates the allocation ability of resources within the region when the technology is stable, in contrast, the efficiency of green dynamic growth indicates whether the region has the ability to improve efficiency when the technology is improved, and it also becomes the basis of how the static efficiency of green growth changes. Comparing the static efficiency of green growth and the value of green total factor productivity, this paper analyzes the growth state and growth potential of green economy from static and dynamic perspectives. The results show that, compared with the ranking of static efficiency of green growth, there is no obvious positive and negative relationship between them. For example, Qingyang's green total factor productivity ranks first, while the static efficiency of green growth is the last, which shows that although the current level of green growth in Qingyang is low, it has good development potential.

It can be seen from **Table 6** that the analysis of the green technology progress index of oil and gas resource-based cities shows that the values of the green technology progress index of oil and gas resource-based cities from 2010 to 2018 are greater than 0.9 and approximate to 1, indicating that green technology progress can promote the efficiency of green growth. The analysis of the green technical efficiency index of oil and gas resource-based cities shows that the technical efficiency values of 11 oil and gas resource-based cities, such as Daqing, Binzhou, Cangzhou and Dongying, are all greater than 1, which shows that green technology can improve the efficiency of green growth.By comparing with the green total factor growth efficiency index ranking, this paper analyzes the impact of the two indexes on the green growth efficiency of oil and gas resource-based cities, among which Yan'an and Suining have the lowest ml value, which is less than 1, Qingyang TC index ranks first, and EC index is 1.0926.For cities with higher ml value, TC is the power source to maintain efficiency improvement, while for cities with higher EC ranking, the value of TC is not necessarily large. To sum up, at present, the greater factor to improve the efficiency of green growth of oil and gas resource-based cities is the progress of green technology, although the efficiency of green technology can also play a certain role, but relatively limited.

CONCLUSION

Based on the panel data of SBM model and Malmquist-Luenberger index, this paper evaluates the green growth efficiency of major oil and gas resource-based cities in China, and draws the following conclusions.

1) Using the non-radial non-angle DEA-SBM model, from the static point of view of China's oil and gas resource-based cities 2010–2018 green growth efficiency evaluation. The evaluation results show that the average static efficiency of the 20 oil and gas resource-based cities ranks in the following order: Yangzhou, Binzhou, Ordos, Zhanjiang, Dongying, Jingzhou, Daqing, Cangzhou, Yulin, Hengyang, Jinzhou, Songyuan, Karamay, Suining, Puyang, Jiuquan, Yan'an, Panjin, Nanyang and Qingyang. They did not reach 1 and did not reach Pareto optimality. It shows that the present situation of green growth of oil and gas resource-based cities is not ideal, the input of production factors does not achieve the desired effect, while the economy is backward, the waste of resources is serious, the environmental situation is not optimistic, and the coordinated development of economy, resources and environment can not be realized.From the perspective of spatial dimension, the static efficiency of green growth of oil and gas resource-based cities in the eastern region is higher than that of other regions, which is in line with the law of environmental Kuznets curve. The economic development level of oil and gas resource-based cities in the eastern region is higher, and the degree of environmental pollution is gradually improved.
2) Based on DEA-SBM model and Malmquist-Luenberger index, this paper evaluates the green growth efficiency of oil and gas resource-based cities in China from 2010 to 2018 from the dynamic perspective. The evaluation results show that more than half of the oil and gas resource-based cities have green growth total factor productivity ml value greater than 1. Specifically, Cangzhou, Daqing, Dongying, Jinzhou, Jingzhou, Nanyang, Panjin, Puyang, Qingyang, Yangzhou and Yulin are in an upward trend of green growth, among which Qingyang, Yulin and Dongying are the most significant.The ml value of Binzhou, Ordos, Hengyang, Jiuquan, Karamay, Songyuan, Suining, Yan'an and Zhanjiang is less than 1, the green growth is in a downward trend, and the efficiency of green growth has great room for improvement. The green total factor growth efficiency of oil and gas resource-based cities is different. The green technological progress has a greater impact on the green growth efficiency of oil and gas resource-based cities, while the green technological efficiency has a smaller impact.

DATA AVAILABILITY STATEMENT

The original contributions presented in the study are included in the article/Supplementary material, further inquiries can be directed to the corresponding author.

AUTHOR CONTRIBUTIONS

All authors listed have made a substantial, direct, and intellectual contribution to the work and approved it for publication.

FUNDING

Daqing City Philosophy and social science planning project, Award Numbers: DSGB2022119 and DSGB2021004.

ACKNOWLEDGMENTS

We appreciate the financial support provided by National Social Science Foundation of China, Grant/Award Number: 19BJY068.

REFERENCES

Beijing Normal University Scientific Development Concept and Economic Sustainable Development Research Base, etc (2012). *China Green Index Annual Report-Regional Comparison*[M]. Beijing: Beijing Normal University Press.

Guo, L., Lu, X., Wu, C., and Qu, Y. (2016). Research on the Construction of China's Green Growth Evaluation Index System[J]. *Sci. Res. Manag.* (6), 141–150. doi:10.19571/j.cnki.1000-2995.2016.06.017

Hall, B., and Kerr, M. (1991). *1991-1992 Green Index:A State-By-State Guide to the Nation's Environmental Health*. Washington, USA: Island Press, 11–25.

OECD (2011). *Towards Green Growth:Monitoring Progress OECD Indicator [R]*. Paris, France: OECD.

Ouyang, Z., Zhao, J., and Gui, Z. (2009). Evaluation of Green Development of Chinese Cities[J]. *China Population·Resources Environ.* 019 (005), 11–15. doi:10.3969/j.issn.1002-2104.2009.05.003

Qian, Z., and Liu, X. (2013). Analysis of Regional Differences and Influencing Factors of China's Green Economic Efficiency[J]. *China Popul. Resour. Environ.* 23 (7), 104–109. doi:10.3969/j.issn.1002-2104.2013.07.016

Qu, Y., Liu, W., and Zhou, W. (2017). Research on Green Growth Efficiency Measurement of Pollution-Intensive Industries in Liaoning Province[J]. *Sci. Technol. Manag.* 19 (01), 1–7. doi:10.16315/j.stm.2017.01.001

Research Group of Sustainable Development Strategy of Chinese Academy of Sciences (2011). *China Sustainable Development Strategy Report: Achieving Green Economic Transition [M]*. Beijing, China: Science Press.

UNEP (2012). *Measuring Progress towards an Inclusive Green Economy [R]*. Nairobi, Kenya: UNEP.

Vlontzos, G., Niavis, S., and Manos, B. (2014). A DEA Approach for Estimating the Agricultural Energy and Environmental Efficiency of EU Countries. *Renew. Sustain. Energy Rev.* 40, 91–96. doi:10.1016/j.rser.2014.07.153

Wang, X., and Wu, C. (2015). International Comparison of Energy Eco-Efficiency from the Perspective of "Greening"——An Empirical Test Based on Panel Data of "Group of Twenty[J]. *Technoeconomics* 034 (007), 70–77. doi:10.3969/j.issn.1002-980X.2015.07.011

World Bank (2012). *Inclusive Green Growth:The Pathway to Sustainable Development [R]*. Washington, USA: World Bank.

Wu, C., and Song, X. (2018). Influencing factors and efficiency evaluation of urban green development in the Yangtze River Economic Belt[J]. *Learn. Pract.* (4), 5–13.

Xu, J., Chen, Z., and Li, R. (2020). Impacts of pore size distribution on gas injection in intraformational water zones in oil sands reservoirs. *Oil Gas. Sci. Technol. - Rev. IFP Energies Nouv.* 75, 75. doi:10.2516/ogst/2020047

Xu, J., Wu, K., Li, R., Li, Z., Li, J., Xu, Q., et al. (2018). Real gas transport in shale matrix with fractal structures. *Fuel* 219, 353–363. doi:10.1016/j.fuel.2018.01.114

Xu, J., Wu, K., Li, R., Li, Z., Li, J., Xu, Q., et al. (2019). Nanoscale pore size distribution effects on gas production from fractal shale rocks. *Fractals* 27 (08), 1950142. doi:10.1142/s0218348x19501421

Yang, Z., and Wen, C. (2017). Evaluation of China's green development efficiency and regional differences [J]. *Econ. Geogr.* 037 (003), 10–18. doi:10.15957/j.cnki.jjdl.2017.03.002

Zhang, H., Chang, L., and Cheng, J. (2016). etc. Green development level measurement and its spatial relationship in Hubei Province [J]. *Econ. Geogr.* 036 (009), 158–165. doi:10.15957/j.cnki.jjdl.2016.09.021

Conflict of Interest: The authors declare that the research was conducted in the absence of any commercial or financial relationships that could be construed as a potential conflict of interest.

frontiers | Frontiers in Earth Science

TYPE Original Research
PUBLISHED 16 September 2022
DOI 10.3389/feart.2022.1009750

OPEN ACCESS

EDITED BY
Jinze Xu,
University of Calgary, Canada

REVIEWED BY
Wendong Wang,
China University of Petroleum,
Huadong, China
Yingzhong Yuan,
Chongqing University of Science and
Technology, China

*CORRESPONDENCE
Zeng Fanhui,
zengfanhui023024@126.com

SPECIALTY SECTION
This article was submitted to
Environmental Informatics and Remote
Sensing,
a section of the journal
Frontiers in Earth Science

RECEIVED 02 August 2022
ACCEPTED 22 August 2022
PUBLISHED 16 September 2022

CITATION
Fengxia L, Fanhui Z, Yunqi S and Yu Z
(2022), A fractal relative permeability
model for two-phase flow through
unsaturated shale porous medium.
Front. Earth Sci. 10:1009750.
doi: 10.3389/feart.2022.1009750

A fractal relative permeability model for two-phase flow through unsaturated shale porous medium

Li Fengxia[1,2], Zeng Fanhui[3]*, Shen Yunqi[1,2] and Zhang Yu[3]

[1]State Key Laboratory of Shale Oil and Gas Enrichment Mechanisms and Effective Development, Beijing, China, [2]State Energy Center for Shale Oil Research and Development, Jiangsu, China, [3]Southwest Petroleum University, Chengdu, China

The accurate calculation of the two-phase relative permeability has a significant impact for effectively characterizing the fluid flow patterns of unsaturated shale reservoir. A new fractal relative permeability model is developed based on two-phase transport feature in confined nanopores, which is upscaled with the aid of fractal theory for two-phase flow through unsaturated shale porous medium. Unlike the earlier models, the presented models considered nanopore wettability, confined viscosity varies with the nanopore diameter (variable water phase viscosity), stress dependence effect, real gas effect, irreducible water saturation and tortuosity effect. The proposed model compares the permeability of single nanopore and multiple nanopores with earlier research, which shows that the fractal relative permeability model agrees well with earlier models and experimental data. The results show that the Monte Carlo model and Abaci experimental model studied by previous researchers are special cases of the proposed fractal model, thus showing that the proposed fractal model has obvious advantages. Further calculations show that 1) The gas phase's relative permeability gradually decreases with the increase of water saturation; 2) Confined viscosity varies with the nanopore diameter has a greater influence on the inorganic pores and a smaller influence on the organic pores on the relative permeability; 3) The relative permeability of the intersection point in the organic pore is higher than that of the inorganic porous, but the water saturation at the intersection is less than that of inorganic pores. Therefore, it lays a solid foundation for revealing the two-phase flow law of shale porous media.

KEYWORDS

shale, two-phase flow, confined viscosity, irreducible water saturation, tortuosity effect, fractal relative permeability model

1 Introduction

Simulating the gas and water fluid flow in the shale multi-scale pore structure of an unsaturated reservoir plays an extremely important role in dealing with key issues such as fracturing fluid flowback and unsaturated reservoir development (Bear and Jacob, 1975; Adler and Brenner, 1988; Berkowitz, 2002). One of the most important basic parameters that can characterize the multiphase flow of oil and gas reservoirs is the two-phase relative permeability. It can not only evaluate the behavior of multiphase fluids, but also provide constructive guidance for unsaturated oil and gas reservoirs (Lei Dong et al., 2015). Laboratory test simulation (Jackson et al., 2018) and theoretical derivation of mathematical formulas (Li, 2010; Yao et al., 2018) are the most important methods for evaluating the relative permeability of gas and water phases. Nevertheless, due to the extremely low permeability and the extremely complex nanopore structure, the relative permeability of the two phases of unsaturated tight reservoirs cannot be accurately obtained (Zhang et al., 2017). For this reason, in order to study the gas-water two-phase flow behavior in tight reservoir shale porous media, mathematical models are widely used to accurately predict the gas-water two-phase relative permeability.

Fractal theory is adopted by a large number of researchers to accurately study the relative permeability of the microscopic pore structure of saturated shale porous media with wet and non-wet phases. Katz et al. (Katz and Thompson, 1985) and Krohn et al. (Krohn and Christine, 1988) have rigorously demonstrated that porous media rocks with complex pore structures have fractal characteristics. Based on the fractal self-similarity theory, numerous researchers extensively apply mathematical modeling and numerical simulation to study the gas-water two-phase fluid flow behavior in rock pore structure, and obtained the two-phase relative permeability model (Tan et al., 2015; Wang et al., 2017). According to the assumption that each capillary bundle is saturated by the wetting and non-wetting phase fluids, Yu et al. (Yu and Li, 2003) uses the fractal capillary bundle model and the Hagen-Poiseuille equation to accurately calculate the fractal permeability of the tight reservoir rock porous media. Liu et al. (Liu and Yu, 2007) proposed a new fractal permeability model that considers the capillary pressure effect. However, although these models use fractal theory, they do not consider the combined effects of tortuous capillaries, viscosity changes with pore diameter, and irreducible water saturation.

Prediction of gas-water two-phase relative permeability in shale multi-scale pore structure is still challenging due to complex pore structures and ultra-low permeability. The flow channel is not straight but tortuous, which is a typical feature of multiphase fluid flowing in real porous medium rock. Clennell (Clennell, 1997) and Khalili (Matyka et al., 2008) demonstrates the great and profound influence of tortuosity on the electrical, hydraulics and diffusion properties in unsaturated rocks with multi-scale pores, and based on this, introduces the concept and characteristics of tortuosity (Carman, 1937). Yu (Yu and Li, 2003) and Liu (Liu et al., 2021) established a porous media permeability model based on fractal theory through mathematical modelling method and considering fractal distribution of tortuosity. The results show that the fractal permeability calculated under the conditions of considering fractal distribution of tortuosity and not considering fractal distribution of tortuosity has a significant difference. Wang (Wang et al., 2018) developed the relationship between volume flow and confined pressure considering the fractal distribution of tortuosity in a single confined nanotube. The results show that the fractal distribution of tortuosity increases the complexity of the pore structure of porous media, thereby reducing the permeability of porous media.

Furthermore, the inherent rock properties of porous media play an important role in the main controlling factors affecting the viscosity of confined water compared with bulk water and bulk gas (Li et al., 2007; Feng et al., 2018). It is known that in hydrophilic nanotubes, due to the large amount of water attached to the boundary wall (Thompson and Robbins, 1990), the viscosity of the bulk water and the bulk gas viscosity are much lower than the effective viscosity of the confined water near the boundary wall (Feibelman, 2013). However, the wettability fluid can effectively slide along the hydrophobic capillary wall (Vinogradova et al., 2009), and the no-slip boundary condition assumption no longer holds (Wu et al., 2017). In addition, the effect of water/micropore wall interaction on the flow behavior of confined water is significantly different from that of water/porous wall interacting (R R, et al., 2012; Lorenz and Zewail, 2014). Real slip conditions can characterize the water/micropore wall interaction effect at the molecular level. However, because the interaction between bulk fluid and solid wall occurs near the boundary region of confined nanopore wall, the apparent viscosity can be used to express the fluid viscosity in the boundary region of pore wall (Wu et al., 2017). Yang (Yang et al., 2019) put forward the order of factors that affect the permeability of shale multiscale pore structure. Analysis results show that shale fluid relative permeability is strongly influenced by the slip length with distinctive flow patterns characterizing on fluid/solid interaction.

To accurately gain the relative permeability of shale gas and water phase (The effective permeability of the two-phase fluid through the rock accounts for the content of the absolute permeability of the single-phase fluid through the rock), it is also very important to the calculation of absolute permeability in the nano-scale range. Hu, et al. (Hu and Huang, 2017) concludes that absolute permeability is an intrinsic property of rock, which absolute permeability remains unchanged with the properties of fluids through rock unless there are physical and chemical reactions between fluids and rock. Therefore, Yu (Yu and Li, 2003) obtained the absolute permeability on the basis of Darcy's law equation under the condition of water saturation of 0 or 1, and then established a two-phase relative permeability model based on fractal theory. Xu (Xu et al., 2013) believes that the absolute permeability calculated under the condition that the shale pore structure is completely saturated with fluid is a special case of the effective permeability of single-phase fluid.

In general, when these models are upgraded from nanoporous microscopic simulation to porous media macroscopic simulation, the comprehensive effect of fluid confined viscosity with nanopore size and wettability change have not been effectively solved in shale porous media gas-water two-phase flow channel. For the purpose of accurately simulating the confined fluid flow in shale porous media, the gas-water two-phase relative permeability model of shale porous media must be established under the conditions of nano-scale interface fluid viscosity with nano-aperture variation, tortuous capillary effect and effective slip boundary. These problems have been well analyzed and addressed in this paper. Additionally, the paper also considered stress dependence effect, real gas effect, irreducible water saturation and tortuosity effect, which these effects the earlier models were not considered at the same time. The basic route and structure of the rest of the article are as follows: Fractal model for gas and water transport is organized in Section 2. The two-phase transport model in the porous shale matrix is organized in Section 3. The Model comparison and validation is organized in Section 4. The effects of the real gas, variable water viscosity, gas viscosity, structural parameters, irreducible water saturation and wetting angle on the two-phase relative permeability model are investigated in Section 5. Finally, several conclusions are provided in Section 6.

2 Fractal model for gas and water transport

2.1 Basic theory

Due to the intricate distribution of porous media pores in tight reservoirs, in the light of the complexity of pore distribution in tight reservoirs, the pore distribution of porous media in tight reservoirs has to be simplified using fractal theory. Fractal Theory is a new theory and subject that is very popular and active today. Fractal theory plays a huge role in the simplification of real complex systems. The tight reservoir porous medium satisfies the fractal characteristics. Therefore, the fractal theory can be used to study the water and gas relative permeability of the tight reservoir. On the vertical section of shale multi-scale pore structure, the cumulative size N whose pore size is greater than or equal to λ obeys the fractal scaling law (Boming Yu and Cheng, 2002):

$$N(\geq\lambda) = \left(\frac{\lambda_{\max}}{\lambda}\right)^{D_f} \tag{1}$$

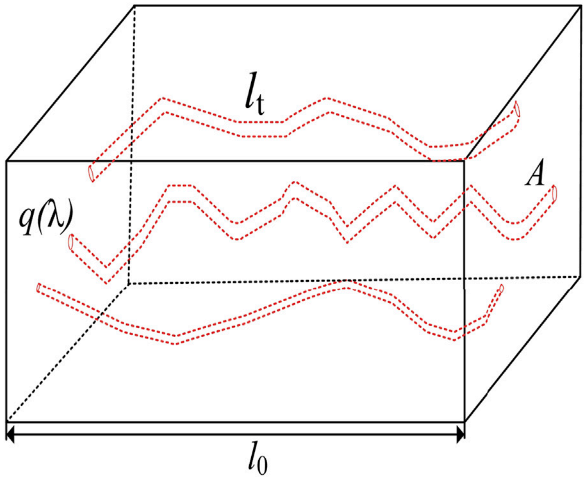

FIGURE 1
Schematic illustration of the physical model of the tortuous capillary in shale porous media (Zeng et al., 2020).

Where $\lambda_{\max}$ is the maximum nanopore size, nm; D_f is the pore fractal dimension, $0 < D_f < 2$.

Differentiating Eq. 1 with respect to λ can be obtained (Yu and Liu 2010):

$$-\mathrm{d}N = D_f \lambda_{\max}^{D_f} \lambda^{-(D_f+1)} \mathrm{d}\lambda \tag{2}$$

Eq. 2 establishes the differential relationship between the number of capillaries and the diameter of nanopores in a unit of shale porous media; the negative sign in Eq. 2 indicates that the larger the diameter of nanopores, the fewer the number of capillary pores.

From Eq. 1, the total number of capillaries from $\lambda_{\min}$ to $\lambda_{\max}$ can be obtained:

$$N_T(\geq\lambda_{\min}) = (\lambda_{\max}/\lambda_{\min})^{D_f} \text{ with } \lambda_{\min} \leq \lambda \leq \lambda_{\max} \tag{3}$$

Simultaneous Eq. 2 and Eq. 3 can be obtained:

$$-\mathrm{d}N/N_T = D_f \lambda_{\min}^{D_f} \lambda^{-(D_f+1)} \mathrm{d}\lambda = f(\lambda)\mathrm{d}\lambda \tag{4}$$

Where $f(\lambda) = D_f \lambda_{\min}^{D_f} \lambda^{-(D_f+1)} \mathrm{d}\lambda$ is the Equation of probability density distribution at the unit interface of shale porous media.

Assuming that the $\lambda_{\min}/\lambda_{\max} = m$, can obtain the pore fractal dimension D_f expression is:

$$D_f = \varepsilon - \ln\phi/\ln m \tag{5}$$

Where ε is the two-dimensional Euclidean dimension, and $\varepsilon = 2$; ϕ is the porosity of shale porous media in Figure 1.

Wheatcraft (Wheatcraft et al., 1991) established the fractal relationship between the length of the tortuous capillary flowing through the porous medium and the fractal shape of the round capillary by using fractal theory and considering the tortuous capillary effect in shale porous media:

$$l_t = l_0^{D_T}\lambda^{1-D_T} \tag{6}$$

Where l_t is the length of the tortuous capillary, nm; D_T is the tortuous fractal dimension of the capillaries, with $1 < D_T < 2$, represents the complexity of fluid flow through shale porous media capillary pore space.

The tortuous fractal dimension can be written:

$$D_T = 1 + \frac{\ln \tau_{av}}{\ln(l_0/\lambda_{av})} \tag{7}$$

Where τ_{av} is the average tortuosity of tortuous capillaries, dimensionless; λ_{av} is the capillaries average diameter, nm.

Considering that the tortuous and bending properties of real capillary are important factors that cannot be ignored in shale porous media, the introduction of tortuous capillary to characterize the complex transport behavior of fluid in porous media. Considering the complex flow path in shale porous media, the average tortuosity can be obtained as:

$$\tau_{av} = \frac{1}{2}\left[1 + \frac{1}{2}\sqrt{1-\phi} + \frac{\sqrt{\left(1-\sqrt{1-\phi}\right)^2 + (1-\phi)/4}}{1-\sqrt{1-\phi}}\right] \tag{8}$$

According to Eq. 4, the average nanopore diameter of the tortuous capillary can be obtained as:

$$\lambda_{av} = \int_{\lambda_{min}}^{\lambda_{max}} \lambda f(\lambda)\mathrm{d}\lambda = \frac{D_f\lambda_{min}}{D_f - 1}\left[1 - (\lambda_{min}/\lambda_{max})^{D_f-1}\right] \tag{9}$$

Equation 9 can be further simplified to obtain:

$$\lambda_{av} = \frac{mD_f}{D_f - 1}\lambda_{max}\left[1 - m^{D_f-1}\right] \tag{10}$$

The average nanopore diameter of capillary in shale porous media can be calculated by Eq. 10. And consider that the porous medium in the cross section of Figure 1 is composed of nanopores with different round diameters. Therefore, the vertical cross-sectional area of the microscopic pore structure of tight reservoirs can be calculated by Eq. 11:

$$A = \frac{\int_{\lambda_{min}}^{\lambda_{max}}\pi\left(\frac{\lambda}{2}\right)^2(-\mathrm{d}N)}{\phi} = \frac{\pi D_f\left(1-m^{2-D_f}\right)}{4(2-D_f)\phi}\lambda_{max}^2 \tag{11}$$

Substituting Eq. 4 into Eq. 11 can further improve Eq. 11:

$$A = \frac{\pi D_f(1-\phi)}{4(2-D_f)\phi}\lambda_{max}^2 \tag{12}$$

The vertical cross-sectional area of micro-pore structure of shale reservoir is as follows:

$$A = l_0^2 \tag{13}$$

By substituting Eq. 12 into Eq. 13, the straight-line distance l_0 can be obtained as follows:

$$l_0 = \sqrt{A} = \frac{\lambda_{max}}{2}\sqrt{\frac{\pi D_f}{2-D_f}\frac{(1-\phi)}{\phi}} \tag{14}$$

Combining Eq. 10 and Eq. 14, the relationship between the straight-line distance of the capillary and the average diameter of the nanopores in the porous medium is:

$$l_0\big/\lambda_{av} = \frac{D_f - 1}{2mD_f\left(1-m^{D_f-1}\right)}\sqrt{\frac{1-\phi}{\phi}\frac{\pi D_f}{(2-D_f)}} \tag{15}$$

Thus, by substituting Eq. 15 and Eq. 8 into Eq. 7, the tortuous fractal dimension D_T can be calculated.

2.2 Gas and water transport in nanopores

Curtis (Curtis et al., 2012) have verified and obtained the conclusion that a large number of inorganic and organic pores are widely present in shale matrix nanopores. However, due to the strong constrained between fluid molecules and the solid surface, the slip-free Hagen-Poiseuille relationship based on the continuum cannot accurately characterize the fluid transport behavior in the nanochannel. Due to the greater difference in density of liquids than gases, the use of gas dynamics theory is ruled out (Gad-El-Hak, 2006). Experimental results and MDS studies have shown that the most suitable for explaining the transfer characteristics of nanofluids must be combined with slip boundary conditions and effective viscosity correction to accurately reveal the flow mechanism of gas and water fluid in confined channel (Thomas and Mcgaughey, 2008; Wu et al., 2017). The physical model of gas and water fluid flow in nanopores is shown in Figure 2.

Figure 2A is the physical model of gas and water fluid flow in organic/inorganic nanopores, where L_{se} represents the effective slip length, and δ is the immovable liquid film thickness occupied by irreducible water; Figure 2B is the gas and water flow model in nanopores.

2.2.1 Transport in nano pores

The inherent characteristics of fluid incompressibility in rock porous media are used as hypothetical conditions. And in the capillary, the flow of the water and gas fluid do not interfere with each other, that is, they flow in a stable laminar flow. The strong wetting effect and water absorption occur near the wall of tortuous capillary nanopores tube, which results in the existence of the partial wetting phase fluid in the form of liquid film. The immovable liquid film thickness δ can be used to characterize the degree of residual water phase fluid in shale porous media, so the liquid film thickness (δ) in this model will not change with the flow behavior generated by the fluid. The distribution and structural parameters of bulk gas, bulk water and irreducible water fluid in the capillary are shown in

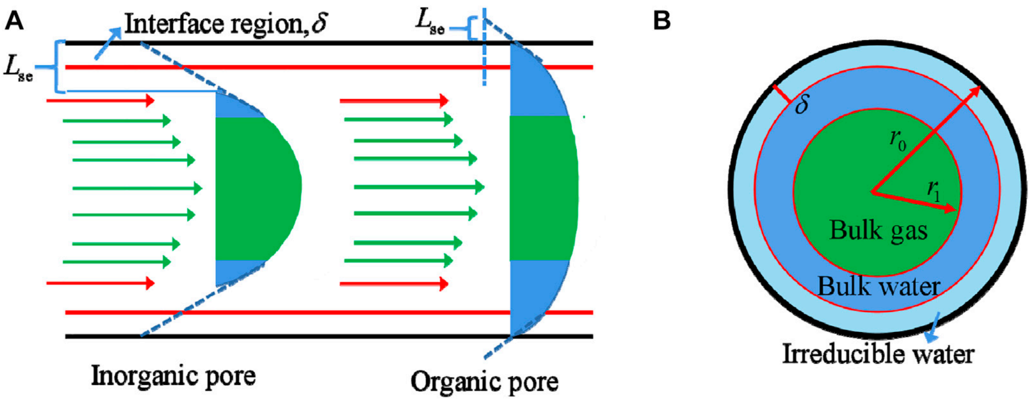

FIGURE 2
Physical model of gas and water fluid flow in organic/inorganic nanopores.

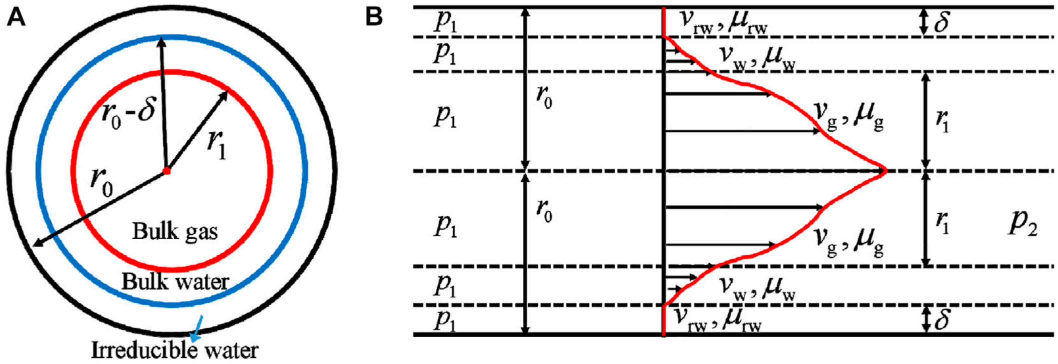

FIGURE 3
Physical model diagram for proposed models: **(A)** distribution of bulk gas, bulk water and bound water in nanopores; **(B)** fluid structure in nanopores.

Figure 3. The length is l, the radius of the nanopore is r_0 and the radius of the bulk gas flow channel is r_1.

Since any nanopore in shale porous media has the same fluid viscosity at the same distance, the fluid flow forms a cylindrical layer velocity field. Under the assumption that the fluid flows forward at a constant speed, the fluid driving force is $\pi r^2 \Delta p$ and the fluid flow resistance is viscous force, that is, $2\pi r l_t \chi$. According to the interaction principle of force in Newton's third law, the relationship between fluid driving force and fluid viscous force is the relationship between force and reaction force when the fluid flows to the axis of a circle with a radius of r meters, then:

$$-2\pi r l_t \chi + \pi r^2 \Delta p = 0 \tag{16}$$

where χ is shear resistance due to friction between adjacent fluids, MPa; Δp is the drive pressure difference, equal to the difference between the inlet pressure p_1 and the outlet pressure p_2, MPa.Equation (16) can be simplified to

$$\chi = \frac{\Delta p}{2 l_t} . r \tag{17}$$

Eq. 17 applies to both water and gas phase. And substituting Newton's law of viscosity into Eq. 17, can get:

$$-\mu_w \frac{\partial v_w}{\partial r} = \frac{\Delta p}{2 l_t} r \tag{18}$$

$$-\mu_g \frac{\partial v_g}{\partial r} = \frac{\Delta p}{2 l_t} r \tag{19}$$

Where μ_w is the water viscosity in the nanopore, Pa.s; μ_g is the gas viscosity in the nanopore, Pa.s; v_w is the water velocity in the nanopore, nm/s; v_g is the gas velocity in the nanopore, nm/s.

$$-\int \partial v_{\mathrm{w}} = \int \frac{\Delta p}{2\mu_{\mathrm{w}} \cdot l_{\mathrm{t}}} r.\partial r \tag{20}$$

$$-\int \partial v_{\mathrm{g}} = \int \frac{\Delta p}{2\mu_{\mathrm{g}} \cdot l_{\mathrm{t}}} r.\partial r \tag{21}$$

With the help of differential Eqs. 20, 21, the velocity distribution of the water and gas phase fluid with r_0 distance from the central axis on the capillary section can be obtained:

$$v_{\mathrm{w}} = -\frac{\Delta p r^2}{4\mu_{\mathrm{w}} l_{\mathrm{t}}} + C_{\mathrm{w}};\ r_1 < r < r_0 - \delta \tag{22}$$

$$v_{\mathrm{rw}} = 0;\ r_0 - \delta \le r \le r_0 \tag{23}$$

$$v_{\mathrm{g}} = -\frac{\Delta p r^2}{4\mu_{\mathrm{g}} l_{\mathrm{t}}} + C_{\mathrm{g}};\ 0 \le r \le r_1 \tag{24}$$

Where v_{rw} is the water fluid velocity at the nanopore boundary, nm/s; δ is the thickness of the liquid film at the nanopore boundary, nm; C_{w} and C_{g} are the velocity integral constants, dimensionless; r_1 is the distance between the cylinder surface of the gas and water phases and the center axis of the nanopore, nm.

$$v_{\mathrm{w}}\big|_{r=r_1} = v_{\mathrm{g}}\big|_{r=r_1} \tag{25}$$

where $r = r_0$-δ is the interface radius between the non-flow-able fluid and the flow-able fluid, and its water phase velocity expression is:

$$v_{\mathrm{w}}\big|_{r=r_0-\delta} = -L_s \frac{\partial v_{\mathrm{w}}}{\partial r}\Big|_{r=r_o-\delta} \tag{26}$$

Where L_{s} is fluid real slip length at walls, nm.

According to Eqs. 22–26, the two-phase velocity equations can be expressed as:

$$v_{\mathrm{w}} = -\frac{\Delta p r^2}{4\mu_{\mathrm{w}} l_{\mathrm{t}}} + \frac{\Delta p (r_0 - \delta)(r_0 - \delta + 2L_{\mathrm{s}})}{4\mu_{\mathrm{w}} l_{\mathrm{t}}};\ r_1 < r < r_0 - \delta \tag{27}$$

$$v_{\mathrm{g}} = \frac{\Delta p r_1^2}{4\mu_{\mathrm{g}} l_{\mathrm{t}}} - \frac{\Delta p r^2}{4\mu_{\mathrm{g}} l_{\mathrm{t}}} + \frac{\Delta p\left[(r_0 - \delta)^2 + 2L_{\mathrm{s}}(r_0 - \delta) - r_1^2\right]}{4\mu_{\mathrm{w}} l_{\mathrm{t}}};\ 0 \le r \le r_1 \tag{28}$$

Yu et al. (Yu and Li, 2003) proposed that the radius of the water and gas interface radius r_1 can be expressed as:

$$r_1 = (\lambda/2 - \delta)\sqrt{S_{\mathrm{g}}} = (\lambda/2 - \delta)\sqrt{1 - S_{\mathrm{w}}} \tag{29}$$

Where λ is nanopore diameter, nm; S_{g} is non-wetting phase saturation, S_{w} is wetting phase saturation, S_{g} =1-S_{w}. Integrating Eq. 27 from $r = r_1$ to $r = \lambda/2$ - δ, and Eq. 28 from r =0 to $r = r_1$, the volume flux of gas phase fluid (q_{g}) and water phase fluid (q_{w}), respectively, can be attained for a single tube.

$$\begin{gathered} q_{\mathrm{w}} = \int_{r_1}^{r_o-\delta} v_{\mathrm{w}} dA = \frac{\pi \Delta p (\lambda/2 - \delta)^2 \cdot S_{\mathrm{w}}}{8\mu_{\mathrm{w}} l_{\mathrm{t}}} \\ \times \left[(\lambda/2 - \delta)^2 \cdot S_{\mathrm{w}} + 4L_{\mathrm{s}}(\lambda/2 - \delta)\right] \end{gathered} \tag{30}$$

$$\begin{gathered} q_{\mathrm{g}} = \int_0^{r_1} v_{\mathrm{g}} dA = \frac{\pi \Delta p (\lambda/2 - \delta)^4 S_{\mathrm{g}}^2}{8\mu_{\mathrm{g}} l_{\mathrm{t}}} + \frac{\pi \Delta p}{4\mu_{\mathrm{w}} l_{\mathrm{t}}} \\ \times \left[(\lambda/2 - \delta)^2 \left(1 - S_{\mathrm{g}}\right) + 2L_{\mathrm{s}}(\lambda/2 - \delta)\right](\lambda/2 - \delta)^2 S_{\mathrm{g}} \end{gathered} \tag{31}$$

2.2.2 Fluid flow feature in confined nanopores

2.2.2.1 Stress dependence effect

Civan (Civan, 2010) proposed the relationship between the diameter of the tortuous capillary nanopore (λ) and the inherent permeability (k) and porosity (ϕ) of the rock as:

$$\lambda_{\mathrm{ef}} = 2\sqrt{2\tau}\sqrt{k/\phi} \tag{32}$$

Where λ_{ef} is the diameter of shale nanopores after considering stress sensitivity, nm.

The inherent permeability and porosity of the rock are (Dong, Hsu et al., 2010):

$$k = k_0 (p_{\mathrm{e}}/p_{\mathrm{o}})^{-s} \tag{33}$$

$$\phi = \phi_0 (p_{\mathrm{e}}/p_{\mathrm{o}})^{-q} \tag{34}$$

Where k the intrinsic permeability of shale porous media nanopores under effective stress, μm^2; k_0 is the inherent permeability of shale porous media under normal atmospheric pressure, μm^2; p_{e} is the difference between confining pressure (p_{c}) and pore pressure (p), that is the effective stress, MPa; p_0 is normal atmospheric pressure, MPa; S is permeability coefficient determined by the inherent properties of the rock, dimensionless; ϕ is the porosity of shale porous media under effective stress, dimensionless; $\phi_0$is the porosity of shale porous media under atmospheric pressure, dimensionless; q is the porosity coefficient determined by inherent properties of rock, dimensionless.

Substituting Eqs. 33, 34 into Eq. 32, the relationship between shale nanopore diameter after considering stress sensitivity and effective stress is:

$$\lambda_{\mathrm{ef}} = 2\sqrt{2\tau}\sqrt{k_0/\phi_0}(p_{\mathrm{e}}/p_{\mathrm{o}})^{0.5(q-s)} \tag{35}$$

According to Eq. 32, the diameter of shale nanopores under atmospheric pressure can be obtained as follows:

$$\lambda = 2\sqrt{2\tau}\sqrt{k_0/\phi_0} \tag{36}$$

Combined Eq. 35 and Eq. 36 can obtain the expression of shale nanopore diameter after considering stress sensitivity:

$$\lambda_{\mathrm{ef}} = \lambda(p_{\mathrm{e}}/p_{\mathrm{o}})^{0.5(q-s)} \tag{37}$$

According to Eq. 37, it establishes the relationship between the diameter of shale nanopore and the diameter of nanopore under atmospheric pressure.

2.2.2.2 Effective slip length determination

The water-wall interaction in the confined nanoporous fluid flow space is greatly affected by the surface configuration of rock particles and the characteristics of physical and chemical reactions (Cottin-Bizonne et al., 2003). Particularly, the wetting property of the nanoporous boundary wall is particularly affected at low shear rates (Tretheway and Meinhart, 2002; Maali et al., 2008). The boundary slip length is closely related to the contact angle of wall surface (Granick et al., 2003). The specific expression for its calculation is:

$$L_s = C/(\cos\theta + 1)^2 \tag{38}$$

Where L_s is the real slip length of the nanopore interface fluid, nm; C is the slip constant, which is 0.41 obtained by MD experimental simulation; θ is the contact angle of the confined nanopore channel, rad.

There is a significant difference between the boundary confined water viscosity and the bulk water viscosity near the wall of the confined nanopore channel, which leads to obvious slippage at the liquid/liquid interface (Mashl and Aluru, 2015). In practical, the effective slip length of confined fluid is affected by the real slip and apparent slip effects (Wu et al., 2017; Zeng et al., 2020), so the effective slip length parameter L_{se} can be obtained:

$$L_{se} = L_{sa} + L_s = \left[\frac{\mu_w}{\mu_d} - 1\right]\left(\frac{\lambda}{8} + L_s\right) + L_s \tag{39}$$

Where L_{se} is effective slip length, nm; L_{sa} is apparent slip length, m; μ_w is the bulk water viscosity, Pa.s; λ is the nano capillary diameter, nm; μ_d is confined fluid effective viscosity, Pa.s.

It is obvious from Eq. 39 that the effective slip length depends not only on the liquid/solid interface fluid wetting properties but also on the fluid viscosity and nanopore size (Thomas and Mcgaughey, 2008).

2.2.2.3 Confined nanofluid flow viscosity

Since the irreducible water viscosity and bulk water viscosity of the fluid exhibit unique properties when flowing in a restricted nanopore (Fradin et al., 2000; Bocquet and Tabeling, 2014), it is necessary to re-determine the effective viscosity of the nanopore fluid. Notably, the area of irreducible water and bulk water flow area is an important factor in determining effective viscosity. Therefore, considering the effective viscosity as the weighted summation of the bulk water viscosity and the irreducible water viscosity according to the area of the flow area (Thomas and Mcgaughey, 2008; Shaat and Mohamed, 2017), the specific expression of the effective viscosity can be obtained as:

$$\mu_d = \mu_w\left[1 - \frac{A_{id}}{A_{td}}\right] + \mu_{rw}\frac{A_{id}}{A_{td}} \tag{40}$$

Where μ_d is the effective viscosity of the confined nanopore fluid, Pa.s; μ_w is the viscosity of the bulk phase water, Pa.s; A_{id} is the area of irreducible water region, nm^2, $A_{id} = \pi[(\lambda/2)^2 - (\lambda/2 - \delta)^2 - (2r_1)^2]$; δ is the liquid film thickness in irreducible water area, nm, determined by MD simulation experiment (Werder, Walther et al., 2002; Thomas and Mcgaughey 2008); μ_{rw} is the irreducible water viscosity, Pa·s;A_{td} is the total area of irreducible water and bulk water area, nm^2, $A_{td} = \pi[(\lambda/2)^2 - (2r_1)^2]$.

The irreducible water viscosity and bulk water viscosity are greatly influenced by the water/wall interaction and the rock wetting properties, and are close with the wetting angle of the water/wall interface. The wetting angle can then be used to express the fluid viscosity in the interface area (Raviv et al., 2001).

$$\frac{\mu_{rw}}{\mu_w} = -3.24\theta + 3.25 \tag{41}$$

Where θ is wetting angle, rad.

In addition, the linear relationship between the wetting angle and the viscosity of the interface region is not limited to CNTs or films, and will have universal applicability in practice (Wang and Cheng, 2019). Notably, rocks are affected by long-term deposition of different fluids, resulting in different wetting properties in shale nanopores, and making the walls of nanopores show different hydrophilicity or hydrophobicity (closely related to contact angle). Therefore, the relationship between the contact angle and the fluid viscosity in the confined area (Eq. 41) is used to characterize the transport characteristics of organic and inorganic pores in shale porous media. According to Eq. 41, it can be seen that the surface of the hydrophilic nanopore exhibits an area of bound water with extremely poor fluidity, and the surface of the hydrophobic nanopore exhibits an area of low viscosity and flow-able bulk water.

The viscosity of the bulk water has the following relationship with the formation temperature of the fluid (Laliberté, 2007).

$$\mu_w = \frac{(T - 273.15) + 246}{[0.05594(T - 273.15) + 5.2842](T - 273.15) + 137.37} \tag{42}$$

Where T is the formation temperature, K.

2.2.2.4 Real gas effect and confined gas viscosity

Under the actual extreme heat and high pressure conditions of the formation, due to the influence of the real gas effect, the gas compression characteristics will be different from the ground conditions and cannot be ignored. Therefore, the pseudo pressure and pseudo temperature are used to characterize the gas compressibility factor (Wu et al., 2016).

$$Z = 0.702p_r^2 e^{-2.5T_r} - 5.524p_r e^{-2.5T_r} + 0.044T_r^2 - 0.164T_r + 1.15 \tag{43}$$

$$p_r = \frac{p}{p_c} \tag{44}$$

$$T_r = \frac{T}{T_c} \tag{45}$$

where p_r is the pseudo-pressure, dimensionless; T_r is the pseudo-temperature, dimensionless; p_c is the methane critical pressure, MPa; T_c is the methane critical temperature, K.

And the gas viscosity in the nanopore can be characterized by Eq. 46 (Tran and Sakhaee-Pour, 2017):

$$\mu_g = \left(1 \times 10^{-7}\right) K \exp\left(X \rho^{Y}\right) \tag{46}$$

$$K = \frac{(9.379 + 0.01607M) T^{1.5}}{(209.2 + 19.26M + T)} \tag{47}$$

$$\rho = 1.4935 \times 10^{-3} \frac{pM}{ZT} \tag{48}$$

$$X = 3.448 + \frac{986.4}{T} + 0.01009M \tag{49}$$

$$Y = 2.447 - 0.2224X \tag{50}$$

Where μ_g is the gas viscosity under consideration of the real gas effect, Pa·s; K is a parameter related to the relative molecular mass and temperature of the gas phase; ρ is the gas density under consideration of the real gas effect, kg/m^3; X and Y are constants, dimensionless.

When a gas flows in the pores of a tight reservoir, the confined gas viscosity is different from the effective gas viscosity, which is presented as a function of the Knudsen number (K_n) in a proportional form as follows:

$$\frac{\mu_{eff}}{\mu_g} = C(K_n) \tag{51}$$

In Eq. 51, μ_{eff} is the confined viscosity of natural gas, Pa·s; $C(K_n)$ is a function of Knudsen number (K_n); The Knudsen number (K_n) is defined as follows (Xu et al., 2019):

$$K_n = l/\lambda \tag{52}$$

In Eq. 52, the mean free path l of gas molecules is expressed by (Roy et al., 2003):

$$l = \frac{\mu_g}{p} \sqrt{\frac{\pi R_g T}{2M}} \tag{53}$$

Where R_g is the universal gas constant, 8.314 J/mol/K.

Tran (Tan et al., 2014) gives the specific expression of $C(K_n)$ as follows (Sone et al., 1990):

$$C(K_n) = \frac{1.270042\pi}{2(1 + 2.222K_n)} \left(\frac{1}{2} + \alpha_m K_n\right) \tag{54}$$

Where:

$$\alpha_m = \beta_0 + \beta_1 \tan^{-1}\left(\beta_2 K_n^{\beta_3}\right) \tag{55}$$

$$\beta_0 = 1.2977 \tag{56}$$

$$\beta_1 = 0.71851 \tag{57}$$

$$\beta_2 = -1.17488 \tag{58}$$

$$\beta_3 = 0.58642 \tag{59}$$

3 Two-phase transport model in shale porous medium

3.1 The two-phase effective permeability in shale porous medium

The total flow rate of non-wetting and wetting phase volume fluxes per unit volume can be obtained by summing all nanoporous flows in shale multi-scale pore structure by fractal theory for gas and water transport method in Section 2 (Tan et al., 2014), and also consider capillary touristy, that is.

$$Q_w = -\int_{\lambda_{min}}^{\lambda_{max}} q_w(\lambda) dN_e \tag{60}$$

$$Q_g = -\int_{\lambda_{min}}^{\lambda_{max}} q_g(\lambda) dN_e \tag{61}$$

Where Q_w is the total volume flow of wetting water phase per unit area in the nanopore of shale porous medium, nm^3/s; Q_g the total volume flow of non-wetting gas phase per unit area of nanopore of shale porous medium, nm^3/s; N_e is the cumulative size of nanopores from the minimum nano-aperture (λ_{min}) to the maximum nano-aperture (λ_{max}) after considering the stress sensitivity (Eq. 37); q_w is the flow rate of the wetting water phase in a single nanopore, nm^3/s; q_g is the flow flux of the non-wetting phase gas in a single nanopore, nm^3/s.

Inserting (Eqs. 2, 6, 30, 31, 39–41, 46) into (Eq. 60) and (Eq. 61), one can get the volume flux of non-wetting and wetting phase fluid.

$$Q_w = -\int_{\lambda_{min}}^{\lambda_{max}} \frac{\pi \Delta p (\lambda/2 - \delta)^2 \cdot S_w}{8\mu_d l_t} \times \left[(\lambda/2 - \delta)^2 S_w + 4L_{se}(\lambda/2 - \delta)\right] dN_e \tag{62}$$

$$Q_g = -\int_{\lambda_{min}}^{\lambda_{max}} \frac{\pi \Delta p (\lambda/2 - \delta)^4 S_g^2}{8\mu_g l_t} + \frac{\pi \Delta p}{4\mu_d l_t} \times \left[(\lambda/2 - \delta)^2 \left(1 - S_g\right) + 2L_{se}(\lambda/2 - \delta)\right] (\lambda/2 - \delta)^2 S_g dN_e \tag{63}$$

Since in Eqs. 62, 63, the effective viscosity μ_d in the denominator term of the integral function is a complex function of the diameter of the nanopore tube (Yang et al., 2019), it cannot be integrated easily. Therefore, in order to further simplify Eqs. 62, 63 to facilitate integration, a large number of shale porous media composed of different pipe diameters are divided into J tiny segments according to the nanopore pipe diameter range ($\lambda_{min} \le \lambda \le \lambda_{max}$). In the range of each tiny segments ($\lambda_{min,i} \le \lambda \le \lambda_{max,i}$, $i = 1, 2, \cdots, J$), the effective viscosity μ_d can be regarded as a constant that does not change with the diameter of the pipe (Zeng et al., 2020). Therefore, in each tiny segment, Eqs. 62, 63 are integrated to obtain the gas phase and water phase flow is:

$$\begin{aligned}
Q_{\mathrm{w},i} = {} & \frac{\pi D_{\mathrm{f}}\Delta p_{\mathrm{w}}}{4\mu_{\mathrm{d},i} l_0^{D_{\mathrm{T}}}}\lambda_{\max}^{D_{\mathrm{f}}} S_{\mathrm{w}}\left\{\frac{1}{32}\left(\frac{\mu_{\mathrm{w}}}{\mu_{\mathrm{d},i}} - S_{\mathrm{g}}\right)\lambda_{\max,i}^{D_{\mathrm{T}}-D_{\mathrm{f}}+3}\frac{\beta_i^{D_{\mathrm{T}}-D_{\mathrm{f}}+3}}{D_{\mathrm{T}} - D_{\mathrm{f}} + 3}\right. \\
& +\frac{1}{16}\left[(4l_{\mathrm{s}} - 3\delta)\frac{\mu_{\mathrm{w}}}{\mu_{\mathrm{d},i}} + \delta\left(4S_{\mathrm{g}} - 1\right)\right]\lambda_{\max,i}^{D_{\mathrm{T}}-D_{\mathrm{f}}+2}\frac{\beta_i^{D_{\mathrm{T}}-D_{\mathrm{f}}+2}}{D_{\mathrm{T}} - D_{\mathrm{f}} + 2} \\
& +\frac{3}{8}\delta\left[(\delta - 4l_{\mathrm{s}})\frac{\mu_{\mathrm{w}}}{\mu_{\mathrm{d},i}} - \delta\left(2S_{\mathrm{g}} - 1\right)\right]\lambda_{\max,i}^{D_{\mathrm{T}}-D_{\mathrm{f}}+1}\frac{\beta_i^{D_{\mathrm{T}}-D_{\mathrm{f}}+1}}{D_{\mathrm{T}} - D_{\mathrm{f}} + 1} \\
& +\frac{1}{4}\delta^2\left[(12l_{\mathrm{s}} - \delta)\frac{\mu_{\mathrm{w}}}{\mu_{\mathrm{d},i}} + \delta\left(4S_{\mathrm{g}} - 3\right)\right]\lambda_{\max,i}^{D_{\mathrm{T}}-D_{\mathrm{f}}}\frac{\beta_i^{D_{\mathrm{T}}-D_{\mathrm{f}}}}{D_{\mathrm{T}} - D_{\mathrm{f}}} \\
& \left.-\frac{1}{2}\delta^3\left[4l_{\mathrm{s}}\frac{\mu_{\mathrm{w}}}{\mu_{\mathrm{d},i}} - \delta\left(1 - S_{\mathrm{g}}\right)\right]\lambda_{\max,i}^{D_{\mathrm{T}}-D_{\mathrm{f}}-1}\frac{\beta_i^{D_{\mathrm{T}}-D_{\mathrm{f}}-1}}{D_{\mathrm{T}} - D_{\mathrm{f}} - 1}\right\}
\end{aligned} \tag{64}$$

$$\begin{aligned}
Q_{\mathrm{g},i} = {} & \frac{\pi D_{\mathrm{f}}\Delta p_{\mathrm{g}}}{4 l_0^{D_{\mathrm{T}}}}\lambda_{\max}^{D_{\mathrm{f}}} S_{\mathrm{g}}\left\{\frac{1}{32}\left[\frac{S_{\mathrm{g}}}{\mu_{\mathrm{eff}}} + \left(1 - 2S_{\mathrm{g}}\right)\frac{1}{\mu_{\mathrm{d},i}} + 2\frac{\mu_{\mathrm{w}}}{\mu_{\mathrm{d},i}^2}\right]\lambda_{\max,i}^{D_{\mathrm{T}}-D_{\mathrm{f}}+3}\frac{\beta_i^{D_{\mathrm{T}}-D_{\mathrm{f}}+3}}{D_{\mathrm{T}} - D_{\mathrm{f}} + 3}\right. \\
& +\frac{1}{16}\left[(4l_{\mathrm{s}} - 3\delta)\frac{\mu_{\mathrm{w}}}{\mu_{\mathrm{d},i}^2} + \delta\left(8S_{\mathrm{g}} - 5\right)\frac{1}{\mu_{\mathrm{d},i}} - \frac{4\delta S_{\mathrm{g}}}{\mu_{\mathrm{eff}}}\right]\lambda_{\max,i}^{D_{\mathrm{T}}-D_{\mathrm{f}}+2}\frac{\beta_i^{D_{\mathrm{T}}-D_{\mathrm{f}}+2}}{D_{\mathrm{T}} - D_{\mathrm{f}} + 2} \\
& +\frac{1}{8}\delta\left[(3\delta - 12l_{\mathrm{s}})\frac{\mu_{\mathrm{w}}}{\mu_{\mathrm{d},i}^2} + \left(9\delta - 12\delta S_{\mathrm{g}}\right)\frac{1}{\mu_{\mathrm{d},i}} + \frac{6\delta S_{\mathrm{g}}}{\mu_{\mathrm{eff}}}\right]\lambda_{\max,i}^{D_{\mathrm{T}}-D_{\mathrm{f}}+1}\frac{\beta_i^{D_{\mathrm{T}}-D_{\mathrm{f}}+1}}{D_{\mathrm{T}} - D_{\mathrm{f}} + 1} \\
& +\frac{1}{4}\delta^2\left[-\frac{4\delta S_{\mathrm{g}}}{\mu_{\mathrm{eff}}} + (12l_{\mathrm{s}} - \delta)\frac{\mu_{\mathrm{w}}}{\mu_{\mathrm{d},i}^2} + \delta\left(8S_{\mathrm{g}} - 7\right)\frac{1}{\mu_{\mathrm{d},i}}\right]\lambda_{\max,i}^{D_{\mathrm{T}}-D_{\mathrm{f}}}\frac{\beta_i^{D_{\mathrm{T}}-D_{\mathrm{f}}}}{D_{\mathrm{T}} - D_{\mathrm{f}}} \\
& \left.+\frac{1}{2}\delta^3\left[-4l_{\mathrm{s}}\frac{\mu_{\mathrm{w}}}{\mu_{\mathrm{d},i}^2} - 2\delta\left(1 - S_{\mathrm{g}}\right)\frac{1}{\mu_{\mathrm{d},i}} + \frac{\delta S_{\mathrm{g}}}{\mu_{\mathrm{eff}}}\right]\lambda_{\max,i}^{D_{\mathrm{T}}-D_{\mathrm{f}}-1}\frac{\beta_i^{D_{\mathrm{T}}-D_{\mathrm{f}}}}{D_{\mathrm{T}} - D_{\mathrm{f}} - 1}\right\}
\end{aligned} \tag{65}$$

Where,

$$\beta_i = \frac{\lambda_{\min,i}}{\lambda_{\max,i}} \tag{66}$$

$$\mu_{\mathrm{d},i}\left(\lambda_{\mathrm{av},i}\right) = \mu_{\mathrm{w}}\left[1 - \frac{A_{\mathrm{id},i}}{A_{\mathrm{td},i}}\right] + \mu_{\mathrm{rw}}\frac{A_{\mathrm{id},i}}{A_{\mathrm{td},i}} \tag{67}$$

$$\lambda_{\mathrm{av},i} = \int_{\lambda_{\min,i}}^{\lambda_{\max,i}} \lambda f(\lambda)\mathrm{d}\lambda = \frac{D_{\mathrm{f}}\lambda_{\min,i}}{D_{\mathrm{f}} - 1}\left[1 - \left(\lambda_{\min,i}/\lambda_{\max,i}\right)^{D_{\mathrm{f}}-1}\right] \tag{68}$$

$$A_{\mathrm{id},i} = \pi\left[\left(\lambda_{\mathrm{av},i}/2\right)^2 - \left(\lambda_{\mathrm{av},i}/2 - \lambda_{\mathrm{c}}\right)^2\right] \tag{69}$$

$$A_{\mathrm{td},i} = \pi\left(\lambda_{\mathrm{av},i}/2\right)^2 \tag{70}$$

Then the flow of nanopores in each tiny part of shale is superimposed algebraically to obtain the gas and water phase flow flux of shale porous media:

$$Q_{\mathrm{w}} = \sum_{i=1}^{J} Q_{\mathrm{w},i} \tag{71}$$

$$Q_g = \sum_{i=1}^{J} Q_{\mathrm{g},i} \tag{72}$$

Where J is the number of tiny segments.

Inserting Eq. 64 into Eq. 71, one can get

$$\begin{aligned}
Q_{\mathrm{w}} = {} & \frac{\pi \Delta p_{\mathrm{w}} D_{\mathrm{f}}}{4 l_0^{D_{\mathrm{T}}}}\lambda_{\max}^{D_{\mathrm{f}}} S_{\mathrm{w}}\sum_i^J\left\{\frac{1}{32}\left(\frac{\mu_{\mathrm{w}}}{\mu_{\mathrm{d},i}} - S_{\mathrm{g}}\right)\lambda_{\max,i}^{D_{\mathrm{T}}-D_{\mathrm{f}}+3}\frac{\beta_i^{D_{\mathrm{T}}-D_{\mathrm{f}}+3}}{D_{\mathrm{T}} - D_{\mathrm{f}} + 3}\right. \\
& +\frac{1}{16}\left[(4l_{\mathrm{s}} - 3\delta)\frac{\mu_{\mathrm{w}}}{\mu_{\mathrm{d},i}} + \delta\left(4S_{\mathrm{g}} - 1\right)\right]\lambda_{\max,i}^{D_{\mathrm{T}}-D_{\mathrm{f}}+2}\frac{\beta_i^{D_{\mathrm{T}}-D_{\mathrm{f}}+2}}{D_{\mathrm{T}} - D_{\mathrm{f}} + 2} \\
& +\frac{3}{8}\delta\left[(\delta - 4l_{\mathrm{s}})\frac{\mu_{\mathrm{w}}}{\mu_{\mathrm{d},i}} - \delta\left(2S_{\mathrm{g}} - 1\right)\right]\lambda_{\max,i}^{D_{\mathrm{T}}-D_{\mathrm{f}}+1}\frac{\beta_i^{D_{\mathrm{T}}-D_{\mathrm{f}}+1}}{D_{\mathrm{T}} - D_{\mathrm{f}} + 1} \\
& +\frac{1}{4}\delta^2\left[(12l_{\mathrm{s}} - \delta)\frac{\mu_{\mathrm{w}}}{\mu_{\mathrm{d},i}} + \delta\left(4S_{\mathrm{g}} - 3\right)\right]\lambda_{\max,i}^{D_{\mathrm{T}}-D_{\mathrm{f}}}\frac{\beta_i^{D_{\mathrm{T}}-D_{\mathrm{f}}}}{D_{\mathrm{T}} - D_{\mathrm{f}}} \\
& \left.-\frac{1}{2}\delta^3\left[4l_{\mathrm{s}}\frac{\mu_{\mathrm{w}}}{\mu_{\mathrm{d},i}} - \delta\left(1 - S_{\mathrm{g}}\right)\right]\lambda_{\max,i}^{D_{\mathrm{T}}-D_{\mathrm{f}}-1}\frac{\beta_i^{D_{\mathrm{T}}-D_{\mathrm{f}}-1}}{D_{\mathrm{T}} - D_{\mathrm{f}} - 1}\right\}
\end{aligned} \tag{73}$$

Where $\triangle p_{\mathrm{w}}$ is the differential pressure of wetting flow. Similarly, inserting Eq. 65 into Eq. 72, one can get:

$$\begin{aligned}
Q_{\mathrm{g}} = {} & \frac{\pi \Delta p_{\mathrm{g}} D_{\mathrm{f}}}{4 l_0^{D_{\mathrm{T}}}}\lambda_{\max}^{D_{\mathrm{f}}} S_{\mathrm{g}}\sum_i^J\left\{\frac{1}{32}\left[\frac{S_{\mathrm{g}}}{\mu_{\mathrm{eff}}} + \left(1 - 2S_{\mathrm{g}}\right)\frac{1}{\mu_{\mathrm{d},i}} + 2\frac{\mu_{\mathrm{w}}}{\mu_{\mathrm{d},i}^2}\right]\lambda_{\max,i}^{D_{\mathrm{T}}-D_{\mathrm{f}}+3}\frac{\beta_i^{D_{\mathrm{T}}-D_{\mathrm{f}}+3}}{D_{\mathrm{T}} - D_{\mathrm{f}} + 3}\right. \\
& +\frac{1}{16}\left[(4l_{\mathrm{s}} - 3\delta)\frac{\mu_{\mathrm{w}}}{\mu_{\mathrm{d},i}^2} + \delta\left(8S_{\mathrm{g}} - 5\right)\frac{1}{\mu_{\mathrm{d},i}} - \frac{4\delta S_{\mathrm{g}}}{\mu_{\mathrm{eff}}}\right]\lambda_{\max,i}^{D_{\mathrm{T}}-D_{\mathrm{f}}+2}\frac{\beta_i^{D_{\mathrm{T}}-D_{\mathrm{f}}+2}}{D_{\mathrm{T}} - D_{\mathrm{f}} + 2} \\
& +\frac{1}{8}\delta\left[(3\delta - 12l_{\mathrm{s}})\frac{\mu_{\mathrm{w}}}{\mu_{\mathrm{d},i}^2} + \left(9\delta - 12\delta S_{\mathrm{g}}\right)\frac{1}{\mu_{\mathrm{d},i}} + \frac{6\delta S_{\mathrm{g}}}{\mu_{\mathrm{eff}}}\right]\lambda_{\max,i}^{D_{\mathrm{T}}-D_{\mathrm{f}}+1}\frac{\beta_i^{D_{\mathrm{T}}-D_{\mathrm{f}}+1}}{D_{\mathrm{T}} - D_{\mathrm{f}} + 1} \\
& +\frac{1}{4}\delta^2\left[-\frac{4\delta S_{\mathrm{g}}}{\mu_{\mathrm{eff}}} + (12l_{\mathrm{s}} - \delta)\frac{\mu_{\mathrm{w}}}{\mu_{\mathrm{d},i}^2} + \delta\left(8S_{\mathrm{g}} - 7\right)\frac{1}{\mu_{\mathrm{d},i}}\right]\lambda_{\max,i}^{D_{\mathrm{T}}-D_{\mathrm{f}}}\frac{\beta_i^{D_{\mathrm{T}}-D_{\mathrm{f}}}}{D_{\mathrm{T}} - D_{\mathrm{f}}} \\
& \left.+\frac{1}{2}\delta^3\left[-4l_{\mathrm{s}}\frac{\mu_{\mathrm{w}}}{\mu_{\mathrm{d},i}^2} - 2\delta\left(1 - S_{\mathrm{g}}\right)\frac{1}{\mu_{\mathrm{d},i}} + \frac{\delta S_{\mathrm{g}}}{\mu_{\mathrm{eff}}}\right]\lambda_{\max,i}^{D_{\mathrm{T}}-D_{\mathrm{f}}-1}\frac{\beta_i^{D_{\mathrm{T}}-D_{\mathrm{f}}-1}}{D_{\mathrm{T}} - D_{\mathrm{f}} - 1}\right\}
\end{aligned} \tag{74}$$

Where $\triangle p_{\mathrm{g}}$ is the differential pressure of non-wetting flow.

According to Darcy's law, the two-phase flow capacity of the porous medium are given by,

$$Q_{\mathrm{w}} = \frac{K_{\mathrm{w}} A \Delta p_{\mathrm{w}}}{\mu_{\mathrm{w}} l_{\mathrm{o}}} \tag{75}$$

$$Q_{\mathrm{g}} = \frac{K_{\mathrm{g}} A \Delta p_{\mathrm{g}}}{\mu_{\mathrm{g}} l_{\mathrm{o}}} \tag{76}$$

Inserting Eqs. 73, 74 into Eqs. 75, 76, one can get the effective permeability in shale gas porous media as.

$$K_{\mathrm{w}} = \frac{Q_{\mathrm{w}}\mu_{\mathrm{w}} l_{\mathrm{o}}}{A\triangle p_{\mathrm{w}}} \tag{77}$$

$$K_{\mathrm{g}} = \frac{Q_{\mathrm{g}}\mu_{\mathrm{g}} l_{\mathrm{o}}}{A\triangle p_{\mathrm{g}}} \tag{78}$$

Where K_{w} is the effective permeability of weting flow, K_g is the effective permeability of non-weting flow.

3.2 The two-phase relative permeability in shale porous medium

According to the definition of absolute permeability, it is the flow capacity when only containing single-phase gas or single-phase water. Under the condition that the fluid passes through the rock porous medium without physical and chemical reaction, the absolute permeability will not change because of the nature of the water or gas passing through the rock, which is the inherent property of the rock porous medium (Yu and Li, 2003; Hu and Huang, 2017). Therefore, it is only gas volume flux when the gas saturation is 1.

$$\begin{aligned}Q_K = {} & \frac{\pi \Delta p_g D_f}{4 l_0^{D_T}} \lambda_{\max}^{D_f} \sum_i^J \left\{ \frac{1}{32} \left[\frac{1}{\mu_{\mathrm{eff}}} - \frac{1}{\mu_{d,i}} + 2 \frac{\mu_w}{\mu_{d,i}^2} \right] \lambda_{\max,i}^{D_T - D_f + 3} \frac{\beta_i^{D_T - D_f + 3}}{D_T - D_f + 3} \right. \\ & + \frac{1}{16} \left[(4 l_s - 3\delta) \frac{\mu_w}{\mu_{d,i}^2} + 3\delta \frac{1}{\mu_{d,i}} - \frac{4\delta}{\mu_{\mathrm{eff}}} \right] \lambda_{\max,i}^{D_T - D_f + 2} \frac{\beta_i^{D_T - D_f + 2}}{D_T - D_f + 2} \\ & + \frac{1}{8} \delta \left[(3\delta - 12 l_s) \frac{\mu_w}{\mu_{d,i}^2} + (9\delta - 12\delta) \frac{1}{\mu_{d,i}} + \frac{6\delta}{\mu_{\mathrm{eff}}} \right] \lambda_{\max,i}^{D_T - D_f + 1} \frac{\beta_i^{D_T - D_f + 1}}{D_T - D_f + 1} \\ & + \frac{1}{4} \delta^2 \left[-\frac{4\delta}{\mu_{\mathrm{eff}}} + (12 l_s - \delta) \frac{\mu_w}{\mu_{d,i}^2} + \frac{\delta}{\mu_{d,i}} \right] \lambda_{\max,i}^{D_T - D_f} \frac{\beta_i^{D_T - D_f}}{D_T - D_f} \\ & \left. + \frac{1}{2} \delta^3 \left[-4 l_s \frac{\mu_w}{\mu_{d,i}^2} + \frac{\delta}{\mu_{\mathrm{eff}}} \right] \lambda_{\max,i}^{D_T - D_f - 1} \frac{\beta_i^{D_T - D_f - 1}}{D_T - D_f - 1} \right\}\end{aligned} \tag{79}$$

According to Darcy's law, the gas flow capacity of the porous medium are given by,

$$Q_K = \frac{K A \Delta p_g}{\mu_g l_o} \tag{80}$$

Inserting Eq. 79 into Eq. 80, one can get the absolute permeability in shale gas porous media as.

$$K = \frac{Q_K \mu_g l_o}{A \Delta p_g} \tag{81}$$

Then, combining Eqs. 77, 78, 81, the initial two-phase relative permeability can be obtained as:

$$K_{rw0} = \frac{K_w}{K} \tag{82}$$

$$K_{rg0} = \frac{K_g}{K} \tag{83}$$

Considering that τ is the water saturation tortuosity when only one fluid is saturated in the porous medium, and τ_w and τ_g are the water-bearing tortuosity of the wetting phase and the gas-bearing tortuosity of non-wetting phase under two-phase seepage conditions. They satisfy the following relationship (Burdine, 1953):

$$\tau_{rw} = \frac{\tau}{\tau_w} = \frac{S_w - S_{wi}}{1 - S_{wi}} \tag{84}$$

$$\tau_{rg} = \frac{\tau}{\tau_g} = \frac{S_g}{1 - S_{wi}} \tag{85}$$

Where S_{wi} is the irreducible water saturation, dimensionless.

Since the water-bearing tortuosity and the gas-bearing tortuosity change with the change of saturation, according to Eqs. 82, 83 combined with Eqs. 84, 85, the following improved formulas are obtained (Burdine, 1953).

$$K_{rw} = \tau_{rw}^2 \frac{K_w}{K} \tag{86}$$

$$K_{rg} = \tau_{rg}^2 \frac{K_g}{K} \tag{87}$$

Put Eqs. 73, 74, 79 into Eqs. 77, 78, 81 respectively, and then put Eqs. 77, 78, 81 into Eqs. 86, 87, we can get:

$$K_{rw} = \tau_{rw}^2 \frac{A_w}{B_w} \tag{88}$$

$$K_{rg} = \tau_{rg}^2 \frac{A_g}{B_g} \tag{89}$$

Where:

$$\begin{aligned}A_w = {} & \mu_w S_w^* \sum_i^J \left\{ \frac{1}{32} \left(\frac{\mu_w}{\mu_{d,i}} - S_g^* \right) \lambda_{\max,i}^{D_T - D_f + 3} \frac{\beta_i^{D_T - D_f + 3}}{D_T - D_f + 3} \right. \\ & + \frac{1}{16} \left[(4 L_s - 3\delta) \frac{\mu_w}{\mu_{d,i}} + \delta \left(4 S_g^* - 1 \right) \right] \lambda_{\max,i}^{D_T - D_f + 2} \frac{\beta_i^{D_T - D_f + 2}}{D_T - D_f + 2} \\ & + \frac{3}{8} \delta \left[(\delta - 4 L_s) \frac{\mu_w}{\mu_{d,i}} - \delta \left(2 S_g^* - 1 \right) \right] \lambda_{\max,i}^{D_T - D_f + 1} \frac{\beta_i^{D_T - D_f + 1}}{D_T - D_f + 1} \\ & + \frac{1}{4} \delta^2 \left[(12 L_s - \delta) \frac{\mu_w}{\mu_{d,i}} + \delta \left(4 S_g^* - 3 \right) \right] \lambda_{\max,i}^{D_T - D_f} \frac{\beta_i^{D_T - D_f}}{D_T - D_f} \\ & \left. - \frac{1}{2} \delta^3 \left[4 L_s \frac{\mu_w}{\mu_{d,i}} - \delta \left(1 - S_g^* \right) \right] \lambda_{\max,i}^{D_T - D_f - 1} \frac{\beta_i^{D_T - D_f - 1}}{D_T - D_f - 1} \right\}\end{aligned} \tag{90}$$

$$\begin{aligned}B_w = {} & \mu_{\mathrm{eff}} \sum_i^J \left\{ \frac{1}{32} \left[\frac{1}{\mu_{\mathrm{eff}}} - \frac{1}{\mu_{d,i}} + 2 \frac{\mu_w}{\mu_{d,i}^2} \right] \lambda_{\max,i}^{D_T - D_f + 3} \frac{\beta_i^{D_T - D_f + 3}}{D_T - D_f + 3} \right. \\ & + \frac{1}{16} \left[(4 L_s - 3\delta) \frac{\mu_w}{\mu_{d,i}^2} + 3\delta \frac{1}{\mu_{d,i}} - \frac{4\delta}{\mu_{\mathrm{eff}}} \right] \lambda_{\max,i}^{D_T - D_f + 2} \frac{\beta_i^{D_T - D_f + 2}}{D_T - D_f + 2} \\ & + \frac{1}{8} \delta \left[(3\delta - 12 L_s) \frac{\mu_w}{\mu_{d,i}^2} + (9\delta - 12\delta) \frac{1}{\mu_{d,i}} + \frac{6\delta}{\mu_{\mathrm{eff}}} \right] \lambda_{\max,i}^{D_T - D_f + 1} \frac{\beta_i^{D_T - D_f + 1}}{D_T - D_f + 1} \\ & + \frac{1}{4} \delta^2 \left[-\frac{4\delta}{\mu_{\mathrm{eff}}} + (12 L_s - \delta) \frac{\mu_w}{\mu_{d,i}^2} + \frac{\delta}{\mu_{d,i}} \right] \lambda_{\max,i}^{D_T - D_f} \frac{\beta_i^{D_T - D_f}}{D_T - D_f} \\ & \left. + \frac{1}{2} \delta^3 \left[-4 L_s \frac{\mu_w}{\mu_{d,i}^2} + \frac{\delta}{\mu_{\mathrm{eff}}} \right] \lambda_{\max,i}^{D_T - D_f - 1} \frac{\beta_i^{D_T - D_f - 1}}{D_T - D_f - 1} \right\}\end{aligned} \tag{91}$$

$$
\begin{aligned}
A_{\mathrm{g}} = S_{\mathrm{g}}^{*}\sum_{i}^{J}\Bigg\{ & \frac{1}{32}\left[\frac{S_{\mathrm{g}}^{*}}{\mu_{\mathrm{eff}}} + \left(1-2S_{\mathrm{g}}^{*}\right)\frac{1}{\mu_{\mathrm{d},i}} + 2\frac{\mu_{\mathrm{w}}}{\mu_{\mathrm{d},i}^{2}}\right]\lambda_{\max,i}^{D_{\mathrm{T}}-D_{\mathrm{f}}+3}\frac{\beta_{i}^{D_{\mathrm{T}}-D_{\mathrm{f}}+3}}{D_{\mathrm{T}}-D_{\mathrm{f}}+3} \\
& +\frac{1}{16}\left[(4L_{\mathrm{s}}-3\delta)\frac{\mu_{\mathrm{w}}}{\mu_{\mathrm{d},i}^{2}} + \delta\left(8S_{\mathrm{g}}^{*}-5\right)\frac{1}{\mu_{\mathrm{d},i}} - \frac{4\delta S_{\mathrm{g}}^{*}}{\mu_{\mathrm{eff}}}\right]\lambda_{\max,i}^{D_{\mathrm{T}}-D_{\mathrm{f}}+2}\frac{\beta_{i}^{D_{\mathrm{T}}-D_{\mathrm{f}}+2}}{D_{\mathrm{T}}-D_{\mathrm{f}}+2} \\
& +\frac{1}{8}\delta\left[(3\delta-12L_{\mathrm{s}})\frac{\mu_{\mathrm{w}}}{\mu_{\mathrm{d},i}^{2}} + \left(9\delta-12\delta S_{\mathrm{g}}^{*}\right)\frac{1}{\mu_{\mathrm{d},i}} + \frac{6\delta S_{\mathrm{g}}^{*}}{\mu_{\mathrm{eff}}}\right]\lambda_{\max,i}^{D_{\mathrm{T}}-D_{\mathrm{f}}+1}\frac{\beta_{i}^{D_{\mathrm{T}}-D_{\mathrm{f}}+1}}{D_{\mathrm{T}}-D_{\mathrm{f}}+1} \\
& +\frac{1}{4}\delta^{2}\left[-\frac{4\delta S_{\mathrm{g}}^{*}}{\mu_{\mathrm{eff}}} + (12L_{\mathrm{s}}-\delta)\frac{\mu_{\mathrm{w}}}{\mu_{\mathrm{d},i}^{2}} + \delta\left(8S_{\mathrm{g}}^{*}-7\right)\frac{1}{\mu_{\mathrm{d},i}}\right]\lambda_{\max,i}^{D_{\mathrm{T}}-D_{\mathrm{f}}}\frac{\beta_{i}^{D_{\mathrm{T}}-D_{\mathrm{f}}}}{D_{\mathrm{T}}-D_{\mathrm{f}}} \\
& +\frac{1}{2}\delta^{3}\left[-4L_{\mathrm{s}}\frac{\mu_{\mathrm{w}}}{\mu_{\mathrm{d},i}^{2}} - 2\delta\left(1-S_{\mathrm{g}}^{*}\right)\frac{1}{\mu_{\mathrm{d},i}} + \frac{\delta S_{\mathrm{g}}^{*}}{\mu_{\mathrm{eff}}}\right]\lambda_{\max,i}^{D_{\mathrm{T}}-D_{\mathrm{f}}-1}\frac{\beta_{i}^{D_{\mathrm{T}}-D_{\mathrm{f}}-1}}{D_{\mathrm{T}}-D_{\mathrm{f}}-1}\Bigg\}
\end{aligned}
\tag{92}
$$

$$
\begin{aligned}
B_{\mathrm{g}} = \sum_{i}^{J}\Bigg\{ & \frac{1}{32}\left[\frac{1}{\mu_{\mathrm{eff}}} - \frac{1}{\mu_{\mathrm{d},i}} + 2\frac{\mu_{\mathrm{w}}}{\mu_{\mathrm{d},i}^{2}}\right]\lambda_{\max,i}^{D_{\mathrm{T}}-D_{\mathrm{f}}+3}\frac{\beta_{i}^{D_{\mathrm{T}}-D_{\mathrm{f}}+3}}{D_{\mathrm{T}}-D_{\mathrm{f}}+3} \\
& +\frac{1}{16}\left[(4L_{\mathrm{s}}-3\delta)\frac{\mu_{\mathrm{w}}}{\mu_{\mathrm{d},i}^{2}} + 3\delta\frac{1}{\mu_{\mathrm{d},i}} - \frac{4\delta}{\mu_{\mathrm{eff}}}\right]\lambda_{\max,i}^{D_{\mathrm{T}}-D_{\mathrm{f}}+2}\frac{\beta_{i}^{D_{\mathrm{T}}-D_{\mathrm{f}}+2}}{D_{\mathrm{T}}-D_{\mathrm{f}}+2} \\
& +\frac{1}{8}\delta\left[(3\delta-12L_{\mathrm{s}})\frac{\mu_{\mathrm{w}}}{\mu_{\mathrm{d},i}^{2}} + (9\delta-12\delta)\frac{1}{\mu_{\mathrm{d},i}} + \frac{6\delta}{\mu_{\mathrm{eff}}}\right]\lambda_{\max,i}^{D_{\mathrm{T}}-D_{\mathrm{f}}+1}\frac{\beta_{i}^{D_{\mathrm{T}}-D_{\mathrm{f}}+1}}{D_{\mathrm{T}}-D_{\mathrm{f}}+1} \\
& +\frac{1}{4}\delta^{2}\left[-\frac{4\delta}{\mu_{\mathrm{eff}}} + (12L_{\mathrm{s}}-\delta)\frac{\mu_{\mathrm{w}}}{\mu_{\mathrm{d},i}^{2}} + \frac{\delta}{\mu_{\mathrm{d},i}}\right]\lambda_{\max,i}^{D_{\mathrm{T}}-D_{\mathrm{f}}}\frac{\beta_{i}^{D_{\mathrm{T}}-D_{\mathrm{f}}}}{D_{\mathrm{T}}-D_{\mathrm{f}}} \\
& +\frac{1}{2}\delta^{3}\left[-4L_{\mathrm{s}}\frac{\mu_{\mathrm{w}}}{\mu_{\mathrm{d},i}^{2}} + \frac{\delta}{\mu_{\mathrm{eff}}}\right]\lambda_{\max,i}^{D_{\mathrm{T}}-D_{\mathrm{f}}-1}\frac{\beta_{i}^{D_{\mathrm{T}}-D_{\mathrm{f}}-1}}{D_{\mathrm{T}}-D_{\mathrm{f}}-1}\Bigg\}
\end{aligned}
\tag{93}
$$

WhereS_{w}^{*} is the water saturation after considering the irreducible water saturation (S_{w}^{*}=S_{w}+S_{wi}); S_{g}^{*} is the gas saturation ($S_{\mathrm{g}}^{*} = 1 - S_{\mathrm{w}}^{*}$) considering the irreducible water saturation.

4 Model comparison and validation

In Section 2 and Section 3, the theoretical calculation model of the two-phase relative permeability in shale multi-scale pore structure is derived. This paper aims to study the analysis model of the two-phase relative permeability in shale multi-scale pore structure. Next, we will first verify the proposed model with earlier experimental and theoretical models. Then, study the real gas effect of porous media, gas viscosity effect, structural parameters of porous media (such as pore fractal dimension D_f and tortuous fractal dimension D_T), variable water viscosity, irreducible water saturation, wetting angle on the two-phase relative permeability are investigated in detail.

4.1 Verification of the proposed model with other models

The proposed fractal two-phase relative permeability model is an idealized semi-analytical model. When macroscopic seepage occurs in the whole shale porous medium, the secondary role of pore connection shape and physicochemical reaction between fluid and rock can be ignored in revealing the two-phase relative permeability. In addition, the convergence value of fluid characteristics in shale multi-scale pore structure can be obtained under sufficient simulation conditions and the convergence criterion is satisfied. An approximation of the two-phase relative permeability can be obtained by setting the error of 10^{-3} and J=10,000 conditions in the following discussion. Other specific parameters are exhibited in Table 1 below.

Then, the rationality and reliability of this proposed model will be verified by mathematical theory verification and experimental simulation results. First, this paper will compare the relative permeability of single capillary with the G. Lei's model (Lei et al., 2015) and Hagen-Poiseuille's model. Second, we will perform multiple capillary nanopore relative permeability comparison on the Monte Carlo's model (Xu et al., 2013) and Abaci's model (Abaci et al., 1992).

4.1.1 Single capillary nanopore relative permeability comparison

Under the condition of water saturation 1, boundary water film thickness 0 and bound water 0, the Hagen-Poiseuille equation under a single capillary and the water flow rate of the degradation model in this paper are calculated, as well as the comparison of the relative permeability between the G. Lei's (Lei et al., 2015) model and the degradation model in this paper. As shown in Figure 4 below.

From Figure 4A, it can be observed the phenomenon that when the water saturation of the model in this paper is 0.4, 0.6, 0.8, and 1, our water phase flow gradually increases with the increase of water saturation, and it reaches Hagen-Poiseuille's result when the water saturation is 1. The results are fully matched, which is sufficient to verify the correctness of the single capillary model in this paper.

Then on this basis, we will consider the single-nanopore flow rate of effective slip length and the two-phase effective permeability and absolute permeability calculated by the generalized Darcy's law with the gas flow obtained when the gas saturation is 1. Then calculate the two-phase relative permeability according to the definition of relative permeability and compare it with the G. Lei model (Lei et al., 2015) considering the effective slip length (L_{se}) and slip length (L_{s}), as shown in Figure 4B As shown. From Figure 4B, it can get the conclusion that for the two-phase relative permeability, the effective slip length (L_{se}) and slip length (L_{s}) are considered to match the G. Lei model better. Therefore, it can prove the correctness of the model in this paper.

4.1.2 Multiple capillary nanopore relative permeability comparison

In this section, the effective slip length (L_{se}), slip length (L_{s}), and slip length (L_{s} = 0) under the condition of τ_{w}=τ_{g}=1 will be considered in comparison with the widely accepted Monte Carlo calculation model (Xu et al., 2013) and Abaci experimental data model (Abaci et al., 1992)

TABLE 1 Simulation basic data table.

Parameter name	Symbol	unit	Numerical value
Fluid type	—	—	Water and gas
Porosity	ϕ	%	4.83
Permeability coefficient	S	-	0.04
Porosity coefficient	q	-	0.08
Irreducible water saturation	S_{wi}	-	0.1
Boundary liquid film thickness	δ	nm	0.2
Shale nanopore maximum diameter	λ_{max}	nm	800
Shale nanopore minimum diameter	λ_{min}	nm	5
Formation pressure	p	MPa	40
Confined pressure	p_c	MPa	50
Formation temperature	T	K	300
Water viscosity	μ_W	Pa·s	—
Effective viscosity	μ_d	Pa·s	—

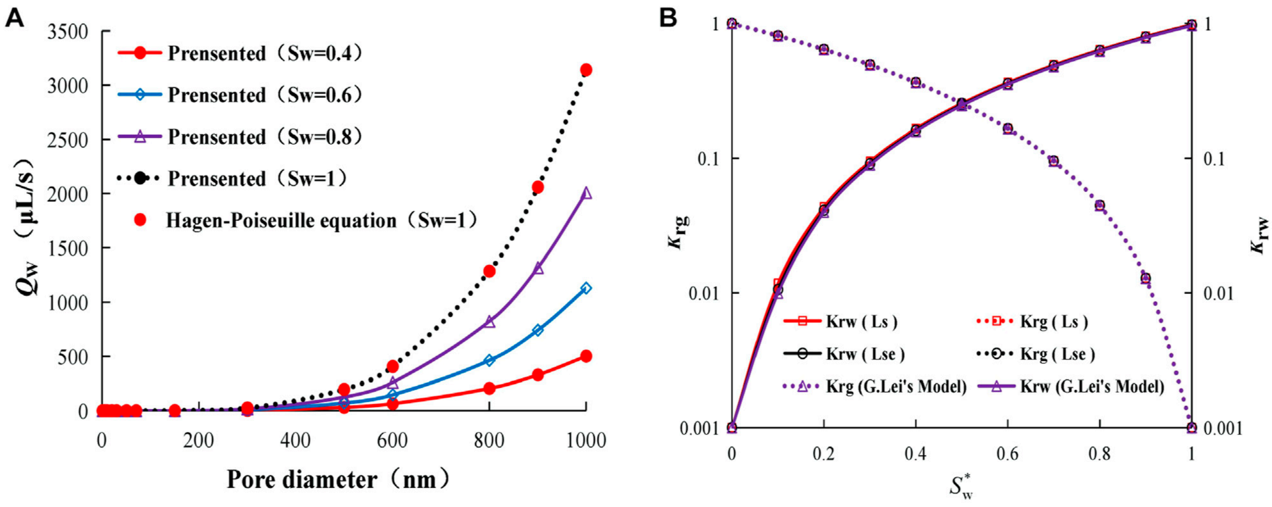

Verification with Hagen-Poiseuille Equation.

Verification with G.Lei model.

FIGURE 4
Single capillary nanopore relative permeability comparison.

parameters. In the experiments of Abaci et al. (Abaci et al., 1992), A relative permeability test was performed on anisotropy sandstones with a porosity of 33%. In the new model we proposed, the other parameters were obtained in the same way as the Monte Carlo calculation model (Xu et al., 2013) and the Abaci experimental model (Abaci et al., 1992) to obtain the results shown in Figure 5 below.

From Figure 5A, it can be seen that for the two-phase relative permeability, the model (considering effective slip, L_{se}) for the gas phase's relative permeability is in good agreement with the Abaci experimental data model (Abaci, Edwards et al., 1992) at $S_w = 0.28–0.73$. Well, there is a slight difference between S_w <0.28 and S_w> 0.73, and the relative permeability of the water phase gradually changes from inorganic (wetting angle = 0°, 40°, 80°) to organic matter (wetting angle = 120°). It gradually becomes larger due to the increase of the effective slip length, which coincides well with the Abaci experimental data (Abaci et al., 1992) when the wetting angle is equal to 80°, which shows that the rock sample selected in the Abaci experiment (Abaci et al., 1992) is hydrophilic in the middle, and it also proves the presented

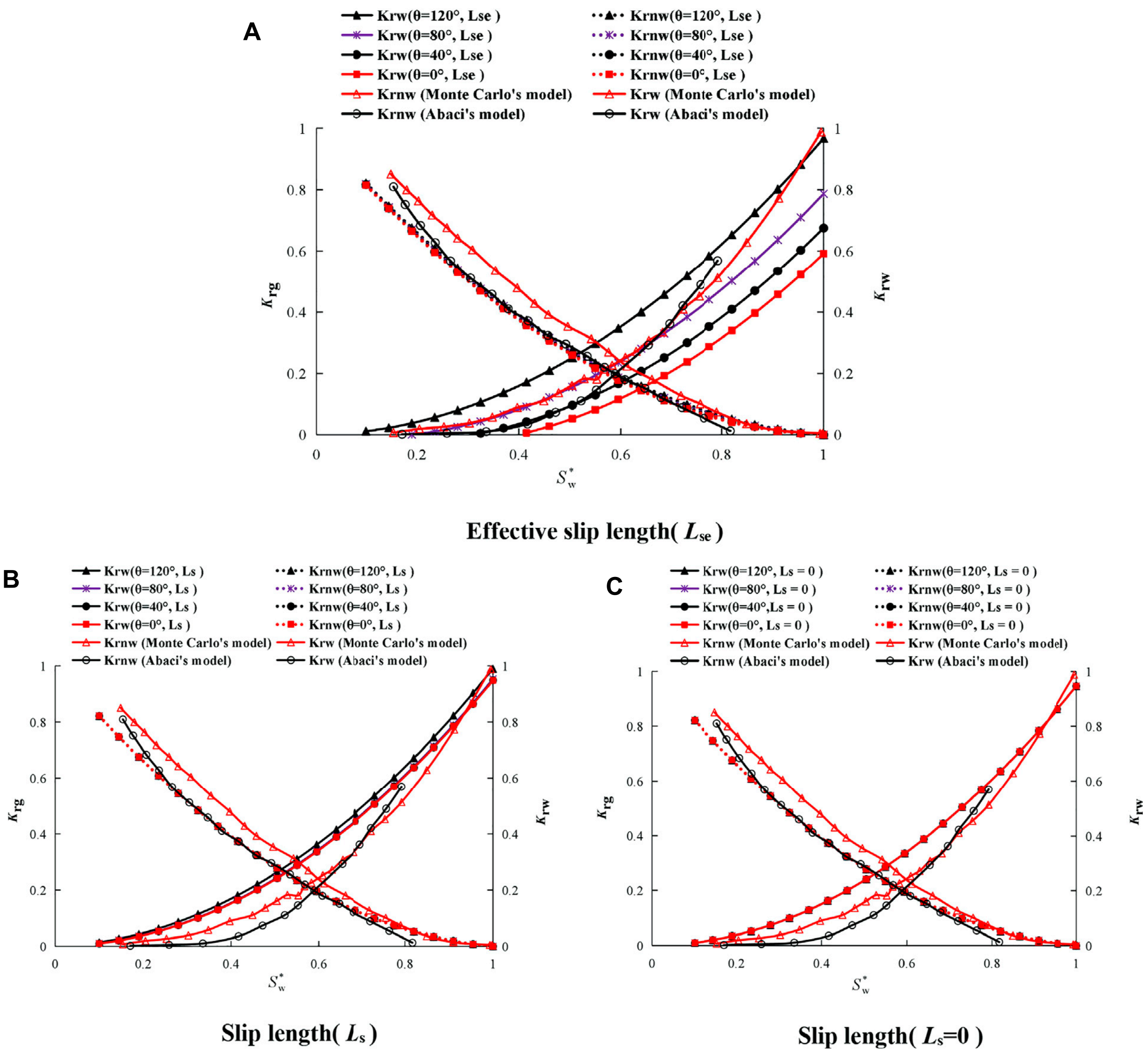

FIGURE 5
Multiple capillary nanopore relative permeability compared with Monte Carlo's and Abaci's model.

model is experimentally correct. Moreover, the results also show that the Monte Carlo model and Abaci experimental model studied by previous researchers are special cases of the proposed fractal model, which indicate that the proposed fractal model has obvious advantages.

However, the reason why the model in this paper (L_{se}, Figure 4A) and (L_s, Figure 4B) shows the water phase's relative permeability is not equal to 1 or 0 under different wetting angles when the water saturation is 1 or 0–0.15; but the model in this paper ($L_s = 0$, Figure 4C) does equal to 1 or 0 when the water saturation is 1 or 0. Because when the water saturation is small and the rock is hydrophobic, on the one hand, the natural gas channel compresses the flow of the bulk water channel, and on the other hand, due to the strong water phase viscosity and boundary water viscosity Water absorption causes the effective slip length to be less than 0; when the water saturation is 1, the effective slip length is less than 0 when the rock is hydrophobic and the water phase's relative permeability is less than 1, and when the rock is hydrophilic, the effective slip length is greater than 0. As a result, the water phase's relative permeability is greater than one.

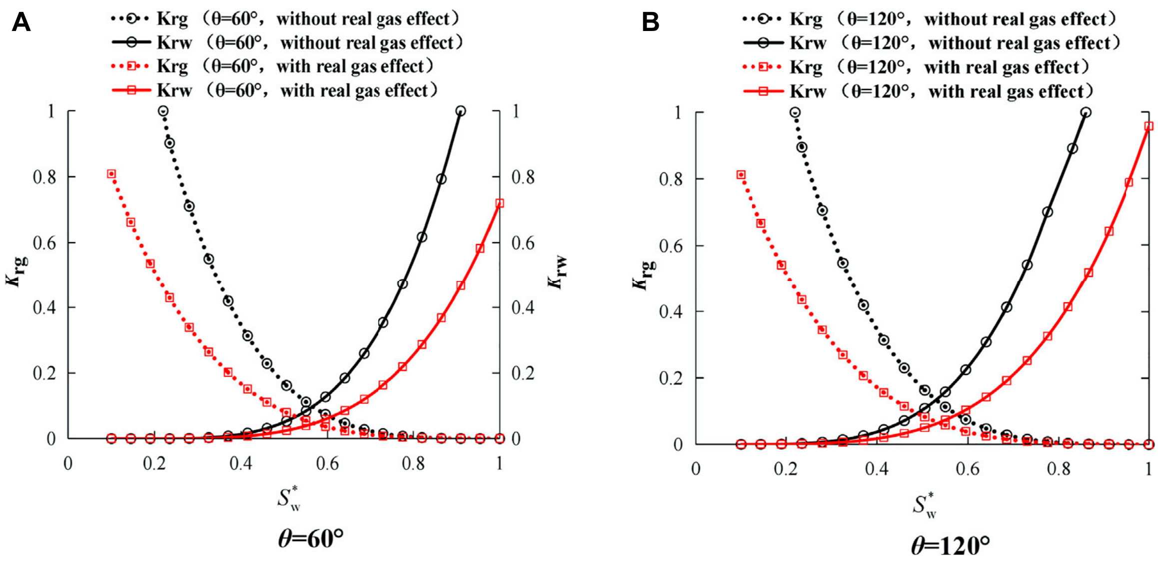

FIGURE 6
Influence of real gas effect on the two-phase relative permeability in porous media.

5 Results and discussion

5.1 Real gas effect

We will analyze the model in this paper considering the real gas effect and analyze it without considering the real gas effect (natural gas viscosity is 0.018 mPa s), as shown in Figure 6 below.

It can be seen from Figure 6 that when the wetting angles are 60° and 120°, the greater the water saturation, the gas phase's relative permeability decreases exponentially from 1 to 0, while the water phase's relative permeability increases exponentially from 0 to 1. The comparison of the relative permeability of gas and water with and without considering the real gas effect shows that the real gas effect has great effect on the two-phase relative permeability. In detail, the gas phase's relative permeability with the real gas effect is 0.52 times (θ=60°) and 0.51 times (θ=120°) that of the gas phase's relative permeability without the real gas effect under the condition of $S_w^* = 0.235$. But the water phase's relative permeability with the real gas effect is 0.53 times (θ=60°) and 0.53 times (θ=120°) that of the water phase's relative permeability without the real gas effect under the condition of $S_w^* = 0.235$. Therefore, it can be seen that the real gas effect is an important factor that cannot be ignored.

5.2 Gas viscosity effect

When two-phase fluid flows in the multi-scale pore structure of shale, natural gas viscosity is an important parameter for obtaining the two-phase relative permeability. Therefore, it is necessary to analyze the effect of natural gas viscosity on the gas-water two-phase relative permeability. The organic wetting angle is 120°, and the inorganic wetting angle is 60°. As shown in Figure 7 below.

It can be observed the phenomenon from Figure 7 that the viscosity of natural gas has an influence on the two-phase relative permeability in inorganic and organic pores. In detail, the relative permeability of gas phase ($\mu_g = 0.05\ \mathrm{mPa \cdot s}$) is 0.64 times ($\theta$=60° and θ=120°) that of the relative permeability of gas phase ($\mu_g = 0.018\ \mathrm{mPa \cdot s}$) under the condition of $S_w^* = 0.235$. However, the relative permeability of water phase ($\mu_g = 0.05\ \mathrm{mPa \cdot s}$) is 0.61 times ($\theta$=60° and θ=120°) that of the relative permeability of water phase ($\mu_g = 0.018\ \mathrm{mPa \cdot s}$) under the condition of $S_w^* = 0.235$. With the increase of the viscosity of natural gas, the relative permeability of gas phase and water phase decreases gradually. This is because with the increase of natural gas viscosity, the shear stress between gas phase and water phase and between gas phase and gas phase increases, and the flow channel of gas phase compressed water phase becomes more significant, showing the increase of flow resistance, thus resulting in the decrease of the relative permeability of two phases.

5.3 Structural parameters

In porous media, there are pore fractal dimensions (D_f) and tortuosity fractal dimensions (D_T) to characterize porous media. Therefore, the influence of structural parameters on the two-

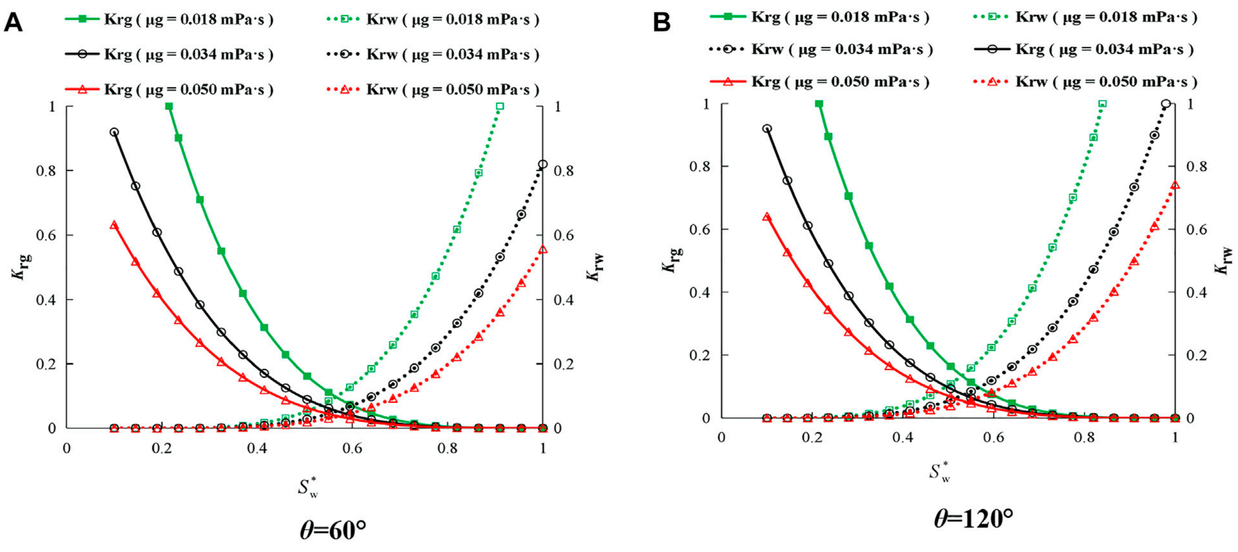

FIGURE 7
Effect of natural gas viscosity on the two-phase relative permeability.

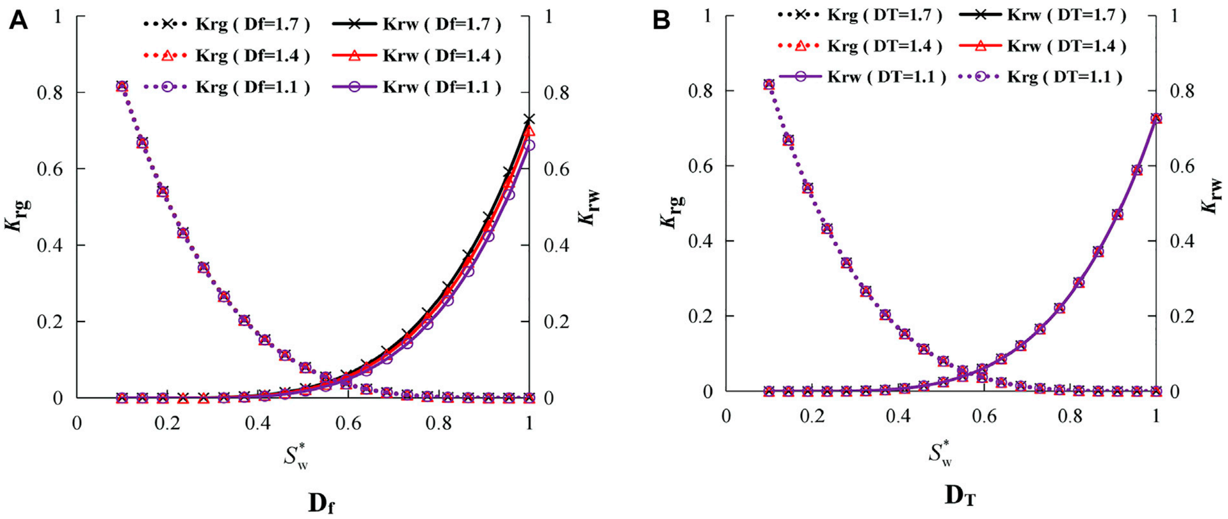

FIGURE 8
Effect of structural parameters on the two-phase relative permeability.

phase relative permeability cannot be ignored, and it is necessary to analyze and study it. Taking an inorganic wetting angle of 60°, the parameter analysis is shown in Figure 8 below.

It can be seen from Figure 8 that the structural parameters have little effect on the gas phase's relative permeability, but have a greater effect on the water phase's relative permeability. With the gradual increase of D_f, the water phase relative permeability gradually increases (Song et al., 2020), and as the D_T gradually increases, the tortuosity fractal dimension has little effect on the water phase's relative permeability.

5.4 Variable water viscosity

In actual shale reservoirs, the water phase viscosity varies with the diameter of the pipe and is close to the bulk water

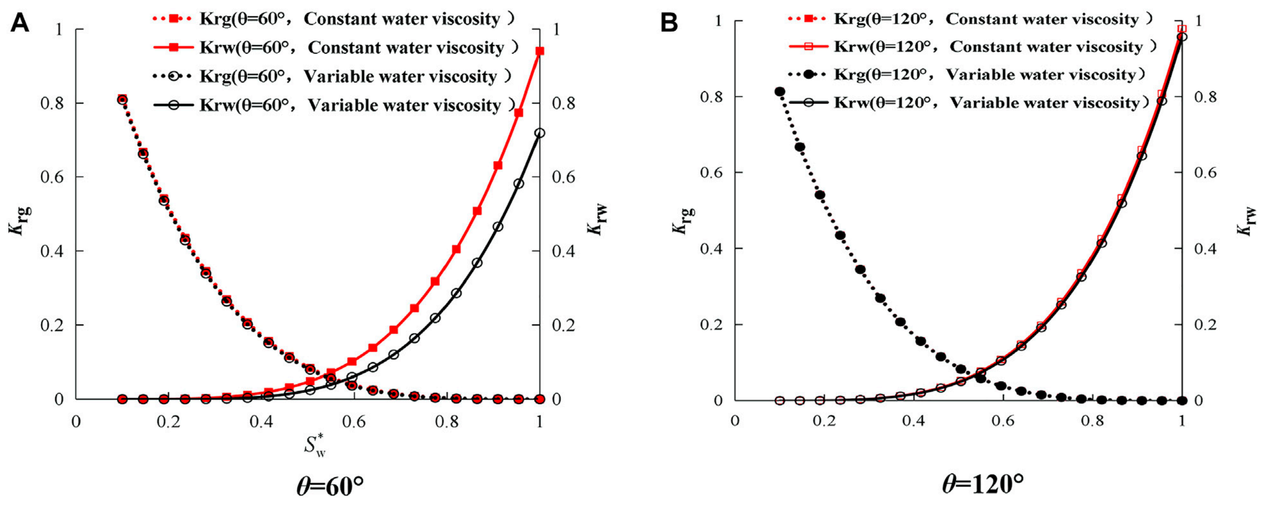

FIGURE 9
Effect of variable water phase viscosity on the two-phase relative permeability in porous media.

viscosity and boundary water viscosity. And the viscosity is also affected by the wetting angle. This effect is called the variable water phase viscosity effect. The opposite of this effect is the constant water phase viscosity, that is, the water phase viscosity is equal to the bulk water viscosity (μ_b). Therefore, it is very important to analyze the effect of the model with variable water phase viscosity and constant water phase viscosity on the two-phase relative permeability. As shown in Figure 9 below.

It can be seen from Figure 9 that variable water phase viscosity has a greater effect on the inorganic pores and a smaller effect on the organic pores on the two-phase relative permeability in the porous medium compared to constant water phase viscosity at a wetting angle equal to 60°or 120°. When the wetting angle is equal to 120°, the viscosity of the water phase has little effect on the two-phase relative permeability in the porous medium. This is because the rock is hydrophilic when the wetting angle is equal to 60°, and the rock is hydrophobic when the wetting angle is equal to 120°. In addition, it is easy to see that when the water saturation is 1 or 0–0.2, the relative permeability of variable water phase viscosity is less than 1 or 0 at a wetting angle equal to 60°, but the water phase does not appear this case at a wetting angle equal to 120°. This is because the rock is hydrophilic at a wetting angle equal to 60°, and the water phase viscosity and boundary water viscosity cause stronger water absorption effect which leading to the effect of effective slip length less than 0 is greater than the natural gas channel compressing the flow of the bulk water channel; while the water saturation is 1 or 0, the relative permeability of variable water phase viscosity is exactly equal 1 or 0 at a wetting angle equal to 120°, it is because the wetting angle is equal to 120°, the rock is hydrophobic, and the water phase viscosity and boundary water viscosity strongly absorb water effect, which results in the effect that the effective slip length is less than 0, which exactly offsets the natural gas channel compressing the bulk water channel flow. Therefore, the viscosity of water in porous media in this model varies with pipe diameter and the water phase viscosity is the area weighting of bulk water viscosity and boundary water viscosity which is more in line with reality.

5.5 Irreducible water saturation

In actual shale reservoirs, the reservoir has irreducible water saturation in the nanopores due to the hydrophilic rocks, irregular pits, and the formation of water films. Therefore, the influence of this model considering irreducible water saturation on the two-phase relative permeability when S_{wi}=0.1, 0.3 and 0.5 cannot be ignored, and it is necessary to analyze and study it. Take the inorganic wetting angle as 60°for parameter analysis, as shown in Figure 10A, and the organic wetting angle as 120° for parameter analysis, as shown in Figure 10B.

It can be seen from Figure 10 that the irreducible water saturation has a significant effect on the gas phase's relative permeability and the water phase's relative permeability. With the increase of irreducible water saturation, the water phase's relative permeability gradually decreases. This is because with the increase of irreducible water saturation, the space of the mobile water phase in the rock nanopores is restricted, causing the water flow rate to gradually decrease.

It is worth noting that for the irreducible water saturation of 0.1, 0.3, 0.5 in inorganic wetting angle as 60°, the relative permeability of the intersection point of the corresponding water phase and gas phase is 0.048 (S_w=0.57), 0.05 (S_w=0.67), 0.057 (S_w=0.76); but for the irreducible water saturation of 0.1,

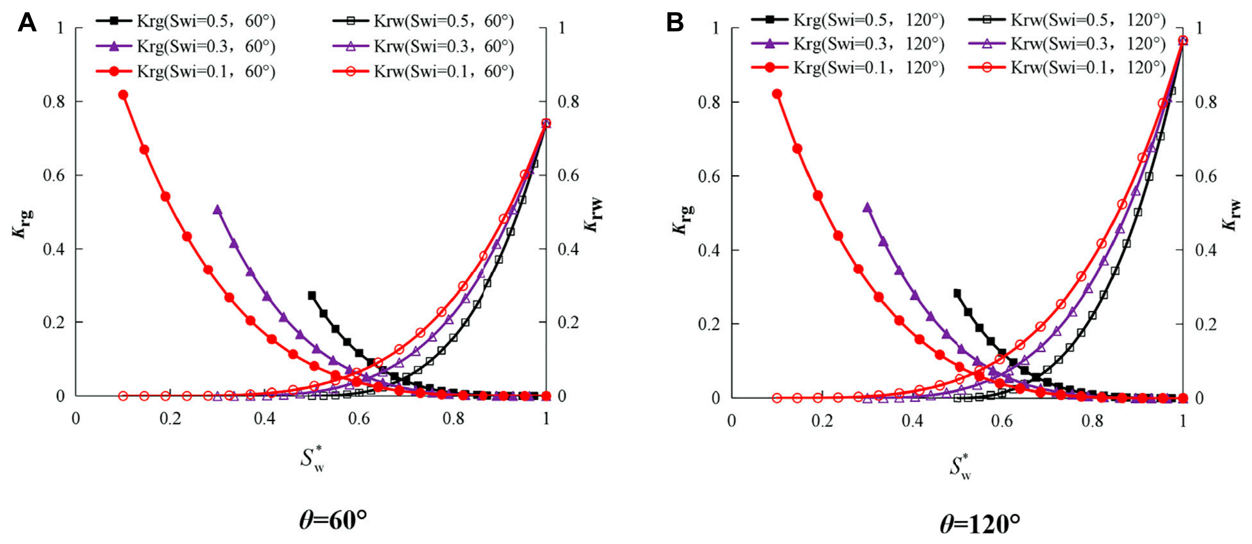

FIGURE 10
Effect of irreducible water saturation on the two-phase relative permeability.

0.3, 0.5 in organic wetting angle as 120°, the relative permeability of the intersection point of the corresponding water and gas phases is 0.063 (S_w=0.53), 0.064 (S_w=0.63), 0.067 (S_w=0.74); it can be drawn the conclusion that the relative permeability of the intersection point in the organic pore is higher than that of the inorganic porous, but the water saturation at the intersection is less than that of inorganic pores. This is because organic pores are hydrophobic, and capillary force acts as a driving force to increase the water phase's flow pressure, causing the relative permeability of the intersection point of organic pores to be greater than that of inorganic pores and the water saturation of the intersection point is smaller than that of inorganic pores; while inorganic pores have hydrophilicity, capillary force acts as resistance to reduce the water phase's flow pressure, causing the relative permeability of the intersection of inorganic pores to be smaller than that of organic pores and the water saturation of the intersection point to be greater than that of organic pores.

5.6 Wetting angle

The shale porous medium is divided into organic pores and inorganic pores according to the wetting angle of organic pores >90°and inorganic pores <90°. The effective slip length and slip length under different wetting angles are quite different, so it is vital to analyze and consider the influence of wetting angle on the two-phase relative permeability. In this section, the effective slip length (L_{se}) will be considered in comparison with slip length (L_s) and slip length (L_s = 0) in organic and inorganic pores, to analyze the effect of wetting angle on the two-phase relative permeability. Take water saturation of 0.4 and 0.5 for analysis.

From Figure 11, it can be observed the phenomenon that with the increase of the wetting angle, the water phase's relative permeability of the proposed model (L_{se}) in organic matter is slowly increased when the water saturation is 0.4 between 90° and 150°. When the angle is larger than 150°, the water phase's relative permeability increases sharply due to the sharp increase of the effective slip length. However, for inorganic matter, the larger the wetting angle, the smaller the water phase's relative permeability, but the smaller the effect on the gas phase's relative permeability. This is because as the wetting angle increases, the hydrophobic properties of organic matter become stronger, while the hydrophilic properties of inorganic matter become weaker and gradually transition to hydrophobic properties.

In addition, when the water saturation of organic matter is 0.4, the water phase's relative permeability curve and the gas phase relative permeability curve intersect at a wetting angle of 150°, and when the water saturation of organic matter is 0.5, the water phase's relative permeability curve and the gas phase relative permeability curves intersect at a wetting angle of 130°. This is because the larger the water saturation, the larger the water phase flow channel, and the smaller the boundary water viscosity (μ_{rw}) for the area weighting that considers the water phase viscosity (μ_d) as the bulk water viscosity and the boundary water viscosity. It is necessary to reduce the wetting angle (Eq. 41,$\frac{\mu_{rw}}{\mu_w} = -3.24\theta + 3.25$) to increase the equivalent effect of boundary water viscosity.

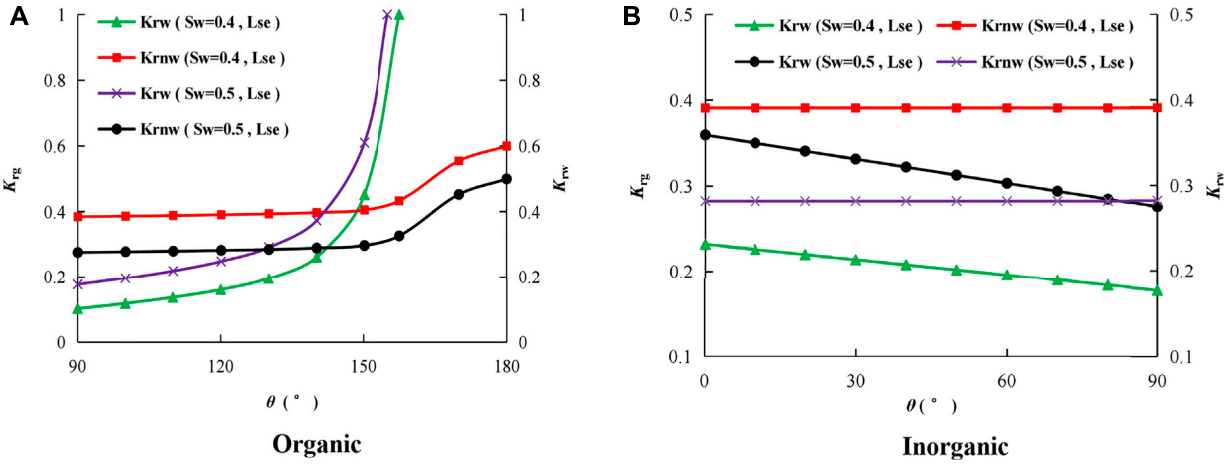

FIGURE 11
Effect of different wetting angles on the two-phase relative permeability.

6 Conclusion

Based on fractal theory, this paper establishes a fractal model that can accurately calculate the two-phase relative permeability in the multi-scale pore structure of shale. Under the same geological parameters, the proposed model is in good agreement with the mechanism model of Hagen-Poiseuille and G. Lei et al., which proves the proposed model correct. Unlike the earlier models, the proposed model considers the three-layer flow composition of nanopore pore boundary layer, bulk water and bulk gas, the difference between organic pores and inorganic pores is affected and controlled by wettability and effective slip length, the viscosity changes with the diameter of the pipe, the stress dependance effect, confined gas viscosity and real gas effect.

The results demonstrate that the gas phase's relative permeability gradually decreases with the increase of water saturation; the water phase's relative permeability gradually increases with the increase of water saturation. Generally, the relative permeability of the intersection point in the organic pore is higher than that of the inorganic porous, but the water saturation at the intersection is less than that of inorganic pores. In real situations, the final relative permeability value is determined by the interplay of the effective stress and slip flow effects. Notably, with the increase of the wetting angle, the water phase's relative permeability of the model (L_{se}) in this paper is slowly increased when the water saturation is 0.4 between 90° and 150°. When the angle is larger than 150°, the water phase's relative permeability increases sharply due to the sharp increase of the effective slip length.

Data availability statement

The original contributions presented in the study are included in the article/supplementary material, further inquiries can be directed to the corresponding author.

Author contributions

LF is responsible for the construction of the overall paper structure, ZF formulates research ideas, technical routes, model establishment and paper writing, SY is responsible for literature research, ZY is responsible for model solving, code writing and paper writing.

Funding

This work was supported by Open Experiment of National Energy Shale Oil Research and Development Center “Geology-engineering integration sweet spot evaluation and intelligent fracturing control technology for continental shale oil” (No. 33550000-21-2C0613-0292).

Conflict of interest

The authors declare that the research was conducted in the absence of any commercial or financial relationships that could be construed as a potential conflict of interest.

Publisher's note

References

Abaci, S., Edwards, J. S., and Whittaker, B. N. (1992). Relative permeability measurements for two phase flow in unconsolidated sands. *Mine Water Environ.* 11 (2), 11–26. doi:10.1007/bf02919583

Adler, P. M., and Brenner, H. (1988). Multiphase flow in porous media. *Annu. Rev. Fluid Mech.* 20, 35–59. doi:10.1146/annurev.fl.20.010188.000343

Bear & Jacob (1972). *Dynamics of fluids in porous media[M].* American Elsevier Pub Co, p738.

Berkowitz, B. (2002). Characterizing flow and transport in fractured geological media: A review. *Adv. Water Resour.* 25 (8/12), 861–884. doi:10.1016/s0309-1708(02)00042-8

Bocquet, L., and Tabeling, P. (2014). Physics and technological aspects of nanofluidics. *Lab. Chip* 14 (17), 3143–3158. doi:10.1039/c4lc00325j

Burdine, N. T. (1953). Relative permeability calculations from pore size distribution data. *J. Petroleum Technol.* 98 (3), 71–78. doi:10.2118/225-g

Carman, P. C. (1937). Fluid flow through granular beds[J]. *Trans. Inst. Chem. Eng.* 15, 150–166.

Christine, Krohn & E. (1988). Fractal measurements of sandstones, shales, and carbonates[J]. *J. Geophys. Res. Solid Earth* 93 (B4), 3297–3305.

Civan, F. (2010). Effective correlation of apparent gas permeability in tight porous media. *Transp. Porous Media* 82 (2), 375–384. doi:10.1007/s11242-009-9432-z

Clennell, M. B. (1997). Tortuosity: A guide through the maze. *Geol. Soc. Lond. Special Publ.* 122 (1), 299–344. doi:10.1144/gsl.sp.1997.122.01.18

Cottin-Bizonne, C., Barrat, J. L., Bocquet, L., and Charlaix, E. (2003). Low-friction flows of liquid at nanopatterned interfaces. *Nat. Mat.* 2 (4), 237–240. doi:10.1038/nmat857

Curtis, M. E., Sondergeld, C. H., Ambrose, R. J., and Rai, C. S. (2012). Microstructural investigation of gas shales in two and three dimensions using nanometer-scale resolution imaging. *Am. Assoc. Pet. Geol. Bull.* 96 (4), 665–677. doi:10.1306/08151110188

Dong, J. J., Hsu, J. Y., Wu, W. J., Shimamoto, T., Hung, J. H., Yeh, E. C., et al. (2010). Stress-dependence of the permeability and porosity of sandstone and shale from TCDP Hole-A. *Int. J. Rock Mech. Min. Sci. (1997).* 47 (7), 1141–1157. doi:10.1016/j.ijrmms.2010.06.019

Feibelman, P. J. (2013). Viscosity of ultrathin water films confined between aluminol surfaces of kaolinite: *Ab initio* simulations. *J. Phys. Chem. C* 117 (12), 6088–6095. doi:10.1021/jp312152h

Feng, D., Li, X., Wang, X., Li, J., Zhang, T., Sun, Z., et al. (2018). Capillary filling of confined water in nanopores: Coupling the increased viscosity and slippage. *Chem. Eng. Sci.* 186, 228–239. doi:10.1016/j.ces.2018.04.055

Fradin, C., Braslau, A., Luzet, D., Smilgies, D., Alba, M., Boudet, N., et al. (2000). Reduction in the surface energy of liquid interfaces at short length scales. *Nature* 403 (6772), 871–874. doi:10.1038/35002533

Gad-El-Hak, M. (2006). Gas and liquid transport at the microscale. *Heat. Transf. Eng.* 27 (4), 13–29. doi:10.1080/01457630500522305

Granick, S., Zhu, Y., and Lee, H. (2003). Slippery questions about complex fluids flowing past solids. *Nat. Mat.* 2 (4), 221–227. doi:10.1038/nmat854

Hu, X., and Huang, S. (2017). *Physics of Petroleum reservoirs[M].* Springer Berlin Heidelberg, 1–506.

Jackson, S. J., Agada, S., Reynolds, C. A., and Krevor, S. (2018). Characterizing drainage multiphase flow in heterogeneous sandstones. *Water Resour. Res.* 54 (4), 3139–3161. doi:10.1029/2017wr022282

Katz, A. J., and Thompson, A. H. (1985). Fractal sandstone pores: Implications for conductivity and pore formation. *Phys. Rev. Lett.* 54 (12), 1325–1328. doi:10.1103/physrevlett.54.1325

Laliberté, M. (2007). Model for calculating the viscosity of aqueous solutions. *J. Chem. Eng. Data* 52 (4), 321–335. doi:10.1021/je0604075

Lei, G., Dong, P. C., Mo, S. Y., Gai, S. H., and Wu, Z. S. (2015). A novel fractal model for two-phase relative permeability in porous media[J]. *Fractals* 23 (02), 1550017. doi:10.1142/s0218348x15500176

Li, K. (2010). More general capillary pressure and relative permeability models from fractal geometry. *J. Contam. Hydrology* 111 (1), 13–24. doi:10.1016/j.jconhyd.2009.10.005

Li, T. D., Gao, J., Szoszkiewicz, R., Landman, U., and Riedo, E. (2007). Structured and viscous water in subnanometer gaps. *Phys. Rev. B* 75 (11), 115415–115416. doi:10.1103/physrevb.75.115415

Liu, L., Sun, Q., Wu, N., Liu, C., Ning, F., and Cai, J. (2021). Fractal analyses of the shape factor in kozeny–carman equation for hydraulic permeability in hydrate-bearing sediments. *Fractals* 29 (07), 2150217. doi:10.1142/s0218348x21502170

Liu, Y., and Yu, B. (2007). A fractal model for relative permeability of unsaturated porous media with capillary pressure effect[J]. *Fractals* 15 (03), 217–222. doi:10.1142/s0218348x07003617

Lorenz, U. J., and Zewail, A. H. (2014). Observing liquid flow in nanotubes by 4D electron microscopy. *Science* 344 (6191), 1496–1500. doi:10.1126/science.1253618

Maali, A., Cohen-Bouhacina, T., and Kellay, H. (2008). Measurement of the slip length of water flow on graphite surface. *Appl. Phys. Lett.* 92 (5), 053101. doi:10.1063/1.2840717

Mashl, R. J., R Aluru, S. Joseph &N., Aluru, N. R., and Jakobsson, E. (2015). Anomalously immobilized Water: A new water phase induced by confinement in nanotubes. *Nano Lett.* 3 (5), 589–592. doi:10.1021/nl0340226

Matyka, M., Khalili, A., and Koza, Z. (2008). Tortuosity-porosity relation in porous media flow. *Phys. Rev. E* 78 (2), 026306. doi:10.1103/physreve.78.026306

Nair, H. A., and Wu, P. N. (2012). Unimpeded permeation of water through helium-leak-tight graphene-based membranes[J]. *Science* 335 (6067), 442–444. doi:10.1126/science.1211694

Raviv, U., Laurat, P., and Klein, J. (2001). Fluidity of water confined to subnanometre films. *Nature* 413 (6851), 51–54. doi:10.1038/35092523

Roy, S., Raju, R., Chuang, H. F., Cruden, B. A., and Meyyappan, M. (2003). Modeling gas flow through microchannels and nanopores. *J. Appl. Phys.* 93 (8), 4870–4879. doi:10.1063/1.1559936

Shaat & Mohamed (2017). Viscosity of water interfaces with hydrophobic nanopores: Application to water flow in carbon nanotubes. *Langmuir* 33, 12814–12819. doi:10.1021/acs.langmuir.7b02752

Sone, Y., Takata, S., and Ohwada, T. (1990). Numerical analysis of the plane Couette flow of a rarefied gas on the basis of the linearized Boltzmann equation for hard-sphere molecules[J]. *Eur. J. Mech. B/fluids* 9 (3), 273–288. doi:10.1002/ctpp.2150300611

Song, W., Yao, J., Li, Y., Sun, H., Wang, D., and Yan, X. (2020). GAS–WATER relative permeabilities fractal model in dual-wettability multiscale shale porous media during injected water spontaneous imbibition and flow back process. *Fractals* 28 (07), 2050103. doi:10.1142/s0218348x20501030

Sun, X., and Ripepi, Y. Yao &N. (2018). A novel method for gas–water relative permeability measurement of coal using NMR relaxation[J]. *Transp. Porous Media* 124 (1), 1–18. doi:10.1007/s11242-018-1053-y

Tan, X. H., Liu, J. Y., Li, X. P., Zhang, L. H., and Cai, J. (2015). A simulation method for permeability of porous media based on multiple fractal model. *Int. J. Eng. Sci.* 95, 76–84. doi:10.1016/j.ijengsci.2015.06.007

Tan, X. H., Li, X. P., Liu, J. Y., Zhang, G. D., and Zhang, L. H. (2014). Analysis of permeability for transient two-phase flow in fractal porous media. *J. Appl. Phys.* 115 (11), 113502. doi:10.1063/1.4868596

Thomas, J. A., and Mcgaughey, A. J. H . (2008). Reassessing fast water transport through carbon nanotubes. *Nano Lett.* 8 (9), 2788–2793. doi:10.1021/nl8013617

Thompson, P. D., and Robbins, M. M. (1990). Origin of stick-slip motion in boundary lubrication. *Science* 250 (4982), 792–794. doi:10.1126/science.250.4982.792

Tran, H., and Sakhaee-Pour, A. (2017). Viscosity of shale gas. *Fuel* 191, 87–96. doi:10.1016/j.fuel.2016.11.062

Tretheway, D. C., and Meinhart, C. D. (2002). Apparent fluid slip at hydrophobic microchannel walls. *Phys. Fluids* 14 (3), L9–L12. doi:10.1063/1.1432696

Vinogradova, O. I., Koynov, K., Best, A., and Feuillebois, F. (2009). Direct measurements of hydrophobic slippage using double-focus fluorescence cross-correlation. *Phys. Rev. Lett.* 102 (11), 118302. doi:10.1103/physrevlett.102.118302

Wang, F., Jiao, L., Lian, P., and Zeng, J. (2018). Apparent gas permeability, intrinsic permeability and liquid permeability of fractal porous media: Carbonate rock study with experiments and mathematical modelling[J]. *J. Petroleum ence Eng.* 173. doi:10.1016/j.petrol.2018.10.095

Wang, F., Liu, Z., Jiao, L., Wang, C., and Guo, H. (2017). A fractal permeabily model coupling boundary-layer effect for tight oil reservoirs[J]. *Fractals* 25 (3), 1750042. doi:10.1142/s0218348x17500426

Wang, Q., and Cheng, Z. (2019). A fractal model of water transport in shale reservoirs[J]. *Chem. Eng. Sci.*. doi:10.1016/j.ces.2018.12.042

Werder, T., Walther, J. H., Jaffe, R. L., et al. (2002). Molecular dynamics simulation of contact angles of water droplets in carbon nanotubes[J]. *Nano Lett.* 1 (12). doi:10.1021/nl015640u

Wheatcraft, S. W., Sharp, G. A., and Tyler, S. W. (1991). Fluid flow and solute transport in fractal heterogeneous porous media[J]. *Transport processes in porous media*. Editors J. Bear and M. Y. Corapcioglu . Dordrecht: Springer Netherlands, 695–722. doi:10.1007/978-94-011-3628-0_14

Wu, K., Chen, Z., Li, J., Li, X., Xu, J., and Dong, X. (2017). Wettability effect on nanoconfined water flow. *Proc. Natl. Acad. Sci. U. S. A.* 114 (13), 3358–3363. doi:10.1073/pnas.1612608114

Wu, K., Chen, Z., Li, X., Guo, C., and Wei, M. (2016). A model for multiple transport mechanisms through nanopores of shale gas reservoirs with real gas effect–adsorption-mechanic coupling. *Int. J. Heat Mass Transf.* 93 (2), 408–426. doi:10.1016/j.ijheatmasstransfer.2015.10.003

Xu, J., Chen, Z., Wu, K., Li, R., Liu, X., and Zhan, J. (2019). On the flow regime model for fast estimation of tight sandstone gas apparent permeability in high-pressure reservoirs[J].. *Energy sources, Part A: Recovery, utilization, and environmental effects*, 1–12. doi:10.1080/15567036.2019.1687625

Xu, P., Qiu, S., Yu, B., and Jiang, Z. (2013). Prediction of relative permeability in unsaturated porous media with a fractal approach. *Int. J. Heat. Mass Transf.* 64 (9), 829–837. doi:10.1016/j.ijheatmasstransfer.2013.05.003

Yang, Y., Wang, K., Zhang, L., Sun, H., Zhang, K., and Ma, J. (2019). Pore-scale simulation of shale oil flow based on pore network model. *Fuel* 251, 683–692. doi:10.1016/j.fuel.2019.03.083

Yu, B., J Li, Z. Li, and Zou, M. (2003). Permeabilities of unsaturated fractal porous media. *Int. J. Multiph. Flow* 29 (10), 1625–1642. doi:10.1016/s0301-9322(03)00140-x

Yu, B., and Liu, W. (2010). Fractal analysis of permeabilities for porous media. *AIChE J.* 50 (1), 46–57. doi:10.1002/aic.10004

Yu, B., and Ping, C. (2002). A fractal permeability model for bi-dispersed porous media. *Int. J. Heat. Mass Transf.* 45 (14), 2983–2993. doi:10.1016/s0017-9310(02)00014-5

Zeng, F., Zhang, Y., Guo, J., Ren, W., Jiang, Q., and Xiang, J. (2020). Prediction of shale apparent liquid permeability based on fractal theory. *Energy fuels*. 34 (6), 6822–6833. doi:10.1021/acs.energyfuels.0c00318

Zhang, T., Li, X., Sun, Z., Feng, D., Miao, Y., Li, P., et al. (2017). An analytical model for relative permeability in water-wet nanoporous media. *Chem. Eng. Sci.* 174, 1–12. doi:10.1016/j.ces.2017.08.023

Frontiers in Earth Science

TYPE Original Research
PUBLISHED 23 September 2022
DOI 10.3389/feart.2022.1026551

OPEN ACCESS

EDITED BY
Jinze Xu,
University of Calgary, Canada

REVIEWED BY
Ran Li,
University of Calgary, Canada
Fanhui Zeng,
Southwest Petroleum University, China

*CORRESPONDENCE
Haiyang Wang,
wang_hai_yang@126.com

SPECIALTY SECTION
This article was submitted to Environmental Informatics and Remote Sensing,
a section of the journal
Frontiers in Earth Science

RECEIVED 24 August 2022
ACCEPTED 05 September 2022
PUBLISHED 23 September 2022

CITATION
Liu E, Yao T, Qiao L, Li J, Wang H and Gao Q (2022), Research on the propagation mechanism of hydraulic fractures in infill horizontal wells.
Front. Earth Sci. 10:1026551.
doi: 10.3389/feart.2022.1026551

Research on the propagation mechanism of hydraulic fractures in infill horizontal wells

Erhu Liu[1], Tingwei Yao[2], Lianlian Qiao[3], Jing Li[3], Haiyang Wang[4]* and Qian Gao[4]

[1]Gas Production Plant 2 of Yanchang Gasfield, Shaanxi Yanchang Petroleum (Group) Co., Ltd., Yan'an, China, [2]Xi'an Changqing Chemical Group Co., Ltd., Xi'an, China, [3]Research Center of Oil and Gas Exploration Company, Shaanxi Yanchang Petroleum (Group) Co., Ltd., Yan'an, China, [4]School of Petroleum Engineering, Xi'an Shiyou University, Xi'an, China

In recent years, infill horizontal well technology has been used to develop oil and gas in the remaining oil areas of unconventional low-permeability reservoirs. However, the initial fractures in parent wells will affect the hydraulic fractures formed by fracturing infilling horizontal wells. The interaction mechanisms between initial fractures and artificial fractures in infill horizontal wells are still unclear. Combined with the boundary element method and the maximum circumferential tensile stress criterion, a numerical model of hydraulic fracturing that can simulate the evolution of fracture trajectory and stress field was established. The analytical solution of the hydraulic fracture-induced stress field was used to verify the accuracy of the model. Using this model, propagation of hydraulic fractures in infill horizontal wells under different conditions was analyzed. Simulation results show that both the fracture spacing and well spacing have a significant impact on the propagation trajectory of hydraulic fractures in infill horizontal wells. The shorter the fracture spacing and well spacing is, the stronger the inter-fracture stress interference between the initial fractures and hydraulic fractures is. Reasonable fracture spacing and well spacing can enhance the induced stress field and form a complex fracture network in the reservoir. Too small well spacing may cause artificial fractures to communicate with initial fractures, thereby reducing hydraulic fracturing efficiency and limiting the stimulation volume of the reservoir.

KEYWORDS

hydraulic fracturing, boundary element method, numerical simulation, infill horizontal wells, fracture propagation

1 Introduction

With the large-scale development of unconventional low-permeability oil and gas reservoirs, staged fracturing technology for horizontal wells has become one of the main reservoir stimulation technologies at present (Wang et al., 2021; Zhou et al., 2020). It is of great significance to study the fracture initiation and propagation law of volume fracturing in horizontal wells and analyze the interaction between hydraulic fractures and natural

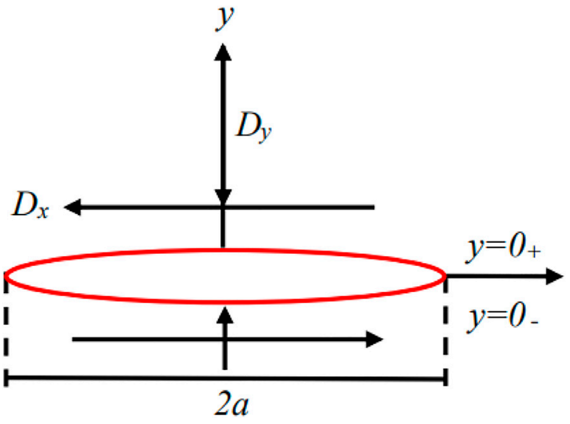

FIGURE 1
Discontinuity of constant displacement of fracture surface.

fractures for predicting the fracture network shape and optimizing the design of hydraulic fracturing construction plans.

Numerical simulation methods such as finite element, boundary element and discrete element are widely used to simulate and study the initiation and propagation process of hydraulic fracturing. Lam et al. considered the plane strain multi-fracture problem and proposed a method to study the effect of the interaction between micro-fractures on the stress intensity factor (Lam and Phua, 1991). The results show that different micro-fracture positions and directions determine the enhancement or shielding of the fracture interaction on the stress intensity factor effect. Wu et al. established a numerical model for simulating complex fracture propagation (Wu et al., 2012). Their study found that when there are multiple branched fractures, the fractures can expand at the same time, and there is a cross phenomenon during the expansion process, and the stress shadow area will have a significant impact on the fracture width. Kresse et al. established a method to calculate the stress shadow area around the fracture based on the displacement discontinuity method, and simulated the influence of the stress shadow area generated by the hydraulic fracture in the previous stage on the extension trajectory of the new fracture (Kresse et al., 2012). Huang et al. predicted the interaction between hydraulic fractures and natural fractures in complex environments through geomechanical simulation (Huang et al., 2014). The study found that natural fractures were reactivated to form complex and high-yield fracture networks after fracturing. He et al. established a three-dimensional horizontal well model, and found that hydraulic fracturing will form wide and short vertical fractures under the influence of *in-situ* stress of normal faults, and slender turning fractures will be formed under the influence of *in-situ* stress of reverse faults (He et al., 2015). Ding et al. established an embedded discrete fracture model for shale and tight oil reservoirs with multiple natural fractures (Ding et al., 2018). This model improves the shortcomings of the traditional dual-porosity medium model and can deal with multiphase flow problems with long-term fracture interaction. Wu et al. studied how the inter-well interference phenomenon occurred in two horizontal wells, and analyzed the fracture propagation and stress field change process of the horizontal wells (Wu et al., 2018). The research results showed that fracture propagation is controlled by stress field and fluid pressure in fractures, and inter-well interference was caused by fracture interaction, and staggered arrangement can be used to prevent fracture communication. Heng et al. established a simulation model for the interaction between natural fractures and hydraulic fractures based on the XFEM method, and quantitatively analyzed the fracture deflection angle (Zheng et al., 2020). The results showed that the smaller the deflection angle of natural fractures, the smaller the horizontal stress difference and the greater the degree of fracture opening. Duan et al. used the discrete element method to evaluate the fracture trajectory and fracturing effect of two horizontal wells (Duan et al., 2021). The study found that the local stress state was changed after the fracture initiation, so that the fractures were redirected and dominant fractures appeared. Yao et al. established a discrete element model of methane hydrate-bearing sediments (MHBSs), and based on the model, they analyzed the fracture propagation behavior of hydraulic fracturing under fluid-solid coupling (Yao et al., 2021). The results showed that the saturation of hydrate directly affects fractures initiation and propagation behavior. Yang et al. simulated and analyzed the fracture propagation of two wells with simultaneous fracturing based on discrete element method (Yang et al., 2021). The study found that the increase of injection

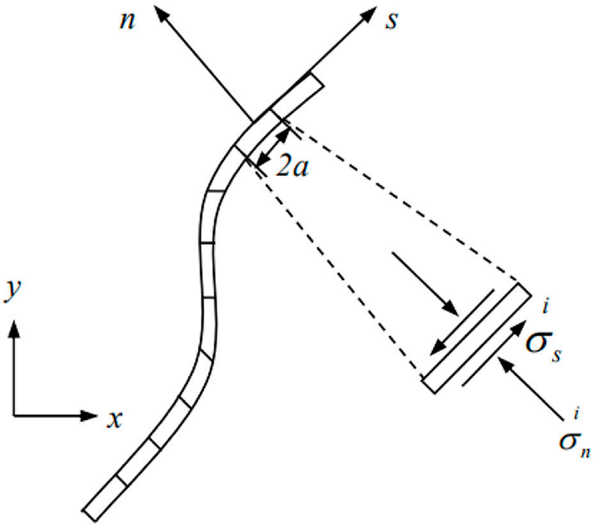

FIGURE 2
Stress and displacement components of the boundary element of the curved fracture segment.

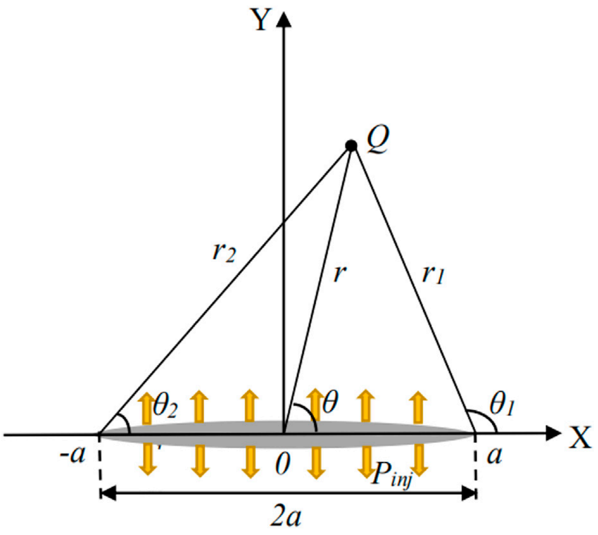

FIGURE 3
Schematic diagram of the calculation of the induced stress field around the fracture.

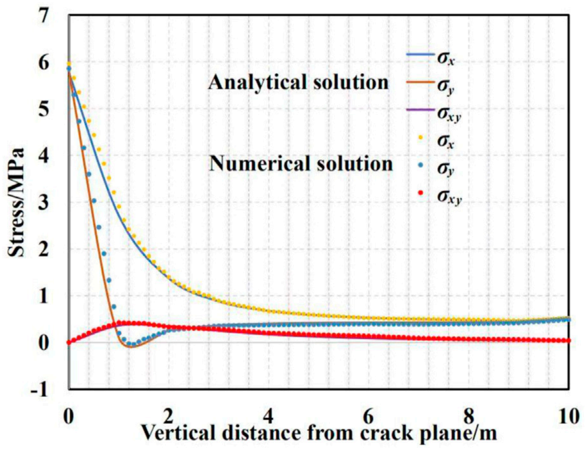

FIGURE 4
Comparison of simulation results between analytical and numerical solutions.

rate and the decrease of principal stress difference are conducive to the formation of fracture network. The stress shadow effect between two wellbore easily induces hydraulic fracture migration.

The true triaxial simulation experiment of indoor hydraulic fracturing is an important means to study fracture propagation. Bieniawski et al. studied the fracture of specimens under different loading conditions and shapes, and established the brittle fracture mechanism of rock in tension and compression (Bieniawski, 1967). Lorenz et al. found through experiments that low confining pressure and brittle rock were favorable conditions for fracturing, and the stress difference required for regional fracture initiation and extension was much lower than that required for shear failure (Lorenz et al., 1991). Beugelsdijk et al. observed the expansion geometry of hydraulic fractures through experiments and found that the greater the horizontal stress difference, the smoother the fracture surface (Beugelsdijk et al., 2000). Yan et al. found through experimental research that stress concentration occurs around the pores of the reservoir, resulting in an increase in rock fracture initiation pressure, while the existence of natural fractures will weaken the stress concentration (Yan et al., 2011). Zhou et al. revealed the interaction mechanism between multiple natural fractures and hydraulic fractures through physical experiments, and analyzed the effect of *in-situ* stress on fracture geometry (Zhou and Xue, 2011). In the case of high *in-situ* stress difference, fractures are more likely to generate multiple random branch fractures; in the case of low *in-situ* stress difference, natural fractures can control the geometry of hydraulic fractures. Wang et al. evaluated the effects of natural fracture approach angle, inclusion strength, and inclusion thickness on fracture propagation in a series of experiments (Wang et al., 2013). The results showed that fractures tend to pass through natural fractures with large approach angles and turn towards natural fractures with low approach angles. The thickness of natural fracture inclusions does not alter the crossing and turning behavior of orthogonally approached samples. Dehghan et al. found that in fractured reservoirs, pre-existing natural fractures reduce the stress concentration around the wellbore, greatly reducing the pressure required for fracture initiation and fracture propagation (Dehghan et al., 2016). Hou et al. conducted large-scale true triaxial hydraulic fracturing experiments (Hou et al., 2018). The study showed that a high level of stress difference will make the main fracture extend longer, but it is not conducive to the formation of complex fracture networks. Well operation can form a complex fracture network. He et al. used DIC digital image processing technology and a high-speed photography system to photograph the dynamic propagation process of fractures, and proposed two types of fracturing mechanisms: particle fracturing and pore-filling fracturing (He and Hayatdavoudi, 2018). Guo et al. found that the fracturing pressure of slick water is the lowest, and the low-viscosity fracturing fluid is easy to activate weak natural fractures or fill fractures, resulting in the opening of micro-fractures, which can effectively reduce the fracturing pressure (Guo et al., 2018). Based on experimental studies, Tan et al. found that too small or too large fracturing fluid viscosity and injection rate are not conducive to the vertical extension of induced fractures and the improvement of reservoir stimulation volume (Tan et al., 2019). Based on laboratory experiments, Liu et al. found that with the increase of fracturing fluid viscosity, formation fracture pressure and fracture propagation distance also increased (Liu et al., 2021).

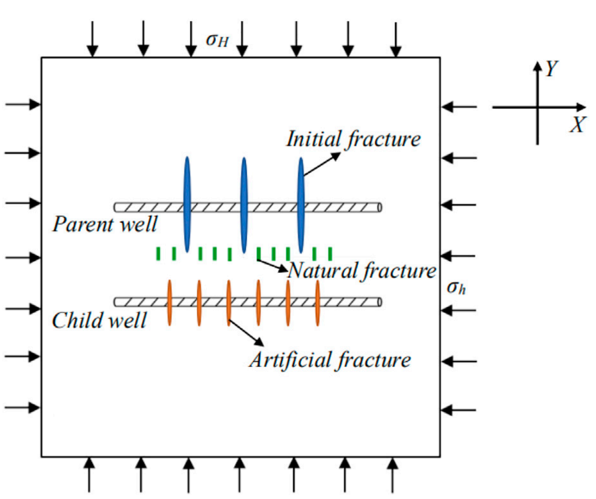

FIGURE 5
Simulation model of hydraulic fracture propagation in infill horizontal wells.

TABLE 1 Hydraulic fracturing simulation parameters.

Formation properties	
Reservoir size/m × m	300 m × 300 m
Young's modulus/MPa	20370
Poisson's ratio	0.23
Maximum horizontal principal stress/MPa	32
Minimum horizontal principal stress/MPa	30
Fracture toughness/MPa·m$^{1/2}$	2.5
Rock density/kg/m^3	2480
Design Parameters	
Injection pressure/MPa	34
Initial fracture length/m	100
Fracture Spacing in parent wells/m	60

In order to exploit the remaining oil areas of low-permeability reservoirs and the dead oil areas under the parent well pattern as much as possible, the stimulation technology of drilling parallel infilling horizontal wells near the parent wells has been gradually applied. Although the above-mentioned literatures have carried out a lot of research on the propagation of hydraulic fractures, the interaction mechanisms between hydraulic fractures in infill horizontal wells and hydraulic fractures in parent wells are still unclear.

Combined with the maximum circumferential tensile stress criterion and the displacement discontinuity boundary element method, a boundary element simulation program is developed in this paper to simulate and study the fracture propagation process and the inter-fracture interference mechanism of hydraulic fracturing. The analytical solution is used to validate the hydraulic fracturing simulation program. By establishing a fracture propagation model for infilling horizontal wells, a series of fracturing numerical simulations are carried out, and the influence mechanism of different factors on the inter-fracture interference and the effect of natural fractures on the fracture network morphology are studied.

2 Basic theory and governing equations

2.1 Displacement discontinuous boundary element method

In 1976, Crouch proposed that in an infinite elastic body, the element can be discretized to simulate the discontinuous distribution of fracture displacement, and the fracture length can be discretized into multiple small elements (Crouch, 1976). As shown in Figure 1, a fracture segment with a length of 2a is placed in an infinite formation, and the upper and lower discontinuous surfaces are denoted as $y = 0_+$ and $y = 0_-$. Dx and D_y represent the discontinuous displacement along the x and y directions, and u_x and u_y represent the displacement along the x and y directions. The positive sign "+" represents the upper surface of the fracture element, and the negative sign "–" represents the lower and upper surface of the fracture element.

$$\begin{cases} D_x = u_x(x, 0_-) - u_x(x, 0_+) \\ D_y = u_y(y, 0_-) - u_y(y, 0_+) \end{cases} \tag{1}$$

The displacement and stress caused by the displacement discontinuity (D_x, D_y) of the fracture to any point i in the two-dimensional plane are expressed as follows:

$$\begin{cases} u_x = D_x\left[2(1-\nu)f'_y - yf'_{xx}\right] + D_y\left[-(1-2\nu)f'_x - yf'_{xy}\right] \\ u_y = D_x\left[2(1-\nu)f'_x - yf'_{xy}\right] + D_y\left[2(1-\nu)f'_y - yf'_{yy}\right] \\ \sigma_{xx} = 2GD_x\left(2f'_{xy} + yf'_{xyy}\right) + 2GD_y\left(f'_{yy} + yf'_{yyy}\right) \\ \sigma_{yy} = 2GD_x\left(-yf'_{xyy}\right) + 2GD_y\left(f'_{yy} + yf'_{yyy}\right) \\ \sigma_{xy} = 2GD_x\left(f'_{yy} + yf'_{xyy}\right) + 2GD_y\left(-yf'_{yyy}\right) \end{cases} \tag{2}$$

where $f(x,y)$ is:

$$f(x, y) = -\frac{1}{4\pi(1-\nu)}\left[y\left(arctg\frac{y}{x-a} - arctg\frac{y}{x+a}\right)\right] - (x-a)\ln\left[(x-a)^2 + y^2\right]^{1/2} + (x+a)\ln\left[(x+a)^2 + y^2\right]^{1/2} \tag{3}$$

where σ_{xx}, σ_{yy}, σ_{xy} represent the normal stress along the x, y, and x-y plane directions; ν represents Poisson's ratio; G represents shear

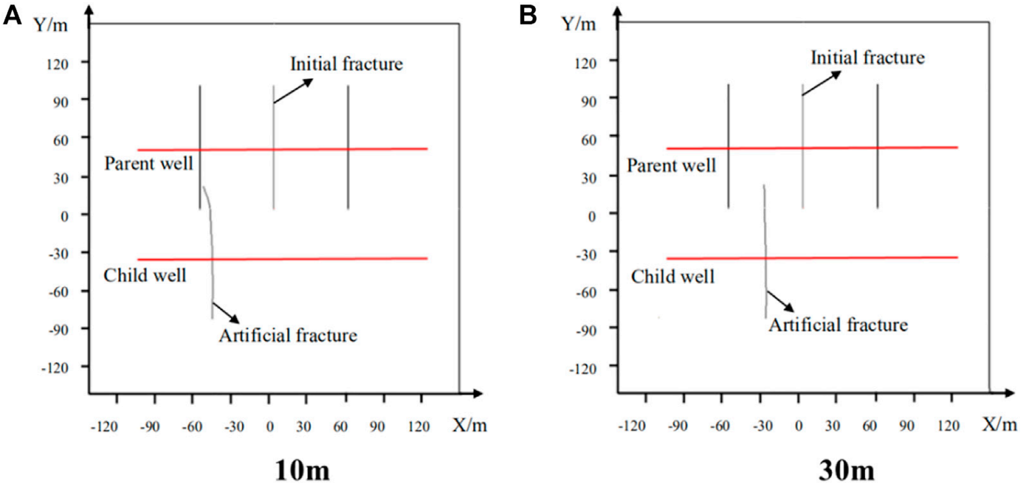

FIGURE 6
The propagation trajectory of a single artificial fracture at different positions.

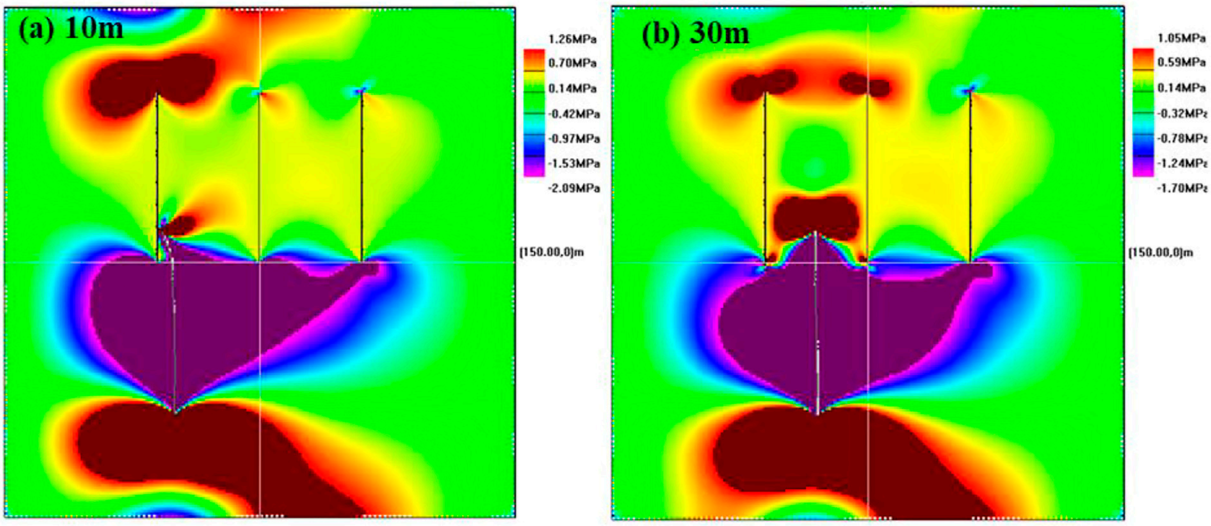

FIGURE 7
Normal stress field distribution in X-axis direction of single artificial fracture propagation.

modulus; $f(x,y)$ represents the analytical solution to the constant displacement discontinuity problem, f'_x and f'_y are the first-order derivatives of $f(x,y)$, f'_{xx}, f'_{xy}, and f'_{yy} are the second-order derivatives of $f(x,y)$, and f'_{xyy} and f'_{yyy} are The third derivative of $f(x,y)$.

The fracture curve in the plane is discretely and uniformly divided into N small units, and the boundary units are represented by two quantities, s-n and x-y, as shown in Figure 2.

The fracture is subjected to a certain pressure, and the displacement discontinuity component is expressed as follows:

$$\begin{cases} \overset{j}{D}_s = {}^j u_s^- - {}^j u_s^+ \\ \overset{j}{D}_n = {}^j u_n^- - {}^j u_n^+ \end{cases} \tag{4}$$

$\overset{j}{D}_s$, $\overset{j}{D}_n$ represent the displacement discontinuity of the unit body j in the s and n directions; $\overset{j}{u}_s$, $\overset{j}{u}_n$ represent the displacement of the unit body j in the s and n directions. The stress and displacement components in any boundary element i are expressed as follows:

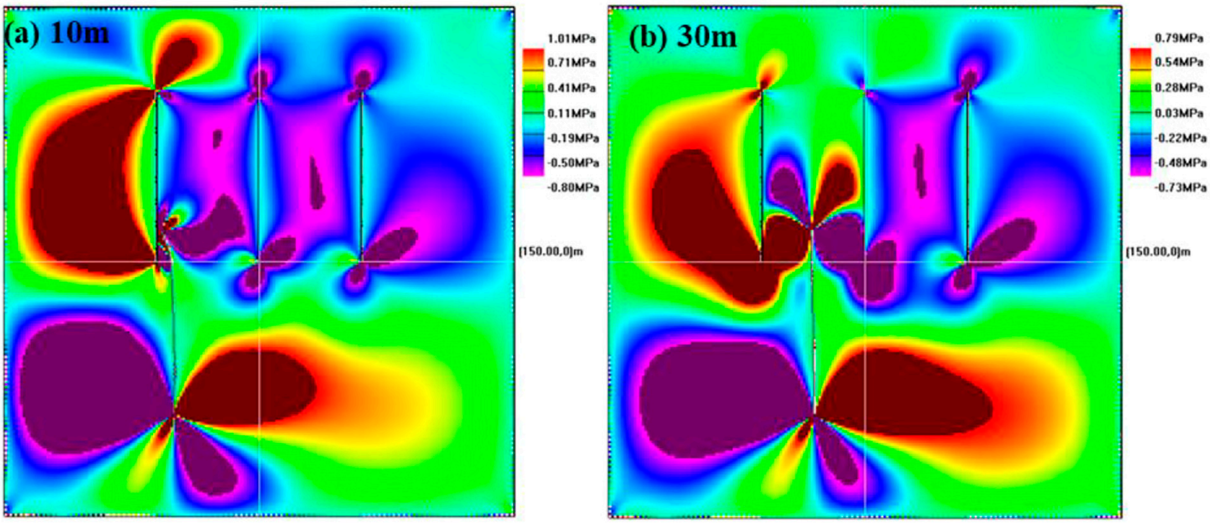

FIGURE 8
Distribution of shear stress field for single artificial fracture propagation.

$$\begin{cases} \overset{i}{\sigma}_s = \overset{j,i}{A}_{ss}\overset{j}{D}_s + \overset{j,i}{A}_{sn}\overset{j}{D}_n \\ \overset{i}{\sigma}_n = \overset{j,i}{A}_{ns}\overset{j}{D}_s + \overset{j,i}{A}_{nn}\overset{j}{D}_n \\ \overset{i}{\sigma}_t = \overset{j,i}{A}_{ts}\overset{j}{D}_s + \overset{j,i}{A}_{tn}\overset{j}{D}_n \\ \overset{i}{u}_s = \overset{j,i}{B}_{ss}\overset{j}{D}_s + \overset{j,i}{B}_{sn}\overset{j}{D}_n \\ \overset{i}{u}_n = \overset{j,i}{B}_{ns}\overset{j}{D}_s + \overset{j,i}{B}_{nn}\overset{j}{D}_n \end{cases} \tag{5}$$

$\overset{i}{\sigma}_s$, $\overset{i}{\sigma}_n$, $\overset{i}{\sigma}_t$ represents tangential stress, normal stress, and normal stress components along the fracture direction; $\overset{j}{u}_s$, $\overset{j}{u}_n$ represents the tangential and normal displacement of a point on the boundary element i; $A_{ss}^{j,i}$, $A_{j,i}^{sn}$, $A_{ns}^{j,i}$, $A_{j,i}^{nn}$, $A_{ts}^{j,i}$, $A_{j,i}^{tn}$ represents the stress influence coefficient; B_{ss}, B_{sn}, B_{ns}, B_{nn} represents the displacement influence coefficient.

The expressions of stress and displacement at the midpoint of element i are as follows:

$$\begin{cases} \overset{i}{\sigma}_s = \sum_{j=1}^{N} \overset{j,i}{A}_{ts}\overset{j}{D}_s + \sum_{j=1}^{N} \overset{j,i}{A}_{sn}\overset{j}{D}_n \\ \overset{n}{\sigma}_s = \sum_{j=1}^{N} \overset{j,i}{A}_{ns}\overset{j}{D}_s + \sum_{j=1}^{N} \overset{j,i}{A}_{nn}\overset{j}{D}_n \\ \overset{i}{\sigma}_t = \sum_{j=1}^{N} \overset{j,i}{A}_{ts}\overset{j}{D}_s + \sum_{j=1}^{N} \overset{j,i}{A}_{tn}\overset{j}{D}_n \\ \overset{i}{\mathrm{u/}}_s = \sum_{j=1}^{N} \overset{j,i}{A}_{ts}\overset{j}{D}_s + \sum_{j=1}^{N} \overset{j,i}{B}_{sn}\overset{j}{D}_n \\ \overset{i}{u}_s = \sum_{j=1}^{N} {}^{j,i}\, B_{ns}\overset{j}{D}_s + \sum_{j=1}^{N} \overset{j,i}{B}_{nn}\overset{j}{D}_n \end{cases} \tag{6}$$

For the 4 boundary element components, we need to obtain 2 components at the same time to solve, giving 2 N linear algebraic equations based on N discretized elements. The stress component is represented by Eq. 7, and the displacement component is represented by Eq. 8, thereby obtaining 2 N displacement discontinuities.

Compared with finite element and discrete element methods, the displacement discontinuous boundary element method has higher computational efficiency, and the numerical simulation accuracy is not affected by the complexity of the natural fracture network. Unfortunately, the displacement discontinuous boundary element method cannot consider the effect of non-uniform pore pressure when simulating fracture propagation. This study focuses on the mechanism of the interaction between hydraulic fractures in parent and child wells, so the model is solved using the displacement discontinuity boundary element method, ignoring the effect of pore pressure.

2.2 Rock failure criteria

To judge the fracture propagation of rock fractures, it is the key to determine the stress intensity factor. The rock is fractured by an external force, which will cause stress concentration at the fracture tip. Rock fractures can be divided into three types: open type (type I), slip type (type II), and tear type (type III) (Zhou et al., 2019). The stress intensity factor can be used to characterize the stress field and displacement field at the fracture tip (Irwin, 1957). K_I, K_{II}, and K_{III} are the stress intensity factors of three types of fracture tips, respectively, where K_I and K_{II} can be expressed as:

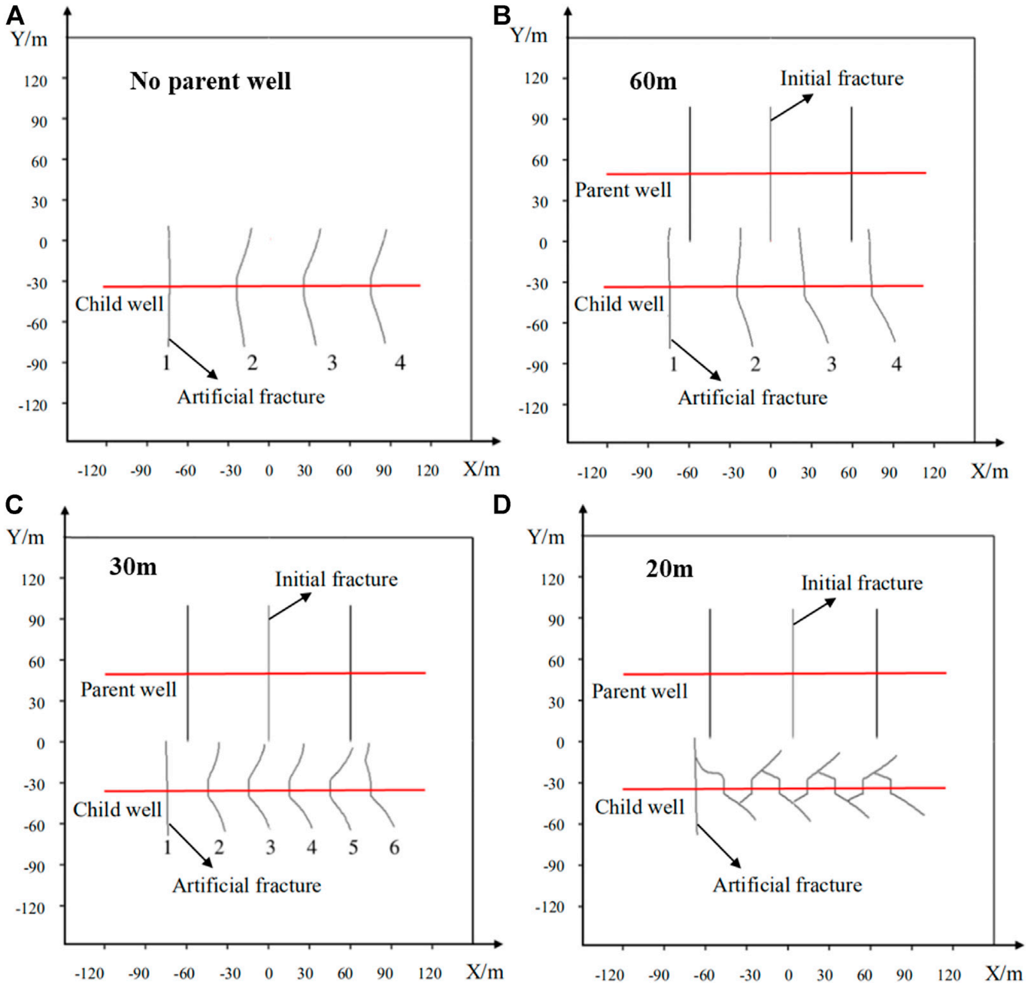

FIGURE 9
Hydraulic fracture propagation trajectories under different fracture spacings.

$$\begin{cases} K_I = \lim\limits_{r\longrightarrow 0}\sqrt{2\pi r}\,\sigma_n = \lim\limits_{r\longrightarrow 0}\dfrac{\sqrt{2}Ga}{\sqrt{\pi}(1-\nu)}\left[\dfrac{1}{(2a-r)\sqrt{r}}\right]D_n \\ K_{II} = \lim\limits_{r\longrightarrow 0}\sqrt{2\pi r}\,\sigma_s = \lim\limits_{r\longrightarrow 0}\dfrac{\sqrt{2}Ga}{\sqrt{\pi}(1-\nu)}\left[\dfrac{1}{(2a-r)\sqrt{r}}\right]D_s \end{cases} \tag{7}$$

The maximum circumferential stress criterion is used to judge the direction of fracture initiation and extension (Erdogan and Sih, 1963), where the stress expression is as follows:

$$\begin{cases} \sigma_r = \dfrac{1}{2\sqrt{2\pi r}}\left[K_I\left(3-\cos\theta\cos\dfrac{\theta}{2}\right)+K_{II}(3\cos\theta-1)\sin\dfrac{\theta}{2}\right] \\ \sigma_\theta = \dfrac{1}{2\sqrt{2\pi r}}\cos\dfrac{\theta}{2}\left[K_I(1+\cos\theta)-3K_{II}\sin\theta\right] \\ \tau_{r\theta} = \dfrac{1}{2\sqrt{2\pi r}}\cos\dfrac{\theta}{2}\left[K_I\sin\theta+K_{II}(3\cos\theta-1)\right] \end{cases} \tag{8}$$

According to the maximum circumferential stress criterion, the fracture will start in the direction of the maximum circumferential stress σ_θ, where the maximum circumferential stress is:

$$(\sigma_\theta)_{\max} = \frac{1}{2\sqrt{2\pi r}}\cos\frac{\theta}{2}\left[K_I(1+\cos\theta)-3K_{II}\sin\theta\right] \tag{9}$$

When the circumferential stress in the direction of the fracture initiation angle θ reaches the maximum value, that is, the critical value σ_c, the fracture starts to propagate forward. From this, it can be obtained that the conditions for judging fracture propagation according to the maximum circumferential stress criterion are:

$$(\sigma_\theta)_{\max} = (\sigma_\theta)_c \tag{10}$$

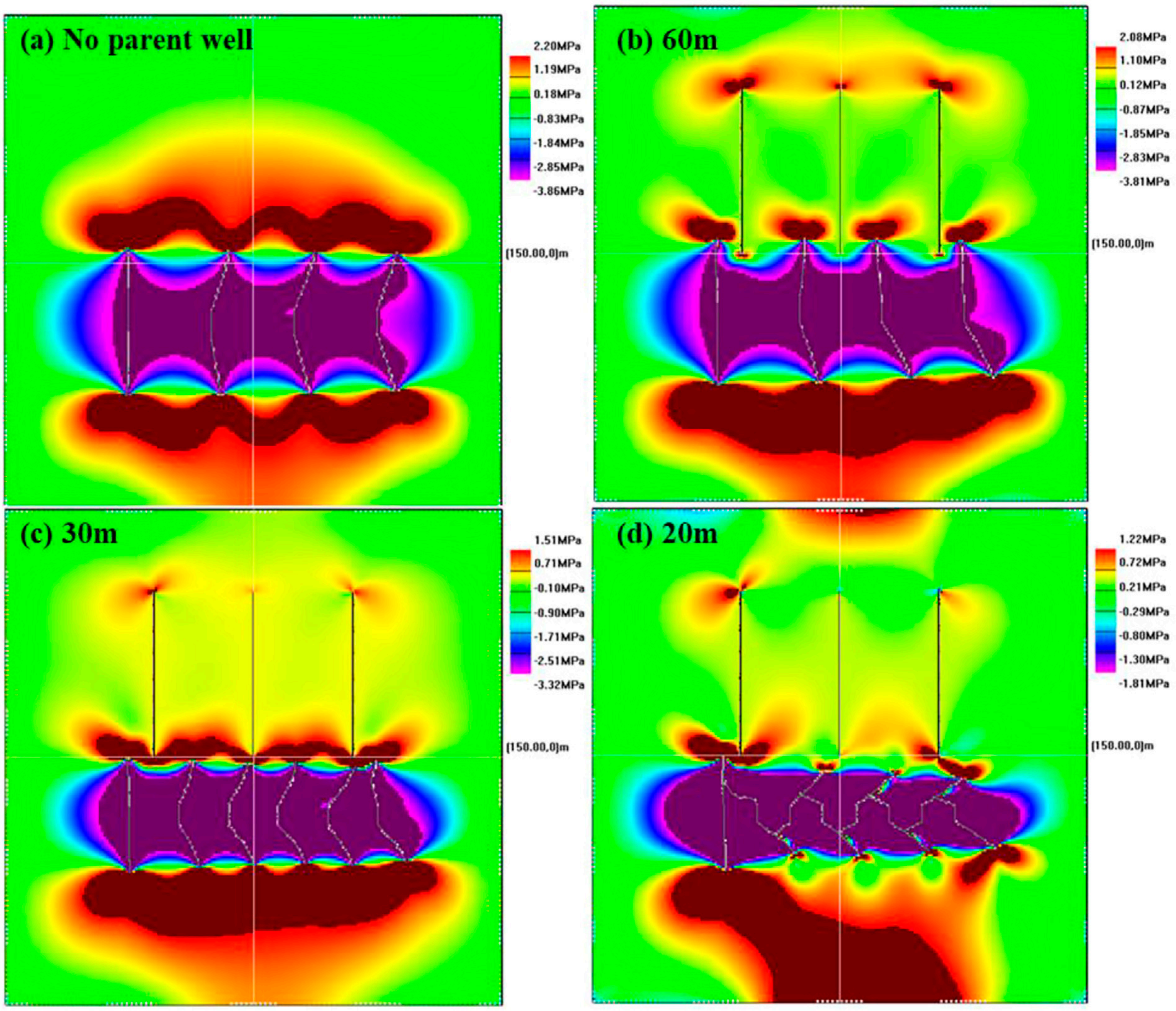

FIGURE 10
Normal stress field distribution in X-axis direction around artificial fractures under different fracture spacings.

2.3 Model validation

Sneddon et al. deduced the induced stress field generated by a single elliptical fracture around a two-dimensional uniform elastic medium under the action of uniform water pressure without considering the fluid loss in the fracture and the pressure drop loss of the plate flow (Sneddon, 1946; Sneddon and Elliot, 1946). As shown in Figure 3, The analytical solution of the induced stress field generated by hydraulic fractures can be expressed as:

$$\begin{cases} \sigma_x = P_{inj}\dfrac{r}{a}\left(\dfrac{a^2}{r_1 r_2}\right)^{\frac{3}{2}}\sin\theta\sin\left[\dfrac{3}{2}(\theta_1+\theta_2)\right] + P_{inj}\left[\dfrac{r}{\sqrt{r_1 r_2}}\cos\left(\theta - \dfrac{\theta_1+\theta_2}{2}\right) - 1\right] \\ \sigma_y = -P_{inj}\dfrac{r}{a}\left(\dfrac{a^2}{r_1 r_2}\right)^{\frac{3}{2}}\sin\theta\sin\left[\dfrac{3}{2}(\theta_1+\theta_2)\right] + P_{inj}\left[\dfrac{r}{\sqrt{r_1 r_2}}\cos\left(\theta - \dfrac{\theta_1+\theta_2}{2}\right) - 1\right] \\ \sigma_{xy} = P_{inj}\dfrac{r}{a}\left(\dfrac{a^2}{r_1 r_2}\right)^{\frac{3}{2}}\sin\theta\cos\left[\dfrac{3}{2}(\theta_1+\theta_2)\right] \end{cases} \tag{11}$$

P_{inj} represents the fluid pressure in the fracture; σ_x, σ_y, τ_{xy} represent the x-direction stress component, the y-direction stress component, and the shear stress component in the induced stress field.

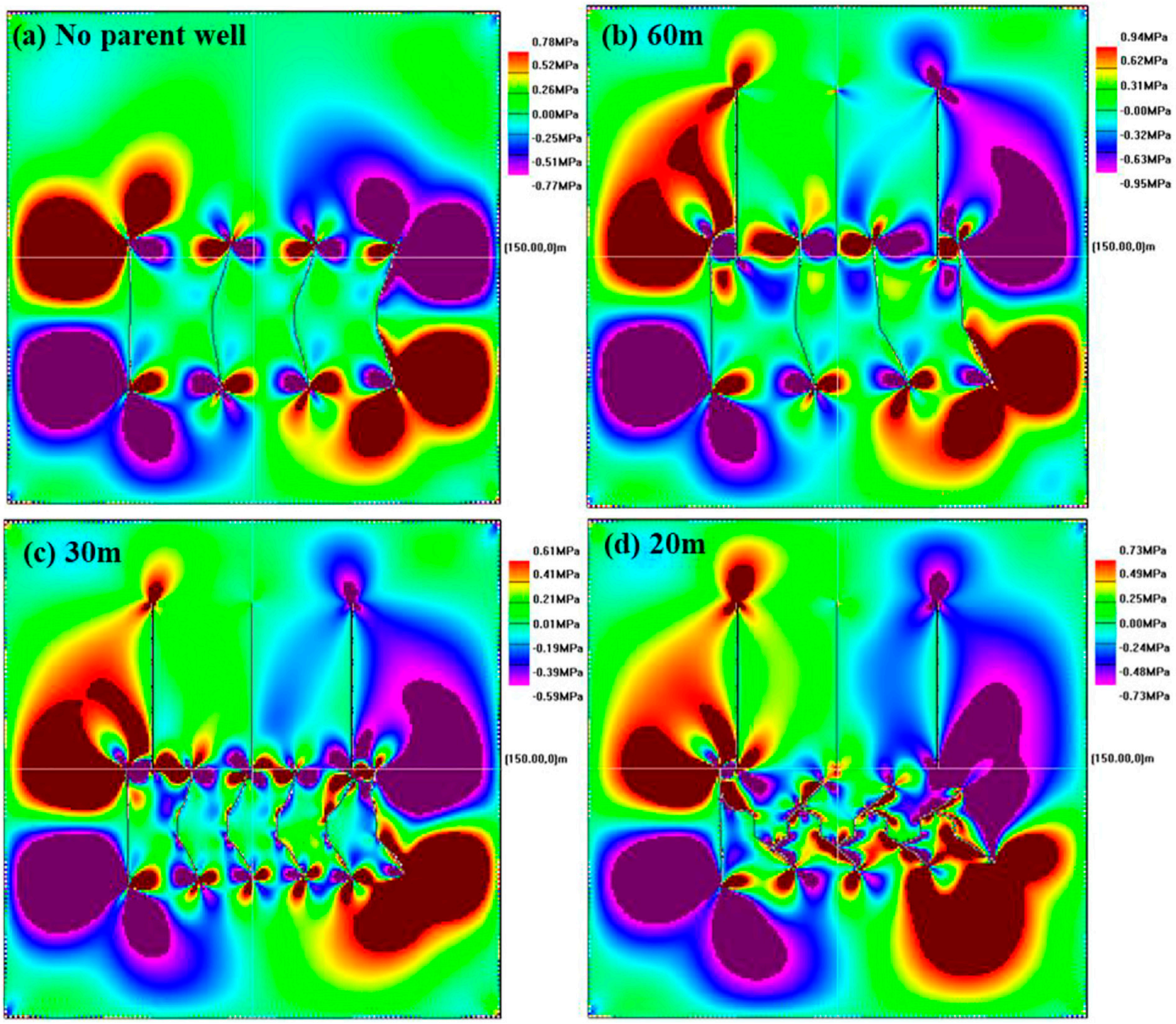

FIGURE 11
Distribution of shear stress field around artificial fractures with different fracture spacings.

(P_{inj}=-4MPa; a = 1 m; x = 0.8 m; y = 0 m~10 m).

It can be seen from Figure 4 that the numerical model of hydraulic fracture propagation established in this paper is basically consistent with the numerical simulation results of the stress field and the calculation results of the analytical solution, thus verifying the accuracy of the model.

3 Discussion of simulation results

3.1 Model establishment

The reservoir is assumed to be infinite and isotropic. Infill horizontal well technology refers to drilling a new horizontal well parallel to a parent well, and performing hydraulic fracturing reservoir reconstruction on the child well, to exploit the remaining oil areas in low-permeability reservoirs and dead oil under the parent well pattern as much as possible. According to the characteristics of infill horizontal wells, this paper establishes a two-dimensional plane hydraulic fracture propagation model as shown in Figure 5 The initial fractures of parent wells are blue, and the artificial fractures generated by hydraulic fracturing of child wells, that is, infill horizontal wells, are orange, the natural fractures in the reservoir are green. The maximum and minimum horizontal principal stresses are uniformly and symmetrically applied to the model boundary, and the simulation parameters used for hydraulic fracturing fracture propagation are shown in Table 1. The simulation parameters in Table 1 are determined according to the field operation characteristics of infill horizontal wells and concerning previous studies (Lindsay et al., 2018; Roussel et al.,

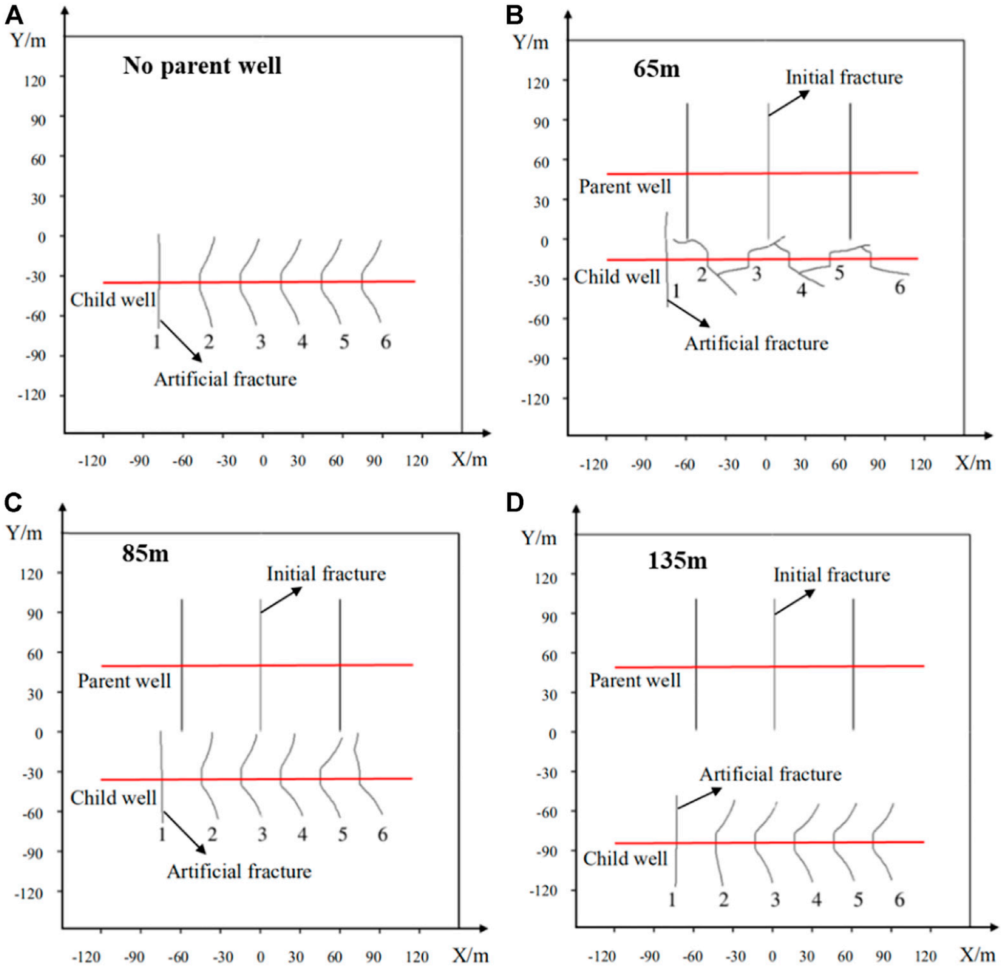

FIGURE 12
Fracture propagation trajectories at different well spacings.

2013; Wang et al., 2022). Note that the compressive stress is assumed to be negative and the tensile stress to be positive.

3.2 Effect of fracture spacing on fracture morphology

3.2.1 Propagation of a single hydraulic fracture

Fracture spacing is an important parameter for staged multi-cluster fracturing. Keeping the initial fracture parameters of the parent well unchanged, by changing the distance between the artificial fracture and the initial fracture, the propagation of a single artificial fracture in the child well is firstly studied. Figure 6 shows the fracture propagation trajectory of a single fracture in a child well at different positions, and the corresponding stress field is shown in Figure 7 and Figure 8. It can be seen from Figure 6 that the distance between the initial fracture and the artificial fracture will affect the propagation trajectory of the fracture. When the distance is small, the initial fracture will attract the artificial fracture, causing the artificial fracture to deflect to the side of the initial fracture.

Figure 7 and Figure 8 show that the distribution of the normal stress field and shear stress field around the fracture shows that when the fracture distance is relatively short, the weak surface of the initial fracture of the parent well will induce the artificial fracture of the child well, and the tensile stress concentration area at the tip of the artificial fracture will decrease, and the shear stress at the fracture tip is enhanced, which causes the artificial fracture to approach the weak surface of the original fracture in the parent well, and the two fractures have easily colluded with each other. Therefore, when infilling horizontal wells and fracturing, the relative positions of artificial fractures and initial fractures should be judged to avoid communication between fractures.

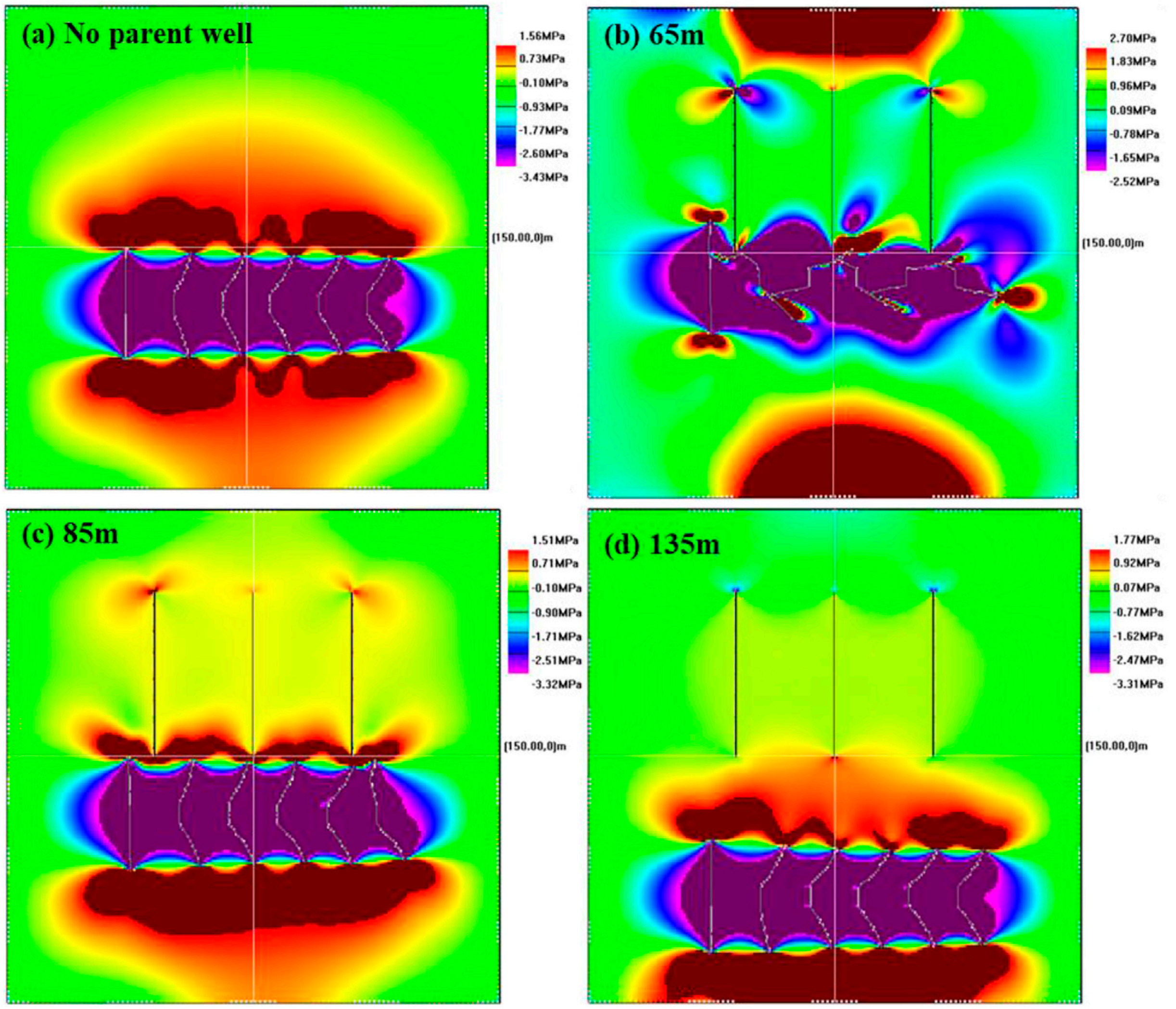

FIGURE 13
Normal stress distribution in the X-axis direction at different well spacings.

3.2.2 Hydraulic fracture expansion of staged multi-cluster fracturing

By changing the fracture spacing of hydraulic fractures in infilling horizontal wells, the propagation of hydraulic fractures in the case of multi-cluster fracturing in child wells is analyzed. The fracturing sequence of child wells is set to fracturing from left to right. Figure 9 shows the fracture trajectory under the competitive expansion of multiple artificial fractures, and the corresponding stress field is shown in Figure 10 and Figure 11 of which Figure 9C is the initial fracture of no parent well comparison group. Figure 9 shows that the fracture spacing has a great influence on the propagation trajectory of hydraulic fractures. Compared with the control group without initial fractures, a complex interaction occurs between the initial fractures in the parent well and the hydraulic fractures in the child well, leading to the fact that the originally mutually exclusive artificial fractures may be induced by the initial fractures to approach each other (Figure 9B and Figure 9C). The smaller the fracture spacing, the more obvious the mutual interference between the hydraulic fractures and the initial fractures, and the larger the hydraulic fracture deflection angle. When the fracture spacing is too small, the hydraulic fractures will communicate with each other near the wellbore (Figure 9D).

Figure 10 and Figure 11 show that the smaller the hydraulic fracture spacing, the greater the stress interference effect, and the rational use of the stress interference effect can increase the complexity of the fracture network. If the fracture spacing is too small, the tensile stress at the tip of the hydraulic fracture decreases, and the compressive stress on both sides increases,

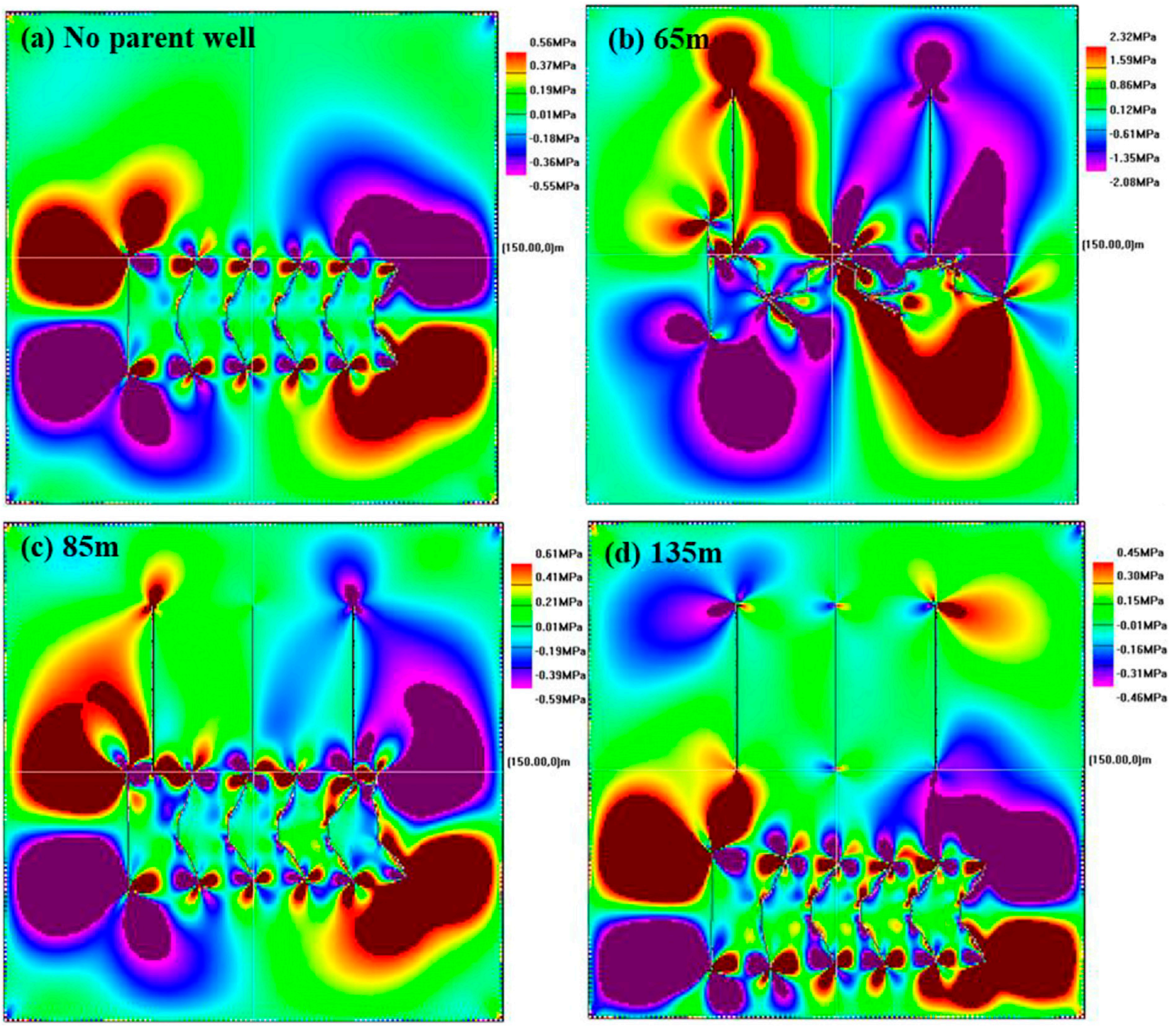

FIGURE 14
Distribution of shear stress under different well spacing.

which is not conducive to the extension and expansion of the fracture, and the fractures are easy to attract and communicate with each other. When the fracture spacing in Figure 10D and Figure 11D is 20 m, the normal stress and shear stress at the tip of the artificial fracture in the middle is small, and the mutual interference between fractures hinders the fracture extension. Therefore, reasonable fracture spacing during staged multi-cluster fracturing in child wells will maximize the complexity of the artificial fracture network and improve oil recovery.

3.3 Effect of well spacing on fracture morphology

The distance between the child well and the parent well may affect the inter-fracture interference. The fracture spacing is fixed, and the fracture propagation under different well spacing is analyzed. The simulation results of fracture trajectory are shown in Figure 12 and the simulation results of stress field are shown in Figure 13 and Figure 14. Comparing Figure 12A and Figure 12D, it can be seen that when the well spacing is large, the initial fracture of the parent well will not affect the fracture of the child well. With the shortening of well spacing, the initial fractures of parent wells begin to interfere with the propagation trajectory of hydraulic fractures in child wells. The shorter the well spacing, the stronger the interference effect, the easier it is for hydraulic fractures to attract each other, and even the phenomenon of inter-fracture communication. Reducing the well spacing can increase the stress interference between wells and make the fractures interact, which is conducive to the formation of complex fracture network between wells.

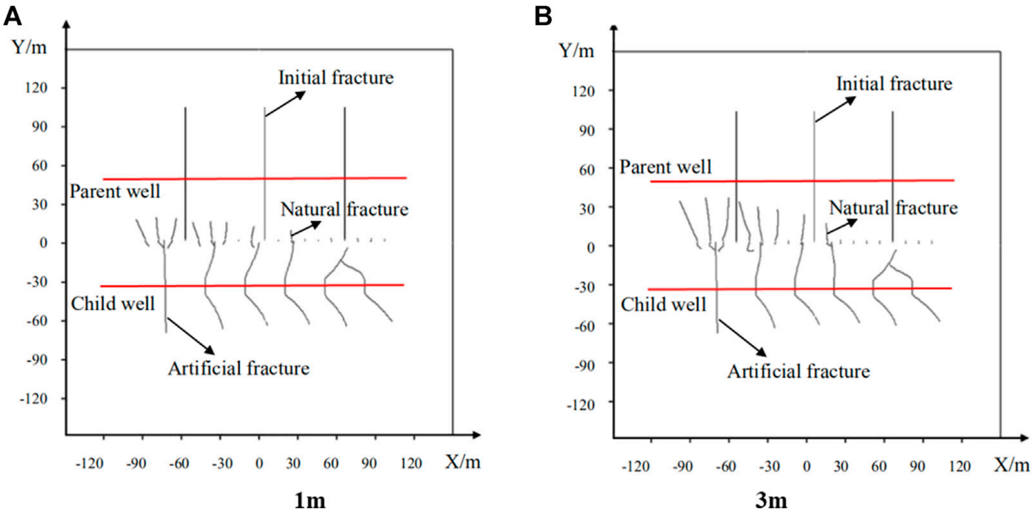

FIGURE 15
Fracture propagation trajectories under different initial lengths of natural fractures.

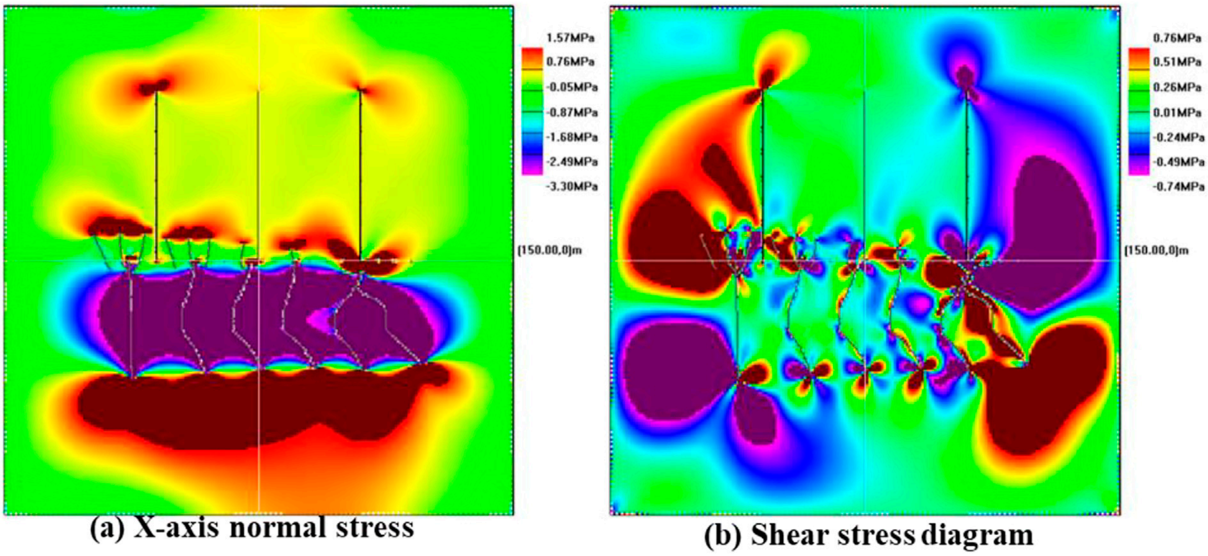

FIGURE 16
Stress field distribution of natural fractures with an initial length of 1 m.

Figure 13 and Figure 14 show that when the well spacing is small, the stress field distribution around the hydraulic fracture is greatly interfered with by the initial fracture of the parent well. The tensile stress concentration area at the tip of the artificial fracture is greatly reduced, and the fractures communicate with each other in the compressive stress area, so it may be difficult for fracture initiation and extension. When the two wells are far apart, compared with the control group without initial fractures, the stress zone where the hydraulic fractures are located is hardly affected by the initial fracture stress field of the parent well.

3.4 Influence of natural fractures on fracture morphology

3.4.1 Influence of natural fracture length

Assuming that the natural fractures are closed in the initial state, the pressure inside the fractures is zero, and the fracture spacing is 10 m, the effect of the natural fracture length on the propagation law of hydraulic fractures in child wells is studied by changing the initial length of the natural fractures.

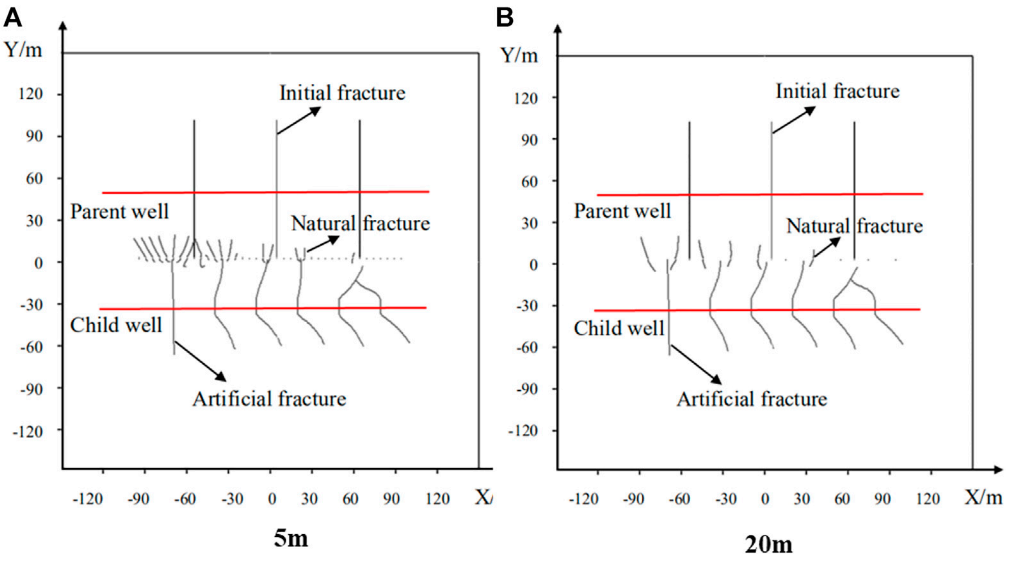

FIGURE 17
Fracture propagation trajectories under different natural fracture densities.

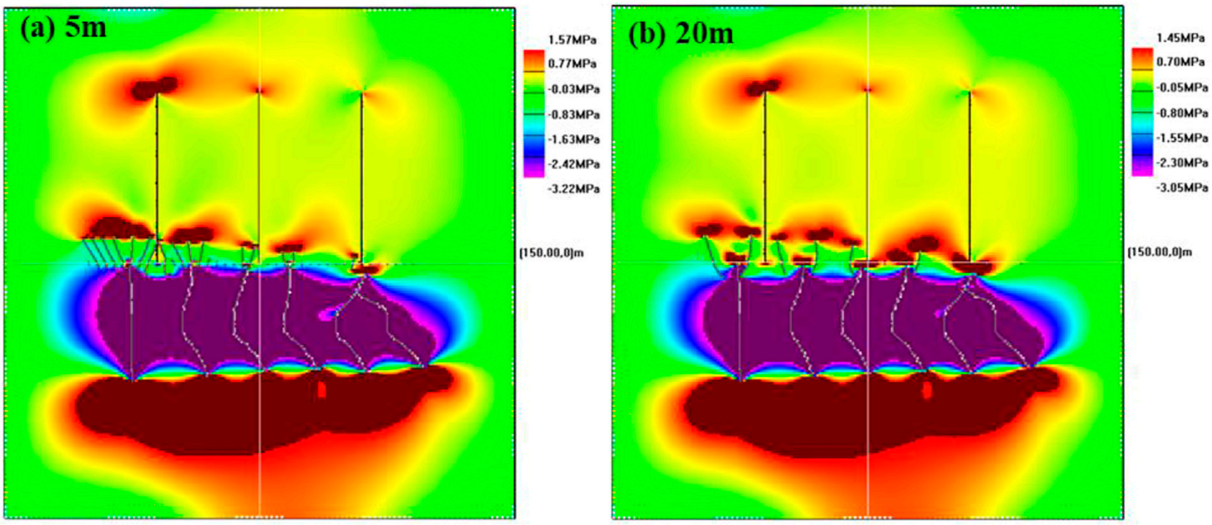

FIGURE 18
Normal stress in the X-axis direction under different natural fracture densities.

Figure 15 shows the initiation and extension of hydraulic fractures with different initial lengths of natural fractures. It can be seen that the propagation of artificial fractures can induce the initiation and extension of nearby natural micro-fractures, and some natural fractures will communicate with artificial fractures. Since the fracturing sequence is set from left to right, the stress interference area first changes from the left area, so the natural fractures in the left first fracturing area extend longer, and the right rear fracturing area may induce insufficient stress, resulting in natural fractures. The fracture extension distance is getting shorter and shorter, even without fracture initiation. The comparison shows that the longer the initial length of the natural fracture is, the longer the final length of the natural fracture that initiates and extends, and the extension of the natural fracture is divergent toward the parent well.

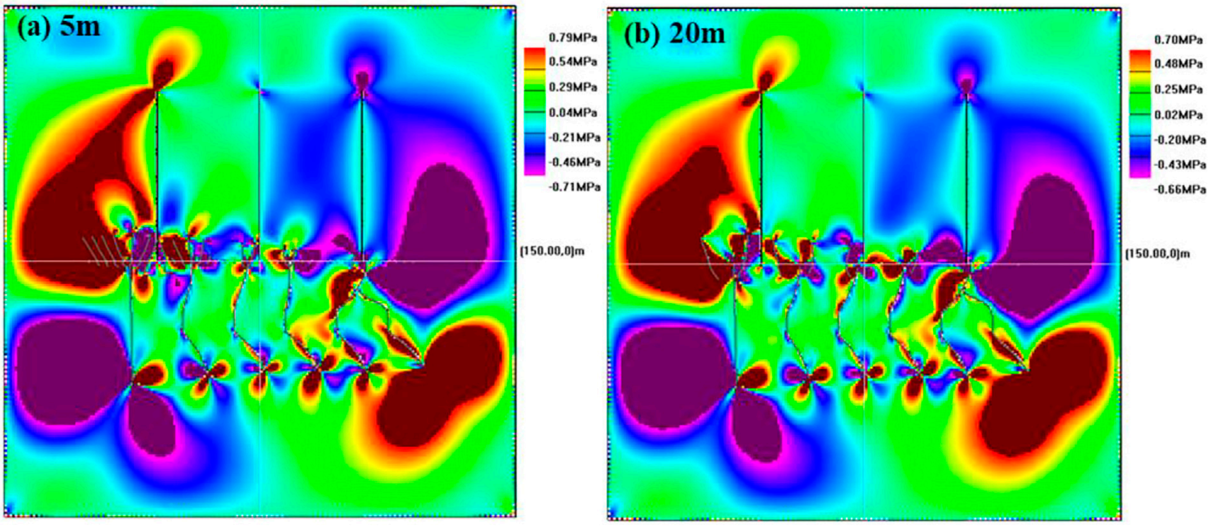

FIGURE 19
Distribution of shear stress under different natural fracture densities.

Figure 16 shows the stress field distribution when the natural fracture length is 1 m. It can be seen that the two tips of natural fractures are located in the stress concentration area, and the upper end is mainly located in the tensile stress concentration area. The natural fracture continues to expand upward and is prone to shear tensile failure. The lower end is located in the compressive stress concentration area. It is difficult to initiate fractures and extend, and it is easier to extend in the direction of the initial fractures in a divergent manner, while the stress values around the fractures without fracture initiation are close to the *in-situ* stress state.

3.4.2 Influence of natural fracture density

The length of natural fractures is fixed, and the natural fractures are densely arranged by changing the fracture spacing, and the influence of natural fracture density on the propagation of hydraulic fractures is analyzed. From Figure 17 of the fracture propagation trajectory, it can be seen that regardless of the density of natural fractures, the natural fractures in the pre-pressurized area on the left can initiate and extend, while most of the natural fractures in the post-pressurized area on the right do not initiate and extend. The length of natural fracture extension is not greatly affected by the density of natural fractures. As shown in Figure 17A, when natural fractures are densely distributed, individual fractures will stop extending after a certain distance due to the influence of surrounding natural fractures, while some natural fractures will communicate with initial fractures and hydraulic fractures, resulting in child wells communicate between wells, thereby reducing fracturing efficiency.

From the stress field distribution results in Figure 18 and Figure 19, it can be seen that the tensile stress area at the tip of the natural fracture in the pre-pressed area on the left is larger, so the natural fracture is more likely to initiate and expand to the parent well under the effect of the induced stress field. However, the natural fracture induced stress in the right back pressure region is obviously insufficient, so most of them do not initiate and propagate.

4 Conclusion

Based on the theory of linear elasticity and rock fracture mechanics, combined with the boundary element displacement discontinuity method, a simulation model of hydraulic fracturing fracture propagation in infill horizontal wells is established. Using this model, this paper analyze different factors on the propagation of hydraulic fractures in infill horizontal wells. The main simulation results are as follows:

1) The fracture spacing and relative position of hydraulic fractures in infill horizontal wells will have a significant impact on the fracture propagation trajectory. The smaller the fracture spacing is, the larger the hydraulic fracture deflection angle is. Too small fracture spacing may cause hydraulic fractures to communicate with each other in the near-wellbore zone. Reasonable fracture spacing of infilling horizontal wells can increase the complexity of the fracture network.
2) The shorter the well spacing between the infill horizontal well and the parent well is, the stronger the inter-fracture stress interference effect is. Reasonable reduction of well spacing can increase the effect of stress interference and is conducive to the formation of complex fracture networks. Too small well

spacing may cause fracture communication between wells and reduce hydraulic fracturing efficiency.

3) Under the action of induced stress, natural fractures will initiate and extend and communicate with hydraulic fractures, and the fracture propagation pattern is divergent along the initial fracture direction of the parent well. The natural fractures in the pre-compression area are more likely to initiate and propagate under the action of induced stress.
4) Under the action of hydraulic fracture-induced stress, the longer the initial length of natural fractures is, the longer the final length of natural fractures is. The natural fracture density has little effect on the natural fracture extension length and fracture shape.

Data availability statement

The original contributions presented in the study are included in the article/supplementary material, further inquiries can be directed to the corresponding author.

Author contributions

HW: Writing—original draft, Formal analysis, Conceptualization. EL: Methodology, Software. TY: Methodology, Investigation. LQ: Writing—review and editing, Resources. JL: Conceptualization, Methodology.

Funding

This work was supported by the National Natural Science Foundation of China (Grant Nos. 51934005, 51874242, 52174029).

Conflict of interest

The authors EL, LQ, and JL were employed by Shaanxi Yanchang Petroleum (Group) Co., Ltd. The author TY was employed by Xi'an Changqing Chemical Group Co., Ltd.

The remaining authors declare that the research was conducted in the absence of any commercial or financial relationships that could be construed as a potential conflict of interest.

Publisher's note

References

Beugelsdijk, L. J. L., De Pater, C. J., and Sato, K. (2000). "Experimental hydraulic fracture propagation in a multifracture medium," in SPE Asia Pacific conference on integrated modelling for asset management. One Petro.

Bieniawski, Z. T. (1967). Mechanism of brittle fracture of rock: Part I—theory of the fracture process[C]. *Int. J. Rock Mech. Min. Sci. Geomechanics Abstr.* 4 (4), 395–406. doi:10.1016/0148-9062(67)90030-7

Crouch, S. (1976). Solution of plane elasticity problems by the displacement discontinuity method, Infinite body solution. *J. Numer. Methods Eng.* 10 (2), 301–343. doi:10.1002/nme.1620100206

Dehghan, A. N., Goshtasbi, K., Ahangari, K., and Jin, Y. (2016). Mechanism of fracture initiation and propagation using a tri-axial hydraulic fracturing test system in naturally fractured reservoirs. *Eur. J. Environ. Civ. Eng.* 20 (5), 560–585. doi:10.1080/19648189.2015.1056384

Ding, D. Y., Farah, N., Bourbiaux, B., Wu, Y., and Mestiri, I. (2018). Simulation of matrix/fracture interaction in low-permeability fractured unconventional reservoirs. *SPE J.* 23 (04), 1389–1411. doi:10.2118/182608-pa

Duan, K., Li, Y., and Yang, W. (2021). Discrete element method simulation of the growth and efficiency of multiple hydraulic fractures simultaneously-induced from two horizontal wells[J]. *Geomechanics Geophys. Geo-Energy Geo-Resources* 7 (1), 1–20. doi:10.1007/s40948-020-00196-4

Erdogan, F., and Sih, G. C. (1963). On the crack extension in plates under plane loading and transverse shear. *J. Basic Eng.* 85, 519–525. doi:10.1115/1.3656897

Guo, Y., Deng, P., Yang, C., Chang, X., Wang, L., and Zhou, J. (2018). Experimental investigation on hydraulic fracture propagation of carbonate rocks under different fracturing fluids. *Energies* 11 (12), 3502. doi:10.3390/en11123502

He, L., Zhongxiao, L., Suling, W., Xu, J., and Zhao, C. (2015). Hydraulic fracture initiation mechanism in the definite plane perforating technology of horizontal well[J]. *Petroleum Explor. Dev.* 42 (6), 869–875. doi:10.1016/S1876-3804(15)30084-7

He, W., and Hayatdavoudi, A. (2018). A comprehensive analysis of fracture initiation and propagation in sandstones based on micro-level observation and digital imaging correlation. *J. Petroleum Sci. Eng.* 164, 75–86. doi:10.1016/j.petrol.2018.01.041

Hou, B., Zhang, R., Zeng, Y., Fu, W., Muhadasi, Y., and Chen, M. (2018). Analysis of hydraulic fracture initiation and propagation in deep shale formation with high horizontal stress difference. *J. Petroleum Sci. Eng.* 170, 231–243. doi:10.1016/j.petrol.2018.06.060

Huang, J., Safari, R., Mutlu, U., Kevin, B., Ingo, G., and Mark, M. (2014). "Natural-hydraulic fracture interaction: Microseismic observations and geomechanical predictions[C]," in SPE/AAPG/SEG Unconventional Resources Technology Conference. One Petro.

Irwin, G. (1957). Analysis of stresses and strains near the end of a crack traversing a plate. *J. Appl. Mech.* 243, 361–364. doi:10.115/1.4011547

Kresse, O., Weng, X., Wu, R., and Gu, H. (2012). "Numerical modeling of hydraulic fractures interaction in complex naturally fractured formations[C]," in 46th US rock mechanics/geomechanics symposium. One Petro.

Lam, K. Y., and Phua, S. P. (1991). Multiple crack interaction and its effect on stress intensity factor. *Eng. Fract. Mech.* 40 (3), 585–592. doi:10.1016/0013-7944(91)90152-q

Lindsay, G., Miller, G., Xu, T., Shan, D., and Baihly, J. (2018). "Production performance of infill horizontal wells vs. pre-existing wells in the major US unconventional basins[C]," in SPE hydraulic fracturing technology conference and exhibition. OnePetro.

Liu, Z., Wang, S., Ye, H., Yang, L., Fan, F., Lian, H., et al. (2021). Experimental study on the effects of pre-cracks, fracturing fluid, and rock mechanical characteristics on directional hydraulic fracturing with axial pre-cracks[J]. *Geomechanics Geophys. Geo-Energy Geo-Resources* 7 (2), 1–14. doi:10.1007/s40948-021-00225-w

Lorenz, J. C., Teufel, L. W., and Warpinski, N. R. (1991). Regional fractures I: A mechanism for the formation of regional fractures at depth in flat-lying reservoirs

[J]. *AAPG Bull.* 75 (11), 1714–1737. doi:10.1306/0C9B29E3-1710-11D7-864000102C1865D

Roussel, N. P., Florez, H. A., and Rodriguez, A. A. (2013). "Hydraulic fracture propagation from infill horizontal wells[C]," in SPE annual technical conference and exhibition. OnePetro.

Sneddon, I. N., and Elliot, H. A. (1946). The opening of a Griffith crack under internal pressure. *Q. Appl. Math.* 4 (3), 262–267. doi:10.1090/qam/17161

Sneddon, I. N. (1946). The distribution of stress in the neighbourhood of a crack in an elastic solid[J]. *Proc. R. Soc. Lond. Ser. A. Math. Phys. Sci.* 187 (1009), 229–260. doi:10.1098/rspa.1946.0077

Tan, P., Jin, Y., Yuan, L., Xiong, Z. Y., Hou, B., Chen, M., et al. (2019). Understanding hydraulic fracture propagation behavior in tight sandstone–coal interbedded formations: An experimental investigation. *Pet. Sci.* 16 (1), 148–160. doi:10.1007/s12182-018-0297-z

Wang, H. Y., Zhou, D., Xu, J., Liu, S., Liu, E., and Gao, Q. (2021). "An optimal design algorithm for proppant placement in slickwater fracturing[C]," in Abu Dhabi International Petroleum Exhibition & Conference. OnePetro.

Wang, H., Zhou, D., Liu, S., Wang, X., Ma, X., and Yao, T. (2022). Hydraulic fracture initiation for perforated wellbore coupled with the effect of fluid seepage. *Energy Rep.* 8, 10290–10298. doi:10.1016/j.egyr.2022.08.011

Wang, W., Olson, J. E., and Prodanovic, M. (2013). "Natural and hydraulic fracture interaction study based on semi-circular bending experiments[C]," in SPE/AAPG/SEG Unconventional Resources Technology Conference. One Petro.

Wu, K., Wu, B., and Yu, W. (2018). Mechanism analysis of well interference in unconventional reservoirs: Insights from fracture-geometry simulation between two horizontal wells. *SPE Prod. Operations* 33 (01), 12–20. doi:10.2118/186091-pa

Wu, R., Kresse, O., Weng, X., Cohen, C., and Gu, H. (2012). "Modeling of interaction of hydraulic fractures in complex fracture networks[C]," in SPE Hydraulic Fracturing Technology Conference. One Petro.

Yan, T., Li, W., and Bi, X. (2011). An experimental study of fracture initiation mechanisms during hydraulic fracturing. *Pet. Sci.* 8 (1), 87–92. doi:10.1007/s12182-011-0119-z

Yang, W., Li, S., Geng, Y., Zhou, Z., Li, L., Gao, C., et al. (2021). Discrete element numerical simulation of two-hole synchronous hydraulic fracturing[J]. *Geomechanics Geophys. Geo-Energy Geo-Resources* 7 (3), 1–15. doi:10.1007/s40948-021-00257-2

Yao, Y., Guo, Z., Zeng, J., Li, D., Lu, J., Liang, D., et al. (2021). Discrete element analysis of hydraulic fracturing of methane hydrate-bearing sediments. *Energy fuels.* 35 (8), 6644–6657. doi:10.1021/acs.energyfuels.1c00248

Zheng, H., Pu, C., and Sun, C. (2020). Study on the interaction between hydraulic fracture and natural fracture based on extended finite element method[J]. *Eng. Fract. Mech.* 230, 106981. doi:10.1016/j.engfracmech.2020.106981

Zhou, D., Wang, H., He, Z. X., Liu, Y., Liu, S., Ma, X., et al. (2020). Numerical study of the influence of seepage force on the stress field around a vertical wellbore. *Eng. Appl. Comput. Fluid Mech.* 14 (1), 1489–1500. doi:10.1080/19942060.2020.1835733

Zhou, D., Zheng, P., Yang, J., Li, M., Xia, Y., Cai, W., et al. (2019). Optimizing the construction parameters of modified zipper fracs in multiple horizontal wells. *J. Nat. Gas Sci. Eng.* 71, 102966. doi:10.1016/j.jngse.2019.102966

Zhou, J., and Xue, C. (2011). "Experimental investigation of fracture interaction between natural fractures and hydraulic fracture in naturally fractured reservoirs [C]," in SPE Europec/Eage Annual Conference and Exhibition. One Petro

frontiers | Frontiers in Earth Science

TYPE Original Research
PUBLISHED 09 January 2023
DOI 10.3389/feart.2022.1015107

OPEN ACCESS

EDITED BY
Jinze Xu,
University of Calgary, Canada

REVIEWED BY
Huzhen Wang,
Northeast Petroleum University, China
Qi Zhang,
China University of Geosciences
Wuhan, China

*CORRESPONDENCE
Xuewei Liu,
dg_liuxwei@petrochina.com.cn
Li Yulin,
1732875754@qq.com

SPECIALTY SECTION
This article was submitted to Environmental Informatics and Remote Sensing, a section of the journal Frontiers in Earth Science

RECEIVED 09 August 2022
ACCEPTED 30 August 2022
PUBLISHED 09 January 2023

CITATION
Liu X, Li D, Jia Y, Liyong Y, Xiaoting G, Tao Z, Ziwei C, Mao L, Juan W, Xiangyun S, Donghua Z, Hongxia T, Yulin L and Yu Z (2023), Optimizing construction parameters for fractured horizontal wells in shale oil.
Front. Earth Sci. 10:1015107.
doi: 10.3389/feart.2022.1015107

Optimizing construction parameters for fractured horizontal wells in shale oil

Xuewei Liu[1,2]*, Dongping Li[1], Yunpeng Jia[1], Yang Liyong[1], Gou Xiaoting[1], Zhao Tao[1], Chen Ziwei[1], Li Mao[1], Wang Juan[1], Sui Xiangyun[1], Zhao Donghua[1], Tang Hongxia[1], Li Yulin[2]* and Zhang Yu[2]

[1]Petroleum Engineering Research Institute, PetroChina Dagang Oilfield Company, Tianjin, China,
[2]State Key Laboratory of Oil and Gas Reservoir Geology and Exploitation, Southwest Petroleum University, Chengdu, China

Shale oil is mainly extracted by fracturing. However, it is difficult to determine the optimum construction parameters to obtain maximum productivity. In this paper, a fuzzy comprehensive production evaluation model for fractured shale oil horizontal wells based on random forest algorithm and coordinated principal component analysis is proposed. The fracturing parameters of the target wells are optimized by combining this model with an orthogonal experimental design. The random forest algorithm was used to calculate the importance of data sample factors. The main controlling factors of the production of fractured horizontal wells in shale oil were obtained. To reduce the noise of the sample data, principal component analysis was used to reduce the dimensions of the main control factors. Furthermore, the random forest algorithm was used to determine the weight of the principal components after reducing the dimensionality. The membership function of the main control factors after reducing dimensionality was established by combining the fuzzy statistics and assignment methods. In addition, the membership matrix of the effect prediction of fractured horizontal wells in shale oil was determined. The fuzzy comprehensive evaluation method is used to score and evaluate the effect of fractured horizontal wells. Combined with the orthogonal experimental design method, the optimized parameter design of a fractured horizontal well considering the comprehensive action of multiple parameters is realized. After construction according to the optimized parameters, production following fracturing increases significantly. This verifies the rationality of the optimization method that is proposed in this paper.

KEYWORDS

shale oil, random forest, principal component analysis, fuzzy comprehensive evaluation, orthogonal test design, construction parameters optimization

1 Introduction

Shale oil resources are rich, and show good exploration and development potential (Rodriguez and Soeder, 2015). Shale oil reservoirs have strong heterogeneity, small pore throat structure, complex fluid phase, and oil and gas properties. The success of exploration and development is due to the effective “liberation” of the reservoir by multi-cluster volume fracturing of horizontal wells (Hu et al., 2020). Meanwhile, the hydraulic fracturing effect of shale oil mainly depends on the matching of construction parameters and geological parameters. The fracturing optimization design largely determines the fracturing improvement effect. The productivity of fractured horizontal wells for shale oil can be improved by establishing an effective optimization method for the construction parameters of fractured horizontal wells for shale oil (Rahmanifard and Plaksina, 2018).

Currently, there are two main methods for fracturing parameters optimization. First, a fracture propagation model is established to simulate the fracture extension process in the fracturing process. The fracture parameters are optimized by maximizing the reconstruction volume (Guo et al., 2015). However, the actual fracture extension is very complex, and the simplified simulation model cannot accurately reflect the real situation of reservoir fracture extension. Second, the reservoir numerical simulation method has been used to set the cumulative production or stimulation period as the objective function, and the optimal objective function has been used to select the best fracture parameters (Moradidowlatabad and Jamiolahmady, 2018). However, it is easy to form a multi-scale fracture network with a highly complex topological structure in the large-scale hydraulic fracturing of shale oil. In addition, the non-Darcy seepage of shale nanopores lengthens the time required for the numerical simulation of a shale reservoir, which greatly reduces the efficiency of the parameter optimization (Xiao et al., 2022). The optimization of the construction parameters of fractured horizontal wells in shale oil faces considerable challenges thanks to the complexity of the shale reservoir’s characteristics and fracture system, as well as the large number of design variables (Ma et al., 2022).

A large amount of valuable fracturing operation and production performance data have been gathered. Consequently, data mining and machine learning are increasingly being used in the study of fracturing parameter optimization. For the supervised machine-learning model with small samples, the approximate model of objective function and constraint function with variable variation is constructed from a small number of sample points. For wells that need to optimize fracturing parameters, the stimulation effect of fractured wells under different parameter combinations is calculated by changing the combination of fracturing parameters and using the established approximate model to optimize the fracturing parameters. Deng et al. (2022) proposed a new integrated optimization algorithm that is based on the field data, aiming at NPV, and realized the integrated optimization of continuous and discrete fracture parameters. Based on a large number of CFD modeling results, Wang et al. (2022a) established an artificial neural network model to optimize construction parameters, which can then be used to optimize the design of the perforation and fracturing parameters. Li-Yang et al. (2022) adopted a BP neural network and genetic algorithm to establish a productivity prediction model and form a genetic optimization design method for horizontal well fracturing. Zhang et al. (2021) used the unsupervised K-means clustering algorithm based on Euclidean distance to cluster reservoirs according to reservoir seepage and geo-mechanical parameters, identify the compressible area of the reservoir fracturing stage, and obtain the fracturing area and fracture morphology through numerical simulation of the reservoir perforation and fracturing process to evaluate the fracturing effect. However, these studies only proposed the optimization of some construction parameters, which should also include horizontal stage length, number of fracturing stages, proppant consumption, and fluid volume (Wang and Chen, 2019). Based on this, some scholars have further established the optimal design model by considering the matching of construction parameters and geological parameters.

Shahkarami et al. (2018) used a publicly available data database from more than 2000 Wells in southwest Pennsylvania to establish a hydraulic fracturing parameter optimization design model that is based on linear regression, support vector machine, artificial neural network, Gaussian process, and other machine-learning methods. Through sensitivity analysis, Nguyen-Le and Shin (2019) determined the framework of controlling factors to put forward a dynamic economic index, and realized the N_p value optimization model considering the comprehensive influence of reservoir parameters and fracturing parameters. Duplyakov et al. (2020) used a boosting algorithm to optimize hydraulic fracturing design based on the data of 22 oil fields, which considered the influence of geological parameters on the optimization of construction parameters. Tan et al. (2021) took the statistical data of fractured wells in WY block as the data set and established a production prediction model based on six machine-learning algorithms, including random forest, support vector regression, back propagation neural network, XGBoost, LightGBM, and multiple linear regression. They then optimized each construction parameter with the goal of improving yield and the cost-profit ratio. Guo et al. (2022) adopted the PCA-GRA method to determine the main control factors of tight oil production. They established a BP neural network model with tight oil production as output and main control factors as input. This model could predict production and optimize construction parameters. Taking 75 fractured horizontal wells in Mahu area as an example, Ma et al. (2021) adopted the random forest algorithm to determine the main control factors of post-pressure productivity according to

16 influencing factors in two types of reservoirs and engineering. They established a productivity prediction model that is optimized by a genetic algorithm with inverse propagation algorithm and neural network, and then optimized the fracturing design of horizontal wells based on this. Hui et al. (2021) used Pearson correlation coefficient and feature selection process method. They used 13 geological and construction parameters (e.g., logging and core experiment) as input variables, and established an optimization model with the goal of maximizing accumulations in 12 months through the Extra Trees algorithm. Their results showed that a 73% increase in fluid volume and a 38% increase in proppant use could double post-fracture production. Under boundary constraints, Duplyakov et al. (2022) used the high-dimensional black box approximation function to optimize fracturing design parameters based on Ridge regression and CatBoost algorithm. They also used particle swarm optimization, sequential least squares programming, surrogate optimization model and differential evolution optimization method to solve the problem. Xiao et al. (2022) proposed a machine-learning assisted global optimization framework that is based on radial basis functions, K-nearest neighbors, and multi-layer perceptrons to quickly obtain the optimal fracture parameters. Syed et al. (2022) established Pearson correlation estimation between each pair of input parameters and developed a prediction model using deep learning that could integrate basic geological information with a completion strategy. Wang et al. (2022b) used fracturing fluid (e.g., reflux ratio and first production) as the objective function, based on the least square method, support vector regression algorithm, and the non-dominant sorting genetic algorithm. They established a fracturing parameters optimization design method using length, horizontal well fracturing series, fracture length, fracture fluid injection, the viscosity of fracturing fluid, fracturing fluid volume, and amount of proppant as optimization variables. They were then able to establish the optimization framework of objective parameters.

This optimization design method of fracturing parameters has achieved satisfactory results. However, the fracturing parameter optimization method based on machine learning still experiences the following problems. First, the reservoir parameter values are derived from the limit value and the average deterministic numerical, without fully considering the reservoir parameters, due to uncertainties or under experimental apparatus, experimental method, or calculation error (e.g., ignoring that these parameters have a characteristic certain fuzziness). Second, when the reservoir parameters, fracturing parameters, and stimulation effect of fractured wells are used to establish a mathematical relationship through mathematical statistics, there is always a strong correlation between these influencing factors. When establishing the optimization model of fracturing parameters, a large number of parameters are directly input into the model. However, the network structure constructed is too complex and the learning of the network model is difficult. The deviation of optimal fracturing parameters will increase when there is no definite mathematical relationship between the stimulation effect and reservoir parameters, and between the fracturing parameters and reservoir parameters. Finally, there are too few optimal fracturing parameters to choose and the final optimization may only be equivalent to finding the local optimal fracturing parameters rather than the global optimal fracturing parameters in the true sense.

To tackle the issues of optimizing the shale oil construction parameters, random forest was used to determine the main control factors and weights of the fracturing effect. The dimensionality of the parameters affecting the fracturing effect was reduced by principal component analysis. The principal components after reducing dimensionality were used as the input parameters of the fuzzy comprehensive evaluation model. The fuzzy mathematical evaluation method was introduced to establish the fracturing effect evaluation model considering the comprehensive effects of single factor and multiple factors, predict the stimulation effect of different fracturing construction parameters, and to select the optimal scheme.

2 Data sources and research methods

2.1 Study area overview

The research area is located between Cangxian Uplift, Xuhei Uplift, and Kongdian Uplift in the hinterland of the Bohai Bay Basin. It is a fault-depression lake basin that was developed under the background of Paleogene regional stretching, and is divided into five tectonic units: Nanpi slope, Kongdong slope, Kongxi slope, Kongdian tectonic belt, and Shenusi faulting (Ren et al., 2010). The main sedimentary strata in the lake basin are Kongdian Formation, which are Kong3 member, Kong2 member, and Kong1 member (from bottom to top). Among them, Kong2 member is a lake flood deposition of Kongdian Formation with thick mud shale and sandstone, coarse-grained deposition of braided river delta medium fine sandstone is developed at the edge of the lake basin, and mud shale is mainly found in the middle of the lake basin. The second member of the hole can be divided into four fourth-order sequences (SQEk_2^4—SQEk_2^1) and 10 fifth-order sequences (Ek_2^1SQ①—Ek_2^4SQ⑩) from bottom to top (Pu et al., 2015), among which SQEk_2^3—SQEk_2^1 is a shale segment with high organic matter abundance 300–500 m thick, covering an area of 1187 km^2. The 21 layers which can be traced and compared in the whole region, which were further divided. The preliminary exploration practice shows that, first, the reservoir has strong heterogeneity, complex physical properties, and many lithologic types encountered in a single well. Post-pressure oil production is

TABLE 1 W Data collection results.

Well no.	Geological factors													Engineering factors									Cumulative oil production in 12 months km (t/km)
	Natural gamma ray	TOC/ %	Ro	S1	OSI	Brittleness index	Young's modulus/ MPa	Poisson's ratio	Minimum horizontal principal stress/MPa	Horizontal principal stress difference coefficient	Total length of fracturing section/m	Angle between wellbore and principal stress direction/ °	Length of horizontal section/m	Average segment length/ m	Mean cluster spacing/ m	Fluid volume per meter/ m^3/m	Slick water ratio	Sand amount per meter/ m^3/m	Proportion of quartz sand	Water and sand ratio/ %	Average displacement/ m^3/min	Shut in well time/ d	
w1	110	3.70	2	2.680	0.724	0.755	37379.796	0.228	83.043	0.280	946	50	1,465	63.07	16.45	36.04	0.80	1.47	0.31	4.07	12.53	12	5047.19
w2	104.87	2.67	2	2.297	0.860	0.801	37671.105	0.228	83.852	0.279	1,228	55	1,314	61.39	15.76	33.13	0.82	1.09	0.31	3.30	10.46	13	3982.93
w3	84.94	4.08	2	6.144	1.506	0.788	39669.410	0.228	89.635	0.288	1,480	60	1706	56.92	8.37	28.20	0.53	2.55	0.50	9.04	12.65	16	3,886.52
w4	91.12	3.51	2	2.967	0.845	0.760	34369.664	0.228	84.481	0.264	1,088	60	1,167	63.98	8.73	27.07	0.50	2.60	0.47	9.59	12.39	29	2047.50
w5	103.67	3.02	2	4.779	1.583	0.763	36482.200	0.228	86.430	0.271	822	45	890	30.44	5.13	41.96	0.70	3.29	0.64	7.83	13.63	20	3982.24
w6	85.28	3.96	2	4.376	1.105	0.761	37138.505	0.228	85.189	0.278	1,078	42	1,241	56.74	7.38	29.22	0.43	2.80	0.48	9.60	12.49	17	2171.42
w7	102.99	3.70	2	4.665	1.261	0.762	36914.719	0.227	88.411	0.275	1,440	60	1,385	55.38	7.94	28.91	0.43	2.50	0.50	8.65	12.61	17	2435.91
w8	108.99	4.20	2	3.243	0.772	0.757	32778.369	0.229	81.958	0.255	853	47	972	56.89	6.91	30.78	0.47	2.73	0.51	8.87	12.47	17	2928.35
w9	98.44	2.23	2	3.053	1.369	0.778	37379.796	0.228	83.043	0.280	904	47	1,100	43.06	6.39	26.98	0.75	2.25	0.65	8.32	13.31	11	2477.33
w10	110.33	2.59	2	2.246	0.867	0.790	37671.105	0.228	83.852	0.279	617	45	693	41.11	5.56	26.81	0.75	2.21	0.68	8.22	12.35	32	2095.80
w11	99.22	2.87	2	1.988	0.693	0.802	37671.105	0.228	83.852	0.279	703	45	664	43.94	5.87	23.66	0.61	2.05	0.39	8.65	12.42	31	1661.26
w12	107.60	1.94	2	2.738	1.411	0.776	37671.105	0.228	83.852	0.279	621	45	651	47.77	5.88	21.52	0.63	1.57	0.68	7.28	11.76	32	3323.65
w13	107.90	2.09	2	2.818	1.348	0.764	37671.105	0.228	83.852	0.279	1,328	31	1,391	57.74	6.87	20.57	0.80	1.49	0.72	7.22	11.76	31	2109.55
w14	82.20	3.24	2	3.441	1.062	0.805	36607.794	0.228	79.756	0.279	414	57	590	45.94	6.63	35.01	0.63	2.16	0.66	6.18	13.35	15	11116.36
w15	101.61	3.63	2	3.853	1.061	0.808	36607.794	0.228	79.756	0.279	566	57	584	43.54	6.32	39.17	0.66	2.38	0.69	6.08	13.04	15	8744.55
w16	92.10	3.83	2	4.506	1.177	0.799	36607.794	0.228	79.756	0.279	515	57	637	42.88	6.15	36.79	0.66	2.07	0.67	5.62	13.44	15	7321.00
w17	52.51	1.81	2	1.097	0.606	0.778	36607.794	0.228	79.756	0.279	536	58	460	29.78	5.21	47.89	0.47	3.22	0.45	6.72	12.70	17	3081.32
w18	92.60	3.35	2	2.010	0.600	0.795	36607.794	0.228	79.756	0.279	589	47	577	32.72	5.50	41.35	0.43	2.80	0.44	6.77	12.59	17	2690.98
w19	91.76	4.04	2	4.949	1.225	0.810	35254.016	0.228	83.251	0.267	956	66	1,003	59.72	8.97	30.70	0.77	2.64	0.75	8.60	11.79	59	8604.46
w20	89.04	2.73	2	4.980	1.824	0.799	36907.946	0.229	86.770	0.274	1,022	66	926	53.79	7.95	29.70	0.67	1.94	0.79	6.54	10.92	8	10426.78
w21	89.41	3.49	1	0.878	0.252	0.785	27104.553	0.231	49.715	0.226	716	20	696	65.12	7.64	26.65	0.58	2.90	0.56	10.87	11.39	25	521.57
w22	91.64	2.15	1	0.477	0.222	0.750	30592.453	0.230	53.840	0.251	1,080	20	1,050	63.51	7.90	20.87	0.56	2.38	0.53	11.42	10.88	20	1049.48
w23	95.51	1.92	1	0.465	0.242	0.758	30592.453	0.230	53.840	0.251	792	20	600	65.96	7.92	22.73	0.58	2.48	0.56	10.90	8.63	22	1360.62
w24	102.20	3.13	2	4.572	1.461	0.806	39669.410	0.228	89.635	0.288	802	47	1,070	53.44	7.71	31.71	0.45	2.88	0.51	9.09	12.78	15	4339.58

TABLE 2 Screening results of the main control factors.

Serial number	Property	Importance	Serial number	Property	Importance
1	Brittleness index	0.3563	9	OSI	0.0245
2	Water and sand ratio/%	0.1355	10	Natural gamma ray	0.0191
3	Proportion of quartz sand	0.0887	11	Length of horizontal section/m	0.0189
4	S1	0.0745	12	Sliding water ratio	0.0183
5	shut in well time/d	0.0489	13	Mean cluster spacing/m	0.0158
6	Fluid volume per meter/m^3/m	0.0476	14	TOC/%	0.0155
7	Angle between wellbore and Principal stress direction/°	0.0380	15	Average displacement/m^3/min	0.0152
8	Total length of fracturing section/m	0.0361	16	Poisson's ratio	0.0120

comprehensively affected by geological factors, engineering parameters and production system, and the fracturing effect is quite different. It is therefore necessary to further clarify the main controlling factors that affect the fracturing effect. Second, the production of different wells varies greatly after fracturing, which reflects the poor matching between the construction parameters of some wells and the reservoir, which affects the stimulation effect. Consequently, research on the optimization of construction parameters matching the geological characteristics of single well is urgently required.

2.2 Data source and analysis

In total, 24 fractured horizontal wells of shale oil in area W were taken as samples to fully collect on-site geological, engineering, and production parameters, as well as production data. The collected data results are shown in Table 1. Well W24 was selected as the test well to verify the rationality of the proposed method and to optimize the construction parameters. The remaining fractured wells were used as training wells to obtain the main control factors of the production of shale oil fractured horizontal wells. The function model of fuzzy comprehensive score and production was fitted.

2.2.1 Main control factors and weight determination method selection

The characteristics of tight shale oil reservoirs and low-pressure coefficient in W area determine whether industrial production can only be obtained through large-scale reconstruction, and whether the oil production is affected by geological and engineering factors. To establish an optimization method for the construction parameters of fractured horizontal wells, the construction parameters can quickly and efficiently be optimized by identifying the main controlling factors and assigning reasonable weights.

In this paper, the random forest algorithm is chosen to select representative main control factors. Compared with traditional prediction models, random forest has the following advantages. First, it has strong adaptability to data sets, does not need the data to meet the preset assumptions or specific functional forms, is insensitive to multivariate collinearity, and is robust to missing data and unbalanced data. Second, the modeling is simple and efficient, and the generalization ability is strong, which can quickly capture the inflection point by using the advantages of multi-path parallel decision tree. With the increase of the number of regression trees, the error of random forest model can be reduced on the whole. Compared with a support vector machine or an artificial neural network, it has fewer calibration parameters, and only needs to specify the number of regression trees and the number of features sampled from each bifurcation node, consequently the training process is simpler and faster. Third, it can deal with high-dimensional data sets and random forest can avoid the common problems of machine learning (e.g., over-fitting and under-fitting). Finally, random forest can get the weight of each variable and avoid the interference of subjective factors when the weight is artificially assigned. Therefore, this paper intends to use random forest to analyze the main control factors and determine the weight.

2.2.2 Principle of the random forest algorithm

The random forest algorithm is another combination prediction algorithm that was proposed by Breiman after the Bagging algorithm (Breiman, 2001). Based on decision trees, it builds multiple decision trees through random repeated sampling technology (Boostrap technology; Freeman, 1998) and random node splitting technology, and finally combines the prediction results of a large number of decision trees and outputs them as a whole. Ensemble learning through multiple decision trees can effectively overcome the problems of over-fitting and low classification accuracy of a single decision tree, and can effectively reduce the generalization error of the learning system (He et al., 2020). The steps that are used by the random forest method to determine the weight are described in the following subsections.

2.2.2.1 Screening the main control factors

The data that are randomly sampled and not drawn during random forest modeling are called out-of-pocket data sets, which are not involved in the fitting of the training set model and can be used to test the generalization ability of the model (Lei et al., 2020). When ranking the importance of the model, the corresponding out-of-pocket data is used to calculate its out-of-pocket error r_1. The order of a feature in the out-of-pocket data is then randomly transformed and the out-of-pocket error r_2 is calculated again. Assuming that the random forest has N trees, the importance of a feature I is:

$$I = \frac{1}{N}\sum_{I=1}^{N}(r_1 - r_2), \tag{1}$$

where I is the importance of a feature, and is dimensionless; N is the number of trees in the random forest, and is dimensionless; r_1 is the out-of-pocket error, and is dimensionless; and r_2 is the out-of-pocket error of a feature sequence after random transformation, and is dimensionless.

The importance of each characteristic parameter of 23 trained fractured horizontal wells can be obtained using the random forest algorithm, among which the most important is the main control factor of the production of fractured horizontal wells in shale oil. The screened results according to the above principles are shown in Table 2. As can be seen from Table 2, the rock brittleness index and the sand-liquid ratio in the main control factors of the production of fractured horizontal wells in shale oil in this block are significantly more important than other main control factors in geological parameters, which indicates that these main control factors contribute greatly to the production of fractured horizontal wells in shale oil.

2.2.2.2 Weight determination

With regard to random forests, impurity has been adopted as the best division of the measurement classification tree and the impurity calculation has been made with the Gini index method, which is one of the most widely used segmentation rules. Assuming that the set T contains records of k categories, then the Gini index is:

$$Gini(T) = 1 - \sum_{j=1}^{k} p_j^2, \tag{2}$$

where $Gini(T)$ is the Gini index of set T, and is dimensionless; k is the number of categories, and is dimensionless; and p_j denotes the frequency of T occurrence of category j, and is dimensionless.

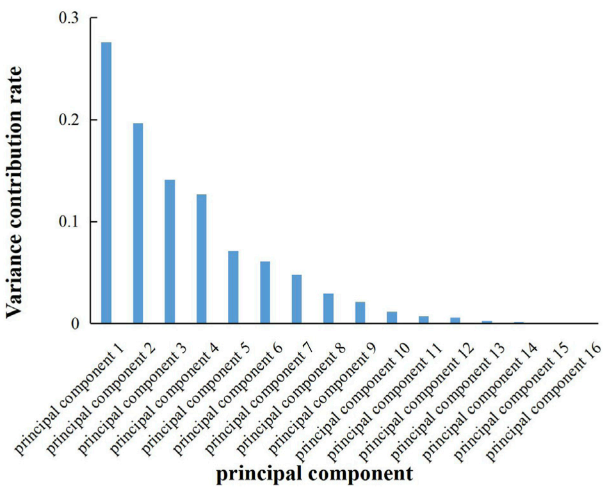

FIGURE 1
Variance explained by principal components.

The maximum useful information can be obtained when the $Gini(T)$ minimum is 0 (i.e., all of the records on this node belong to the same category). $Gini(T)$ is maximum when all of the records in this node are uniformly distributed with respect to the category field, which indicates that the minimum useful information is obtained. If the set T is divided into s parts T_i ($i = 1,2...,s$). To calculate the Gini coefficient, the reduction in the Gini coefficient of the variable x_i used to split at each split node is calculated. Then, the Gini index for this segmentation is:

$$Gini_{split}(T) = \sum_{i=1}^{s} Gini(T_i)N_i \Big/ (N), \tag{3}$$

where $Gini_{split}(T)$ is the segmented Gini index, and is dimensionless.

For the classification regression tree, if the node T does not satisfy that the samples in T belong to the same category or there is only one sample left in T, then this node is a non-leaf node. The original segmentation Gini index of the ith classification regression tree is $Gini_{split}(x_i)$, and the Gini index after randomly replacing the variable attribute value j of the separation point is $Gini_{split}(x_{ij})$. Therefore, the importance of attribute j in the corresponding single classification regression tree can be expressed as $Gini_{split}(x_i)$-$Gini_{split}(x_{ij})$. The importance $\bar{\Delta}_j$ of variable j is calculated by the average Gini index of trees in the forest; that is, the average Gini index reduction value is:

$$\bar{\Delta}_j = \left(\sum_{i=1}^{B}\left(Gini_{split}(x_i) - Gini_{split}(x_{ij})\right)\right)/B, \tag{4}$$

where $\bar{\Delta}_j$ is the importance of variable j, and is dimensionless; and $Gini_{split}(x_i)$ is the original segmented Gini index of the ith classification regression tree, and is dimensionless. $Gini_{split}(x_{ij})$ is the Gini index after randomly replacing the variable attribute value j of the separation point, and is dimensionless. B is the number of trees in the random forest, and is dimensionless.

The weight of indicator variables is:

TABLE 3 Characteristics of the principal components corresponding to the main control factors.

Factor	Principal component 1 feature	Principal component 2 feature	Principal component 3 feature	Principal component 4 feature	Principal component 5 feature	Principal component 6 feature
Natural gamma ray	−0.6294	−0.0382	−0.2730	−0.2370	0.2411	−0.0358
TOC/%	−0.3358	−0.2247	−0.0680	0.1522	−0.3050	0.5284
S1	0.0635	−0.4047	−0.0761	−0.1452	−0.2608	0.0660
OSI	0.1721	−0.3788	−0.0489	−0.2933	−0.0891	−0.2678
Brittleness index	0.2358	−0.2054	0.2843	−0.1062	0.2192	0.4102
Length of horizontal section/m	0.0753	−0.1526	−0.5061	0.0511	−0.1259	−0.0314
Total length of fracturing section/m	0.2732	−0.0693	−0.4955	−0.0212	−0.1918	−0.0333
Angle between wellbore and principal stress direction/°	0.2374	−0.4080	0.0840	0.0838	−0.0378	0.1706
Mean cluster spacing/m	0.1084	−0.0592	−0.3744	0.2753	0.3352	0.2641
Fluid volume per meter/ m^3/m	−0.0065	−0.2092	0.3009	0.3817	0.0452	−0.0208
Proportion of quartz sand	0.1335	−0.0740	0.1907	−0.5495	−0.0503	−0.0871
Water and sand ratio/%	−0.0175	0.3036	−0.0537	−0.2002	−0.4582	0.0982
Shut in well time/d	−0.0913	0.0630	0.0060	−0.3884	−0.0054	0.5320
Average displacement/ m^3/min	−0.4576	−0.3059	0.1961	0.0761	−0.1979	−0.1695
Poisson’s ratio	0.1283	0.3828	0.0634	0.0135	−0.0783	0.2112
Slick water ratio	−0.0328	−0.1226	−0.1030	−0.2680	0.5464	0.0151

$$w_j = \frac{\bar{\Delta}_j}{\sum_{j=1}^{n} \bar{\Delta}_j}, \tag{5}$$

where w_j is the weight coefficient of the jth index variable, and is dimensionless; and n is the number of indicator attributes, and is dimensionless.

Because the dimensionality of the main control factors needs to be reduced before the weight is determined, the weight results of each principal component are shown in Section 3.1 (Model Establishment).

2.3 Optimization of fracturing parameters

2.3.1 Reducing dimensionality with principal component analysis

The random forest algorithm requires high levels of time and cost, and is only suitable for small data sets (Chen and Min, 2022). Taking the main control factors of the production of a large number of shale oil fractured horizontal wells as input parameters of the model will increase the difficulty and complexity of the analysis problem, and reduce the optimization efficiency. The problem can be simplified based on the principal component analysis of the dimensionality reduction, integrating multiple correlation factors for the linear unrelated principal component, using the correlation between the main control factors with a dimension reduction after less principal components instead of many factors, and using the principal component as much as possible to leave the factors reflected in information. The calculation steps are as follows:

1) Data collection, with m evaluation fracturing wells and e main control factor indicators, a sample matrix $\boldsymbol{a}$ with size of $m \times e$ can be formed:

$$a = \begin{pmatrix} a_{11} & \dots & a_{1e} \\ \vdots & \ddots & \vdots \\ a_{m1} & \cdots & a_{me} \end{pmatrix} = [\, a_1 \ \cdots \ a_e \,], \tag{6}$$

where $\boldsymbol{a}$ is the sample matrix; a_{ij} is the main control factor; and a_j is the vector of main control factors.

2) When the index dimensions are inconsistent, the mean and standard deviation are calculated to obtain standardized data (Li et al., 2020), and the correlation coefficient matrix R is established. The original sample matrix is normalized to:

$$A = \begin{pmatrix} A_{11} & \dots & A_{1e} \\ \vdots & \ddots & \vdots \\ A_{m1} & \cdots & A_{me} \end{pmatrix} = [\, A_1 \ \cdots \ A_e \,], \tag{7}$$

where $\boldsymbol{A}$ is the sample matrix after standardization; A_{ij} is the main control factor after standardization; and A_j is the normalized vector of master factors.

Thus, the corresponding correlation coefficient matrix of the sample matrix can be obtained:

$$R = \left(r_{ij}\right)_{e\times e} = \begin{pmatrix} r_{11} & \cdots & r_{1e} \\ \vdots & \ddots & \vdots \\ r_{e1} & \cdots & r_{ee} \end{pmatrix}, \tag{8}$$

where $\boldsymbol{R}$ is the correlation coefficient matrix; and r_{ij} is the correlation coefficient, where:

$$r_{ij} = \frac{1}{m-1}\sum_{q=1}^{m}\left(A_{qi}-\bar{A}_i\right)\left(A_{qj}-\bar{A}_j\right) = \frac{1}{m-1}\sum_{q=1}^{m}A_{qi}A_{qj}, \tag{9}$$

$$\bar{A}_i = \frac{1}{m}\sum_{i=1}^{m}A_{ij}. \tag{10}$$

The correlation coefficient matrix shows the correlation degree among e indexes.

3) Calculate the eigenvalues and eigenvectors of $\boldsymbol{R}$.

Eigenvalues: $\lambda_1 \geq \lambda_2 \geq \cdots \geq \lambda_m \geq 0$ ($\boldsymbol{R}$ is a positive semidefinite matrix, $t_r(R) = \sum_{i=1}^{m}\lambda_i = m$)

Feature vector:

$$c_1 = \begin{bmatrix} c_{11} \\ \vdots \\ c_{e1} \end{bmatrix}, c_2 = \begin{bmatrix} c_{12} \\ \vdots \\ c_{e2} \end{bmatrix}, \ldots, c_e = \begin{bmatrix} c_{1e} \\ \vdots \\ c_{ee} \end{bmatrix}. \tag{11}$$

4) Calculate the variance contribution rate b_i and cumulative contribution rate $b(o)$ of each eigenvector of corresponding eigenvalue:

$$b_i = \frac{\lambda_i}{\sum_{o=1}^{m}\lambda_o}, i = 1, 2, \cdots, m, \tag{12}$$

$$b(o) = \frac{\sum_{o=1}^{i}\lambda_o}{\sum_{o=1}^{m}\lambda_o}, i = 1, 2, \cdots, m, \tag{13}$$

where b_i is the variance contribution rate of each eigenvector of the eigenvalue, and is dimensionless; and $b(o)$ is the cumulative contribution rate of each eigenvector of the eigenvalue, and is dimensionless.

5) Calculate the number of principal components and calculate the expression of each principal component. In general, the number of eigenvectors corresponding to eigenvalues whose value is greater than or equal to 1 and cumulative contribution rate exceeds 85% is taken as the number of principal components. The score of each principal component is calculated according to the linear expression composed of its corresponding feature vector and each index. The ith principal component F_i is calculated as follows:

$$F_i = c_{1i}A_1 + \cdots + c_{ei}A_e, i = 1, 2, \cdots, n, \tag{14}$$

where F_i is the ith principal component, and is dimensionless.

The data of 16 main control factors selected from the collected data of 23 fractured horizontal wells were used as input, and the output was used as the objective function to reduce the dimension of principal components. The variance contribution rate of principal components is shown in Figure 1. The analysis found that the information of the first six principal components accounted for 87% in total, so the first six principal components were selected to replace the original 16 feature parameters.

The characteristics of principal components corresponding to the factors of the six principal components are shown in Table 3. According to the data in Table 3, the main control factor data selected from different fractured horizontal wells are substituted into Eqs 7, 14 to obtain the principal component values of different fractured wells. The results are shown in Supplementary Table S1. The normalized principal component matrix is obtained as shown in Supplementary Table S2.

2.3.2 Fuzzy comprehensive evaluation mathematical model

The post-fracturing effect of shale horizontal wells involves geological and engineering parameters, which are specifically related to petrophysical properties, oil content, mineral composition, fracturing operation parameters, and many other contents. However, each project usually includes multiple parameters, so the optimization of fracturing parameters based on conventional methods is a huge challenge. In addition, ambiguity exists in the optimization of construction parameters for fractured horizontal wells. There are uncertainties in the boundaries of single factors in various types of fractured wells, such as the fuzzy boundaries of porosity, oil content, displacement, sand amount, and so on. There are many factors affecting the production of fractured horizontal wells with different advantages and disadvantages, and each parameter has “I,” “II,” “III,” or “IV” ratings. It is difficult to evaluate multiple parameters that are interwoven together. It can also be seen that there are some defects in using classical mathematical methods to deal with deterministic problems to deal with fuzzy reservoir quality evaluation data. Fuzzy mathematics is an effective tool to deal with the problem of uncertainty fuzziness. It uses the concept of membership function to describe the problem where the boundary of objective things is not clear. The steps of fuzzy comprehensive evaluation are described in the following subsections.

2.3.2.1 Establish the evaluation factor set

The factor is the evaluation index that is involved in the production of fractured wells. In the production evaluation of fractured wells, the factor set is a fuzzy subset composed of n principal components involved in the evaluation well, which is denoted as $\boldsymbol{F}$=(F_1F_2, ..., F_n).

2.3.2.2 Establish the evaluation set

Evaluation set $\boldsymbol{v}$ = (v_1,v_2, . . . ,v_n),$\boldsymbol{v}$ is a fully ordered set (i.e., the rank difference between any two comments in $\boldsymbol{v}$). Note that $\boldsymbol{v}$ is the set of evaluation criteria corresponding to the evaluation factor in $\boldsymbol{F}$. In the production evaluation of fractured wells, $\boldsymbol{v}$ is the set of production levels (levels I, II, III, and IV) corresponding to each evaluation factor. In this paper, $\boldsymbol{v}$ = [100,75,50,25].

2.3.3.3 Fuzzy weight vector of evaluation factors

Usually, the importance of each factor to the evaluation result is different, so it is necessary to assign a corresponding weight w_i (i = 1,2,3,......,n) to each factor F_i, thus forming the weight set $\boldsymbol{W}$. The determination of the weight of the accurate quantization index will directly affect the quantization result. Here, random forest is introduced to seek the primary and secondary relationship of each factor in the system and find out the important factors affecting each evaluation index. The weight w_i of different principal component factors can be obtained by substituting the principal component factor data of different fractured wells into Eqs 2–5.

$$W = (w_1, w_2, \cdots, w_n). \tag{15}$$

2.3.3.4 Determine the single factor evaluation matrix

2.3.3.4.1 Determine the membership function. Membership functions are generalizations of indicator functions in general sets. A function can indicate whether elements in a set belong to a particular subset. An element's indicator function may have a value of 0 or 1, while an element's membership function may have a value between 0 and 1, which indicates the "degree of truth" that the element belongs to a fuzzy set. Membership function is the foundation of fuzzy mathematics engineering applications. There are generally four methods to determine the membership function: fuzzy statistical method, assignment method, borrowing the existing "objective" scale method, and binary contrast ranking method (Xie and Liu, 2013). In view of the objectivity of membership determination, this paper relies on the correlation between the normalized principal component factors and production in Table 2 in the Appendix, according to the corresponding reservoir quality grades (I, II, III, and IV) of each evaluation factor. The fuzzy statistics method and assignment method are integrated to determine the membership function and three forms of membership function are selected, which are large, small, and intermediate. According to the normalization range of different principal component data, the results of different forms of membership functions of different reservoir quality grades are shown in Table 4.

2.3.3.4.2 Membership matrix of fractured wells. We can get different membership function form of the principal component factors through the existing m fracturing wells of geological and engineering parameters dimension reduction after principal component factors and yield of fitting relationship. The membership is divided into class I, II, III, and IV level grades, and into slants big, partial, small, and middle-type membership function expression, respectively. The n principal component factors of m fractured wells were substituted into the membership function expression of four grades to obtain m n ×4 membership matrix $\boldsymbol{H_i}$.

$$H_i = \begin{bmatrix} h_{11} & h_{12} & \cdots & h_{14} \\ h_{21} & h_{22} & \cdots & h_{24} \\ \vdots & \cdots & \cdots & \vdots \\ h_{n1} & h_{n2} & \cdots & h_{n4} \end{bmatrix}, \tag{16}$$

where $\boldsymbol{H_i}$ is the membership matrix; h_{ij} is the membership degree of different principal components, and is dimensionless.

2.3.2.5 Fuzzy comprehensive evaluation

$$\begin{aligned} D_i &= (d_1, d_2, \cdots, d_4) = W \circ H_i \\ &= (w_1, w_2, \cdots, w_n) \circ \begin{bmatrix} h_{11} & h_{12} & \cdots & h_{14} \\ h_{21} & h_{22} & \cdots & h_{24} \\ \vdots & \cdots & \cdots & \vdots \\ h_{n1} & h_{n2} & \cdots & h_{n4} \end{bmatrix}, \end{aligned} \tag{17}$$

where $\boldsymbol{D_i}$ is the fuzzy set of comprehensive evaluation of the ith fractured well; and d_j is the fuzzy comprehensive evaluation value of different principal components of fractured wells.

$$f_i = \sum_{j=1}^{m} (d_j \times v_j) \Big/ \sum_{j=1}^{m} d_j, \tag{18}$$

where $\boldsymbol{f_i}$ is the fuzzy comprehensive score of the ith fractured well.

2.3.3 Optimizing construction parameters

2.3.3.1 Orthogonal experimental design

Orthogonal experiment design, and its analysis of the variance method and intuitive analysis are based on probability theory, mathematical statistics, linear algebra theory of scientific arrangement of the test scheme, and the correct analysis of the test results. Meanwhile, the qualitative index quantitatively determines the parameters of the influence of trend, primary and secondary order, and significant degree to obtain a mathematical optimization method as quickly as possible. By introducing the method of orthogonal experimental design and using the "orthogonal table" to

TABLE 4 Membership function table.

Category	Normalized value	Membership function
Partial large	1–0.75 0.75–0.5 0.5–0.25 0.25–0	$G_1 = \begin{cases} 1 & 0.875 \le x \\ \frac{x-0.625}{0.25} & 0.625 \le x \le 0.875 \\ 0 & x \le 0.625 \end{cases}$ $G_2 = \begin{cases} 0 & 0.875 \le x \\ \frac{0.875-x}{0.25} & 0.625 \le x \le 0.875 \\ \frac{x-0.375}{0.25} & 0.375 \le x \le 0.625 \\ 0 & x < 0.375 \end{cases}$ $G_3 = \begin{cases} 0 & 0.625 \le x \\ \frac{0.625-x}{0.25} & 0.375 \le x \le 0.625 \\ \frac{x-0.125}{0.25} & 0.125 \le x \le 0.375 \\ 0 & x < 0.125 \end{cases}$ $G_4 = \begin{cases} 0 & 0.375 \le x \\ \frac{x-0.625}{0.25} & 0.125 \le x \le 0.375 \\ 1 & x \le 0.125 \end{cases}$
Partial small	0–0.25 0.25–0.5 0.5–0.75 0.75–1	$G_1 = \begin{cases} 0 & 0.375 \le x \\ \frac{x-0.625}{0.25} & 0.125 \le x \le 0.375 \\ 1 & x \le 0.125 \end{cases}$ $G_2 = \begin{cases} 0 & 0.625 \le x \\ \frac{0.625-x}{0.25} & 0.375 \le x \le 0.625 \\ \frac{x-0.125}{0.25} & 0.125 \le x \le 0.375 \\ 0 & x < 0.125 \end{cases}$ $G_3 = \begin{cases} 0 & 0.875 \le x \\ \frac{0.875-x}{0.25} & 0.625 \le x \le 0.875 \\ \frac{x-0.375}{0.25} & 0.375 \le x \le 0.625 \\ 0 & x \le 0.375 \end{cases}$ $G_4 = \begin{cases} 1 & 0.875 \le x \\ \frac{x-0.625}{0.25} & 0.625 \le x \le 0.875 \\ 0 & x \le 0.625 \end{cases}$
Middle type	0.375–0.625 0.25–0.375 0.625–0.75 0.125–0.25 0.75–0.875 0–0.125 0.875–1	$G_1 = \begin{cases} 1 & 0 \le x \le 0.0625 \\ e^{-[(x-0.0625)/s]^2} & 0.0625 \le x \le 0.1875 \\ e^{-[(x-0.9375)/s]^2} & 0.8125 \le x \le 0.9375 \\ 1 & 0.9375 \le x \le 1 \\ 0 & other \end{cases}$ $G_2 = \begin{cases} e^{-[(x-0.1875)/s]^2} & 0 \le x \le 0.1875 \\ e^{-[(x-0.8125)/s]^2} & 0.8125 \le x < 1 \\ 0 & other \end{cases}$ $G_3 = \begin{cases} e^{-[(x-0.3125)/s]^2} & 0.0625 \le x < 0.3125 \\ e^{-[(x-0.6875)/s]^2} & 0.6875 \le x < 0.9375 \\ 0 & other \end{cases}$ $G_4 = \begin{cases} e^{-[(x-0.4375)/s]^2} & 0.3125 \le x < 0.4375 \\ 1 & 0.4375 \le x < 0.5625 \\ e^{-[(x-0.5625)/s]^2} & 0.5625 \le x < 0.6875 \\ 0 & other \end{cases}$

Where G is the membership function; x is the normalized principal component value; and s is the peak value of normal distribution of normalized principal components.

arrange the multi-factor experimental schemes, the intrinsic essential laws contained in a large number of schemes are reflected by a limited number of typical and representative schemes, and the influence trend, primary and secondary order, and the significance degree of parameters on cumulative yield can be quantitatively determined (Zeng et al., 2012). In addition, an orthogonal test can eliminate part of the interference caused by test errors and the results are easy to analyze (Dai et al., 2022).

The target block of the shale oil fracturing engineering parameters of horizontal wells can be optimized and compared through random forest algorithm optimization of fluid, quartz sand proportion, shut in well time/d, sand amount per meter and slippery water ratio, average cluster spacing, the average displacement. These seven factors can influence the production of cumulative gain according to the factors to select the four levels (Table 5). We use a four-level experimental design, and therefore the $L_\alpha(4^\beta)$ orthogonal table should be selected. There are seven factors in the experiment. If the interaction between the factors is not considered, then the orthogonal table with $\beta \ge 7$ should be selected. $L_{216}(4^7)$ is the minimum $L_\alpha(4^\beta)$ orthogonal table meeting the condition of $\beta \ge 7$. The orthogonal table was used to conduct the 12-month cumulative production experiment, and the influence of various factors on the cumulative production was investigated, from which the optimal parameter scheme of horizontal well was obtained.

Through the orthogonal design, 216 simulation schemes can be used to complete 4^7=16384 simulation schemes. This greatly

TABLE 5 Factor level table of horizontal well fracturing parameter optimization experiment.

Parameters of the horizontal	Fluid volume per meter/m^3/m	Water and sand ratio/%	Slick water ratio	Proportion of quartz sand	Mean cluster spacing/m	Average displacement/ m^3/min	Shut in well time/d
1	20.57	3.30	0.43	0.31	5.21	8.63	8
2	25.92	5.33	0.53	0.43	8.02	9.88	13.25
3	31.27	7.36	0.63	0.55	10.83	11.13	18.50
4	41.96	11.42	0.82	0.79	16.45	13.63	29

reduces the simulation workload and is conducive to improving the efficiency.

2.3.3.2 Procedure for selecting the construction parameters

1) The random forest method was used to screen out the main controlling factors that affect the production of m training fracturing wells.
2) Principal component analysis was used to reduce the dimensions of the selected main control factors into n principal components to obtain a principal component matrix with m rows and n columns.
3) Based on the relationship between the principal component data of different columns in the principal component matrix and the yield, the membership function is divided into four parts. The analytical formula of different intervals is obtained for each part according to the form of membership function.
4) The membership matrix of m n rows and four columns of fractured wells can be calculated by substituting the data of each column in the principal component matrix of m rows and n columns into the membership function in Step 3.
5) Based on the relationship between the principal component data of different columns in the principal component matrix and the production, the weight values of the main control factors of shale oil fractured horizontal wells can be obtained using random forest.
6) The fuzzy comprehensive scores of different fractured horizontal wells can be obtained using Eqs 17, 18.
7) The function model of main control factors and production was obtained by fitting the relationship between the fuzzy comprehensive score of different fractured horizontal wells and production.
8) A fracturing construction parameter scheme for U test fractured horizontal wells based on the principle of positive price experiment was designed according to the range of fracturing construction parameters.
9) The schemes in Step 8 are evaluated and compared using the fuzzy comprehensive evaluation model. The scheme with the highest score is the optimized construction parameter. The predicted production of the optimized test fractured horizontal well can be obtained by substituting the score into the function model in Step 7.

3 Results and analysis

3.1 Model establishment

3.1.1 Weight determination

Based on the data in Supplementary Table S1, the principal components of different fractured horizontal wells were applied to determine the weights by the random forest algorithm. The results are shown in Figure 2, which shows that the weight of principal components reaches 0.63.

3.1.2 Fuzzy comprehensive evaluation

The principal component data of different fractured wells in Supplementary Table S2 were substituted into the membership function and the fuzzy set results of comprehensive evaluation of different fractured horizontal wells were obtained using Eqs 16, 17, as shown in Supplementary Table S3. The fuzzy comprehensive scores of different fractured horizontal wells can be obtained by substituting the fuzzy set data of comprehensive evaluation of different fractured horizontal wells in Supplementary Table S3 into Eq. 18. Figure 3 shows the fitting result of the score and 12-month kilometer cumulative production obtained by fitting the score to the 12-month kilometer cumulative production. Figure 4 is the fitting result of the score obtained without dimension reduction and the 12-month kilometer cumulative production. It can be obtained by comparison that the model accuracy is higher and the fitting effect is better after dimension reduction. Therefore, the rationality of the proposed method is fully illustrated.

3.2 Model verification

After reducing the dimensionality of the main control factor data of well W24 by principal components, the data were substituted into Eqs 15–17 to obtain the fuzzy comprehensive score and fitted to obtain the predicted production. A comparison between the actual production and the predicted production results is shown in Table 6. It can be found from this that the relative error of the prediction results is 4.8%, which verifies the rationality of the model in this paper.

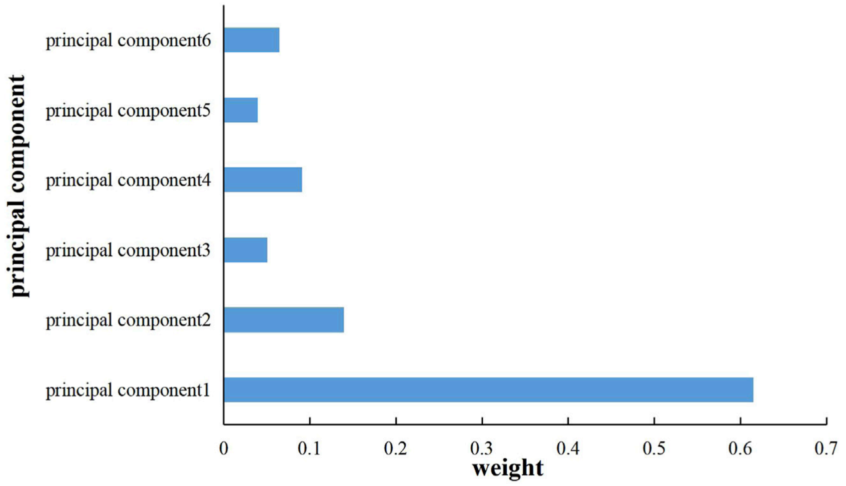

FIGURE 2
Principal component weight values.

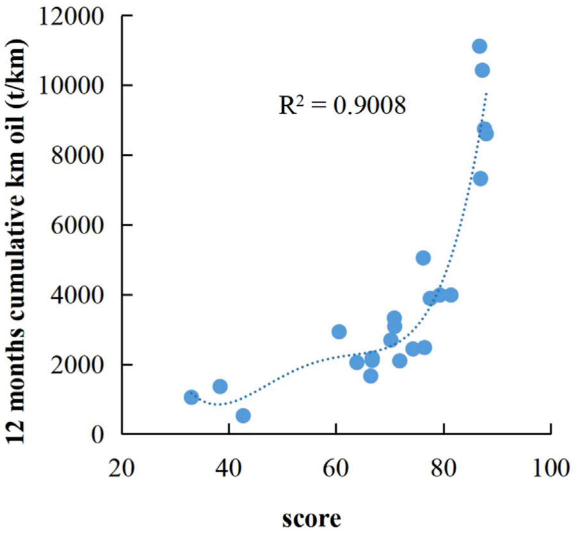

FIGURE 3
Fitting results after reducing dimensionality.

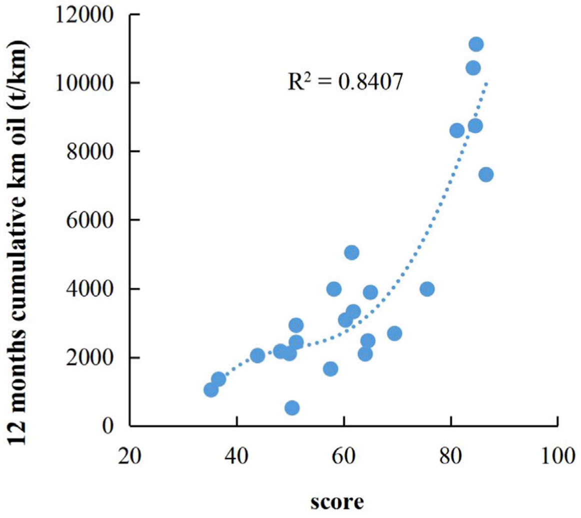

FIGURE 4
Fitting results without reducing dimensionality.

3.3 Field application

The data of the L_{216} (4^7) orthogonal test design scheme can be substituted into the established fuzzy comprehensive evaluation model to predict the output under different construction parameter combinations, as shown in Table 7, which lists the yield prediction results after optimizing parameter combination under 216 simulation schemes. It can be seen that under different construction parameter combinations, the predicted 12-month cumulative production of km varies significantly from 2588.81 t/km to 10742.54 t/km. This shows that the optimization of construction parameters matching with the reservoir can significantly increase production. The optimal No. 147 scheme is selected for construction and the cumulative output of 12 months km is 10144.7 T. The cumulative yield over the 12 months prior to parameter optimization (Table 1) was significantly improved.

Finally, we compare typical wells (The results are shown in Table 8): wells w24 (before optimization) and w25 (after

TABLE 6 Comparison between the actual yield and the model's prediction results.

Well no.	Total score	Cumulative oil production in 12 months km (t/km)		Relative error (%)
		Actual production	Predicted production	
W24	60.72	4339.58	4549.12	4.8

TABLE 7 Design scheme of the orthogonal experiment.

Scheme	Fluid volume per meter/ m^3/m	Water and sand ratio/%	Slick water ratio	Proportion of quartz sand	Mean cluster spacing/ m	Average displacement/ m^3/min	Shut in well time/d	Forecast 12-month cumulative production in km (t/km)
1	42	3.3	0.5	0.4	5.2	13.6	13	6094.97
2	25.9	3.3	0.6	0.8	10.8	8.6	13	7351.56
3	42	11.4	0.6	0.4	16.5	9.9	13	3,717.09
4	25.9	11.4	0.6	0.3	5.2	9.9	29	2192.47
5	25.9	3.3	0.5	0.6	8	9.9	29	6384.71
6	42	5.3	0.6	0.6	16.5	8.6	29	7537.50
7	20.6	11.4	0.6	0.6	10.8	9.9	13	2588.81
8	25.9	11.4	0.5	0.4	10.8	13.6	29	3,296.80
...	...	...	...	...	...	...	...	...
144	31.3	11.4	0.8	0.3	10.8	11.1	8	3,565.52
145	25.9	5.3	0.4	0.4	5.2	11.1	29	4364.63
146	20.6	7.4	0.5	0.6	8	11.1	13	4066.95
147	42	3.3	0.8	0.8	8	8.6	8	10742.54
148	20.6	7.4	0.6	0.6	5.2	13.6	29	5,703.61
149	31.3	11.4	0.5	0.8	5.2	11.1	13	3,830.10
...	...	...	...	...	...	...	...	...
213	31.3	11.4	0.5	0.4	16.5	13.6	19	3,882.65
214	31.3	5.3	0.6	0.8	10.8	13.6	8	6689.87
215	20.6	3.3	0.6	0.3	5.2	8.6	8	4193.63
216	31.3	5.3	0.6	0.6	8	11.1	13	7072.04

TABLE 8 Comparison table of the optimization parameters and construction effect.

Plan	Fluid volume per meter/ m^3/m	Water and sand ratio/%	Slick water ratio	Proportion of quartz sand	Mean cluster spacing/ m	Average displacement/ m^3/min	Shut in well time/d	12-month cumulative production in km (t/km)
w24	31.7	9.1	0.45	0.51	7.71	12.7	15	4339.58
W25	42	3.3	0.8	0.8	8	8.6	8	10144.7

optimization) are two adjacent horizontal wells of similar length on the same platform. The production of well w25 was 2.34 times that of well w24 after the implementation of optimized parameters, and the stimulation effect was obvious (Figure 5). A comparison of the construction scale of the two wells shows that the fluid volume, the proportion of slick water, the

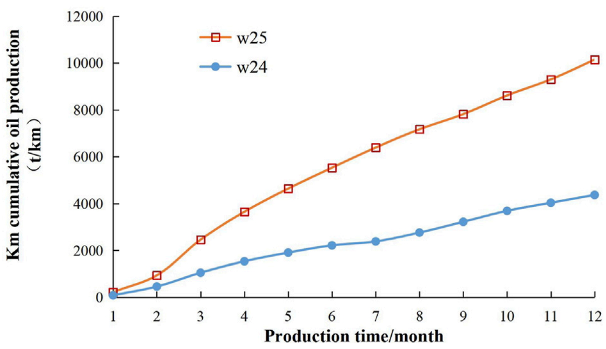

FIGURE 5
Production comparison of W24 and W25.

proportion of quartz sand, and the cluster spacing of well w25 are increased, while the cluster spacing and the average displacement are decreased. This shows that the production can be significantly increased by optimizing the construction parameters.

4 Conclusion

1) Using the random forest method, the main controlling factors of the production of fractured horizontal wells in block W are, successively, the brittleness index (mineral), sand-liquid ratio, quartz sand proportion, S1, soaking length, meter liquid volume, angle between wellbore and principal stress direction, total length of fracturing stage, OSI, natural gamma ray, and so on. Among them, the brittleness index (mineral) has a far greater impact on the yield than other main controlling factors, with an importance of 0.36.
2) After reducing the dimensionality of the 16 original input variables through principal components, the first six principal components extracted contain most of the information of the original variables and these principal components are linearly independent. Selecting the first six principal components as input parameters of the model can reduce noise and error. The R^2 value of the model after reducing dimensionality is 0.9 and that of the model without reducing dimensionality is only 0.84.
3) The fuzzy comprehensive evaluation yield model based on principal component analysis and random forest algorithm that we established in this paper shows that the average relative error of the test well is 4.8%, which verifies the rationality of the model in this paper.
4) Compared with adjacent wells, the fluid volume, slippage water proportion, quartz sand proportion, and cluster spacing of the fractured horizontal well in W25 all increased after optimized parameters, while the cluster spacing and average displacement decreased. W25 well was 2.34 times more productive than the offset well. This shows that the production can be significantly increased by optimizing the construction parameters.

Data availability statement

The raw data supporting the conclusion of this article will be made available by the authors, without undue reservation.

Author contributions

DL conceived and designed the experiments; YL and YJ performed the experiments; XL, GX, ZT, LM, CZ, WJ, SX, ZD, TH, ZY, and LY wrote the paper.

Funding

This research was supported by the Natural Science Foundation of China (Grant No. U21A20105).

Conflict of interest

XL, DL, YJ, YL, XG, ZT, CZ, LM, WJ, SX, ZD, and TH were employed by PetroChina Dagang Oilfield Company.

The remaining authors declare that the research was conducted in the absence of any commercial or financial relationships that could be construed as a potential conflict of interest.

Publisher's note

Supplementary material

The Supplementary Material for this article can be found online at: https://www.frontiersin.org/articles/10.3389/feart.2022.1015107/full#supplementary-material

References

Breiman, T. (2001). Random forests[J]. *Mach. Learn* 45 (1), 5–32.

Chen, R., and Min, M. (2022). Random forest algorithm based on PCA and hierarchical selection in Spark[J]. *Comput. Eng. Appl.* 58 (06), 118–127.

Dai, S., Wang, H., An, S., and Yuan, L. (2022). Mechanical properties and microstructural characterization of metakaolin geopolymers based on orthogonal tests. *Materials* 15 (8), 2957. doi:10.3390/ma15082957

Deng, H., Sheng, G., Zhao, H., Meng, F., Zhang, H., Ma, J., et al. (2022). Integrated optimization of fracture parameters for subdivision cutting fractured horizontal wells in shale oil reservoirs. *J. Petroleum Sci. Eng.* 212, 110205. doi:10.1016/j.petrol.2022.110205

Duplyakov, V. M., Morozov, A. D., Popkov, D. O., Shel, E., Vainshtein, A., Burnaev, E., et al. (2022). Data-driven model for hydraulic fracturing design optimization. Part II: Inverse problem. *J. Petroleum Sci. Eng.* 208, 109303. doi:10.1016/j.petrol.2021.109303

Duplyakov, V., Morozov, A., Popkov, D., Vainshtein, A., Osiptsov, A., Burnaev, E., et al. (2020). "Practical aspects of hydraulic fracturing design optimization using machine learning on field data: Digital database, algorithms and planning the field tests[C]," in SPE Symposium: Hydraulic Fracturing in Russia. Experience and Prospects.

Freeman, T., Jr. (1998). Bootstrap methods and their applications[J]. *Interfaces* 28 (6), 71–72.

Guo, D., Kang, Y., Wang, Z., Zhao, Y., and Li, S. (2022). Optimization of fracturing parameters for tight oil production based on genetic algorithm. *Petroleum* 8 (2), 252–263. doi:10.1016/j.petlm.2021.11.006

Guo, J., Lu, Q., Zhu, H., Wang, Y., and Ma, L. (2015). Perforating cluster space optimization method of horizontal well multi-stage fracturing in extremely thick unconventional gas reservoir. *J. Nat. Gas Sci. Eng.* 26, 1648–1662. doi:10.1016/j.jngse.2015.02.014

He, J., Wen, X., Nie, W.-L., Li, L., and Yang, J. (2020). Prediction of fracture zones using random forest algorithm [J]. *Oil Geophys. Prospect.* 55 (1), 161–166.

Hu, S., Zhao, W., Hou, L., Yang, Z., Zhu, R., Wu, S., et al. (2020). Development potential and technical countermeasures of continental shale oil in China[J]. *Petroleum Explor. Dev.* 47 (04), 819–828.

Hui, G., Chen, S., He, Y., Wang, H., and Gu, F. (2021). Machine learning-based production forecast for shale gas in unconventional reservoirs via integration of geological and operational factors. *J. Nat. Gas Sci. Eng.* 94, 104045. doi:10.1016/j.jngse.2021.104045

Lei, J., Ju-Hua, L., and Jia-Lin, X. (2020). Application of random forest algorithm in multi-stage fracturing of shale gas field [J]. *Petroleum Geol. oilfield Dev. daqing* 39 (06), 168–174.

Li, Yongxiang, Cao, Zeyang, and Yang, Zhiwei (2020). Evaluation of maintenance support ability of maintenance personnel based on principal component analysis[J]. *Mod. Def. Technol.* 48 (04), 110–116.

Li-Yang, S., Wang, J.-w., and Chang-yin, L. (2022). Intelligent fracturing design method for horizontal Wells based on BP-GA algorithm[J]. *Fault block oil field* 29 (03), 417–421.

Ma, C., Xing, Y., Qu, Y., Cheng, X., and Wu, H. (2022). A new fracture parameter optimization method for the horizontal well section of shale oil[J]. *Front. Earth Sci.* 10, 2296–6463.

Ma, J., shi, S., jin, C., Zhang, J., He, X., Li, X., et al. (2021). Optimization of fracture design for horizontal wells in Mahu region based on machine learning. *J. Shenzhen Univ. Sci. Technol.* 38 (06), 621–627. doi:10.3724/sp.j.1249.2021.06621

Moradidowlatabad, M., and Jamiolahmady, M. (2018). The performance evaluation and design optimisation of multiple fractured horizontal wells in tight reservoirs. *J. Nat. Gas Sci. Eng.* 49, 19–31. doi:10.1016/j.jngse.2017.10.011

Nguyen-Le, V., and Shin, H. (2019). Development of reservoir economic indicator for Barnett Shale gas potential evaluation based on the reservoir and hydraulic fracturing parameters. *J. Nat. Gas Sci. Eng.* 66, 159–167. doi:10.1016/j.jngse.2019.03.024

Pu, X., Han, W., Zhou, L., Chen, S., Zhang, W., Shi, W., et al. (2015). Lithologic characteristics and geological significance of fine-grained facies area of kong2 high level system domain in cangdong sag, huanghua depression[J]. *China Pet. Explor.* 20 (05), 30–40.

Rahmanifard, H., and Plaksina, Q., (2018). Application of fast analytical approach and AI optimization techniques to hydraulic fracture stage placement in shale gas reservoirs. *J. Nat. Gas. Sci. Eng.* 52, 367–378. doi:10.1016/j.jngse.2018.01.047

Ren, J., Liao, Q., Lu, G., Fu, L., Zhou, J., Qi, P., et al. (2010). Tectonic deformation pattern and evolution process analysis in huanghua depression[J]. *Tect. metallogeny* 34 (04), 461–472.

Rodriguez, R. S., and Soeder, D. J. (2015). Evolving water management practices in shale oil & gas development. *J. Unconv. Oil Gas Resour.* 10, 18–24. doi:10.1016/j.juogr.2015.03.002

Shahkarami, A., Ayers, K., Wang, G., and Ayers, A. (2018). "Application of machine learning algorithms for optimizing future production in marcellus shale, case study of southwestern Pennsylvania[C]," in SPE/AAPG Eastern Regional Meeting.

Syed, F. I., Alnaqbi, S., Muther, T., Dahaghi, A. K., and Negahban, V. (2022). Smart shale gas production performance analysis using machine learning applications[J]. *Petroleum Res. Engl.* 7 (1), 21–31.

Tan, C., Yang, J., Cui, M., Hua, W., Chunqiu, W., Hanwen, D., et al. (2021). Lithosphere, 2021.Fracturing productivity prediction model and optimization of the operation parameters of shale gas well based on machine learning[J]

Wang, J., Singh, A., Liu, X., Rijken, M., Tan, Y., and Naik, S. (2022). Efficient prediction of proppant placement along a horizontal fracturing stage for perforation design optimization. *SPE J.* 27 (02), 1094–1108. doi:10.2118/208613-pa

Wang, L., Yao, Y., Wang, K., Adenutsi, C. D., Zhao, G., and Lai, F. (2022). Data-driven multi-objective optimization design method for shale gas fracturing parameters. *J. Nat. Gas Sci. Eng.* 99, 104420. doi:10.1016/j.jngse.2022.104420

Wang, S., and Chen, S. (2019). Insights to fracture stimulation design in unconventional reservoirs based on machine learning modeling. *J. Petroleum Sci. Eng.* 174, 682–695. doi:10.1016/j.petrol.2018.11.076

Xiao, C., Zhang, S., Ma, X., Zhou, T., and Li, X. (2022). Surrogate-assisted hydraulic fracture optimization workflow with applications for shale gas reservoir development: A comparative study of machine learning models. *Nat. Gas. Ind. B* 9 (3), 219–231. doi:10.1016/j.ngib.2022.03.004

Xie, Jijian, and Liu, Chengping (2013). *Fuzzy mathematics method and its application[M]*. Wuhan: Huazhong University of Science and Technology Press.

Zeng, F., Guo, J., He, S., and Zeng, L. (2012). Optimization of fracture parameters for fractured horizontal Wells in tight sandstone gas reservoirs [J]. *Nat. gas industry* 32 (11), 54–58.

Zhang, d., Yulong, w., and Li, S. (2021). Stage optimization of multi-stage perforation fracturing based on unsupervised machine learning[J]. *J. China Univ. Petroleum Nat. Sci. Ed.* 45 (04), 59–66.

frontiers | Frontiers in Earth Science

TYPE Original Research
PUBLISHED 11 January 2023
DOI 10.3389/feart.2022.1013167

OPEN ACCESS

EDITED BY
Francesco Ascione,
University of Salerno, Italy

REVIEWED BY
Songyan Li,
China University of Petroleum, China
Wei Zhou,
Chang'an University, China

*CORRESPONDENCE
Xiangyang Mo,
xiangyangmo98@163.com
Wenbin Cai,
caiwenbin@xsyu.edu.cn

SPECIALTY SECTION
This article was submitted to Environmental Informatics and Remote Sensing, a section of the journal Frontiers in Earth Science

RECEIVED 06 August 2022
ACCEPTED 28 September 2022
PUBLISHED 11 January 2023

CITATION
Cai W, Mo X, Li W, Liu S, Zhou D, Zhang H and Huang Z (2023), Study of fatigue damage of pumping rods based on finite element simulation.
Front. Earth Sci. 10:1013167.
doi: 10.3389/feart.2022.1013167

Study of fatigue damage of pumping rods based on finite element simulation

Wenbin Cai[1]*, Xiangyang Mo[1]*, Wen Li[2], Shun Liu[1], Desheng Zhou[1], Huiren Zhang[1] and Zhimin Huang[1]

[1]College of Petroleum Engineering, Xi'an Shiyou University, Xi'an, China, [2]Research Institute of Engineering Technology, PetroChina Xinjiang Oilfield Company, Karamay, China

This study performed in-depth analysis of onsite fatigue damage and stress distribution in pumping rods. Two aspects of fatigue damage were analyzed: macroscopic morphology and chemical properties. In terms of chemical properties, the crystalline phase composition and hardness of the product at fatigue damage were analyzed; the stress distribution was analyzed in term so of the rod-body stress and the connection-section stress. The cross-sectional characteristics of the fatigue crack expansion were summarized, and the types of fatigue fracture and the influencing factors of the pumping rod were obtained from these cross-sectional characteristics. Finally, modeling and stress analysis of the pumping rod were performed using SolidWorks and ABAQUS software. By comparing the stress cloud diagrams of different thread root shapes, the factors that cause fracture in the pumping rod and the locations of stress concentrations and dangerous cross-sections of the rod were determined. The highest principal stresses were obtained at the rod body near the upsetting flange of the pumping rod, and fatigue damage was the most likely to occur at this location. The shoulder of the unloading groove and the upsetting flange area were relatively safe because of their large cross-sectional area and less likelihood to produce stress concentrations. The results of this study can provide scientific guidance and reference for the development of pumping rods for efficient oil production and the improvement of oil and gas production efficiency.

KEYWORDS

pumping rods, fatigue fracture, stress distribution, crack extension, finite element simulation

1 Introduction

The pumping rod is a crucial link in a pumping system but weaker than ground equipment. A common form of damage to the pumping rod is fracture, wherein the rod is subjected to asymmetric cyclic loading during service; the cracks form and expand until fracture occurs (Gibbs and Neely, 1966). Fractures do not only influence production but also cause large economic losses. According to a field survey, the sum of the well operation cost and discounted production of crude oil was 20–30 thousand yuan per rod breaking

FIGURE 1
Fatigue cross-sectional shape of the pumping rod.

accident. In one oil field, there were a total of 821 pumping rod breakage accidents from 1995 to 1998, accounting for 62% of the total number of wells repaired and economic losses of more than 20 million yuan (Chen et al., 1994). Thus, ensuring normal operation of the pumping rod helps improve crude oil production and reduce production costs with significant social and economic benefits.

Several studies have been performed worldwide, and the fatigue life of the pumping rod column was investigated from the perspective of crack expansion (Li et al., 1994a; Zhang et al., 2000; Ding et al., 2019). The German engineer Wöhler experimentally analyzed fatigue phenomena and laid the foundation for fatigue research in a paper on the subject. In the 1950s, researchers began to use techniques such as electron microscopy to investigate cracking, thus inspiring the development of fracture mechanics theory. Ghofrani and Ulmanu (Ulmanu and Ghofrani, 2001) applied the theory of crack expansion and calculated the fatigue life of pumping rods. Li Qi et al. (Li et al., 1994b) analyzed the expressions of the stress intensity factor of rod cracks and the crack extension life based on the theoretical principle of fracture mechanics. Guoli et al. (Wang and Wei, 1994) obtained the fatigue crack expansion rate of the rod and column. Xiaobing et al. (Xu and Yuan, 1993) performed theoretical analysis and experimental simulation to apply fracture mechanics theory to predict the fatigue life of a pumping rod with a crack extension. Xiuhua et al. (Du et al., 2006) used the fracture mechanics theory to investigate the influence of the crack expansion condition of the rod-post surface on the cracking of the rod-post system. Zizi et al. (Xiang et al., 2010) constructed the calculation models for the fatigue crack expansion rate and fatigue limit at threshold stress-intensity factor and fatigue life.

To effectively prevent and reduce oil-well repair to fix pumping rod fracture and further reduce the costs of oil-field development, the present study analyzed fatigue fracture samples of pumping rods from an oil field site and used SolidWorks and ABAQUS software to model and statically analyze pumping rods and rod head thread connections. This study also predicted the locations where stress concentration pumping rods are prone to be concentrated during operation and provided guidance for the selection and application of pumping rods.

2 Analysis of onsite pumping rod fatigue damage

2.1 Macroscopic analysis of fatigue damage of sucker rods

Under complex well conditions, the fatigue life of the pumping rod considerably decreased, and several obvious signs of fatigue fracture were observed in the fracture area. Furthermore, a substantial amount of information related to the fatigue fracture process was retained, with obvious morphological characteristics representative of fatigue fracture (Li, 2006). As displayed in Figure 1, a layer of red-brown oil well corrosion products

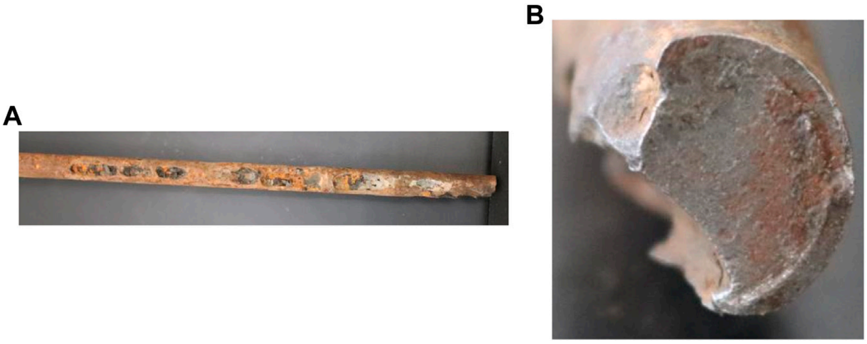

FIGURE 2
Fatigue cross-sectional shape of the pumping rod.

FIGURE 3
Fatigue cross-sectional shape of the pumping rod.

formed on the fracture surface of the pumping rod, and the fracture crack originated on the outer surface of the pumping rod. The area of the transient fracture zone accounts for about 1/5 of the entire fatigue fracture area, indicating that fracture load level was low in the transient fracture zone of the pumping rod; the fracture was relatively less severe, and no necking phenomenon occurred in the brittle transient fracture. Thus, the fracture occurred because of the alternating load and corrosion media under the combined effect of low stress brittle fracture.

As displayed in Figure 2, the pumping rod was fractured from the rod body (As shown on the left A), are several corroded pits (As shown on the right B) were formed in the rod body. The corrosion caused a reduction in the fracture surface area of the pumping rod and in the load-bearing capacity. The formation of corrosion pits in the pumping rod body at the site of a local stress concentration resulted in fatigue cracks at the bottom of the corrosion pits in the cyclic alternating load and corrosion medium. Therefore, fatigue cracks continued to expand forward until the final fracture occurred, and the cycle corresponding to the low circumference corrosion fatigue fracture was relatively short.

As displayed in Figure 3, the fatigue fracture occurred because of manufacturing defects in the pumping rod. Dark black inclusions were observed inside the rod when it was manufactured. During the upward and downward movement, the pumping rod was subjected to alternating load, resulting in gradual sprouting and expansion of the crack source. The fracture occurred rapidly when the fatigue crack expanded to the inclusions.

2.2 Pumping rod material performance analysis

Two typical rod specimens were selected for testing the composition and hardness and analyzing the composition of the crystalline phase of the fatigue damage products to determine the factors influencing the fatigue damage of the pumping rods. The two specimens were numbered 1 and 2, as displayed in Figures 4, 5.

TABLE 1 Chemical composition of specimen.

Sample1	C	Si	Mn	Cr	Mo
	0.328	0.317	0.586	1.036	0.200
Sample2	C	Si	Mn	Cr	Mo
	0.308	0.259	0.527	1.024	0.175
National standard	C	Si	Mn	Cr	Mo
	0.26–0.33	0.17–0.37	0.40–0.70	0.80–1.10	0.15–0.25

2.2.1 Analysis of the chemical composition of pumping rods

A Q4 TASMAN direct reading spectrometer was used to test the composition of specimen No. 1 and No. 2, and the results are displayed in Table 1.

Comparison of the data in Table 1 indicated that the chemical composition of specimen No.1 and No.2 satisfied the national standard.

2.2.2 Analysis of crystalline phase composition of products at fatigue damage

An X-ray diffractometer XRD-6000 was used to analyze the crystal phase composition at the fatigue fracture of specimen No. 1 and No. 2. The experimental conditions were as follows: filtered Cu, high voltage intensity of 40 kV, current of 30 mA, continuous scanning at 2θ angle 10–90° and rate of 10°/min.

Samples obtained from specimen No. 1 and No. 2 were ground into powder and then analyzed for their physical phases. Figures 6, 7 display the XRD patterns of specimen No. 1 and specimen No. 2.

XRD analysis of specimen No. 1 and No. 2 revealed that the primary components of the products formed at the fatigue damage of the pumping rods were FeS compounds, Fe_2O_3, and silicon compounds. The FeS in the specimens was supposed to be produced by the corrosion of H_2S in the well fluid. The production of Fe_2O_3 is closely related to the CO_2 corrosion and HCO_3^- occurring in the well fluid, and the silicon-like compounds should be substances in the formation.

2.2.3 Hardness test

The specimens were intercepted at two typical pumping rod fractures, and the TH-500 Rockwell hardness tester was used to

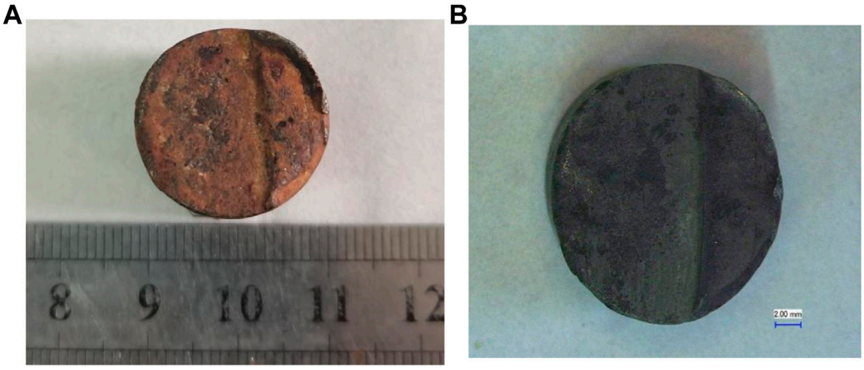

FIGURE 4
Before and after fracture cleaning of specimen No. 1. **(A)** Before fracture cleaning. **(B)** After fracture cleaning.

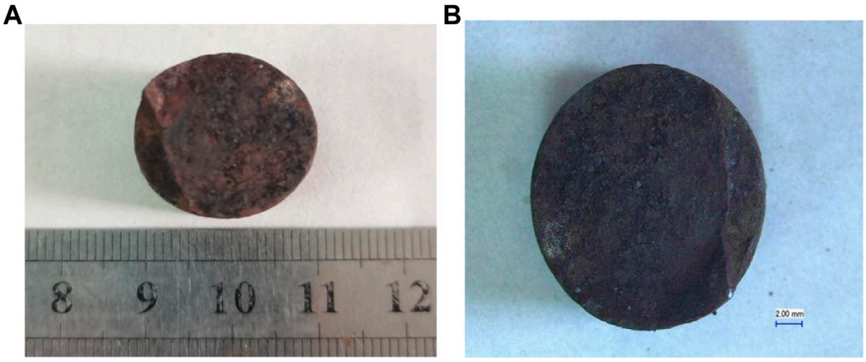

FIGURE 5
Before and after fracture cleaning of specimen No. 2. **(A)** Before fracture cleaning. **(B)** After fracture cleaning.

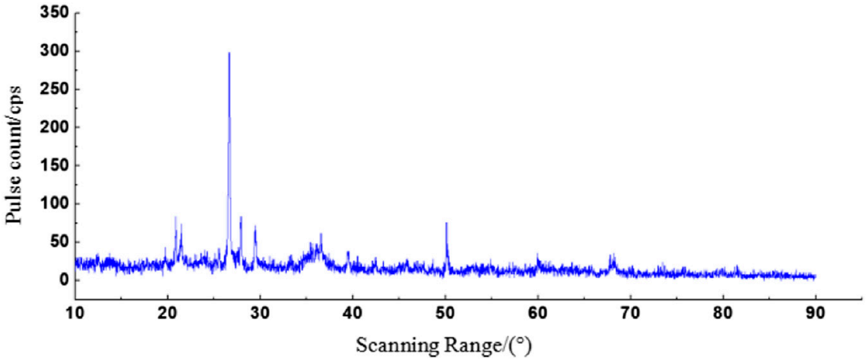

FIGURE 6
XRD pattern of specimen No. 1.

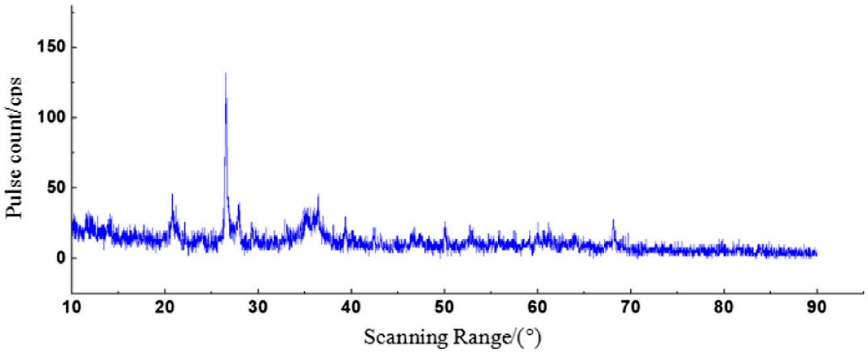

FIGURE 7
XRD pattern of specimen No. 2.

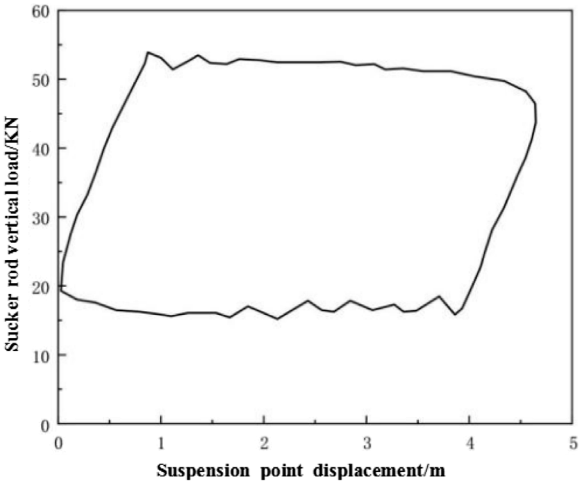

FIGURE 8
Function of the oil well.

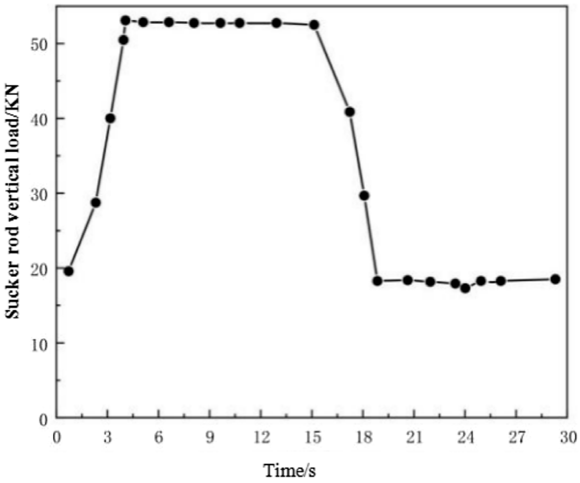

FIGURE 9
Load variation diagram.

conduct multi-point hardness tests and obtain average values; the results are displayed in Table 2.

As illustrated in Table 2, the hardness values of specimens No. 1 and No. 2 were 35.8 HRC and 33.5 HRC, respectively. Therefore, the hardness of the pumping rod after fatigue fracture was consistent with the provisions of SY/T5029-2013 Pumping Rod.

3 Analysis of pumping rod stress distribution

3.1 Analysis of rod stress

The simulation model of the pumping rod was constructed using SolidWorks software. The pumping rod column was subjected to cyclic alternating loads during the upward and downward strokes. Because of the complex downhole working environment, the load on the pumping rod column should have been simplified for fatigue life simulation analysis of the pumping rod column; therefore, a simulation model of the pumping rod was established.

The pumping rod model was constructed using SolidWorks modeling software and imported into the finite element analysis software ABAQUS to correct a few dimensional errors that

TABLE 2 Hardness test results.

Specimen	Measured value					Average value
1	32.6	37.4	35.3	35.6	38.1	35.8
2	31.1	34.8	33.6	33.3	34.5	33.5

TABLE 3 Well production data.

Oil pumping machine model	CYJ12-4.8-73HB	Crude oil density (kg/L)	0.9312	Stroke (m)	4
Pumping rod specifications	HY(φ22 mm)	Crude oil viscosity (MPa.s)	237	Strokes (min-1)	4
Pump hanging depth (m)	1,205	Dynamic fluid level (m)	973	Electric motor power (kw)	22

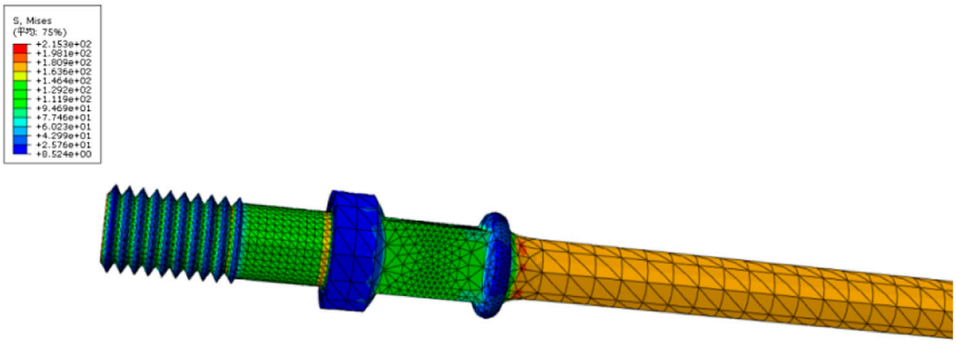

FIGURE 10
Pumping rod equivalent force cloud.

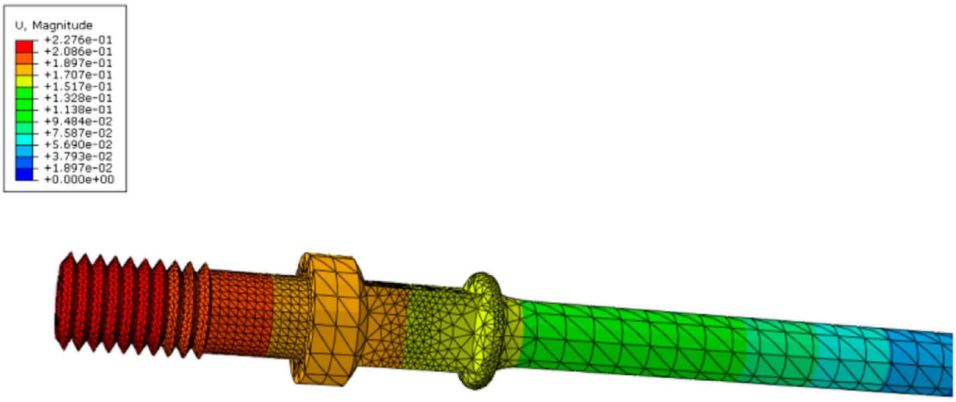

FIGURE 11
Pumping rod deformation cloud.

occurred during the import. The pumping rod model was then meshed, and the tetrahedral meshing method was used because of the complex shape of the threads. The meshes at the wrench side, threads, and upsetting flange of the pumping rod were encrypted.

The alternating load consistent with that used in practice was calculated using the production data of an oil well in Shengli Oilfield; its well production data is displayed in Table 3.

As displayed in Figure 8, the workover diagram of the pumping rod over the length of one stroke was obtained by combining the well production data, the variation in the load of the pumping rod, and the displacement of the suspension point over one stroke (Lin and Smith, 1999). Furthermore, according to the suspension point displacement combined with the motion of the pumping machine, the obtained work graph of the pumping rod was transformed into a curve of load variation with time as displayed in Figure 9.

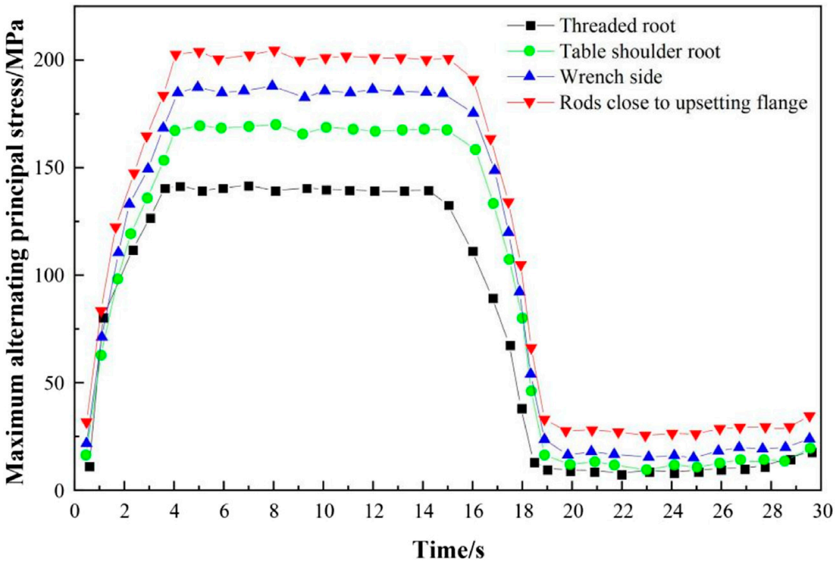

FIGURE 12
Stress variation curves at different locations within one stroke of the pumping rod.

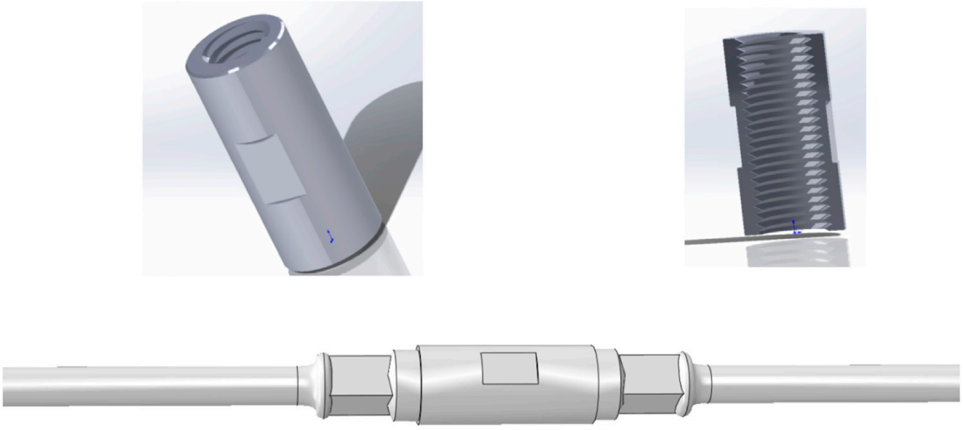

FIGURE 13
Connection diagram of joint and pumping rod.

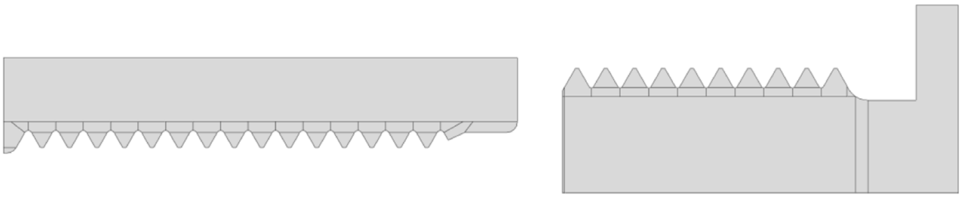

FIGURE 14
Cutting thread surface drawing.

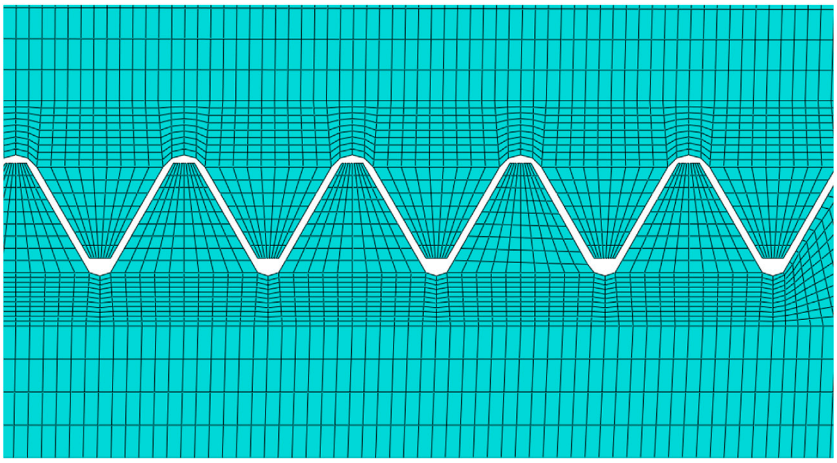

FIGURE 15
Mesh division diagram.

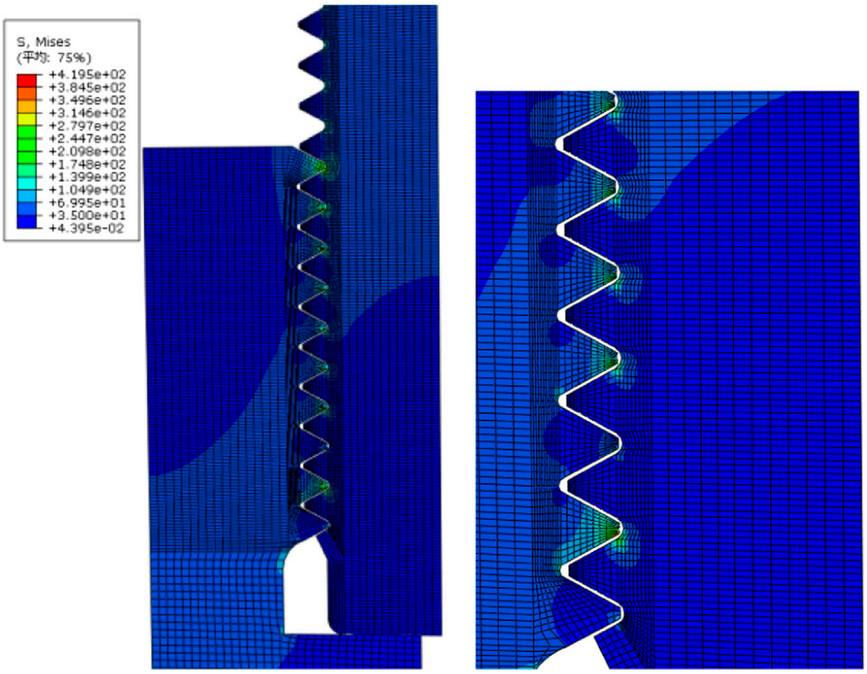

FIGURE 16
Equivalent force cloud on the contact surface of the thread.

The alternating load was applied within one stroke according to the aforementioned calculations, using the amplitude curve in ABAQUS.

As displayed in Figure 10, the cloud map of the maximum principal stress distribution on the pumping rod was obtained through simulation analysis, which revealed that the maximum principal stresses at the root of the threads at both ends of the rod, the root of the shoulder, the wrench side, and near the upsetting flange of the rod were large and hazardous. The shoulder of the unloading groove and the upsetting flange area were relatively safe

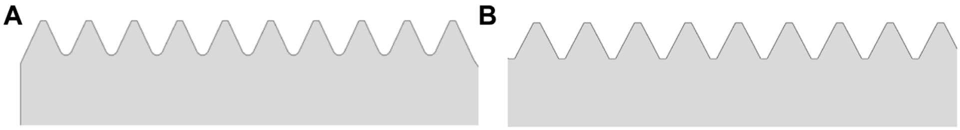

FIGURE 17
Thread root shape.

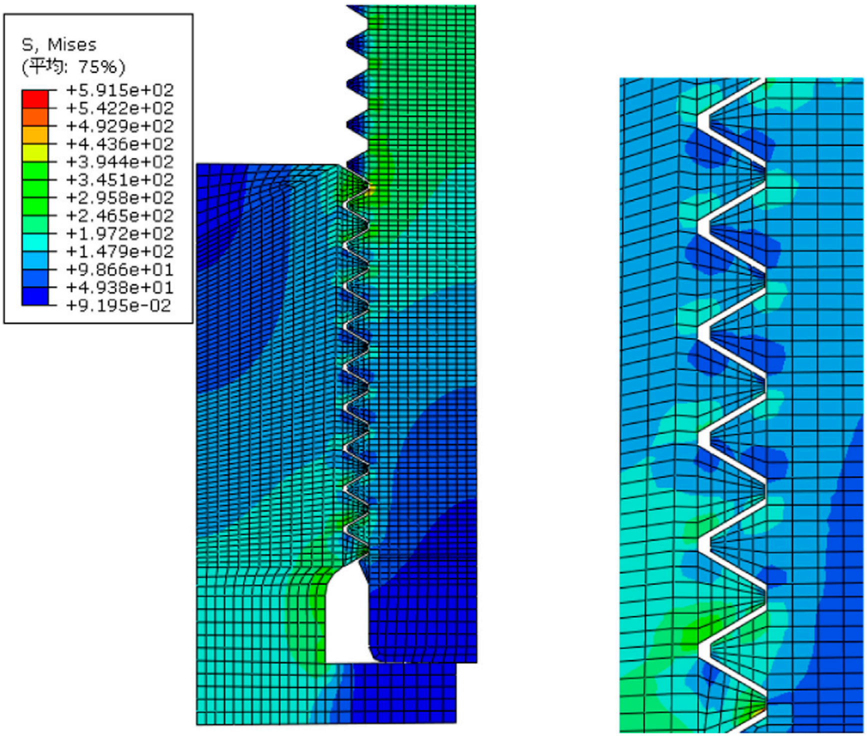

FIGURE 18
Trapezoidal stress cloud of the thread root.

due to the large cross-sectional area and low stress concentration (Zhao, 2007; Bian et al., 2011). As displayed in Figure 11, the deformation cloud was small along the axis of the pumping rod in the working process, where the maximum deformation was 0.2267 mm.

As illustrated in Figure 12, the principal stress variation curves during strokes at the root of the thread, the root of the shoulder, the wrench side, and the rod body near the upsetting flange in the pumping rod were plotted according to the results of static analysis using ABAQUS. The maximum principal stress occurred during the upward stroke and the minimum principal stress occurred during the downward stroke of the pumping rod. Thus, the maximum principal stress was observed near the upsetting flange of the rod body, and the possibility of fatigue damage was the highest at this location of the rod, making it a hazardous section.

3.2 Stress analysis of pumping rod connection section

The geometric model of the pumping rod coupling was constructed using SolidWorks modeling software and imported into ABAQUS software. The coupling was assembled with the pumping rod in the assembly environment, as displayed in Figure 13.

To simplify the complex contact situation at the joint between the pumping rod coupling and the rod head, the 3D model analysis was converted into a 2D stress analysis in the XY plane.

The type of mesh and the density of the mesh directly influenced the accuracy of the finite element analysis of the connecting section of the pumping rod (Hein and Hermanson, 1993; Galeev et al., 2020). Therefore, tetrahedral cells were used

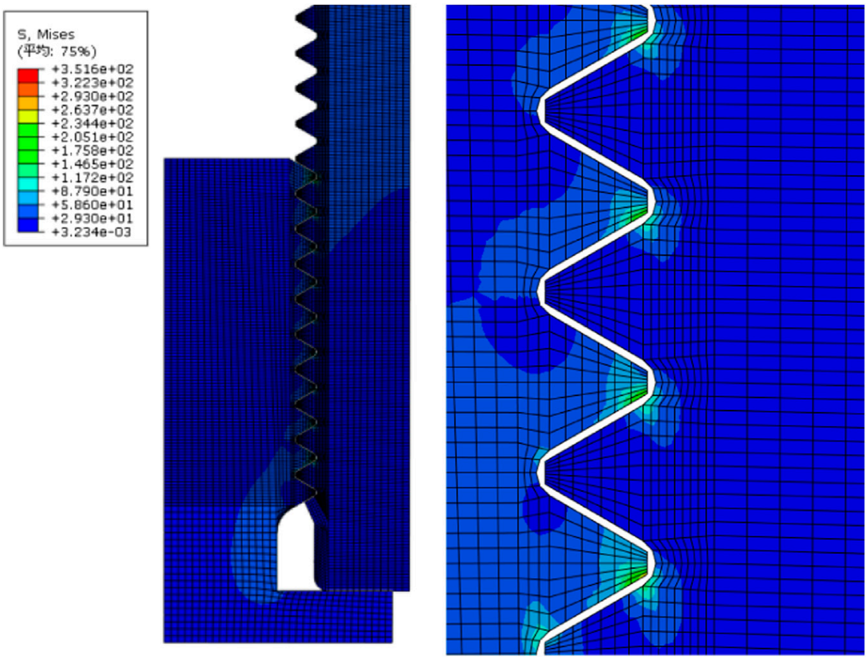

FIGURE 19
Circular stress cloud of the thread root.

for meshing, as displayed in Figure 14. Because the geometry of the threaded surface of the connecting section of the pumping rod was relatively complex, cutting the surface of the threaded surface to a quadrilateral was necessary for meshing; the irregular surface was thus cut into a quadrilateral and then meshed.

As displayed in Figure 15, the mesh at the threads was divided more densely for accurate analysis.

In the finite element analysis of the pumping rod threaded joint, the threaded contact surface was constrained to make the male and female threads work together. Then, a displacement constraint was applied to prevent the radial displacement of the threads during the loading process. Thereafter, the load was applied to one end of the rod coupling, and a uniform load was applied to the right shoulder of the rod head (Xu et al., 2017; Xu et al., 2019).

Figure 16 illustrates the equivalent force cloud on the thread contact surface obtained through finite element analysis.

As displayed in Figure 16, the maximum equivalent force in operation at the threaded connection between the pumping rod head and the pumping rod coupling was observed at the tip of the threaded connection, with a maximum equivalent force of 419.5 MPa, and the equivalent force at other locations other than the threaded connection was smaller.

To analyze the effect of fatigue life of pumping rods with different thread root shapes, two different thread root shapes of rod head joints were simulated in this study, and the models are displayed in Figure 17, where the root shape of the left A thread is trapezoidal and the root shape of the right B thread is rounded.

The shape of the thread root at the rod head had notable influence on the fatigue life of the rod in the broken pumping rods in the oil field site. The comparison between the stress clouds displayed in Figures 18, 19 revealed that stress was more obvious when the thread root shape was trapezoidal, and the maximum equivalent force value was greater than that of the pumping rod with a circular thread bottom because the trapezoidal shape facilitated stress concentration at the sharp corner of the root, resulting in the formation of a crack source and expansion of the crack until fracture (Jha and Arumugham, 2001).

4 Conclusion

Fatigue fracture samples from oilfield sites were analyzed for morphological characteristics, material composition, and hardness at fatigue fracture. The cross-sectional characteristics of the fatigue crack extension were summarized and used to infer the types of fatigue fracture and the influencing factors of the pumping rods. Fatigue fracture with large dimensional changes was primarily observed at certain sites of the pumping rod, for example, on the wrench side, in the transition area, and in threaded parts.

SolidWorks and ABAQUS software were used for modeling and static analysis of the pumping rod and threaded connection of the rod head. The primary stress in the rod body and the likelihood of fatigue damage were the highest near the header flange. In addition, no large deformation was observed along the axial direction during the operation of the pumping rod. The comparison of the stress cloud diagrams of different thread root shapes revealed that the stress readily concentrated at the root tip when the bottom of the thread groove was trapezoidal, thereby causing the formation of a crack source and extension of the crack until fracture.

Data availability statement

The original contributions presented in the study are included in the article/supplementary material, further inquiries can be directed to the corresponding author.

Author contributions

Conceptualization, WC; methodology, XM; validation, WL; formal analysis, SL; investigation, DZ; resources, HZ; datacuration, ZH.

Funding

This work is supported by the National Natural Science Foundation of China (grant no. 52074225). The Graduate Innovation and Practical Ability Training Project of Xi'an Shiyou University (No. YCS22111007).

Acknowledgments

The authors would like to thank all the reviewers who participated in the review, as well as MJEditor (www.mjeditor.com) for providing English editing services during the preparation of this manuscript.

Conflict of interest

WL, was empolyed by PetroChina Xinjiang Oilfield Company.

The remaining authors declare that the research was conducted in the absence of any commercial or financial relationships that could be construed as a potential conflict of interest.

Publisher's note

References

Bian, Y. J., Shi, W., Lao, J. Y., Chen, J., and Sun, S. L. (2011). The analysis on causes of rupture for a sucker rod made of 20CrMo alloy. *Adv. Mat. Res.* 1336, 626–630. doi:10.4028/www.scientific.net/amr.295-297.626

Chen, H., Luo, J., and Tang, K. (1994). Analysis of surface defects and cracks in pumping rods. *Pet. Mach.* 22 (7), 5.

Ding, W., Peng, Z. H., Zhang, Y., Ren, X., Zhang, X., and Wu, C. (2019). Fatigue analysis of HL grade pumping rods based on damage mechanics. *Pet. Drill. Technol.* 47 (04), 47–53. doi:10.11911/syztjs.2019041

Du, X. H., Li, Q., and Li, J. P. (2006). Fatigue strength of oil tubing in pumping engine wells and its fatigue fracture analysis. *Pet. Min. Mach.* 35 (6), 4. doi:10.3969/j.issn.1001-3482.2006.06.020

Galeev, A. S., Bikbulatova, G. I., Boltneva, Y. A., and Sabanov, S. L. (2020). Determination of lower sucker-rod breakage in wells equipped with sucker-rod pumps. *IOP Conf. Ser. Mat. Sci. Eng.* 860 (1), 012029. doi:10.1088/1757-899x/860/1/012029

Gibbs, S. G., and Neely, A. B. (1966). Computer diagnosis of down-hole conditions in sucker rod pumping wells. *J. Petroleum Technol.* 18 (01), 91–98. doi:10.2118/1165-PA

Hein, N. W., and Hermanson, D. E. (1993). *A new look at sucker rod fatigue life*. Houston, Texas: Society of Petroleum Engineers. doi:10.2118/26558-MS

Jha, A. K., and Arumugham, S. (2001). Metallographic analysis of embedded crack in electron beam welded austenitic stainless steel chemical storage tank. *Eng. Fail. Anal.* 8 (2), 157–166. doi:10.1016/s1350-6307(00)00003-0

Li, Z. H., Chen, H. P., and Luo, J. X. (1994a). Finite element analysis of stress intensity factor for elliptical cracks on sucker rod surface. *Pet. Mach.* 22 (12), 5.

Li, Q. (2006). *Reliability study of surface cracks and remaining life of pumping rods*. Harbin, Heilongjiang, China: Harbin Engineering University. doi:10.7666/d.y937152

Li, Q., Wei, J. L., Zhong, B. M., and Qin, H. (1994b). Study of remaining life of pumping rods. *J. Daqing Petroleum Coll.* 1994 (04), 53–56.

Lin, X. B., and Smith, R. A. (1999). Finite element modelling of fatigue crack growth of surface cracked plates: Part II: Crack shape change. *Eng. Fract. Mech.* 63 (5), 503–522. doi:10.1016/s0013-7944(99)00040-5

Ulmanu, V. V., and Ghofrani, R. (2001). Fatigue life prediction method for sucker rods based on local concept. *Erdol Erdgas Kohle* 117 (4), 189–195.

Wang, G. L., and Wei, J. Q. (1994). Study on the remaining life of pumping rod body and transition section. *Mech. Pract.* 16 (1), 4.

Xiang, Y., Lu, Z., and Liu, Y. (2010). Crack growth-based fatigue life prediction using an equivalent initial flaw model. Part I: Uniaxial loading. *Int. J. Fatigue* 32 (2), 341–349. doi:10.1016/j.ijfatigue.2009.07.011

Xu, J., Wu, K., Li, R., Li, Z., Li, J., Xu, Q., et al. (2019). Nanoscale pore size distribution effects on gas production from fractal shale rocks. *Fractals* 27 (08), 1950142. doi:10.1142/s0218348x19501421

Xu, J., Wu, K., Yang, S., Cao, J., and Chen, Z. (2017). "Nanoscale free gas transport in shale rocks: A hard-sphere based model," in Paper presented at the SPE Unconventional Resources Conference, Calgary, Alberta, Canada, February 2017. doi:10.2118/185022-MS

Xu, S. B., and Yuan, X. Z. (1993). Life estimation of pumping rods with transverse cracks on the surface. *Pet. Mach.* 21 (5), 7.

Zhang, H., Liu, H. L., and Sun, Y. M. (2000). Finite element analysis of directional well rod pumping system. *J. Petroleum* 2000 (06), 102–106+32. doi:10.3321/j.issn:0253-2697.2000.06.019

Zhao, H. Q. (2007). *Fracture failure analysis of sucker rods*. Dongying, Shandong, China: Petroleum Mining Machinery. doi:10.3969/j.issn.1001-3482.2007.07.018

frontiers | Frontiers in Earth Science

TYPE Original Research
PUBLISHED 18 January 2023
DOI 10.3389/feart.2022.1015199

OPEN ACCESS

EDITED BY
Jinze Xu,
University of Calgary, Canada

REVIEWED BY
Gang Hui,
China University of Petroleum, China
Yong Tang,
Southwest Petroleum University, China

*CORRESPONDENCE
Mingqiang Hao,
haomingq@petrochina.com.cn

SPECIALTY SECTION
This article was submitted to Economic Geology, a section of the journal Frontiers in Earth Science

RECEIVED 09 August 2022
ACCEPTED 26 September 2022
PUBLISHED 18 January 2023

CITATION
Hao M, Liu X, Xia J and Liu Y (2023), Study of nonlinear flow mechanisms and microfracture networks in low-permeability reservoirs.
Front. Earth Sci. 10:1015199.
doi: 10.3389/feart.2022.1015199

Study of nonlinear flow mechanisms and microfracture networks in low-permeability reservoirs

Mingqiang Hao*, Xuewei Liu, Jing Xia and Yang Liu

Research Institute of Petroleum Exploration and Development, PetroChina, Beijing, China

As efficient technologies boost oil yields and economic benefits, horizontal wells and hydraulic fracturing are widely used in low- permeability reservoirs. To better evaluate the reserve and improve recovery, it is essential to determine fluid flow patterns and transport mechanisms. Laboratory experiments, field operations, and analytical studies have identified nonlinear flow and microfracture networks during the fluid flow in a reservoir with fractured horizontal wells. However, the interactions between nonlinear flow and microfracture networks are still not fully understood. In this study, nonlinear flow experiments and triaxial compression tests were carried out to analyze nonlinear flow characteristics in the vicinity of microfracture networks. By analyzing the effects of microfracture networks on nonlinear flow, two-phase flow, rock stress sensitivity, and artificial fractures, we found that fluid capacity in capillaries with smaller dimensions decreased along with a drop in the pressure gradient, generating a nonlinear flow pattern. The area of nonlinear flow was diminished by the presence of microfractures, which improved flow efficiency and reservoir quality. Considering the size of fracture apertures, microfractures behave more like matrix pores than natural fractures. Also, microfractures significantly increase rock stress sensitivity and reduce the threshold permeability, which enhances fluid flow capacity. This study contributes to our understanding of flow behavior, predicting production and improving recovery in low-permeability reservoirs.

KEYWORDS

nonlinear flow mechanisms, microfracture networks, low-permeability reservoirs, horizontal well, hydraulic fracturing technologies

Introduction

Low-permeability reservoirs have become one of the main targets in the oil and gas industry owing to the rapid development of horizontal well technology (Asadi et al., 2020; Yu et al., 2021; Zeinabady et al., 2022), drilling and steering technology, and fracturing processes (Bunger and Lecampion, 2017; Xu et al., 2019; Heider, 2021; Marsden et al., 2022). Because of the characteristics of low permeability and low porosity, fluid flow patterns and transport mechanisms in low-permeability reservoirs deviate from the traditional flow rules such as Darcy's Law in conventional reservoirs. To better evaluate the reserve and improve recovery, there is a need to clarify fluid flow behaviors in a complex rock structure.

Numerous studies have shown that interactions at the solid–liquid interface have significant effects on flow patterns due to the small pores and narrow throats, as well as the existence of clay minerals in the complicated structures of tight, low-permeability reservoirs (Al-Yaseri et al., 2021; Fatah et al., 2021; Kim and Devegowda, 2022; Zhang et al., 2022). The fluid flow tends to become nonlinear and shows deviations from Darcy's Law. This concept can be verified by a graph of the relationship between the pressure gradient and the flow rate, which can be divided into a pseudo-linear flow section, a nonlinear flow section, and a non-flow section. The two separate endpoints of the nonlinear flow section are the minimum threshold pressure gradient and the maximum threshold pressure gradient. Data from experiments, field operations, and analytical studies have identified nonlinear flow in a low-permeability, porous medium.

Displacement experiments are conventional tools for studying fluid flow properties and microfractures in low-permeability reservoirs. Wang et al. (2011) used a self-designed micro-flux measuring instrument to investigate the low-rate flow pattern in low-permeability samples from the Daqing oilfield. They discovered that low-velocity flow was nonlinear, and apparent fluid permeability depended on differences in the pressure gradient. Using 23 cores from ultralow-permeability reservoirs, Zeng et al. (2011) carried out displacement experiments to determine the flow curves of a single oil or water phase. They confirmed the existence of nonlinearity and pseudo-threshold pressure and declared that nonlinearity increased with lower permeability. Song et al. (2019) studied nonlinear flow characteristics in low-permeability reservoirs using cores with a permeability of 4–8 mD. They attributed their results to flow resistance and solid–liquid interactions. Yu et al. (2022) studied the permeability enhancement due to microfracture networks in hydraulic fracturing, and their results indicated that pore and throat radius were significantly increased due to the existence of microfracture networks.

Field observations are crucial for verifying experimental conclusions. Ji et al. (2008) proposed a method to calculate the oil production in low-permeability reservoirs with non-Darcy seepage flow. The model's predictions were consistent with the field production data in 72 blocks of the Daqing oilfield. They further adapted the nonlinear model to design and evaluate development methods for other low-permeable reservoirs in the Daqing oilfield. Wang et al. (2006) designed and tested several non-Darcy flow models for low-permeability reservoirs with different well patterns in order to maximize oil production by optimizing design parameters such as well spacing. They declared that the oil production of 31 oilfields was significantly improved based on their proposed models.

Analytical analysis is another tool to evaluate the effects of nonlinear phenomena. Ren and Guo (2017) established a nonlinear flow model based on multiple fractured horizontal wells, and their results indicated that nonlinear effects increased the flow capacity and affected the flow pressure. Xu et al. (2017) and Xu et al. (2018) derived a nonlinear flow model based on Knudsen diffusion, slippage, and adsorption for pores and microfractures, and they claimed that the free gas ratio could enhance the nonlinear flow capacity. Bezyan et al. (2019) constructed a nonlinear flow model including adsorption, based on particle swarming optimization, and they showed that taking adsorption into account could lead to higher production. Xu et al. (2019a) and Wu et al. (2020) analyzed the apparent permeability of nanopores in tight sandstone, and discovered that different flow regimens existed at the nanopore scale. Li et al. (2020) calculated the apparent permeability for microfracture networks and concluded that slippage and desorption were beneficial because they led to a later apparent permeability increase. Li et al. (2021) analyzed the impacts of microfracture networks on rock permeability, and their study showed that the permeability was increased, and there was a smaller tortuosity.

Though many studies of nonlinear flow have been performed in the past, the interaction between nonlinear flow and microfracture networks was not focused on in an in-depth investigation. In this research, both nonlinear flow experiments and microfracture experiments were conducted to determine the interactions between nonlinear flow mechanisms and microfracture networks. The potential influencing factors on nonlinear flow such as pore structure were investigated, and the impacts of microfracture networks on nonlinear flow regimens were analyzed. From this analysis, the flow behaviors and mechanisms can be clarified, the production predictions made, and a working method devised for improving recovery in low-permeability reservoirs.

Experimental methods

The experiments on nonlinear flow and microfractures were designed to elucidate their influence on nonlinear flow in low-permeability reservoirs. Table 1 shows the details of experiments using different low-permeability core samples.

Nonlinear flow experiments

Figure 1 illustrates how the nonlinear flow experiments were conducted, mainly involving measurements of pressure and flow rate. The constant pressure method was adopted for these

TABLE 1 Details of nonlinear flow and microfracture experiments.

Order	Type	Measurement	Core sample source
1	Nonlinear flow experiments	Threshold pressure and flow rate	Changyuan, Longxi, Qijianan, Gulongnan, and Puxi oilfield
2	Microfracture experiments	Permeability changing rate	Changqing oilfield

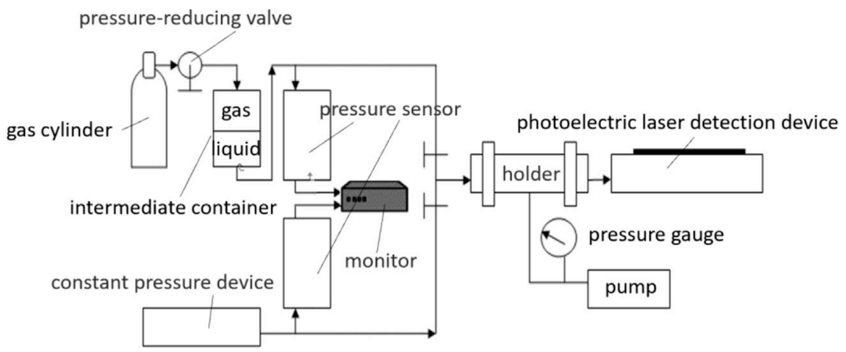

FIGURE 1
Nonlinear flow experiment.

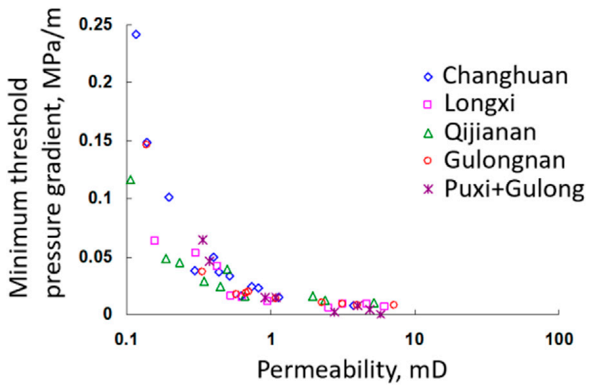

FIGURE 2
Comparisons of threshold pressure gradient of different blocks.

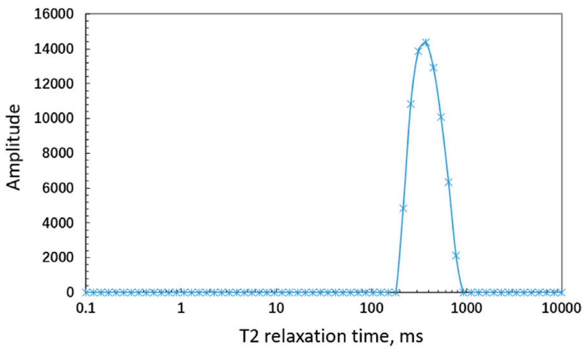

FIGURE 3
T2 spectrum of glycerin in a large space.

experiments. To achieve a constant low pressure, a water column with a height ranging from 20 cm to 150 cm was maintained. The accuracy in this experiment was ±1 cm. For maintaining a constant high pressure of 0.01 MPa–0.7 MPa, pressurized gas was applied above the water. The required constant pressure conditions were satisfied by a combination of these two methods. At the same time, a photoelectric laser detection device was used to measure how long it took for water to flow through a certain pipe, based on which the average flow rate was obtained. The time and length accuracies were 0.1 s and 0.02 mm, respectively. After the readings were made, the nonlinear curve was drawn for the obtained flow rates under different pressures.

As shown in Figure 2, there is a power law relationship between the threshold pressure gradient and reservoir permeability in all blocks. The smaller the permeability, the larger the threshold pressure gradient. The minimum threshold pressure gradient and the pseudo-threshold pressure gradient increased significantly for permeabilities < 1.0 mD.

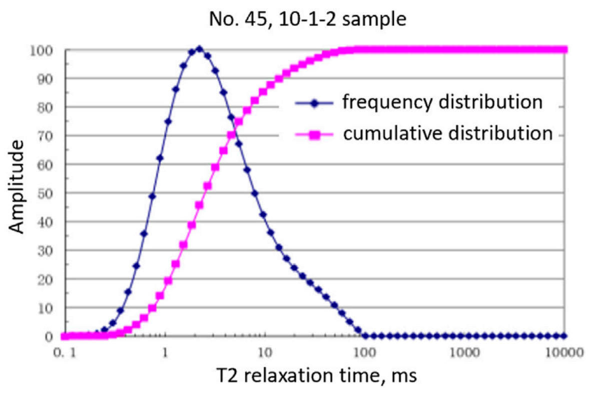

FIGURE 4
T2 spectrum of glycerin in a porous medium.

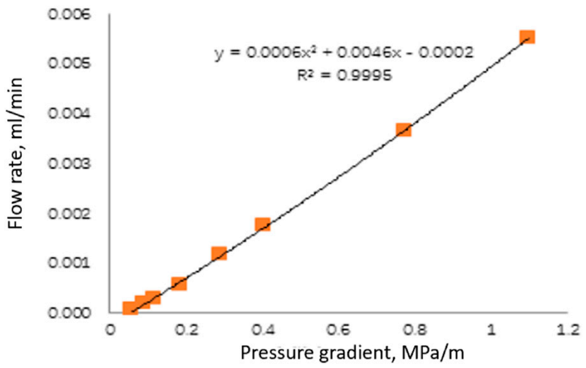

FIGURE 5
Nonlinear flow curves of a block in Huabei oilfield.

Solid–fluid interactions are the dominant mechanism for generating nonlinear flow in low-permeability reservoirs. According to the T2 spectrum of glycerin in a large space (Figure 3), the T2 relaxation fell within the range of 200–600 ms, with a peak at 400 ms. The peak amplitude was 14,000, and the average was around 7000. In glycerin-saturated cores, because of the solid–fluid interactions, the binding energy of glycerin hydrogen protons increased and thus generated a smaller T2 relaxation time (Figure 4). As a result, this led to a decline in T2 relaxation to 0–100 ms, with the peak being reduced to 2 ms. Because of the effect of the solid phase, the reservoir porosity varied, and the number of channels involved in the flow changed along with the pressure, thereby producing nonlinear single-phase flow.

Nonlinear flow characteristics are dependent on the pore structure and follow a flow model. The most frequently used model is the one-dimensional capillary model, in which all the capillaries contribute to fluid flow under a certain displacement pressure. As the pressure drops, the fluid becomes unable to flow in a certain percentage of the capillaries due to solid–fluid interactions, thus causing the flow capacity to drop and nonlinear flow characteristics to appear. For this reason, the capillary sizes and the heterogeneity of the medium are the determining factors of nonlinear flow.

The dual-porosity model is another common flow model. It consists of two continua with different porosity. Pores with larger porosity provide the main flow area, while pores with smaller porosity only partially contribute to the flow. Once a balance is achieved between the two continua, the effects of the smaller pores on fluid flow are insignificant. As the nonlinear flow experiments are conducted during the balanced phase, the results of the nonlinear experiment primarily reflect the effects of the larger pores on the nonlinear flow characteristics. The capillary model is able to capture the flow features in conventional low-permeability reservoirs since most of the pores are relatively large enough to provide flow space. In terms of tight reservoirs, slit pores and intergranular fractures are the primary flow channels. By comparison, only a fraction of nanopores are accessible to fluid flow because of the small pore sizes and the tiny throats. The dual-porosity model is more suitable to describe such flow features.

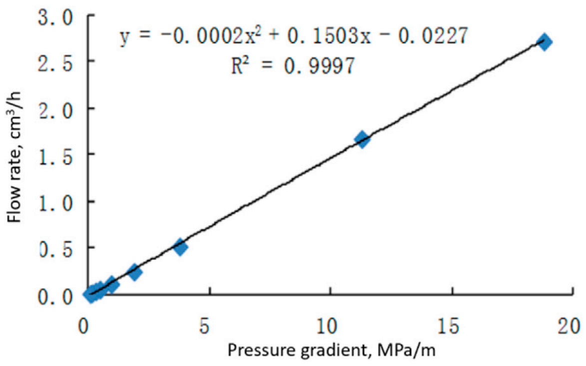

FIGURE 6
T2 nonlinear flow curves of a tight core in Jilin oilfield.

For conventional low-permeability reservoirs, the relationship between the pressure gradient and the flow rate follows a quadratic polynomial, as shown in Figure 5. The fitting accuracy reached >99.9% when a quadratic polynomial was used for the nonlinear flow curves of a block in the Huabei oilfield. The dual-porosity model was used in the case of tight reservoirs, which were usually fitted by using a pseudo-linear flow equation with a threshold pressure gradient. Figure 6 shows that the coefficients of the quadratic term are small enough to be eliminated, leaving a first-order equation that can be used to express the flow features.

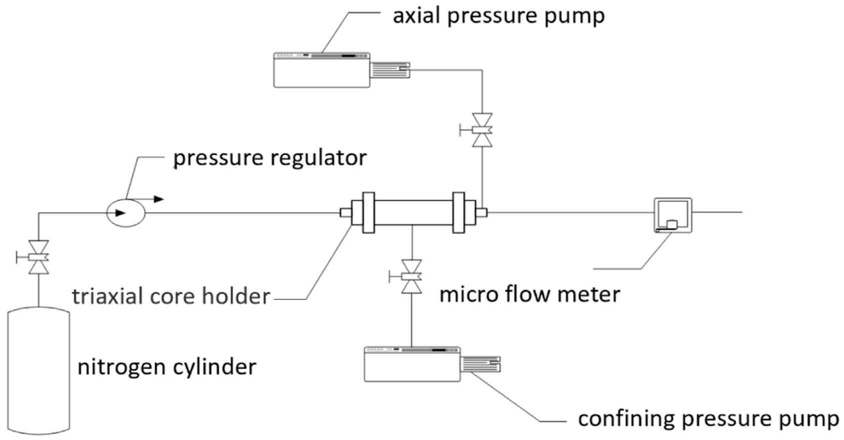

FIGURE 7
Triaxial compression test equipment.

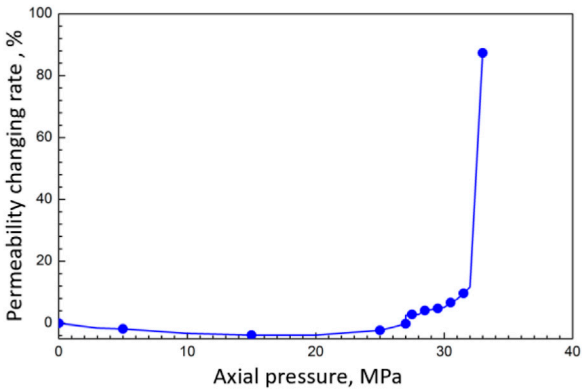

FIGURE 8
Relationship between axial pressure and permeability changing rate.

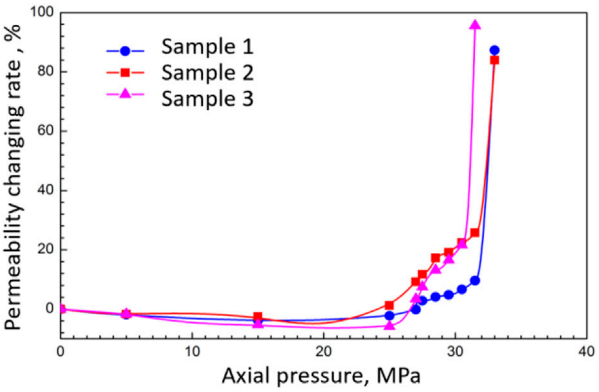

FIGURE 9
Triaxial compression test equipment.

Microfracture experiment

Microfractures are generated under stress that is comparable to the compressive strength or tensile strength of grains and matrix. As the stress increases further, the fractures are formed. Since microfractures are more widely distributed than fractures, it is necessary to understand how fractures are formed and determine the types of fractures and their relationships. The following experiments were focused on the generation of fractures and their influences on fluid flow.

The samples were cylindrical cores collected from the Chang 6 ultralow-permeability sandstone outcrops in the Changqing oilfield. The cores were 25 mm in diameter with a length of 60 mm. The triaxial compression test equipment consisted of a nitrogen cylinder, pressure regulator, triaxial core holder, confining pressure pump, axial pressure pump, and microflow meter (Figure 7). A compression pressure of 3 MPa was applied by means of the pressure pump to increase the axial pressure. The confining pressure of 3 MPa was chosen based on the difference between the *in situ* pressure and the formation pore pressure. In this way, the core shear stress was changed, and fractures were generated. Semi-quantitative monitoring of fractures is carried out by testing the alteration of permeability by nitrogen or water injection. The triaxial compression test equipment was used to create fractures in one-dimension cores under a confining pressure of 3 MPa. Gas permeability was measured at different axial pressures starting from 0 MPa, and the permeability changing rate was calculated (Figure 8).

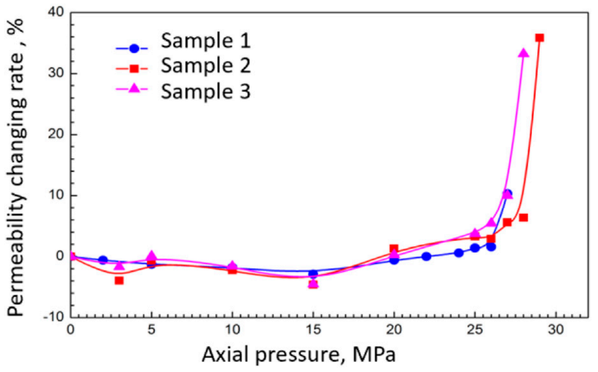

FIGURE 10
Fracture generation curves in water-saturated cores.

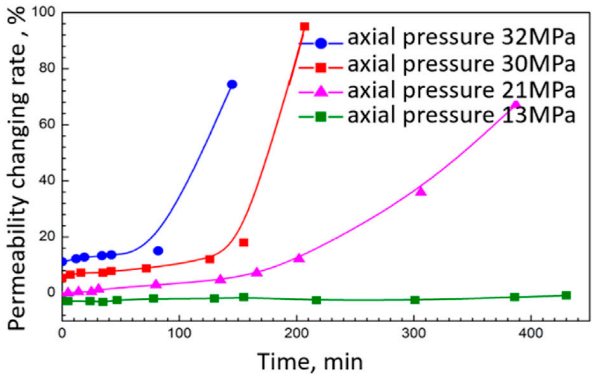

FIGURE 12
Fracture generation curves in slit cores.

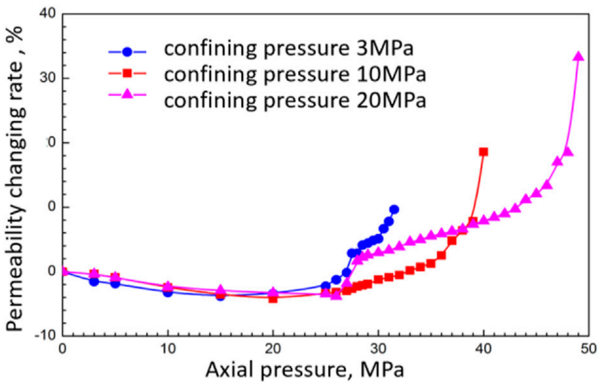

FIGURE 11
Fracture generation curves in dry cores.

The curve showing how the permeability rate increased with axial pressure during parallel core experiments is shown in Figure 9. When axial pressure dropped below 20 MPa, the rock matrix was compressed under stress. Along with the increase in axial pressure, the area of gas flow channels was reduced, and the gas permeability decreased, which was a stress-sensitive stage. If the axial pressure was further increased above 20 MPa, rock failure was initiated, and fractures appeared under the external stress, generating more gas flow channels and correspondingly greater gas permeability. With an axial pressure higher than 30–32 MPa, the gas permeability rose sharply as connected fractures were created in cores. The fracture generation process in reservoirs can be divided into three sequential stages: the grain compression stage, the microfracture generation stage, and the fracturing stage. Only when pressure is high enough can microfractures and fractures appear; otherwise, only grain compression occurs. In other words, when fractures are detected, it means that microfractures have already been generated.

Fracture generation curves in water-saturated cores are presented in Figure 10. Dry cores were converted to brine-saturated cores, and it can be seen that microfractures appeared at axial pressures >15 MPa, which is significantly lower than that for dry cores. The reason for the drop in axial pressure is the lower strength of the cement in cores when soaked in brine. Therefore, the fracture curves obtained with dry cores are quite different from the curves from real reservoirs. The experiment illustrates the effects of confining pressure on fracture generation. It shows the minimum principal stress when the confining pressure is smaller than the axial pressure. Figure 11 presents the experimental results at various confining pressures. The fact that the axial pressure required to generate microfractures increases with a larger confining pressure confirms that stress difference is the reason for fracture generation.

Results and discussion

Analysis of reservoir classification based on fracture types

Different kinds of fractures are generated in different reservoirs because of diverse stress conditions. Reservoirs can be classified according to the fractures generated under various stresses. Under a constant confining pressure, experiments were conducted to measure how permeability rates changed with different axial pressures. It can be concluded from Figure 12 that core permeability rises with time due to the microfractures generated under large axial stresses, while it remains almost constant at a lower axial pressure, implying that no microfractures were involved.

TABLE 2 Fracture generation curves in slit cores.

No.	Porosity, %	Permeability before being fractured, mD	Permeability changing rate after being fractured, %
M2-1	14.3	0.27	6.24
M2-2	14.4	0.24	8.34
M2-3	14.6	0.30	20.89

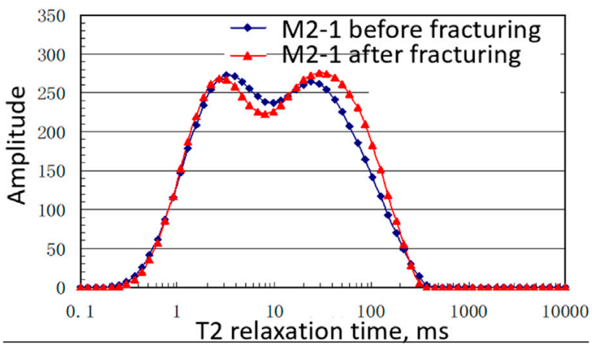

FIGURE 13
T2 spectral comparisons of slit cores before and after being fractured.

Figure 12 shows that permeability remains almost unchanged at an axial pressure of 13 MPa over a period of 400 min, demonstrating that fractures were not present in the rocks. Increasing the axial pressure to 21 MPa results in a slowly rising permeability, which is attributed to the creation of a large number of microfractures. When the axial pressure reaches 30 MPa, the permeability growth rate undergoes a slow rise due to the presence of microfractures, and then rapidly increases with the help of fractures. If axial pressure is as high as 32 MPa, fractures are generated immediately without the development of microfractures. Therefore, reservoirs can be classified into four types based on the development of fractures under different stresses. The first type is reservoirs without fractures, the flow channels of which are mainly composed of pores and throats. Water injection is not efficient since interfacial resistance prevents fluid flow. Belonging to the matrix-dominant reservoirs, this type of reservoir is difficult to develop. The second type includes microfracture-developed reservoirs, in which microfractures are the main flow channels. Water injection can be applied due to the lower interfacial resistance even though it is also matrix dominant. Creating artificial fractures can further improve its recovery factor by improving reservoir connectivity. The third type includes reservoirs with abundant microfractures and fractures. Effective displacement is thus more liable to be achieved because the flow resistance is low and fracture connectivity is high. The fourth type includes fracture-developed reservoirs, in which fractures are dominantly developed. Since the fluid flow around the matrix in the reservoir is due to the high mobility in the fractures, the matrix is not available for exploration.

Analysis of the scale of microfractures

Nuclear magnetic resonance (NMR) methods have been adapted to measure the pore characteristics of rocks before and after being fractured. The results are shown in Table 2 and Figure 13. NMR was carried out after the stress was unloaded. In this case, the alteration in pore size reflects changes in pore scale after microfracture development. The NMR curves in Figure 13 have the following features. First, the total porosity makes little difference. Second, the rises and falls in amplitude of different intervals in the T2 spectra were captured. When the proportion of tiny pores is small, the proportion of larger pores increases. The generated microfractures are the outcome of cement failure around grains, which is conducive to connecting some tiny pores. Also, it is obvious that there are no changes in T2 relaxation time and spectral interval. The scale of the microfractures is still in the range of the original pore scale, and the generated microfractures can be regarded as matrix pores. The role of microfractures outweighs that of fractures in fluid flow since microfractures are created in large numbers.

Analysis of the impacts of microfractures on nonlinear flow

Microfractures have significant impacts on fluid flow, especially nonlinear flow, two-phase flow, and stress sensitivity. A group of cores was compared in experiments to evaluate these effects, which are shown in Table 3 and Figure 14. The results reveal that the nonlinear section shrinks and the nonlinearity decreases, further confirming that microfractures have modified the physical properties of the reservoir, reduced nonlinear flow, and improved fluid mobility.

TABLE 3 Fracture generation curves in slit cores.

No.	Length, cm	Diameter, cm	Porosity, %	Permeability before being fractured, mD	Permeability changing rate after being fractured, %
1–1	4.380	2.526	15.25	1.0492	0
1–2	4.336	2.522	14.66	1.1180	1.98
1–3	4.488	2.528	15.26	0.8488	6.26
1–4	4.722	2.522	15.02	0.8973	9.75

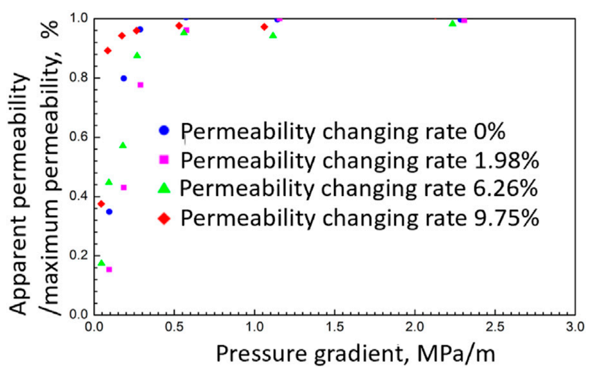

FIGURE 14
Nonlinear flow plot in fractures with different abundance.

Analysis of the impacts of microfractures on two-phase flow

Oil–water relative permeability curves are critical to making oilfield development plans and forecasts. It is generally acknowledged that the two-phase flow area is reduced, and relative permeability curves tend to be straight after fractures are developed. Determining the characteristics of relative permeability curves and fracture development is required to determine the impacts of microfractures on two-phase flow. With the unsteady method, four slit samples were fractured and measured to obtain oil–water relative permeability curves, as shown in Table 4. In comparison with Figure 15, it should be noted that residual water saturation became smaller concomitant with the development of microfractures. Also, with a more developed fracture structure, the two-phase flow region expanded, but it began to decrease when fracture development reached a critical value. Microfractures provide a large number of flow channels, which supplement fluid flow in a conventional porous medium, further improving displacement efficiency. However, if microfractures are overdeveloped, displacement efficiency tends to drop because of the greater heterogeneity. The water relative permeability curve differs in shape with different fracture development degrees. It appears convex before microfractures are initiated and becomes concave in synchrony with the growth of microfractures. It should also be noted that the maximum water relative permeability was improved. Microfractures are predicted to reduce the resistance from the capillary force and improve fluid flow capacity, thereby changing the shape of the curve. Even though their contribution to permeability is limited, microfractures can increase water flow ability and lower the permeability requirement for water-flooding.

Analysis of the impacts of microfractures on rock stress sensitivity

Analysis of the impacts of microfractures on rock stress sensitivity is necessary because fractures are one of the primary causes of stress sensitivity. To start the stress sensitivity experiments, one of two prepared outcrop slit cores is required to be fractured. A regular stress sensitivity test is applied under a changing back pressure, during which rock stress

TABLE 4 Properties of cores before and after being fractured.

No.	Length, cm	Diameter, cm	Porosity, %	Permeability before being fractured, mD	Permeability changing rate after being fractured, %
1–1	5.138	2.522	15.07	3.01	0
1–2	5.216	2.530	14.68	3.23	2.4
1–3	4.910	2.530	14.83	3.15	5.1
1–4	5.188	2.526	14.71	3.06	11.2

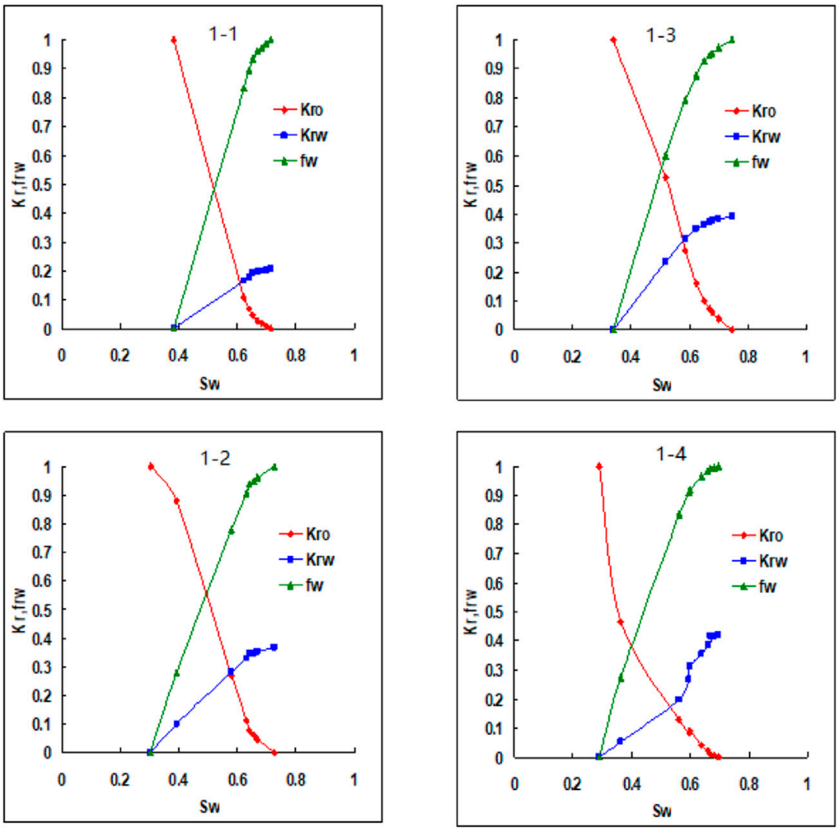

FIGURE 15
Oil–water relative permeability curves of cores before and after being fractured.

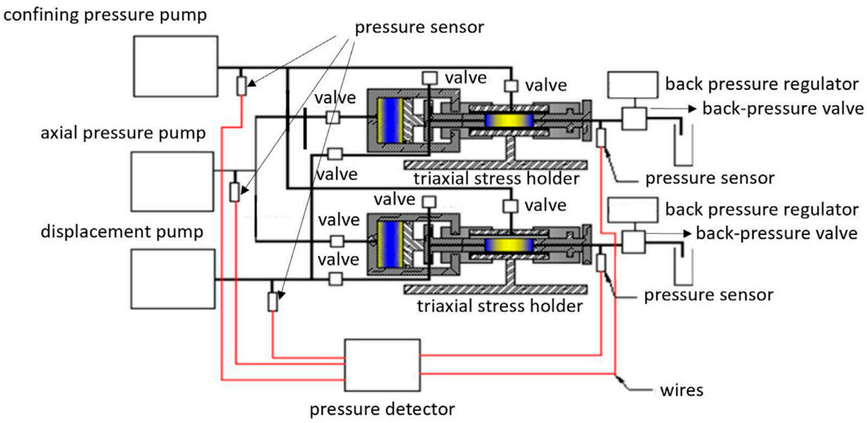

FIGURE 16
Rock stress sensitivity test flow graph of parallel cores.

TABLE 5 Rock properties of the stress sensitivity test.

No.	Core no.	Length, cm	Diameter, cm	Permeability before being fractured, mD	Permeability improvement ratio (%)	Stress sensitivity coefficient at 25 MPa (%)
1	107–1	5.30	2.55	0.060	120	75
2	107–2	5.16	2.55	0.056	0	28

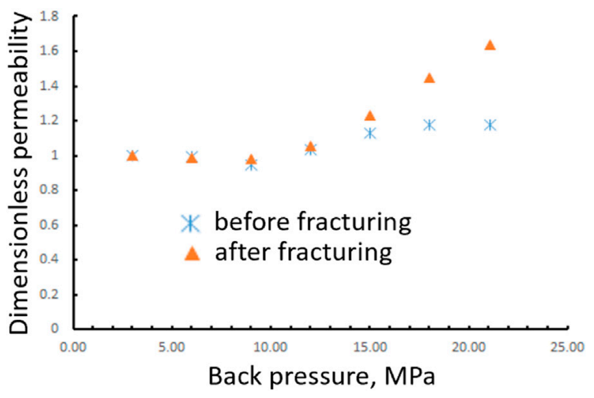

FIGURE 17
Rock stress sensitivity test curve.

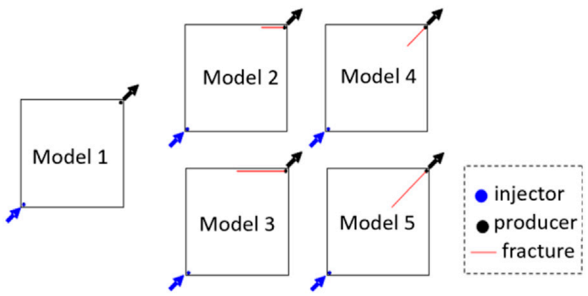

FIGURE 18
Models of artificial fracture experiments.

sensitivity is measured under modified solid and liquid stresses. Since stress sensitivity is mainly caused by changing fluid pressure, it is more reliable to measure it by changing fluid pressure. To reflect the real reservoir conditions, an axial pressure of 25 MPa is required to be loaded. Figure 16 illustrates the experimental flow graphs. The confining pressure pump and the axial pressure pump maintain stable confining pressure and axial pressure. Also, the back-pressure valve alters fluid pressure by changing the exit pressure; the displacement pump displaces fluid at a constant flow rate, allowing the core conductivity to be further tested. At fixed axial pressure, confining pressure, and flow rate, the fluid flow capacity can be measured under different fluid pressures if the back pressure changes, which then corresponds to stress sensitivity. A comparison between the parameters of the two samples in Table 5 confirms that stress sensitivity was much higher after the growth of fractures, which is thus an important parameter for quantitatively evaluating microfractures.

In Figure 17, it is obvious that the magnitude of rock stress sensitivity can be divided into two stages at critical pressure. Stress sensitivity is weak when pressure remains below the critical value. At this time, sensitivity comes from larger throats as fractures remain closed, leading to weak stress sensitivity due to low compressibility and expansibility of the low-permeability layers. Rock stress sensitivity increases sharply after pressure exceeds the critical value and microfractures start to open, providing extra flow channels and producing a larger permeability. The critical value is called reopening pressure. Through comparisons between permeabilities with and without microfractures, it can be concluded that microfractures are the primary cause of rock stress sensitivity.

Analysis of the impacts of artificial fractures on fluid flow

Artificial fractures share common properties in terms of fluid flow, for example, directional flow capacity, directional flow rules, and stress sensitivity. But as artificial fractures are much larger than microfractures, the shared properties are even more obvious and the roles in fluid flow are different from those applying to microfractures. The outcrop planar model was introduced to analyze how artificial fractures perform during fluid flow. Figure 18 describes the five planar models to be used in detail. In each model, there is one injector and one producer. The direction from injector to producer is the main flow direction. One model has no fracture; two models have fractures parallel to the main flow direction; and the other two models have fractures that are at 45° to the main flow direction. The two fractures have different lengths. A brine of 20,000 PPM was injected and Figures 19 and 20 show the water flow rate of the various models and how the water was displaced.

Figure 20 reveals that the swept area expanded when fractures extended at an angle of 45° to the main flow direction, while it

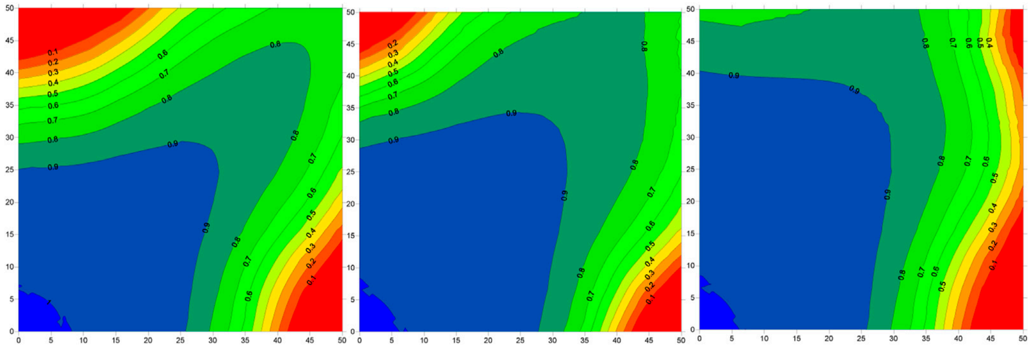

FIGURE 19
Water displacement in models 1, 2, and 3.

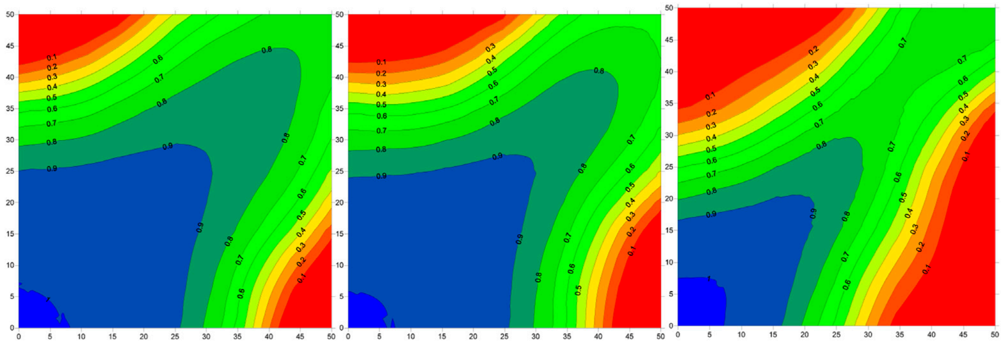

FIGURE 20
Water displacement in models 1, 4, and 5.

decreased when the fractures ran parallel with the main flow direction. It was determined that fractures improved fluid conductivity and increased production area when they acted as extra water producers. By contrast, the swept area shrank when fractures were parallel to the main flow direction since parallel fractures only helped to add fluid conductivity, which intensified the heterogeneity along the flow direction and reduced the sweep efficiency. Accordingly, it was concluded that fractures contributed to higher conductivity; the smaller the angle between fractures and the main flow direction, the more contributions fractures provide for a certain fracture length.

To reduce the possibility of fracturing, horizontal wells are usually drilled vertically into natural fractures to obtain parallel fractures. If natural fractures are viewed as the main flow direction, the direction of the fracturing fractures is then consistent with that of the main flow, which promotes efficient displacement by reducing the pressure drop distance and increasing the local displacement pressure difference. Therefore, it is highly recommended to control horizontal well length during water-flooding.

Conclusion

Based on nonlinear flow experiments and triaxial compression tests, this paper revealed the interactions between nonlinear flow and the microfracture network. It also analyzed the impact of microfracture networks on nonlinear flow, two-phase flow, rock stress sensitivity, and artificial fractures. This paper basically contributes to the sum of knowledge by increasing our understanding of nonlinear flow in a complex fracture network. This paper also determined that the pore structure and stress environment play significant roles in the industrial practice of hydraulic fracturing. The key innovation point of this paper was to integrate the nonlinear flow mechanism with the complex pore-fracture system based on experiment and analysis. The following conclusions can be drawn from the study results:

1) The capillary sizes and medium heterogeneity are the determining factors of nonlinear flow. As the pressure drops, fluid is not able to flow in a portion of capillaries, the flow capacity drops, and its nonlinear flow characteristics appear.

2) Under the impact of microfractures, the nonlinear region shrinks, and the nonlinearity decreases. Microfractures yield better reservoir physical properties, reduce nonlinear flow, and improve fluid mobility.
3) Microfractures can be regarded as parts of matrix pores as their size is still at micro-scale. As the number of microfractures greatly increases, the role of microfractures in fluid flow is more important than that of natural fractures. Under a stress of 21 MPa, the permeability change increases from 10% to 70% in 200 min.
4) Microfractures significantly increase rock stress sensitivity and reduce the threshold of permeability to allow fluid flow. Fractures can be generated immediately if the stress reaches 32 MPa, as shown in this study.

Data availability statement

The original contributions presented in the study are included in the article/Supplementary material; further inquiries can be directed to the corresponding author.

Author contributions

MH: results and discussions XL: nonlinear flow experiments JX: microfracture experiment YL: data analysis.

Conflict of interest

MH, XL, JX, and YL were employed by the company PetroChina.

Publisher's note

References

Al-Yaseri, A., Abdulelah, H., Yekeen, N., Ali, M., Negash, B. M., and Zhang, Y. (2021). Assessment of CO_2/shale interfacial tension. *Colloids Surfaces A Physicochem. Eng. Aspects* 627, 127118. doi:10.1016/j.colsurfa.2021.127118

Asadi, M. B., Dejam, M., and Zendehboudi, S. (2020). Semi-analytical solution for productivity evaluation of a multi-fractured horizontal well in a bounded dual-porosity reservoir. *J. Hydrology* 581, 124288. doi:10.1016/j.jhydrol.2019.124288

Bezyan, Y., Ebadi, M., Gerami, S., Rafati, R., Sharifi, M., and Koroteev, D. (2019). A novel approach for solving nonlinear flow equations: The next step towards an accurate assessment of shale gas resources. *Fuel* 236, 622–635. doi:10.1016/j.fuel.2018.08.157

Bunger, A. P., and Lecampion, B. (2017). Four critical issues for successful hydraulic fracturing applications. *Rock Mech. Eng.* 5, 551–593.

Fatah, A., Bennour, Z., Mahmud, H. B., Gholami, R., and Hossain, M. (2021). Surface wettability alteration of shales exposed to CO2: Implication for long-term integrity of geological storage sites. *Int. J. Greenh. Gas Control* 110, 103426. doi:10.1016/j.ijggc.2021.103426

Heider, Y. (2021). A review on phase-field modeling of hydraulic fracturing. *Eng. Fract. Mech.* 253, 107881. doi:10.1016/j.engfracmech.2021.107881

Ji, B., Li, L., and Wang, C. (2008). Oil production calculation for areal well pattern of low-permeability reservoir with non-Darcy seepage flow. *Acta Pet. Sin.* 29 (2), 256. doi:10.7623/syxb200802018

Kim, C., and Devegowda, D. (2022). Molecular dynamics study of fluid-fluid and solid-fluid interactions in mixed-wet shale pores. *Fuel* 319, 123587. doi:10.1016/j.fuel.2022.123587

Li, T., Li, Q., Hu, Y., XianPeng, X., Feng, X., Zhu, Z., et al. (2021). Quantitative characterization of irregular microfracture network and its effect on the permeability of porous media. *Petroleum Explor. Dev.* 48 (2), 430–441. doi:10.1016/s1876-3804(21)60034-4

Li, Y., Dong, P., and Zhou, D. (2020). "A new dynamic apparent permeability model for gas flow in microfractures of shale," in Asia Pacific Unconventional Resources Technology Conference, Brisbane, Australia, 18-19 November, 2019, 1260–1277. doi:10.15530/AP-URTEC-2019-198302

Marsden, H., Basu, S., Striolo, A., and MacGregor, M. (2022). Advances of nanotechnologies for hydraulic fracturing of coal seam gas reservoirs: Potential applications and some limitations in Australia. *Int. J. Coal Sci. Technol.* 9 (1), 27–18. doi:10.1007/s40789-022-00497-x

Ren, J., and Guo, P. (2017). Nonlinear flow model of multiple fractured horizontal wells with stimulated reservoir volume including the quadratic gradient term. *J. Hydrology* 554, 155–172. doi:10.1016/j.jhydrol.2017.09.005

Song, F., Bo, L., Zhang, S., and Sun, Y. (2019). Nonlinear flow in low permeability reservoirs: Modelling and experimental verification. *Adv. Geo-Energy Res.* 3 (1), 76–81. doi:10.26804/ager.2019.01.06

Wang, X., Yang, Z., Sun, Y., and Liu, X. (2011). Experimental and theoretical investigation of nonlinear flow in low permeability reservoir. *Procedia Environ. Sci.* 11, 1392–1399. doi:10.1016/j.proenv.2011.12.209

Wang, Y., Ji, B., and Guo, W. (2006). Effective development technique for peripheral reservoirs with ultra-low permeability and ultra-low abundance in Daqing Oilfield. *Acta Pet. Sin.* 27 (6), 70–74. doi:10.3321/j.issn:0253-2697.2006.06.015

Wu, T., Pan, Z., Connell, L. D., Camilleri, M., and Fu, X. (2020). Apparent gas permeability behaviour in the near critical region for real gases. *J. Nat. Gas Sci. Eng.* 77, 103245. doi:10.1016/j.jngse.2020.103245

Xu, J., Chen, Z., Wu, K., Li, R., Liu, X., and Zhan, J. (2019). On the flow regime model for fast estimation of tight sandstone gas apparent permeability in high-pressure reservoirs. *Energy Sources, Part A Recovery, Util. Environ. Eff.* 2019, 1–12. doi:10.1080/15567036.2019.1687625

Xu, J., Wu, K., Li, R., Li, Z., Li, J., Xu, Q., et al. (2019a). Nanoscale pore size distribution effects on gas production from fractal shale rocks. *Fractals* 27 (08), 1950142. doi:10.1142/s0218348x19501421

Xu, J., Wu, K., Li, Z., Pan, Y., Li, R., Li, J., et al. (2018). A model for gas transport in dual-porosity shale rocks with fractal structures. *Ind. Eng. Chem. Res.* 57 (18), 6530–6537. doi:10.1021/acs.iecr.8b00021

Xu, J., Wu, K., Yang, S., Cao, J., and Chen, Z. (2017). "Nanoscale free gas transport in shale rocks: A hard-sphere based model," in SPE Unconventional Resources Conference, Calgary, Alberta, Canada, 15-16 February, 2017 (OnePetro). doi:10.2118/185022-MS

Yu, K., Zhao, K., and Ju, Y. (2022). A comparative study of the permeability enhancement in coal and clay-rich shale by hydraulic fracturing using nano-CT and SEM image analysis. *Appl. Clay Sci.* 218, 106430. doi:10.1016/j.clay.2022.106430

Yu, P., Dempsey, D., and Archer, R. (2021). A three-dimensional coupled thermo-hydro-mechanical numerical model with partially bridging multi-stage contact fractures in horizontal-well enhanced geothermal system. *Int. J. Rock Mech. Min. Sci.* 143, 104787. doi:10.1016/j.ijrmms.2021.104787

Zeinabady, D., Clarkson, C. R., Zanganeh, B., and Shahamat, S. (2022). First-time implementation of multiple flowback DFITs ("DFIT-FBA") along a horizontal well. *J. Nat. Gas Sci. Eng.* 102, 104601. doi:10.1016/j.jngse.2022.104601

Zeng, B., Cheng, L., and Li, C. (2011). Low velocity nonlinear flow in ultra-low permeability reservoir. *J. Petroleum Sci. Eng.* 80 (1), 1–6. doi:10.1016/j.petrol.2011.10.006

Zhang, W., Feng, Q., Wang, S., Zhang, X., Zhang, J., and Cao, X. (2022). Molecular simulation study and analytical model for oil–water two-phase fluid transport in shale inorganic nanopores. *Energies* 15 (7), 2521. doi:10.3390/en15072521

Frontiers in
Earth Science

Investigates the processes operating within the major spheres of our planet

Advances our understanding across the earth sciences, providing a theoretical background for better use of our planet's resources and equipping us to face major environmental challenges.

Discover the latest Research Topics

See more →

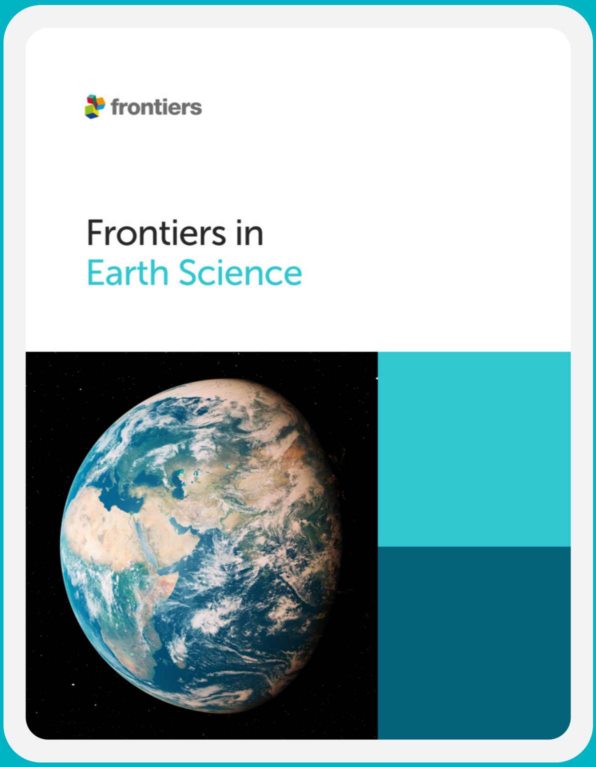

frontiers

Frontiers in
Earth Science

Frontiers

Avenue du Tribunal-Fédéral 34
1005 Lausanne, Switzerland
frontiersin.org

Contact us

+41 (0)21 510 17 00
frontiersin.org/about/contact